

**INTEGRIN SPECIFICITY AS A NOVEL STRATEGY FOR
ENHANCING TRANSPLANTED STEM CELL SURVIVAL AND
TISSUE REPAIR IN VIVO**

A Dissertation
Presented to
The Academic Faculty

By

Amy Yee Lae Clark

In Partial Fulfillment
Of the Requirements for the Degree
Doctor of Philosophy in
Bioengineering

Georgia Institute of Technology

May 2016

Copyright © 2016 Amy Clark

INTEGRIN SPECIFICITY AS A NOVEL STRATEGY FOR
ENHANCING TRANSPLANTED STEM CELL SURVIVAL AND
TISSUE REPAIR IN VIVO

Approved by:

Dr. Andrés J García, Advisor
George W. Woodruff School of
Mechanical Engineering
Georgia Institute of Technology

Dr. Thomas Barker
Wallace H. Coulter Department of
Biomedical Engineering
*Georgia Institute of Technology and
Emory University*

Dr. Edward Botchwey
Wallace H. Coulter Department of
Biomedical Engineering
*Georgia Institute of Technology and
Emory University*

Dr. Robert Guldberg
George W. Woodruff School of
Mechanical Engineering
Georgia Institute of Technology

Dr. Todd McDevitt
Roddenberry Center for Stem Cell
Biology & Medicine
Department of Bioengineering &
Therapeutic Sciences
*Gladstone Institutes and University of
California, San Francisco*

Date Approved: March 30, 2016

In memory of Great Aunt Margaret

ACKNOWLEDGEMENTS

I would first and foremost like to thank my parents for their infinite love and support. Thank you for providing me with everything and anything I ever needed or wanted and setting me up for success. Thank you for working so hard to give us the best life and for all of the things that you did for me, Alan and Jenny that I never knew about. Thank you for supporting me and my decisions, even if you didn't quite agree and for loving me unconditionally. You are my inspiration and my role models. Dad, your resourcefulness and unwavering determination to fix or make everything yourself has empowered my creativity and out-of-the-box thinking. As the original engineer, you are the first and most influential inspiration I had for pursuing engineering. Mom, thank you for always being there for us growing up. Your strength, selflessness, and compassion inspire me to be a better wife, sister, daughter, and (way in the future) mother every day. I love you two and am so grateful for everything you have done for me. No amount of thank you's would ever be enough.

Alan, Jenny, and Nicole - Thank you for being role models for me and for supporting and believing in me, and for bringing Tyler, Kaelyn, Landon and Hudson into our lives. Thank you for helping me settle in to Atlanta when I first got here. Alan, thanks for making fun of me when I was 5 for singing my "Mr. Sun" song wrong— you saved me from pursuing a singing career, but inspired me to pursue biomedical engineering by being the smartest, most compassionate doctor I know. Jenny, thank you for being like a mom to me, in addition to the best sister in the world. Your strength and love for Tyler and KK inspire me every day. And Nicole, thank you for always putting up with Cheng antics.

To my husband, best friend, #1 fan, motivator, and doggy daddy. I would not have finished this PhD so sane and humble and with moderate to high levels of stress (which is pretty good for a PhD) without you by my side these past 6 years. You were my rock, and my dinner provider, and my laundry doer when 14 hour days would turn my brain to mush. Thank you for coming with me to lab in the middle of the night and for always trying to help in any way that you could. I loved that you were so interested in what I did, and would continue to ask me to update you on my project's progress even though the last thing I wanted to do when I got home was talk more science. This PhD is as much yours as it is mine, and I am so grateful I had you by my side the whole way through. I do have to also thank my PhD, though, because it brought me to Atlanta, and brought me to you. So many of our life's milestones are entwined with my time at tech, I can't help but look back fondly at everything, even the most stressful, difficult times in my PhD, but I am so excited to start a new journey with you. Thank you to Cooper, our dog and the light of our lives, for loving unconditionally and whole heartedly, especially on the worst of days.

Thank you to my new family, the Clark/Stearn team for welcoming me with open and loving arms. Kirsten, Andy, Lincoln, and nephew-to-be, I'm so glad to have you in Atlanta. Karn and Phil, it's your turn to make a move now! Thank you always being so supportive and interested in what I do.

I would like to thank my 8th grade science teacher, Mr. Lawson, at Adams Middle School for making science fun and inspiring, and giving me the nickname, "Dr. Cheng." I didn't quite become Dr. Cheng, but Dr. Clark has a nice ring to it. I would also like to acknowledge my high school homeroom and math teacher, Dr. Oppegaard. I think he was

the first PhD I ever really met. Most of us wondered what he was doing teaching high school math, but you could tell he really loved what he did.

To my thesis advisor, Andrés García. I feel very, very fortunate to have had the opportunity to work in your lab. I honestly don't know why you took a chance with me. I didn't know anything about cells or how to pipette when I first started. I just remember your booming voice and corny jokes at the BioE orientation day, and I knew I wanted to join your lab. You have been an unforgettable mentor, teacher, cheerleader, advocate, therapist, and friend. Thank you for everything you have done for me and the lab, for always having an open door, for talking us off ledges, for providing “perspective”, and for always having our best interests in mind. You have always valued our opinion on the direction of our projects and how to make the lab better. Thank you for pushing us and always expecting the best from us on this “bleeding edge of science.”

Thank you to my committee members for their encouragement, guidance and feedback – Dr. Tom Barker for all your knowledge on ECM and what “integrin-specificity” really means. Dr. Ed Botchwey, thank you for your insight into modulating the immune system and for sharing your lab space and equipment. Thank you Dr. Todd McDevitt for your expertise into the world of stem cells, for making an effort to still attend updates and meetings in person all the way from San Fran, and especially for suggesting I convince Andrés to put me on the Stem Cell IGERT when I was interviewing for labs, because without that funding, I don't think I would be where I am today. Thank you Bob Guldberg, for not only keeping IBB great, but also for your input on biomaterials and bone, and all of the bone-related expertise and technical know-how that your lab provides, and for the lair – which was a unique and wonderful grad office experience.

To the PRL vets and staff – Dr. Laura, Dr. Richard, Kim, Altair, Ogeda, Andrea, Brittany, Josh – thank you for always having a smile and a most welcoming hello ready every time I saw each of you. Thank you for keeping the PRL in tip top shape and always going above and beyond to make sure that our research went as smooth as possible. I most definitely could not have done this without y'all.

To the Garcia lab, thank you for humoring me when I would get into my organizational, throw everything out, move everything around moods. I hope I helped make things easier for you, even if I may have made some things more difficult. A special thanks to Jose Garcia and Chris Johnson, who were willing to come in for surgery on a Saturday for me, but instead, spent a Friday night with me in the PRL. Jose, with our projects so similar, we've shared many a frustration over GFOGER and the defect and MSC and the struggle on what to do with your life- thank you for always being willing and ready to help or listen. Chris Johnson, thank you for easing up on the negative nanciness and always pointing out my RBF, and for being our resident MD and my climbing buddy. Devon Headen, D-von, thank you for being our fixer and for your don't-beat-around-the-bush attitude. Efrain – thank you for always trying to round everyone up to do fun things, and keeping the lab like a party with all of your music. Charu Kumar, thank you for everything you've already done for the lab. I know I'll be leaving the lab in good hands.

Dave Dumbauld, you were so friendly and welcoming to me when I was just a little, scared 1st year – so out of character for an Ohio State fan! Ed Phelps, the PEG-mal pioneer, thank you for being a role model, even though I was terrified of you, and for making me remember how much I love rock climbing, and for pushing me to be a better climber. Asha Shekaran, the GFOGER queen, thank you for teaching me the ways of being an A+ surgeon

and for leading the way in GFOGER, and for lighting up the room with your laugh. Ted Lee – you are one of a kind and unforgettable. Thank you for your words of wisdom, and for always rallying the troops. Your stress-free approach to research was something I envied and tried to copy. Stacie Gutowski, thank you for all of your delicious baked goodies and always being prepared with anything anyone might ever need for any situation. Rachel Sy, you were the original lab organizer and always reminded us when we were being slobs. Ram Selvam, thank you for sharing your bench with me from day 1. Apoorva Salimath, I will always remember those nights we stayed up together all night working on our biomaterials proposals. I am grateful to have had such a good friend by my side (literally and figuratively) since the beginning of grad school. Nduka Enemchukwu, you are one of the nicest people I have ever met and will fondly remember the philosophical talks in the TC room. Ankur Singh, you always brought delicious tandoori chicken and are an inspirational scientist.

To the Guldburglars, thank you for sharing all of your things and space with us Garcia folk. Special thanks to Albert Cheng, my long, lost brother, and Hazel Stevens for helping me in my IHC time of need. And special thanks to Hazel for always putting up with Garcia lab shenanigans. Thank you to Angela Lin, for her expertise on all things microCT and biomechanics related, and for helping/not judging when we would lose things in the vivaCT.

To the IBB staff, thank you for keeping everything running in tip top shape. Special thanks to Allen Echols, for always being so friendly and quick to help. Laura Paige, you honor Chris Ruffin's memory well, and have made the BioE program better each year. Steve Woodard, thank you for your help with the new IVIS and your always cheerful

attitude. And to Nadia Boguslavsky, Dalia Arafat, Aqua Asberry, Andrew Shaw, and Xingping Huang (at Emory) for being so helpful and on top of their cores.

To the friends that I have made during my time at GT, thank you for the happy hours, and the beer festivals, and the lunch outings, and potlucks, and wonderful memories. The PhD is as much an emotional and personal challenge as it is technical and intellectual, and without you all by myside to vent, philosophize, laugh with, or let loose, this would not have been an easy, enjoyable ride as it was with y'all in my life.

And lastly, I would like to dedicate this thesis to the memory of my great aunt Margaret, whose recent and unexpected passing was just too soon.

Research reported in this publication was supported in part by the Office of the Director, National Institutes of Health under Award Numbers S10OD016264, R01 AR062368, R01 AR062920, and Cell and Tissue Engineering Training Grant T32 GM008433. This research project was supported in part by National Science Foundation IGERT for Stem Cell Manufacturing DGE 0965945 and the Viral Vector Core of the Emory Neuroscience NINDS Core Facilities grant, P30NS055077.

TABLE OF CONTENTS

ACKNOWLEDGEMENTS	iv
LIST OF TABLES	xii
LIST OF FIGURES	xiii
LIST OF ABBREVIATIONS	xvi
SUMMARY	xviii
CHAPTER 1: SPECIFIC AIMS	1
SPECIFIC AIM 1	2
SPECIFIC AIM 2	3
SPECIFIC AIM 3	4
SIGNIFICANCE	5
CHAPTER 2: LITERATURE REVIEW	6
ENGINEERING THE MATRIX MICROENVIRONMENT FOR CELL DELIVERY AND ENGRAFTMENT FOR BONE REPAIR	6
BIOLUMINESCENT IMAGING	20
CHAPTER 3: ENGINEERING AN INTEGRIN-SPECIFIC CELL MICROENVIRONMENT	22
ABSTRACT	22
INTRODUCTION	24
METHODS	27
RESULTS	33
DISCUSSION	44
CHAPTER 4: THE ABILITY OF INTEGRIN-SPECIFIC HYDROGELS TO PROMOTE HMSC SURVIVAL AND BONE REPAIR IN VIVO	48
ABSTRACT	48
INTRODUCTION	50
METHODS	53
RESULTS	59
DISCUSSION	73
CHAPTER 5: THE EFFECT OF INTEGRIN-SPECIFIC HYDROGELS AND HMSC ON THE REPAIR ENVIRONMENT IN VIVO	82
ABSTRACT	82
INTRODUCTION	84

METHODS.....	86
RESULTS.....	89
DISCUSSION	110
CHAPTER 6: FUTURE CONSIDERATIONS	116
APPENDIX.....	119
KINETICS OF TIME TO MAXIMUM SIGNAL FOR BIOLUMINESCENT IMAGING	119
PUBLICATIONS	120
Well-defined Poly(lactic acids) Containing Poly(ethylene glycol) Side-chains. Macromolecules.....	120
Bone regeneration using an alpha 2 beta 1 integrin-specific hydrogel as a BMP-2 delivery vehicle. Biomaterials.	128
Microphysical space of a liver sinusoid device enables simplified long-term maintenance of chimeric mouse-expanded human hepatocytes. Biomedical Microdevices.	137
Integrin-specific hydrogels functionalized with VEGF for vascularization and bone regeneration of critical-size bone defects. Journal of Biomedical Materials Research Part A.	147
Human Mesenchymal Stem Cell Behavior on Segmented Polyurethanes Prepared with Osteogenic Chain Extenders. Journal of Materials Science: Materials in Medicine.	159
Tobacco Mosaic Virus Functionalized Alginate Hydrogel Scaffolds for Bone Regeneration in Rats with Cranial Defect. ACS Biomaterials Science and Engineering.....	170
REFERENCES	180

LIST OF TABLES

Table 1. Peptide hydrogel components.	28
Table 2. Mesh size calculations for a 4.5% (w/v) PEG hydrogel with 1 mM ligand.....	35
Table 3. Gene targets for qPCR microarray.	88
Table 4. Secreted cytokine levels of hMSC encapsulated in ligand-functionalized hydrogels.	100

LIST OF FIGURES

Figure 1. Schematic of cell delivery vehicle performance <i>in vivo</i> over time.....	9
Figure 2. Schematic of functionalized hydrogel preparation.	12
Figure 3. Protease-degradable PEG hydrogel reaction scheme.	26
Figure 4. Ligand tethering efficiency and material properties.	34
Figure 5. Rheology of varying weight percent hydrogels.....	35
Figure 6. Integrin-specificity of ligand-functionalized hydrogels.	36
Figure 7. Viability and spreading of encapsulated hMSC.	38
Figure 8. Mutated, non-adhesive peptide control for GFOGER does not support cell adhesion.	39
Figure 9. GAOGER does not support spreading of encapsulated hMSC.	39
Figure 10. Western blot for FAK phosphorylation.	40
Figure 11. Encapsulated cell number in ligand-functionalized hydrogels.	41
Figure 12. Proliferation of encapsulated hMSC in ligand-functionalized hydrogels.	42
Figure 13. Osteogenic differentiation of encapsulated hMSC.	43
Figure 14. Murine radial segmental defect.	56
Figure 15. Representative 3-D microCT reconstruction of segmental defect at day 3. Dashed lines show schematic of bone volume quantification.	58
Figure 16. Schematic of luciferase reaction for bioluminescent cell tracking	59
Figure 17. hMSC ^{FLuc} exhibit normal growth and differentiation capacities.	61
Figure 18. Effect of genetically modified hMSC on bone repair.....	63
Figure 19. Effect of PEG weight percent and hMSC delivery on bone repair.	64
Figure 20. Effect of cell dose on cell survival.	65

Figure 21. Effect of cell dose on bone repair.	65
Figure 22. Effect of ligand density on bone repair.	66
Figure 23. $\alpha 2\beta 1$ -specific GFOGER hydrogel enhances hMSC survival.	67
Figure 24. hMSC and $\alpha 2\beta 1$ -specific GFOGER enhance bone repair.	69
Figure 25. hMSC and $\alpha 2\beta 1$ -specific GFOGER result in improved tissue of repaired bone.	71
Figure 26. Human cells detected in defect by immunostaining.	72
Figure 27. Discriminant analysis of gene expression.	91
Figure 28. Hierarchical clustering of <i>in vivo</i> gene expression using Ward's method.	92
Figure 29. Defects treated with hMSC in GFOGER hydrogels exhibit differential gene expression profile compared to other ligands.	93
Figure 30. Gene expression heat map.	94
Figure 31. Differentially expressed inflammation genes <i>in vivo</i> at 1 week.	96
Figure 32. Differentially expressed vascularization genes <i>in vivo</i> at 1 week.	98
Figure 33. Differentially expressed bone genes <i>in vivo</i> at 1 week.	99
Figure 34. Discriminant analysis of cytokine secretion from encapsulated hMSC without IFN- γ /TNF- α stimulation.	102
Figure 35. Hierarchical clustering of cytokine secretion from encapsulated hMSC without IFN- γ /TNF- α stimulation.	103
Figure 36. hMSC in GFOGER hydrogels exhibit differential secretory cytokine profile compared to other hydrogels without exogenous stimulation.	104
Figure 37. Cytokines with significant secretion levels for encapsulated hMSC without IFN- γ /TNF- α stimulation.	106
Figure 38. Discriminant analysis of cytokine secretion from encapsulated hMSC with IFN- γ /TNF- α stimulation.	107
Figure 39. Hierarchical clustering of cytokine secretion from encapsulated hMSC with IFN- γ /TNF- α stimulation.	108

Figure 40. Stimulation masks effect of ligand on cytokine secretion profile.	109
Figure 41. Cytokines with significant secretion levels for hMSC encapsulated in ligand-functionalized hydrogels when stimulated with TNF- α and IFN- γ	109
Figure 42. Roles for mesenchymal stem cells as medicinal signaling cells.	115
Figure 43. Time to maximum signal for individual time points after transplantation. ..	119

LIST OF ABBREVIATIONS

VPM	bi-cysteine peptide crosslinker containing MMP-sensitive cleavage site
RGD	GRGDSPC adhesive peptide
GFOGER	synthetic triple helical ligand containing ‘GFOGER’ hexapeptide sequence
RDG	GRDGSPC nonadhesive scrambled peptide
GAOGER	mutated synthetic triple helical nonadhesive ligand
PEG	polyethylene glycol
PEG-mal	4-arm polyethylene glycol maleimide
DA	diacrylate
IVIS	<i>in vivo</i> imaging system
BMP	bone morphogenetic protein
VEGF	vascular endothelial growth factor
rBMSC	rat bone marrow stromal cells
ECM	extracellular matrix
PHD	prolyl hydroxylase domain proteins
DFO	deferoxamine
DMOG	dimethyloxalylglycine
DTT	dithiothreitol
$\alpha 2\beta 1$	alpha-2 beta-1 integrin
$\alpha v\beta 3$	alpha-v beta-3 integrin
FAK	focal adhesion kinase
EdU	5-ethynyl-2'-deoxyuridine

ALP	alkaline phosphatase
NSG	NOD.Cg-Prkdc ^{scid} Il2rg ^{tm1Wjl} /SzJ
PS	protamine sulfate
PB	polybrene
NuMa	nuclear mitotic apparatus
MANOVA	multivariate analysis of variance
ANOVA	analysis of variance
qPCR	quantitative polymerase chain reaction
RNA	ribonucleic acid
hMSC	human mesenchymal stem cells
hMSC ^{FLuc}	human mesenchymal stem cells expressing firefly luciferase
RFLuc	red firefly luciferase
BLI	bioluminescent imaging
rhTNF- α	recombinant human tumor necrosis factor alpha
rhIFN- γ	recombinant human interferon gamma
BSA	bovine serum albumin
MMP	matrix metalloproteinase

SUMMARY

Despite the promising clinical results for the use of human mesenchymal stem cells (hMSC) in musculoskeletal defect treatment, inadequate control of cell survival, engraftment and fate limits the success of this cell-based therapy. Integrin-mediated cell adhesion plays a central role in tissue formation, maintenance, and repair by providing anchorage forces and triggering signals that regulate cell function. We hypothesize that biomaterials presenting integrin-specific adhesive motifs will direct hMSC engraftment and function to improve bone repair. The objective of this project is to engineer bioartificial hydrogels presenting integrin-specific ligands as biomimetic cell delivery vehicles for enhanced in vivo engraftment and function – an innovative strategy as it focuses on engineering specificity to integrin receptors to promote survival and cell-based repair without the use of exogenous growth factors.

We investigated the performance of a cell-mediated degradable hydrogel functionalized with integrin-specific ligands in supporting the survival of transplanted hMSC and tissue repair in a segmental bone defect. This was accomplished by incorporating the adhesive $\alpha 2\beta 1$ integrin-specific GFOGER ligand, adhesive $\alpha v\beta 3$ integrin-specific RGD ligand, non-adhesive RDG peptide, or non-adhesive GAOGER peptide combined with human mesenchymal stem cells in a protease-degradable PEG-maleimide hydrogel. Cell survival was tracked through transgenic luciferase expression and bone repair was monitored by microcomputer tomography. We hypothesized that hydrogel delivery vehicles that promoted cell viability in combination with the pro-osteogenic properties of the carrier would result in superior bone repair. We found that

$\alpha 2\beta 1$ -specific GFOGER-functionalized hydrogels promoted enhanced hMSC survival and bone repair, with differential expression of vascularization and inflammation-related genes *in vivo* compared to RGD- or RDG-functionalized hydrogels, highlighting integrin-specificity as an important consideration in the design of cell delivery vehicles for engraftment and tissue repair. We have generated new insights into transplanted hMSC survival, engraftment and function in a bone repair model allowing for direct correlations among hydrogel formulation and integrin specificity, transplanted cell survival, and bone repair outcomes. This work is significant and innovative because improved design of cell delivery vehicles may improve efficacy of current hMSC therapies in the clinic.

CHAPTER 1: SPECIFIC AIMS

INTRODUCTION

Cell-based strategies have emerged as promising therapies for the treatment of diseased or injured organs. Adult human mesenchymal stem cells (hMSC) constitute a critical component of the hematopoietic stem cell niche (microenvironment) in the bone marrow and have the potential to differentiate into multiple lineages, including bone, cartilage, and fat, while also providing immunomodulatory functions. Although hMSCs have shown promising results in clinical trials, inadequate control of cell fate and cell engraftment in host tissues significantly limits the success of this cell-based therapy. Integrin-mediated cell adhesion plays a central role in tissue formation, maintenance, and repair by providing anchorage forces and triggering signals that regulate cell function.

The objective of my project is to **engineer advanced materials using biofunctional hydrogels, integrin-specific ligands, and *in vivo* imaging for stem cell differentiation, delivery, and engraftment.** I hypothesize that **biomaterials presenting integrin-specific adhesive peptides will promote hMSC survival leading to improved engraftment and bone repair.** The proposed research is innovative because it focuses on engineering specificity to integrin receptors to promote stem cell survival and tissue repair without the use of exogenous growth factors, integrates novel *in vivo* imaging, and utilizes novel hydrogel chemistry. This project will establish a defined system for hMSC differentiation, delivery and engraftment to treat injured tissues. The following specific aims will be pursued:

SPECIFIC AIM 1

Engineer integrin-specific hydrogels that support hMSC adhesion, survival, proliferation and differentiation *in vitro*.

Two ligands of varying integrin-binding specificity will be used to examine the role of integrin specificity on hMSC function: RGD for $\alpha V\beta 3$ integrin and collagen-mimetic GFOGER peptide for $\alpha 2\beta 1$ integrin. To incorporate these ligands and protease-degradable cross-links, Michael addition chemistry will be utilized in a four-arm 20 kDa polyethylene glycol-maleimide (PEG-mal) system in which ligands and crosslinking peptides are functionalized with cysteine residues. This system holds many advantages over PEG-diacrylate (DA) hydrogels (currently, the most widely used hydrogel chemistry) in that it avoids the use of cytotoxic free radicals and UV light, enables *in situ* crosslinking for *in vivo* delivery, has a well-defined structure and allows for stoichiometric incorporation of bioactive peptides, and avoids large degradation products consisting of non-degradable DA backbone. Degradable cross-links allow for cell migration, and varying the density of polymer controls hydrogel stiffness and degradation rate. Control groups include gels with scrambled or mutated, non-adhesive ligands. Ligand-incorporated hydrogels will be characterized in terms of material properties and specificity for integrins $\alpha V\beta 3$ and $\alpha 2\beta 1$. We will also determine the effect of ligand on cell functions such as proliferation, survival, osteogenic differentiation, and the immunomodulatory properties of encapsulated hMSC.

SPECIFIC AIM 2

Evaluate the ability of integrin-specific hydrogels to promote hMSC survival and bone repair *in vivo*.

Using hydrogels presenting pro-osteogenic ligands and protease-degradable sites, hMSCs will be delivered to a non-healing segmental defect in the radii of immunodeficient mice. This rigorous bone repair model holds many advantages over other models – it allows me to evaluate the efficacy of my gels without spontaneous defect healing; the ulna provides sufficient stabilization for the defect, thus no need for additional fixation hardware; and the smaller animal model allows for easy use of *in vivo* imaging approaches. The survival and engraftment of transplanted hMSCs in integrin-specific hydrogels will be monitored using a luciferase reporter system. hMSCs will be transduced with a constitutively active red firefly luciferase (RFluc) gene to track transplanted cell numbers. This system reduces the number of animals, animal-to-animal variability, and permits direct correlations between hydrogel formulations, transplanted cell numbers, and bone repair. Following luciferin injections, bioluminescence will be quantified in the whole mouse with an *In Vivo* Imaging System (IVIS). At the end point of the study, hydrogels will be explanted and analyzed for cell numbers, differentiation and functional markers (bone, cartilage) using immunohistochemical techniques. Mineral quality and amount will be assessed using live micro-computer tomography and immunohistochemistry. I hypothesize that hydrogel delivery vehicles that promote cell viability in combination with the pro-osteogenic properties of the carrier will result in superior bone repair.

SPECIFIC AIM 3

Investigate the effect of integrin-specific hydrogels and hMSC on the repair environment *in vivo*.

The ability of integrin-specific ligand-functionalized hydrogels and hMSC to modulate the *in vivo* repair environment will be characterized by vascularization and inflammation analyses. The effect of integrin-specific ligands on the inflammatory environment will first be characterized *in vitro*. hMSC will be encapsulated in ligand-functionalized hydrogels and stimulated with pro-inflammatory cytokines. Secreted factors in the conditioned medium will be analyzed for multiple cytokines using magnetic bead-linked immunoassays (Luminex xMAP). Hydrogel formulations identified in aims 1 and 2 will be used to deliver hMSC in ligand-functionalized hydrogels to the murine radial segmental defect. Gene expression will be performed 1 week after cell transplantation. Genes related to vascularization, wound healing, inflammation, bone, survival, and matrix interactions will be analyzed on explanted tissue using high-throughput quantitative polymerase chain reaction (qPCR) micro array technology (Fluidigm). Lastly, the ability of integrin-specific ligands and hMSC to enhance vascularization in the defect will be assessed. Vessels will be perfused with a radio-opaque contrast agent and visualized using micro-computer tomography. I hypothesize that hydrogel delivery vehicles that promote cell survival and bone repair also modulate the inflammatory environment and enhance vascularization.

SIGNIFICANCE

Although hMSC have shown promising results in clinical trials, inadequate control of cell fate and cell engraftment in host tissues significantly limits the success of this cell-based therapy. This work is significant and innovative because improved design of cell delivery vehicles may improve efficacy of current hMSC therapies in the clinic. This work is innovative because it focuses on engineering integrin-specificity to promote transplanted cell survival and modulate the repair environment for better tissue repair without the use of exogenous growth factors. Integration of innovative *in vivo* imaging approaches with my engineered hydrogels will generate new insights into transplanted hMSC survival, engraftment and function in a relevant non-healing bone repair model and allow for direct correlations among hydrogel formulation, transplanted cell numbers and differentiation, and bone repair outcomes.

CHAPTER 2: LITERATURE REVIEW

ENGINEERING THE MATRIX MICROENVIRONMENT FOR CELL DELIVERY AND ENGRAFTMENT FOR BONE REPAIR ¹

Clinical significance

Cell-based therapies represent promising strategies for tissue repair, particularly in cases in which host cells, due to disease, age, or excessive trauma, are unable to repair the defect or deficiency alone, even with additional delivered therapeutics. Current cell therapies fail to address long term engraftment or delivery timing and location. For instance, cell therapies for myocardial infarction typically consist of a cell suspension delivered by injection or infusion and, although proved to have an excellent safety profile, efficacy has been inconsistent with modest improvements at best with long term engraftment rates of less than 1% as the majority of delivered cells die or are washed away as quick as 1 hour post transplantation [1,2]. These methods not only fail to retain cells at the delivery site [3], but they also fail to address the effects of specific delivery location and timing on efficacy, factors shown to influence stem cell survival and functional outcome in injuries such as traumatic brain injury [4]. Long term cell engraftment has been shown to correlate with enhanced therapeutic outcomes [5-7], and has also been shown to be greater in cases in which cells are delivered in an appropriate biomaterial carrier versus in media alone [8]. For example, when alginate-encapsulated human mesenchymal stem cells (hMSC) were delivered in a hydrogel patch to injured myocardium, not only were

¹ Adapted from: Cheng AY, García AJ. Engineering the matrix microenvironment for cell delivery and engraftment for tissue repair. *Current Opinion in Biotechnology*. 2013;24(5):864-71.

improved cardiac function and reduced scarring observed compared to non-encapsulated hMSC in a hydrogel patch, but significantly improved retention of hMSC at the injury site was also observed compared to non-encapsulated hMSC in a hydrogel patch and direct injection of hMSC [2]. The combination of encapsulation and hydrogel patch may have shielded the cells from the host immune system and prevented clearance of the cells resulting in prolonged cell retention and a prolonged paracrine effect. Thus, in many cell therapy applications, an appropriate carrier must be used to deliver transplanted cells and promote cell engraftment and function for a successful outcome.

The ideal carrier would provide the appropriate microenvironment for the interactions between transplanted and host cells. For tissue repair, as shown in **Figure 1**, the ideal carrier would result in 1. Transplanted cells integrated with host tissue and vascularization; 2. Replacement by healthy, normal tissue over the course of healing; and 3. Complete function restored.

Nonunion bone defects and bone graft substitutes

Although bone has the innate ability to remodel and regenerate, large, non-healing bone defects and non-union fractures remain a significant clinical problem. Current clinical treatments for large bone defects (defect length > 3 cm in forearm, > 6 cm in femur) due to disease, injury or tumor resection include bone grafting techniques using materials such as autografts or allografts, but these techniques exhibit high failure rates [9]. Autografts are harvested from a different site in the same patient and contain the appropriate cues, cells, and matrix for osteogenesis, but donor site morbidity and pain and limited tissue availability limit this treatment. Autografts also rely on the regenerative capacity of a patient's own cells which may be reduced due to age or disease. Allografts are harvested

from a different individual and may address some of the sourcing limitations of autografts, but carry a risk of disease transmission and immune rejection and are often processed, thereby reducing the biologic activity or mechanical properties of the graft [9]. Protein therapeutics have emerged as a promising alternative to auto- and allografts, particularly bone morphogenetic protein- (BMP) 2 and 7. Since the FDA's approval in 2002, BMPs have mainly been used for vertebral fusions with success rates similar to autografts minus the need for donor tissue. However, the supraphysiological dose required for the stimulation of bone formation leads to complications such as neuropathology, ectopic bone formation, and severe inflammation [10].

Mesenchymal stem cells

Mesenchymal stem cells (MSC) have emerged as a promising cell source for regenerative medicine applications for musculoskeletal deficiencies [11,12]. They are usually harvested from bone marrow, but have also been isolated from adipose tissue, fetal tissue, and skeletal muscle [13] and are multipotent, hypoimmunogenic, and can home to injured tissues [14]. MSC transplantation has been shown to enhance bone, cartilage, and intervertebral disc repair in clinical and preclinical models [15,16], but engraftment rates of delivered hMSCs are extremely low (<3%) [12]. The lack of information regarding cell fate after transplantation, cell dose, cell source, and appropriate scaffold properties limits the therapeutic effect of hMSCs for treatment of large musculoskeletal defects.

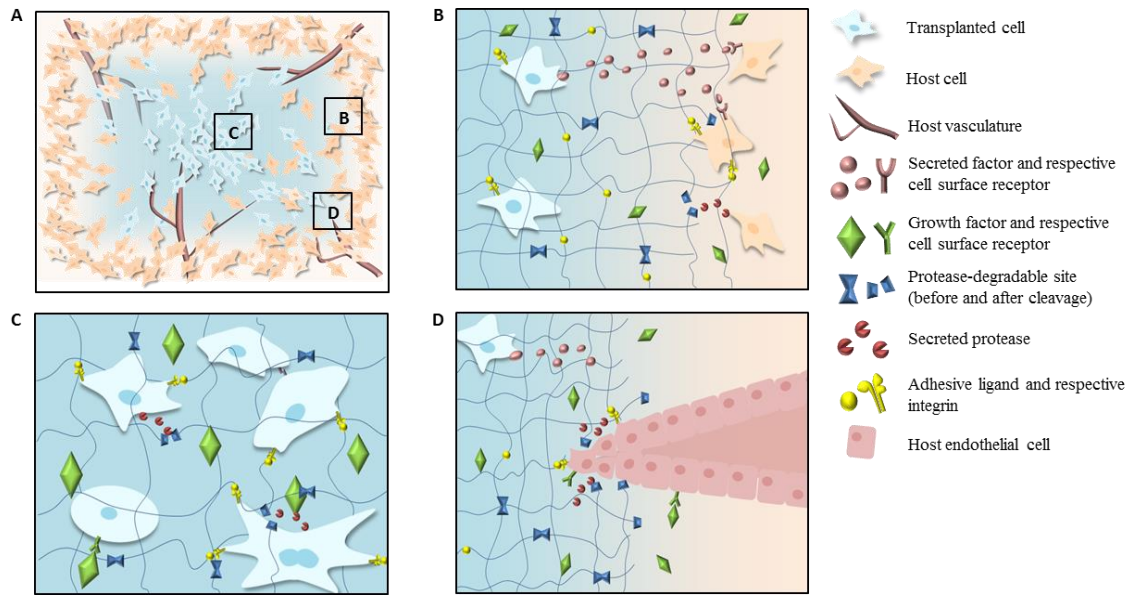


Figure 1. Schematic of cell delivery vehicle performance *in vivo* over time. A) Overview of integration of vehicle and transplanted cells into host tissue. B) Transplanted cells interact with host cells in many ways. Transplanted cells may release trophic or chemotactic factors that activate host cells and host cells in the injury site may release factors that drive differentiation or behavior of the transplanted cells as well as remodel the delivery vehicle and implant site. As cells degrade the matrix by releasing proteases, growth factors and other therapeutic molecules are released on demand. C) In response to specific adhesive ligands, growth factors, and/or soluble cues from the tissue environment, transplanted cells in the matrix undergo proliferation, cell-cell communication, migration and differentiation as the cells degrade the matrix. D) In response to pro-angiogenic growth factors (delivered or cell-secreted) and facilitated by adhesive ligands and matrix degradability, host vasculature infiltrates the matrix delivering nutrients to the transplanted cells and/or facilitates cell recruitment and trophic factor transport.

In addition to their differentiation potential, hMSC have been reported to also provide anti-apoptosis, angiogenesis [17], growth factor production [18], neuroprotection [19], anti-fibrosis [2,20], and chemo-attraction functions [21]. They also exhibit immunosuppressive properties in response to allogeneic immune responses [22,23] and anti-inflammatory effects after activation with pro-inflammatory cytokines [24,25] secreted by inflammatory cells or through exogenous stimulation in culture.

One strategy to enhance MSC function has been forced aggregation of cells into aggregates or spheroids. Aggregation and culture of 3D hMSC spheroids has been shown to enhance anti-inflammatory and paracrine functions. hMSC spheroid or aggregates exhibited increased PGE2, TGF- β 1 and IL-6 secretion and high suppression of macrophage-secreted TNF α compared to monolayer controls [26], increased TSG6 expression [27], and rescued expression of CXCR4, a lymphocyte and hematopoietic stem cell homing receptor which is lost during monolayer culture [28]. Spheroid culture of hMSC also significantly enhances differentiation potential resulting in increased osteogenic and adipogenic differentiation. These enhanced properties may be due to increased cell-cell contacts in the microtissue environment that more closely mimic the natural environment in the body compared to monolayer culture.

Cell-delivery vehicle materials

Materials used as delivery vehicles include natural materials, synthetic polymers, and ceramics. Natural materials such as purified collagen, hyaluronic acid, alginate, and chitosan have been extensively used in regenerative medicine and tissue engineering. Materials derived from natural sources can be biologically active, promote cell adhesion and growth, and enzymatically or hydrolytically degradable. However, natural materials display lot-to-lot variability, risk of immunogenicity and pathogen transmission, and structural complexity that renders modifications difficult. Calcium phosphate ceramics, namely tricalcium phosphate, hydroxyapatite, and bioactive glasses, are of clinical interest in bone tissue engineering due to their similarities to the inorganic phase of bone. Although these ceramics have been shown to enhance osteoblast adhesion and differentiation, their use is limited due to their brittleness and difficulty in shaping for implantation, thus, most

cell-delivery strategies that incorporate ceramics do so in combination with either natural or synthetic polymers as a composite material [29-31]. Synthetic polymers provide an alternative to natural materials as cell-delivery vehicles. Because of their defined chemical composition, synthetic materials are often reproducible and can be modified to control material properties such as degradation rate, mechanical properties, and shape. As most synthetic polymers lack cell adhesion sites, polymers usually need to be chemically modified to support cell adhesion and other bio-functionalities, and this yields the opportunity of engineering specificity into the material [8,32]. Tuning of the degradation rate is a strong advantage over ceramics and natural polymers, as synthetic polymers can be used to deliver therapeutic molecules at controlled and defined rates.

A particularly attractive class of materials for cell delivery is hydrogels. Hydrogels are water-swollen physically or chemically cross-linked polymer networks that can be engineered from natural materials such as alginate or synthetic polymers such as polyethylene glycol (PEG). Specific advantages of hydrogels are minimal adverse host reactions (e.g., biocompatibility), high water content, relatively mild reaction conditions, and opportunity for minimally invasive delivery as injectable carriers. Hydrogels also offer the advantage of allowing multiple factors to be incorporated in tunable ratios creating a biomimetic 3D niche in which mechanical properties, presentation of bioactive molecules, and degradation of the gel can be tuned independently as shown in **Figure 2**.

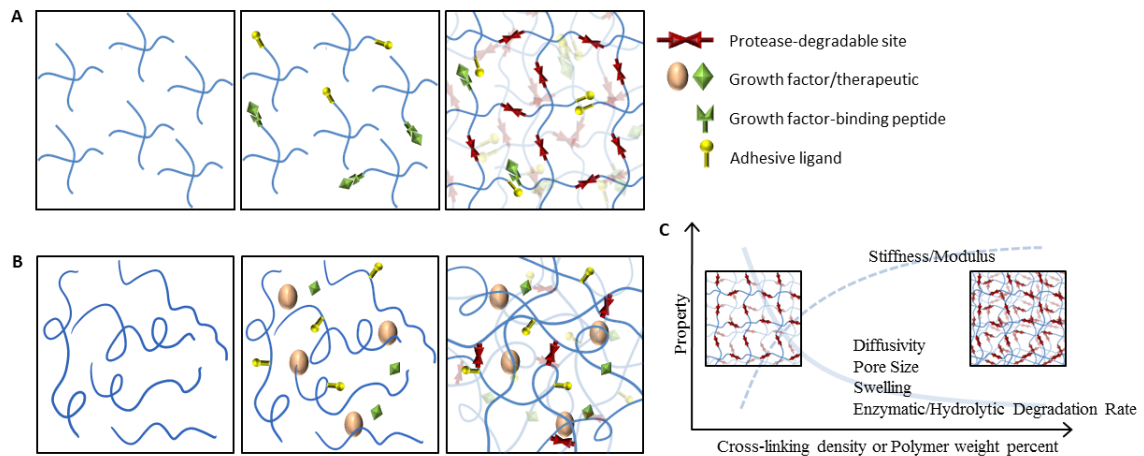


Figure 2. Schematic of functionalized hydrogel preparation. A) Multi-arm polymer precursors are functionalized with adhesive ligands, growth factor tethering peptides (affinity-based or proteolytically labile-covalent cross-links), and growth factors. The addition of protease degradable cross-linkers creates a 3D hydrogel network. B) Alternatively, polymer chain precursors may also be functionalized with adhesive ligands and mixed with soluble growth factors or therapeutics to deliver untethered, but encapsulated molecules. Addition of cross-linkers creates a 3D hydrogel network. C) Cross-linking density or polymer weight percent may be tuned independently of functionalization. Increasing cross-link density or polymer weight percentage increases stiffness, but decreases diffusivity, pore size, swelling, and degradation rate.

Matrix Stiffness/Polymer Mesh Structure

Bulk material stiffness has been widely accepted as a driving force behind stem cell fate in two-dimensional cultures [33,34], but recent studies have raised the question of whether bulk stiffness directly determines cell fate or if bulk stiffness affects ligand presentation which in turn alters cell behavior [35]. Several groups have shown that stem cell shape in 2D can regulate cell fate [33,36,37], however, Mooney has demonstrated that in 3D, cell morphology is not correlated with fate and that encapsulated cells interpret changes in matrix stiffness as changes in adhesive ligand presentation [38]. In addition to matrix stiffness, Mooney has also recently shown that cells respond to matrix stress relaxation with altered spreading and cell fate, suggesting stress relaxation as an additional

design parameter for biomaterials to direct encapsulated cell fate [39]. Although matrix stiffness and cell shape may play a role in determining cell fate in vitro, these findings are based on isolated, well-controlled cultures of, usually, one cell type. In vivo, the environment supplied by the carrier must not only provide directional cues to the transplanted cells, but allow for their engraftment as well as the infiltration of host cells. As bulk material stiffness is generally tuned by varying cross-linking density [40], polymer weight percent [40-42], or cross-linking chemistry [42], it is difficult to decouple the effects of material stiffness on encapsulated cells from the effects of cross-linking density on proliferation, morphological changes, migration and matrix permeability, and the effects that those in turn have on cell fate. For example, increasing polymer weight percentage, which often increases cross-linking density, or holding polymer weight percent constant while increasing cross-linking density decreases diffusivity which limits nutrient transport and increases elastic modulus [40,41], which in turn decreases the proliferation rate of encapsulated fibroblasts [40] and the spreading of encapsulated C2C12 murine myoblasts [42]. For example, the inhibitory effect from increasing matrix density and stiffness on capillary formation in a fibrin clot results from reduced diffusivity rather than matrix elasticity. When pro-angiogenic factor-secreting fibroblasts were distributed throughout the 3D gel, inhibitory effects from increasing fibrin density were abrogated, and capillary formation was equivalent between different gel densities [43]. Enemchukwu et al adjusted polymer weight percentages and macromer molecular weights such that each hydrogel formulation exhibited equivalent mean cross-link densities. They showed that although differences in permeability were observed due to differences in macromer arm length, hydrogel mechanical properties were equivalent and there were no differences in epithelial

morphogenesis between the two hydrogel formulations [44]. Undoubtedly, additional analyses are needed to clearly establish rational design rules for the effects of carrier mechanical properties and structure on cell delivery.

Matrix degradation for tissue ingrowth and therapeutic release

Controlled degradation of the cell carrier is critical for tissue ingrowth and cell migration/outgrowth as well as delivery of biotherapeutics incorporated within the carrier. Engineering degradability into a cell carrier can be accomplished by incorporating cross-links that are enzymatically or hydrolytically degradable. Enzymes responsible for matrix degradation include matrix metalloproteinases (MMPs), which are the main class of enzymes used in remodeling the extracellular matrix (ECM), and hyaluronidase, the protease for hyaluronic acid which is found in the ECM of many connective tissues. Enzymatic degradation by cell-secreted hyaluronidase or MMPs can be achieved by incorporating cross-linking peptides that contain an MMP degradable site [32,45] or incorporating hyaluronic acid, mimicking the natural cell-controlled degradation of ECM. Degradable matrices can also be used for cell-mediated growth factor delivery with tunable degradation and release rates by capturing growth factors in a degradable cross-linked matrix [32,46,47] or by covalently or non-covalently tethering growth factors to the matrix using affinity-based and other motifs [48-50].

Vascularization and co-delivery of cells and growth factors

Many groups have reported a significant loss in transplanted cells within the first week after implantation [51,52]. By monitoring the kinetics of expression of three ischemic markers of transplanted hMSCs 30 days post-implantation, Becquart demonstrated that local tissue ischemia is a major cause for cell early cell loss [52]. This highlights the need

for vascularization to promote transplanted cell survival and engraftment. A material must be degradable to allow for the infiltration of macrophages, fibroblasts and endothelial cells while promoting vascularization through either the release of growth factors or other soluble mediators. Many groups have demonstrated that both material degradability and angiogenic agents can work in concert to prolong the beneficial effects of angiogenic therapies. Cell-demanded release of encapsulated vascular endothelial growth factor (VEGF) by means of matrix-metalloproteinase mediated degradation of a synthetic matrix significantly increased the rate of reperfusion in hind-limb ischemia [50] and produced extensive vascularization with functional blood vessels in hydrogels implanted subcutaneously [50,53] and in the mouse cornea [54]. Additionally, the delivery of VEGF alone to promote vascularization and bone formation has resulted in mixed reports in the literature with some groups reporting enhanced vascularization and bone formation when delivered with a biomaterial [55,56], while other groups have shown no difference in bone formation even with enhanced vascularization [57-59]. An alternative strategy to increase angiogenesis and associated bone regeneration is the activation of the hypoxia-inducible factor-1 α , which is the main regulator of adaptive responses to low levels of oxygen and is required during skeletal development [60]. The genetic or pharmacologic manipulation of the HIF-1 α pathway has been shown to increase angiogenesis and improve bone formation [61-63]. Rat bone marrow stromal cells (rBMSC) genetically modified to overexpress HIF-1 α enhanced bone healing and vascularization in a rat calvarial defect model, although did not completely heal the defect, while control rBMSC resulted in little to no bone healing [64]. Another strategy for the activation of the HIF-1 α pathway is the inhibition of prolyl hydroxylase domain proteins (PHD) which cause downstream degradation of HIF-1 α .

Delivery of siRNA against PHD or delivery of small molecule inhibitors of PHD such as deferoxamine (DFO) or dimethyloxallylglycine (DMOG) increased vascularization and callus size formation [65,66]. The effect of co-delivery of angiogenic factors and cells on the engraftment and survival of the transplanted cells is rarely addressed. Delivery of human bone marrow stromal cells (BMSC) on a VEGF-releasing biodegradable polymer scaffold into a femoral defect showed increased bone formation compared to the scaffold alone and human BMSC-seeded scaffolds, but no comparison was provided on extent of engraftment or cell retention between VEGF and no VEGF groups [67].

Many cell and growth factor co-delivery systems rely on genetically modified cells that produce a sustained supply of growth factors. There have been many successful *in vivo* studies in small animal models in which cells provide a constant supply of growth factors rather than being the therapeutic agent themselves. For example, adipose-derived stem cells modified to express VEGF or bone morphogenetic proteins (BMPs) significantly enhance bone healing [68,69], but this approach risks deleterious effects from overexpression of target therapeutics [46,70] and still requires a proper carrier to retain cells at the defect site and promote cell survival. When BMP-2 overexpressing mouse MSC were delivered to the mouse radial segmental defect on a collagen sponge, a significant increase in bone formation was observed compared to control MSC [71]. Because cell survival and released BMP-2 amounts were not studied, it is unknown if the increase in bone formation (including large amounts of ectopic bone) was due to sustained release of BMP-2 over the course of healing or an initial, burst release of BMP-2 followed by significant cell death. The latter scenario may explain the very low amounts of healing observed in the control MSC group.

The host environment in a tissue injury is difficult to recapitulate *in vitro* due to multiple cell types, densely arranged cells, an inflammatory response, and vascular ingrowth needed to sustain transplanted cells. In order to recapitulate the cell density of tissues *in vitro*, cell density would need to be as high as 10^9 cells/cm³, and without a vascular system, this construct would fail due to inadequate nutrient supply. Multicellular 3D tissue constructs with perfused vascular networks will enable more accurate *in vitro* study of the interactions between tissues and cell delivery systems [72]. It is noteworthy to mention that although it has been shown that co-delivery of VEGF and cells can improve bone formation, few groups have directly addressed the effect of exogenous VEGF on cell engraftment and survival in bone regeneration, most likely due to focus being placed on the bone healing properties of VEGF rather than its pro-angiogenic effects on cell survival. Most *in vivo* cell-delivery studies in bone repair use new bone formation and/or mechanical testing as indicators of therapy efficacy and do not address cell engraftment or, at the bare minimum, provide evidence that some transplanted cells are present at the end of the study. Cell engraftment is rarely studied as a means to improve functional outcome which raises the question of whether cell engraftment is important if the overall outcome, i.e. functional restoration of the injured tissue, is improved.

Cell adhesive interactions

An appropriate carrier must support the adhesion, migration, organization, and differentiation of the transplanted cells and host cells. These behaviors rely on an intricate interaction between various cues supplied by the extracellular environment which include insoluble molecules within the ECM such as proteins, soluble molecules such as growth factors, hormones, and cytokines, and cell-cell interactions. Integrins are a family of cell

surface receptors that primarily mediate adhesion of cells to ECM proteins and also transduce signals across the cell membrane. Each $\alpha\beta$ heterodimeric combination exhibits unique binding characteristics and mediates cellular activities such as migration, proliferation, survival and differentiation [73]. Therefore, as a major mediator of important cellular responses, engineering integrin binding activity within a 3D environment may improve transplanted cell survival and function. As synthetic polymers such as polyethylene glycol have become a popular choice for biomaterials for their non-fouling properties, additional steps must be taken to functionalize these synthetic materials to promote cell adhesion. Encapsulating fibroblasts in a polyethylene glycol hydrogel with protease-degradable sites, RGD, neither or both demonstrated that both adhesive sites and degradability were required for cell spreading and migration within a 3D synthetic hydrogel carrier [45,50].

Materials may be functionalized to promote adhesion by 1. Incorporating small adhesive ligands, such as RGD oligopeptides [32,42,50,74]; 2. Components found in ECM such as collagen [75] or hyaluronic acid [76]; or 3. Functionalizing with small chemical groups, such as phosphates, to promote specific protein interactions [77]. There has been some degree of success using full length ECM proteins to functionalize biomaterials by tethering or passive adsorption, but these proteins come with batch to batch variability, limited control over presentation, and difficulty in making modifications. For example, $\alpha2\beta1$ binds the sequence GFOGER, one of the major recognition sites on type I collagen [78], which makes up more than 90% of the organic phase of bone. When compared to full length type I collagen, the GFOGER collagen-mimetic peptide significantly improved *in vivo* peri-implant bone regeneration and osseointegration, as characterized by bone-implant

contact area and mechanical fixation [79]. Use of a non-fouling material, such as PEG, allows for engineering integrin specificity in the cell carrier by incorporation of specific adhesive ligands. GFOGER-functionalized PEG hydrogels resulted in healing of 30% of murine radial segmental defects, and when combined with low doses of BMP-2, full bridging of 100% of segmental defects was achieved [80]. RGD, the shortest known adhesive sequence, is found in many proteins such as fibronectin, vitronectin, bone sialoprotein, and osteopontin [81], and promiscuously binds to a number of integrin receptors. Although RGD helps to mediate functional vascularization, the integrins specific for RGD may not be appropriate for every tissue engineering application. Emerging evidence supports a role for integrin binding specificity in directing cellular responses to biomaterials [82]. RGD-functionalized biomaterials generally failed to promote bone healing, with [51,83] or without encapsulated cells [80]. When RGD is combined with synergy site PHSRN from fibronectin in the correct structural presentation, affinity for integrin $\alpha 5\beta 1$ increases 40-fold compared to RGD alone [84,85]. $\beta 1$ integrins have been shown to contribute to bone marrow cell adhesion, mineralization, and bone healing and $\alpha 5\beta 1$ is present on osteoblasts and osteoclasts during all stages of osteogenesis. Titanium implants functionalized with a fibronectin fragment specific for $\alpha 5\beta 1$ performed significantly better in an osseointegration study compared to RGD functionalization in terms of pull-out force and bone-implant contact area [85], consistent with other reports in the failure of RGD to promote functional osseointegration [86].

Engineering specificity of short peptide ligands to integrins is dependent on affinity of the receptor for the ligand as well as the expression levels of the receptor subunits on the cell type of interest. Four $\beta 1$ integrins are responsible for binding to collagen: $\alpha 1\beta 1$,

$\alpha 2\beta 1$, $\alpha 10\beta 1$, and $\alpha 11\beta 1$, which have all been previously reported to be expressed by hMSC at differential levels [87]. $\alpha 1\beta 1$, expressed at low basal levels on hMSC, was not required for hMSC survival on collagen I and did not exhibit an increase in expression upon osteogenic differentiation, whereas $\alpha 2\beta 1$ and $\alpha 11\beta 1$ were required for survival of hMSC on Collagen I and exhibited increased expression upon osteogenic stimulation [88]. $\alpha 10\beta 1$ is also expressed at low basal levels on hMSC and is mainly restricted to cartilage [89,90]. The hexapeptide GFOGER was originally identified as the major binding sequence of integrin $\alpha 2\beta 1$ [91,92], but since then, has been reported to also bind integrins $\alpha 1\beta 1$, $\alpha 10\beta 1$, and $\alpha 11\beta 1$ [92,93]. Although the newly discovered $\alpha 11\beta 1$ also recognizes GFOGER, Zhang et al report a significantly lower affinity of $\alpha 11\beta 1$ to collagen I compared to $\alpha 2\beta 1$ [94]. Due to the low expression of $\alpha 1\beta 1$ and $\alpha 10\beta 1$ on hMSC, and the low affinity of $\alpha 11\beta$, within the scope of this project, GFOGER will be referred to as integrin $\alpha 2\beta 1$ -specific. RGD promiscuously binds to a number of receptors and can be found in many ECM proteins, but the linear secondary structure of RGD has been shown to preferentially mediate hMSC adhesion through integrin $\alpha v\beta 3$ [85], although still binding other integrins such as $\alpha 5\beta 1$ at high densities.

BIOLUMINESCENT IMAGING

Bioluminescent imaging has emerged as a powerful tool for monitoring gene expression or tracking cells *in vivo*. Bioluminescence is produced during the reaction between the luciferase enzyme and its substrate and has been used in various applications, including bone tissue engineering [95-98]. Because different luciferase variants react with specific substrates to produce distinct spectral signals, cells can be engineered to express

multiple types of luciferase to track multiple gene targets in the same cell [99,100]. *In vivo* imaging provides sensitive measurements of cell numbers and longitudinal data on transplanted cells within the same subject population [97]. This system reduces the number of animals, animal-to-animal variability, and permits direct correlations between cell delivery vehicles design and transplanted or differentiated cell numbers.

Bioluminescent imaging provides many advantages over other cell tracking modalities. Because the light-emitting reaction does not require an excitation source, unlike fluorescent proteins, there is very little background. The enzyme luciferase is only expressed by live cells, which provides an advantage over quantum dot or nanoparticle based tracking which may confound results if materials are phagocytosed by other cell types. Although bioluminescence exhibits many advantages, there are still limitations to this method. The stable expression of the foreign luciferase gene must be induced by means of viral transduction. Because most bioluminescent tracking schemes require the exogenous delivery of the appropriate substrate, usually through a systemic injection into the intraperitoneal cavity, the kinetics of the substrate movement first, to the defect site, and second, into the implant material to the transplanted cells, must be determined for each model. As with all cell tracking modalities, though, the signal must be validated as representative of actual cell number due to other possible confounding factors [101].

CHAPTER 3: ENGINEERING AN INTEGRIN-SPECIFIC CELL MICROENVIRONMENT

ABSTRACT

Hydrogels are an attractive class of materials for cell encapsulation due to properties that mimic the extracellular matrix such as high water content and simple diffusion of waste and nutrients, minimal adverse host reactions, relatively mild reaction conditions, and opportunity for minimally invasive delivery as injectable carriers. Due to their defined chemical compositions, synthetic polymers can be prepared in reproducible and predictable fashions and can be modified to tune material properties such as degradation rate, mechanical properties, and shape/configuration - large advantages over natural polymers that display heterogeneity and structural complexity that renders modifications difficult. The lack of cell adhesion sites on most synthetic polymers yields the opportunity for engineering specificity into the material by incorporating cell adhesive sites or growth factors, independently of substrate mechanical properties. In this aim, we have engineered an integrin-specific stem cell microenvironment using biomimetic adhesive ligands using a novel hydrogel chemistry without the use of cytotoxic photoinitiators and UV light. We have shown that we can control material properties of the matrix independently of ligand peptide and tune material properties such as storage modulus by varying hydrogel parameters. Ligand-functionalized hydrogels exhibited binding specificity to target integrins, and we observed differences in cell morphology in 3-D due to ligand activity while maintaining high cell viability. In addition, integrin-specific hydrogels supported for FAK activation and upregulated osteoblastic

differentiation as compared to hydrogels presenting non-adhesive control peptides. This study supports ligand-functionalized PEG-mal hydrogels as a viable carrier for hMSC delivery *in vivo*.

INTRODUCTION

Hydrogels have emerged as an attractive class of materials to engineer cell microenvironments [102,103]. Hydrogels are water-swollen, physically or chemically cross-linked polymer networks that can be engineered from natural materials such as alginate or synthetic polymers such as poly(ethylene glycol) (PEG). Specific advantages of hydrogels are minimal adverse host reactions, high water content, relatively mild reaction conditions, tissue-like elastic properties and opportunity for minimally invasive delivery as injectable carriers. Hydrogels also offer the advantage of allowing multiple factors to be incorporated in tunable ratios creating a biomimetic 3-D niche in which mechanical properties, presentation of bioactive molecules, and degradation of the gel can be tuned independently. An elegant example where the biophysical and biochemical properties of the hydrogel were systematically varied to regulate the complex epithelial morphogenesis program has been recently described [44].

The earliest materials used for cell encapsulation, namely fibrin, collagen, and alginate, were naturally occurring and biodegradable, and demonstrated promise in early studies [104-106]. Although these naturally-derived materials may be biologically active, promote cell adhesion and growth, and may be enzymatically or hydrolytically degradable, they display lot-to-lot variability, risk of immunogenicity and pathogen transmission, and structural complexity that renders control over degradation or gelation rates difficult. Synthetic polymers provide an alternative to natural materials as cell microenvironments. Because of their defined chemical composition, synthetic materials can be reproducibly prepared and can be modified to control material properties such as degradation rate, mechanical properties, and shape/formulation (e.g., bulk, microparticles, fibers). As most

synthetic polymers used for hydrogels lack cell adhesion sites and are relatively resistant to protein adsorption, they usually need to be chemically modified to support cell adhesion and other bio-functionalities, and this yields the opportunity of engineering specificity into the material [8,32]. Poly(ethylene glycol) (PEG) holds many advantages as a synthetic polymer hydrogel building block. It exhibits low protein adsorption, providing a non-fouling background, a minimal inflammatory profile, well-established chemistry, and a long history of safety *in vivo*. Maleimide-thiol hydrogel chemistry with maleimide end-functionalized PEG macromers and cysteine-terminated peptides allows for mild reaction conditions at high reaction efficiencies, small degradation products, and “plug-and-play” functionality [42]. This system holds many advantages over PEG-diacrylate (DA) hydrogels (currently, the most widely used hydrogel chemistry) in that it avoids the use of cytotoxic free radicals and UV light, enables in situ crosslinking for *in vivo* delivery, has a well-defined structure and allows for stoichiometric incorporation of bioactive peptides, and avoids large degradation products consisting of non-degradable DA backbone. Additionally, the base macromer has no local or systemic toxicity and is rapidly cleared via the urine. Exemplary applications of this system include islet transplantation, growth factor delivery for cardiac therapy, and low dose BMP-2 delivery for bone healing [2,107,108].

The hydrogel scheme and molecules used in this project are outlined in **Figure 3**. Four-arm, maleimide-end functionalized 20 kDa PEG macromer was reacted with one of four cysteine-terminated peptide ligands: 1. $\alpha v\beta 3$ -specific linear RGD, 2. $\alpha 2\beta 1$ -specific GFOGER, 3. Non-adhesive, scrambled control RDG, or 4. Non-adhesive, mutated control

GAOGER; and cross-linked with the cysteine-flanked VPM peptide containing a protease-degradable site.

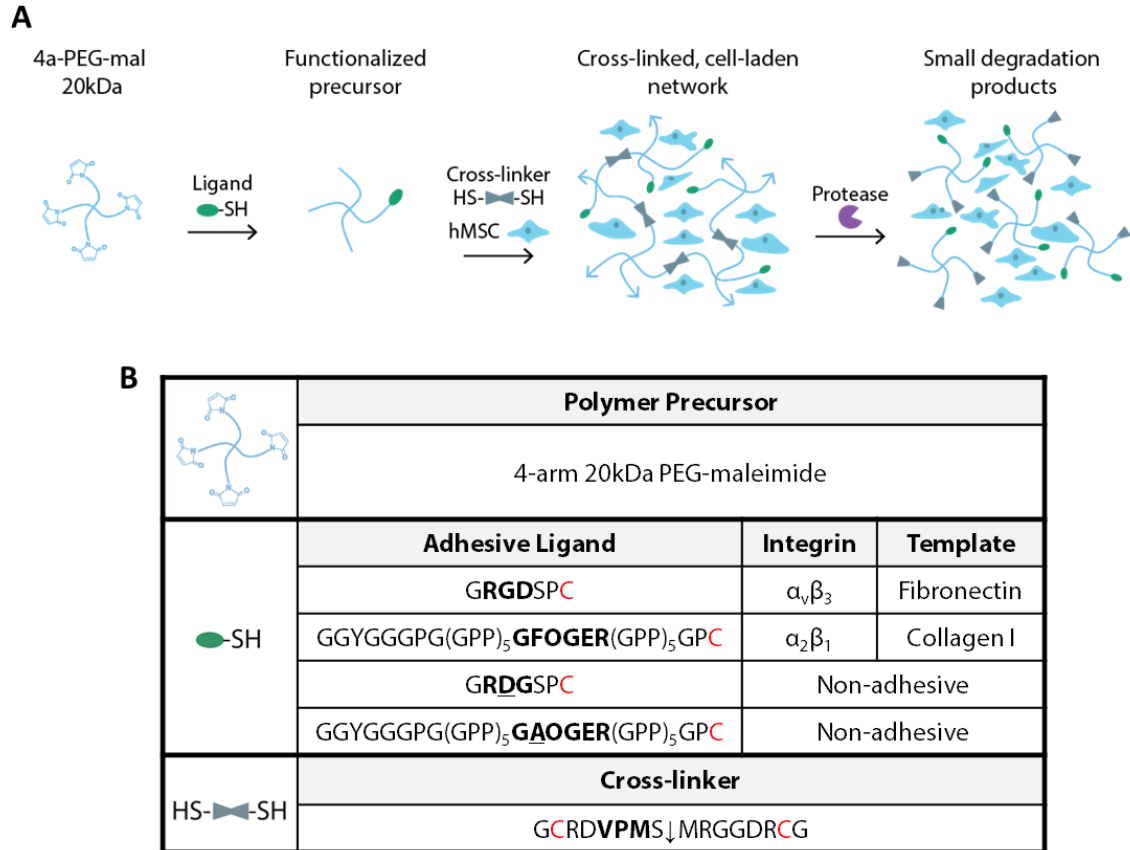


Figure 3. Protease-degradable PEG hydrogel reaction scheme. A) Cell-laden 4 arm-PEG-maleimide hydrogel reaction scheme (cells not shown to scale relative to hydrogel). B) Hydrogel components consist of 4-arm PEG-mal, peptide ligands RGD, GFOGER, RDG, and GAOGER, and cross-linker VPM.

METHODS

Ligand tethering efficiency

Four-arm, maleimide-end functionalized (>95%) PEG macromer (PEG-mal, 20 kDa, Laysan Bio) was reacted with GFOGER peptide (GGYGGGPG(GPP)₅GFOGER(GPP)₅GPC, O = hydroxyproline), RGD peptide (GRGDSPC), or the scrambled, non-adhesive RDG peptide (CRDGSPC) in 10 mM HEPES in PBS, pH 7.4 for 15 min at 37 °C. The reaction diluted in PBS 100-fold and diluted PEG-adhesive peptide (10 µL) plus thiol-quantitation reagent (100 µL, Measure-iT Thiol Assay Kit, Thermo Fisher) was added per well of a 96-well plate and read using a microplate reader. Dilutions of GFOGER, RGD, or RDG in 10 mM HEPES in PBS were used as standards. All samples and standards were measured in triplicate.

Hydrogel Synthesis

20 kDa PEG-mal, adhesive and control peptides (GFOGER, RGD, RDG, GAOGER), GCRDVPMSMRGGDRCG (VPM) cross-linker peptide, and dithiothreitol (DTT, Sigma Aldrich) in 100 mM HEPES in PBS, pH 6-6.5 were used. The peptide sequences and hydrogel components are listed in **Table 1**. PEG-mal hydrogels were synthesized by reacting PEG-mal with adhesive peptides, a 75:25 cross-linker mixture of VPM:DTT, and 10 mM HEPES at a volume ratio of 2:1:1:1 at the required concentrations to obtain the desired final concentration of PEG-mal and adhesive peptide. The concentration of cross-linker used for the synthesis of each hydrogel was calculated to stoichiometrically balance the number of free thiols on the cross-linker with the number of free (unreacted) maleimide groups remaining in the adhesive peptide-functionalized PEG-maleimide solution. For *in vitro* cell culture studies, cell-laden hydrogels were fabricated

by mixing PEG-mal, adhesive peptide, 75:25 VPM:DTT, and cell suspension at a volume ratio of 2:1:1:1 and allowed to cross-link at 37 °C before swelling with media.

Table 1. Peptide hydrogel components.

Abbreviated name	Peptide sequence	Source
VPM	GCRDVPMSMRGGDRCG	AAPPTEC, Genscript
RGD	GRGDSPC	AAPPTEC
RDG	GRDGSPC	AAPPTEC
GFOGER	GGYGGGP(GPP) ₅ GFOGER(GPP) ₅ GPC, O = hydroxyproline	AAPPTEC, Genscript, Activotec UK
GAOGER	GGYGGGP(GPP) ₅ GAOGER(GPP) ₅ GPC, O = hydroxyproline	AAPPTEC

Rheometry

12.5 µL hydrogels were cast as discs in 4.5 mm diameter silicone isolators (Grace Bio-Labs, Sigma) on Sigmacote-treated slides (Sigma). The gels were allowed to cross-link at 37 °C, removed from the isolators, and swollen in PBS overnight. Rheological measurements were made using a cone and plate rheometer (MCR302, Anton Paar). The sample was loaded onto the plate, the cone was lowered, and excess sample was removed. Storage and loss moduli were measured over a range of angular frequencies with a strain that corresponded to the linear viscoelastic region.

Swelling Studies

50 µL hydrogels were allowed to cross-link at 37 °C and swollen in PBS overnight. Swollen hydrogels were weighed and snap frozen in liquid nitrogen. Following lyophilization, dry hydrogels were weighed. Mass swelling ratio is presented as

$$Q = \frac{\text{mass}_{\text{wet}}}{\text{mass}_{\text{dry}}} \quad (1)$$

Mesh Size Calculations

Mesh size was calculated using several methods: 1. rheological measurements and rubber elasticity theory [109], and swelling measurements and the Flory and Rehner equation modified by Merrill and Peppas [110,111] based on 2. experimental data or 3. theoretical values. Rubber elasticity theory relates mesh size, ξ , to storage modulus, G' as follows:

$$\xi = \left(\frac{G' N_A}{RT} \right)^{-\frac{1}{3}} \quad (2)$$

where R is the molar gas constant and T the temperature. Swelling measurements were used to calculate mesh size using the following equations:

$$\xi = v_{2,s}^{-\frac{1}{3}} (\bar{r}_0^2)^{\frac{1}{2}} \quad (3)$$

$$(\bar{r}_0^2)^{\frac{1}{2}} = l \left(\frac{2\bar{M}_c}{M_r} \right)^{\frac{1}{2}} C_n^{\frac{1}{2}} \quad (4)$$

$$\frac{1}{\bar{M}_c} = \frac{2}{\bar{M}_n} - \frac{\left(\frac{\bar{v}}{\bar{V}_1} \right) [\ln(1 - v_{2,s}) + v_{2,s} + \chi v_{2,s}^2]}{v_{2,r} \left[\left(\frac{v_{2,s}}{v_{2,r}} \right)^{\frac{1}{3}} - \frac{1}{2} \left(\frac{v_{2,s}}{v_{2,r}} \right) \right]} \quad (5)$$

where $v_{2,s}$ and $v_{2,r}$ are the polymer volume fraction of the gel in the swollen and relaxed states, respectively, $(\bar{r}_0^2)^{\frac{1}{2}}$ is the unperturbed mean-square end-to-end distance of the PEG, l is the average value of the bond length = 1.46 Å, \bar{M}_c is the average molecular mass between the cross-links in the network (experimental value calculated from equation 5; theoretical value taken as $2 * MW_{\text{multimer arm}} + MW_{\text{crosslinking peptide}}$), M_r is the

molecular mass of PEG repeating unit (44 g/mol), C_n is the characteristic ratio of PEG = 4, \bar{v} is the specific volume of PEG $\bar{v} = \frac{\rho_{H_2O}}{\rho_{PEG}} = \frac{1 \frac{g}{cm^3}}{1.12 \frac{g}{cm^3}}$, V_1 is the molar volume of the solvent (18 cm³/mol for water), and χ is the polymer-solvent interaction parameter (0.4 for PEG-water).

hMSC Culture

Bone marrow-derived hMSC (Texas A&M) were maintained in growth media: α MEM (Thermo Fisher) with 16.5% fetal bovine serum screened for hMSC growth (Stem Cell Tech), 2-4 mM L-glutamine (Thermo Fisher), 100 units/mL penicillin, and 100 μ g/mL streptomycin at 37 °C, 5% CO₂. hMSC were sub-cultured at 70-80% confluency, and for all experiments early passage (<6) cells were used.

Adhesion Studies

20 μ L of 6% (wt/v) hydrogels with 1.0 mM ligand were cast on the bottom of a well on a 48 well plate covering the entire surface. hMSC were incubated with anti- α 2 integrin (Millipore), anti- α v β 3 integrin (Millipore), mouse IgG1 isotype control (R&D Systems) at 10 μ g/mL, or without antibody, and then seeded on top of hydrogel discs at 7000 hMSC/cm². After 15 min, hMSC were rinsed with PBS and fixed in 4% paraformaldehyde. Nuclei were then stained with 4',6-diamidino-2-phenylindole (DAPI, Life Technologies) and visualized with a Nikon C2+ laser scanning confocal head on a Nikon Eclipse-Ti microscope and Elements software (Nikon). Images were analyzed for cell number using ImageJ (NIH).

Viability Studies

hMSC-laden hydrogels were cultured free-floating in media and at specified time points, stained with Calcein AM (Thermo Fisher) for live hMSC and ethidium homodimer (Life Technologies) for dead hMSC. Gel-encapsulated hMSC were visualized with a Nikon C2+ laser scanning confocal head on a Nikon Eclipse-Ti microscope and Elements software (Nikon). Maximum projections on z-stacks were analyzed using ImageJ (NIH).

Cell number

At specified time points, hydrogels were incubated in 1 mg/mL collagenase, type I (Thermo Fisher) at 37 °C until fully degraded. Cells were lysed by sonication and freeze-thaw cycles. Whole cell lysate was assayed for DNA content and cell number using a CyQuant kit according to manufacturer's instructions (Thermo Fisher) and a cell standard curve.

EdU Staining for Cell Proliferation

hMSC-laden hydrogels were cultured free-floating in media. At day 7, cells were incubated with 10 μ M EdU for 48 hr. EdU detection was visualized using a Click-iT EdU kit according to manufacturer's instructions (Thermo Fisher). Nuclei were stained with DAPI and visualized with a Nikon C2+ laser scanning confocal head on a Nikon Eclipse-Ti microscope and Elements software (Nikon) and images were analyzed using ImageJ (NIH).

Osteogenic differentiation – 3-D

hMSC were seeded at 5e6 cells/mL within 4.5% or 10% (wt/v) hydrogels with 1.0 mM ligand and cultured in osteogenic medium (Lonza). After 9 days of culture in induction medium, hMSCs were lysed and assayed for alkaline phosphatase activity (ALP) by

incubating with 4-methylumbelliferyl phosphate disodium salt (MUP) substrate as previously described [112]. Hydrogels were incubated in 1 mg/mL collagenase type I (Thermo Fisher) at 37 °C until fully degraded. Cells were resuspended in 50 mM Tris HCl (pH 7.4) and lysed by sonication and freeze-thaw cycles. Samples and ALP standards were loaded into a 96-well plate, then incubated with 60 µg/mL MUP substrate at 37 °C for 1 hr and read at 360 nm excitation/465 nm emission. The enzymatic activity was standardized using purified calf intestinal ALP at known dilutions and normalized to the amount of DNA content using a CyQuant kit according to manufacturer's instructions (Thermo Fisher).

FAK Phosphorylation

hMSC were encapsulated and cultured in ligand-functionalized hydrogels overnight. Cells were washed twice with PBS and lysed by sonication on ice in cell extraction buffer containing protease and phosphatase inhibitors (Thermo Fisher). The lysates were cleared by centrifugation at 10,000 rpm for 15 min at 4 °C and extract was stored at -80 until analysis. Protein concentration was determined using a micro BCA kit (Pierce). Equivalent amounts of reduced, boiled (10 min at 70 °C) lysate were loaded on Bolt 10% Bis-Tris Plus gels (Thermo Fisher) and subsequently transferred onto PVDF membranes. Membranes were probed with mouse monoclonal antibody against GAPDH (Abcam), mouse monoclonal antibody against FAK and rabbit polyclonal antibody against FAK [pY397] (Thermo Fisher) at a 1:1000 dilution in 5% BSA TBST solution followed by fluorescent secondary antibodies (Li-Cor). Immunoblots were visualized on a Li-Cor Odyssey imaging system and analyzed using Image Studio Lite (Li-Cor).

RESULTS

Characterizing hydrogel material properties

We first examined the effects of ligand functionalization on bulk material properties. Tethering efficiency of peptide ligands GFOGER, RGD, and RDG to PEG-mal macromer was evaluated. PEG-mal was reacted with ligand at concentrations for a 1.0 mM ligand or 0.3 mM ligand hydrogel. Unreacted thiols were quantified using a thiol-reactive fluorescent dye. **Figure 4A** shows that GFOGER, RGD, and RDG all react with PEG-mal at high efficiency (>95%) and tethering efficiency is not affected by ligand concentration. Rheological properties were then quantified for ligand-functionalized hydrogels on a cone and plate rheometer. 4.5% (w/v) PEG-mal, 1.0 mM ligand hydrogels were cast in silicone isolators (to maintain uniform shape) and swollen overnight. The storage modulus (G') was determined over a range of angular frequencies at a constant strain. GFOGER, RGD, and RDG-functionalized hydrogels exhibited storage moduli of 64.7, 61.8, and 61.1 Pa, respectively, but were not significantly different, (**Figure 4B**) and loss moduli of 2-5 Pa (data not shown). The mass swelling ratio was determined for 4.5% (w/v) PEG gels presenting 1.0 mM GFOGER and RGD as the ratio of the wet, swollen weight to the dry weight. **Figure 4C** shows mass swelling ratios of 38.7 and 36.4 for GFOGER and RGD, respectively; these ratios are not statistically different. Mesh size is a measure of the distance between cross-links and controls the diffusion of nutrients, signaling molecules, and waste. Mesh size was estimated by three methods: rubber elasticity theory, Flory and Rehner equations with experimentally determined molecular mass between cross-links, and Flory and Rehner equations with theoretical molecular mass between cross-links. All three methods yielded values with relatively good agreement.

Table 2 shows estimated mesh sizes in the range of 15-40 nm for the three calculation methods, with no statistical difference among ligands. In addition, hydrogels containing 1.0 mM GFOGER were made at different PEG weight percentages ranging from 4.5% to 3%. **Figure 5** shows the decreasing storage moduli as PEG weight percent decreases, as expected due to increasing cross-linking density in higher weight percent gels. Estimates of mesh size for each weight percent were calculated using rubber elastic theory as 39 nm, 43 nm, 46 nm, and 53 nm for 4.5%, 4.0%, 3.5%, and 3.0% (w/v) PEG hydrogels, respectively.

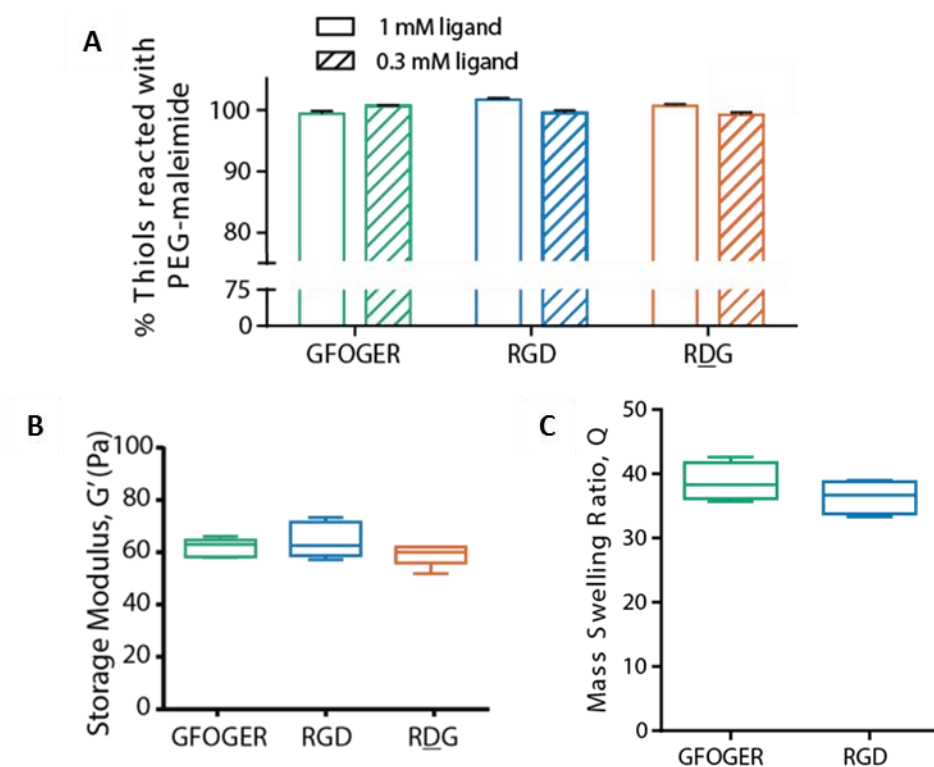


Figure 4. Ligand tethering efficiency and material properties. A) Quantification of free thiols in solution following reaction of PEG-mal and ligand at two different ligand concentrations indicates virtually all ligand reacted with PEG-mal is functionalized to the end maleimide groups. (Bar represents mean, error bars represent SD). B) Storage moduli of bulk hydrogels determined by cone and plate rheological measurements. C) Mass swelling ratios of bulk hydrogels. (Whiskers represent min and max, box extends from 25th to 75th percentiles, line represents median. N=4-6).

Table 2. Mesh size calculations for a 4.5% (w/v) PEG hydrogel with 1 mM ligand.

Ligand	$\xi \pm \text{S.D. (nm)}^a$	$\xi \pm \text{S.D. (nm)}^b$	$\xi \pm \text{S.D. (nm)}^c$
GFOGER	40 ± 0.7	18 ± 0.7	23 ± 0.5
RGD	40 ± 1.4	17 ± 0.8	22 ± 0.5
RDG	41 ± 1.0	-	-

^a Calculated by rubber elasticity theory and rheological measurements

^b Calculated by Flory and Rehner equations with experimental \bar{M}_c

^c Calculated by Flory and Rehner equations with theoretical \bar{M}_c

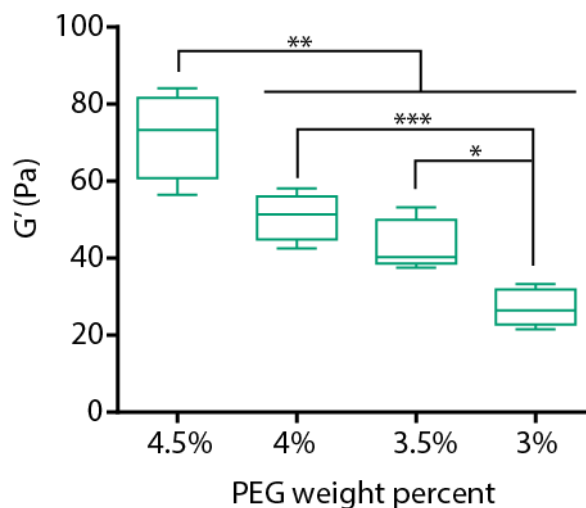


Figure 5. Rheology of varying weight percent hydrogels. Storage moduli of bulk hydrogels with 1 mM GFOGER determined by cone and plate rheological measurements. (Whiskers represent min and max, box extends from 25th to 75th percentiles, line represents median. N=5; ANOVA: *p<0.05, **p<0.005, ***p<0.001).

Integrin specificity of GFOGER and RGD hydrogels

Integrin specificity of ligand-functionalized hydrogels was determined by studying short term adhesion of hMSC on top of thin hydrogels with and without incubation in function-blocking antibodies for integrin $\alpha 2$ or integrin $\alpha \nu \beta 3$. When hMSC were incubated with anti- $\alpha 2$ antibody and seeded on top of GFOGER-functionalized hydrogels, there was ~50% reduction in adherent cells compared to hMSC on GFOGER hydrogels without

antibody incubation (**Figure 6A**). When hMSC were incubated with anti- $\alpha v \beta 3$, there was ~75% reduction in adherent cells compared to hMSC on RGD hydrogels without antibody incubation (**Figure 6B**). Minimal hMSC adhesion was observed on hydrogels without ligand or on RGD functionalized hydrogels. For both GFOGER and RGD hydrogels, there was a slight decrease in the number of adherent cells when incubated with the isotype control suggesting that the nonspecific antibody interactions influenced the number of adherent cells, although not significantly different from hMSC on ligand-functionalized hydrogels without antibody incubation. Antibody blocking of target integrins did not completely block cell adhesion to the ligand-functionalized hydrogels, likely due to robustness of the wash assay used in this study to apply controlled detachment forces. A more robust adhesion assay, such as the spinning disk assay, may offer finer control over detachment forces [113].

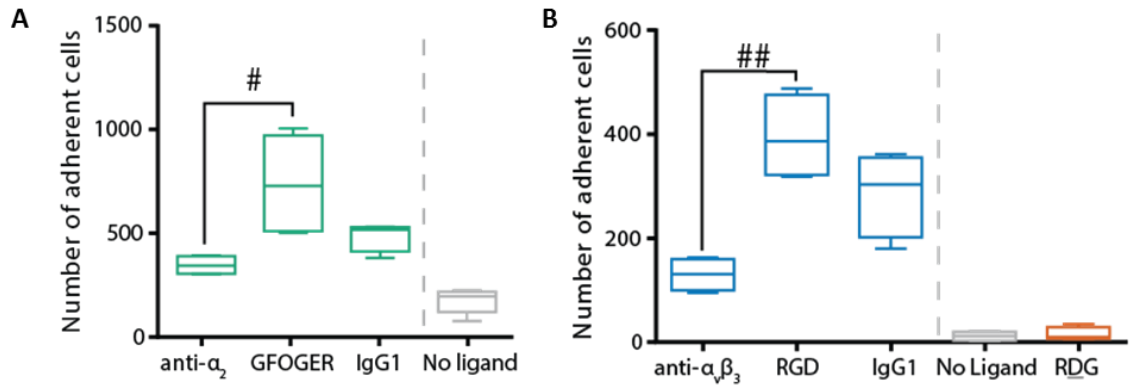


Figure 6. Integrin-specificity of ligand-functionalized hydrogels. A) Antibody-mediated blocking of α_2 integrin on hMSC reduces adhesion on thin GFOGER-functionalized hydrogels. B) Blocking $\alpha v \beta 3$ integrin on hMSC reduces adhesion on thin RGD-functionalized hydrogels. (Whiskers represent min and max, box extends from 25th to 75th percentiles, line represents median. N=4-5; Kruskal-Wallis: #p<0.05, ##p<0.005).

Effect of encapsulation on hMSC viability

We then assessed hMSC behavior in 3-D ligand-functionalized hydrogels. hMSC were encapsulated in 4.5% 1.0 mM GFOGER, RGD or RDG functionalized hydrogels. After 7 days in culture, live cells were stained with cell-permeant Calcein AM and dead cells were stained with cell-impermeant ethidium homodimer. Maximum projections of representative z-stacks taken by confocal microscopy are shown in **Figure 7A** with Calcein AM in green and ethidium homodimer in red. Insets show high magnification images of actin staining with phalloidin and nuclei staining with DAPI. Cell viability and spreading area was quantified by analyzing staining with image analysis. Calcein AM and ethidium homodimer stain area was quantified for individual maximum projections of multiple z-stacks, and the live cell percentage was determined as the ratio of Calcein stain area to ethidium homodimer stain area. **Figure 7B** shows 91.6%, 93.6% and 87.5% live cells for GFOGER, RGD, and RDG gels respectively. The viability percentage for RDG hydrogel was significantly lower than RGD. Cell area was quantified as Calcein stain area as this label stains the entire cell body. GFOGER and RGD exhibited higher spread area (17.2% and 14.7%) compared to the non-adhesive RDG (7.1%). Networks consisting of multiple cells and elongated cells were observed in GFOGER and RGD functionalized gels whereas in RDG gels, cells remained single and round, or formed small multi-cell clusters or aggregates (**Figure 7C**). No significant difference was observed in results obtained from analyzing images of individual slices along the z-axis or maximum projections of z-stacks.

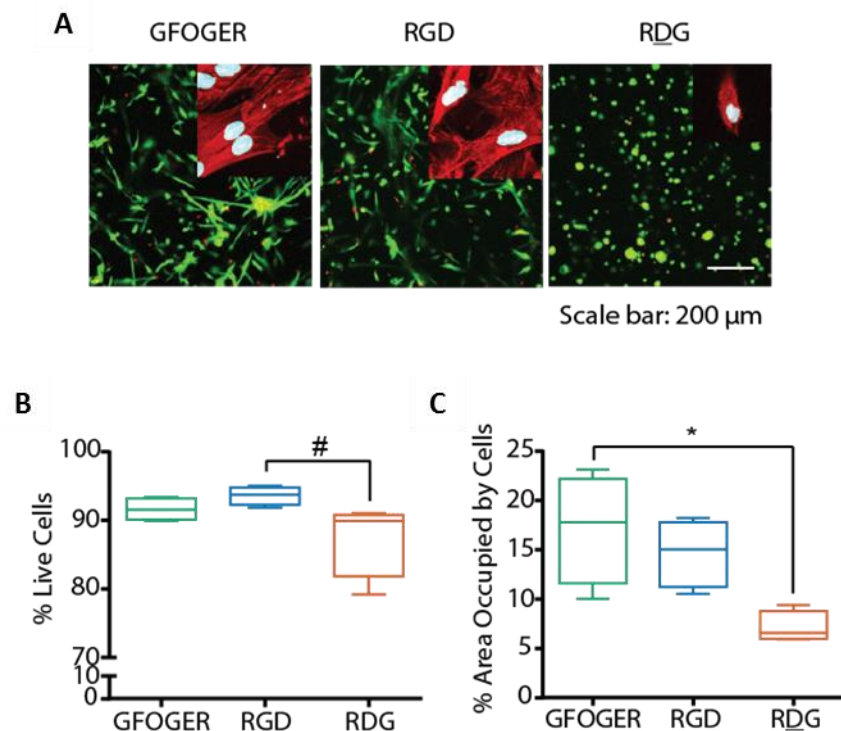


Figure 7. Viability and spreading of encapsulated hMSC. A) Encapsulated hMSC were cultured for 7 days and stained with Calcein AM (green) and ethidium homodimer (red). Inset shows high magnification view of actin (red) and nuclei (cyan). B) Quantification of viability staining indicates high viability (>90%) in GFOGER- and RGD-functionalized hydrogels. C) Quantification of spread cell area indicates significantly more spreading in GFOGER- and RGD-functionalized hydrogels compared to non-adhesive RDG-functionalized hydrogel. (Whiskers represent min and max, box extends from 25th to 75th percentiles, line represents median. N=4-5; ANOVA: * p <0.05; Kruskal-Wallis: # p <0.05).

GAOGER control hexapeptide

An inactive control peptide was designed to account for the size and structure of GFOGER. The phenylalanine in the GFOGER sequence was replaced with alanine to significantly reduce integrin binding and adhesion while the rest of the peptide sequence was conserved [114]. When hMSC were seeded on top of GFOGER, GAOGER, or no ligand hydrogels, minimal adhesion was observed on GAOGER hydrogels or hydrogels without ligand (**Figure 8**). While GAOGER hydrogel functionalization does not affect

viability of encapsulated hMSC after 1 week in culture, GAOGER functionalization significantly reduces cell spreading in 3-D compared to GFOGER functionalized hydrogels (**Figure 9**).

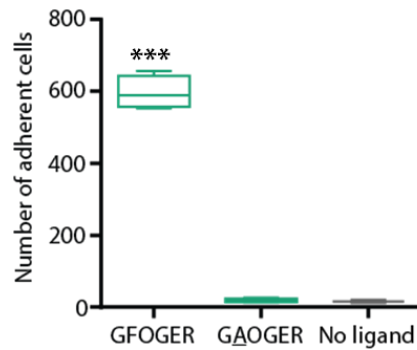


Figure 8. Mutated, non-adhesive peptide control for GFOGER does not support cell adhesion. Phenylalanine in GFOGER sequence was replaced with alanine to block integrin binding. Minimal hMSC adhesion was observed on GAOGER-functionalized hydrogels. (Whiskers represent min and max, box extends from 25th to 75th percentiles, line represents median. N=2-4; ANOVA: ***p<0.0005).

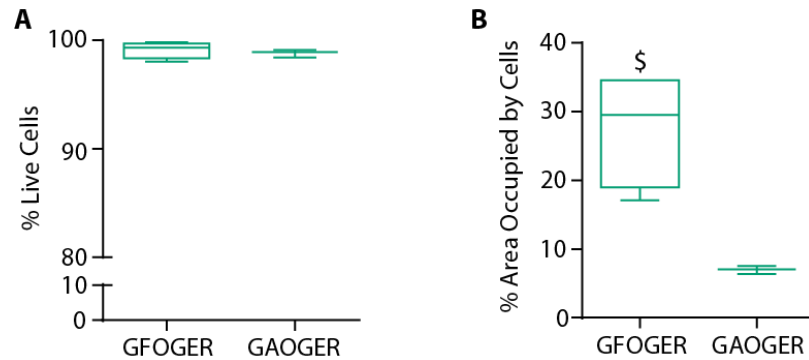


Figure 9. GAOGER does not support spreading of encapsulated hMSC. hMSC were encapsulated in GFOGER or GAOGER functionalized hydrogels. After 7 days in culture, hMSC were stained with Calcein AM and ethidium homodimer. A) Quantification of viability staining indicates high viability (>90%) in GFOGER- and GAOGER-functionalized hydrogels. B) Quantification of spread cell area indicates significantly more spreading in GFOGER-hydrogels compared to non-adhesive GAOGER-functionalized hydrogel. (Whiskers represent min and max, box extends from 25th to 75th percentiles, line represents median. N=3-4; t-test: \$p<0.05).

Integrin-mediated signaling requires the recruitment of many intracellular proteins to the focal adhesion, including focal adhesion kinase (FAK), a key regulator of adhesion and motility [115,116]. As a result of integrin binding, tyrosine and serine residues are phosphorylated leading to the formation of docking sites for a variety of signaling molecules. In particular, tyrosine 397 is the autophosphorylation site of FAK and is involved in its initial activation, binding Src family SH2 domains and the p85 subunit of PI3-kinase [117]. GFOGER and RGD hydrogel functionalization led to increased levels of FAK-Y397 phosphorylation of encapsulated hMSC compared to their inactive peptide controls (1.5-fold increase in GFOGER vs. GAOGER and 1.4-fold increase in RGD vs. RDG, **Figure 10**). The phosphorylation of FAK combined with the spread cell morphology in 3-D indicates that encapsulated hMSC are able to initiate integrin binding with the peptide ligands which activates focal adhesion signaling.

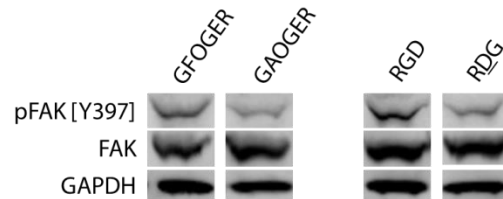


Figure 10. Western blot for FAK phosphorylation. hMSC exhibited 1.5- and 1.4- fold greater phosphorylation of FAK at Y397 when encapsulated in hydrogels functionalized with active peptides, GFOGER and RGD, compared to inactive peptides, GAOGER and RDG, respectively.

Encapsulated hMSC growth and proliferation

We next examined the behavior of hMSC encapsulated in ligand-functionalized hydrogels. First, we assessed the number of cells by DNA content over 1 week in 3-D

culture. **Figure 11** shows no significant differences in initial cell loading on day 1 or cell number on day 7 among GFOGER, RGD, or RDG hydrogels. There was also no significant difference between days 1 and 7 for any of the ligands.

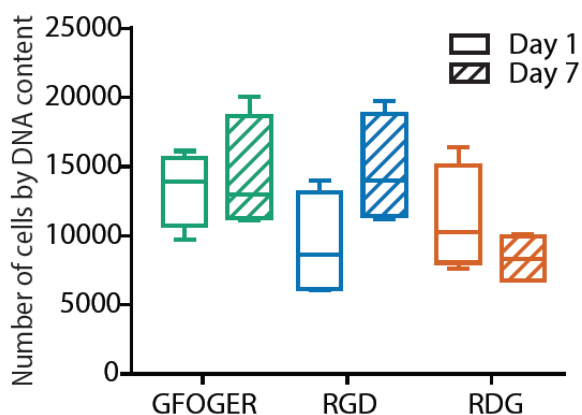


Figure 11. Encapsulated cell number in ligand-functionalized hydrogels. Cell number over 1 week in culture was assessed for cell-laden ligand-functionalized hydrogels. No significant differences were detected between time points or among groups. (Whiskers represent min and max, box extends from 25th to 75th percentiles, line represents median. N=4).

We then examined proliferation of hMSC inside ligand-functionalized hydrogels by incorporation of 5-ethynyl-2'-deoxyuridine (EdU), a nucleoside analog of thymidine which is incorporated into DNA during active DNA synthesis. hMSC-laden hydrogels were cultured for 7 days and then exposed to EdU for 48 h. EdU incorporation was detected by covalently binding a fluorescent azide using click chemistry. **Figure 12** shows low proliferation rates with median values around 2%. Proliferation rates were not significantly different among ligands.

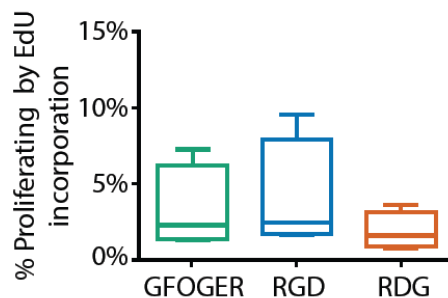


Figure 12. Proliferation of encapsulated hMSC in ligand-functionalized hydrogels. Proliferation was assessed by EdU incorporation (48 hr exposure) after 1 week in culture of encapsulated hMSC. No significant differences were detected among ligands. (Whiskers represent min and max, box extends from 25th to 75th percentiles, line represents median. N=4).

Osteogenic differentiation of encapsulated hMSC

To examine osteogenic differentiation, alkaline phosphatase activity, an early marker of osteogenic differentiation, was assessed. hMSC were encapsulated in ligand-functionalized hydrogels and cultured in osteogenic media or growth media. Alkaline phosphatase activity was measured and is shown in Figure 13. For cell laden hydrogels functionalized with the adhesive peptides GFOGER or RGD, ALP levels for osteogenically stimulated samples were 3-fold higher than growth controls, whereas ALP levels for hMSC in RDG hydrogels was not different between growth media and osteogenic stimulation.

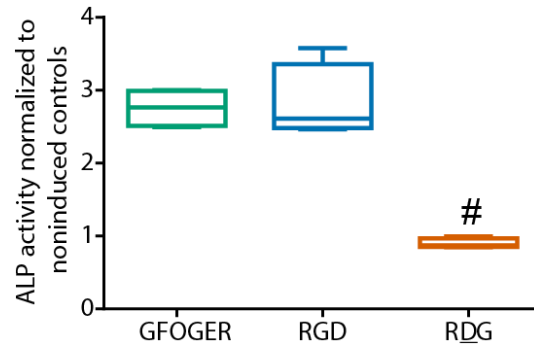


Figure 13. Osteogenic differentiation of encapsulated hMSC. Cell-laden hydrogels were cultured in osteogenic induction medium. Alkaline phosphatase activity, an early marker of differentiation, was assessed on day 9. (Whiskers represent min and max, box extends from 25th to 75th percentiles, line represents median. N=4; Kruskal-Wallis: #p<0.05).

DISCUSSION

Hydrogels are an attractive class of materials for cell encapsulation due to properties that mimic the extracellular matrix such as high water content and simple diffusion of oxygen, nutrients, and waste. Due to their defined chemical compositions, synthetic polymers are often reproducible and can be modified to tune material properties such as degradation rate, mechanical properties, and shape - large advantages over natural polymers that display heterogeneity and structural complexity that renders modifications difficult. The lack of cell adhesion sites on most synthetic polymers yields the opportunity of engineering specificity into the material by incorporating cell adhesive sites or growth factors, independent of substrate mechanical properties.

PEG-mal hydrogels have been successfully used in a wide array of applications: the study of epithelial morphogenesis [44], a therapeutic neural electrode coating [118], enhancement of islet survival after transplantation [107], cell delivery and growth factor delivery for cardiac repair after injury [2,108], growth factor delivery for bone repair [80], and skeletal muscle constructs [119]. This study aimed to develop PEG-mal as a novel, integrin-specific microenvironment and cell-delivery vehicle for hMSC.

We found that GFOGER, RGD and RDG all exhibited high conjugation efficiencies to PEG-mal, which is a significant advantage compared to other Michael addition chemistries with reactivity towards thiols [42]. The bulk material properties storage modulus and swelling ratio were not different among ligands for hydrogels of the same weight percent and ligand density. However, because of the large difference in the structure and size of the ligands – GFOGER is a 12 kDa triple helix and RGD/RDG are linear 0.69 kDa peptides – there may be differences in the local microstructures, local

material properties, or ligand accessibility among hydrogels containing different peptides. Rubber elasticity theory and the Flory and Rehner equations estimated the mesh size of our hydrogels at 15-40 nm, within the range of other published PEG hydrogel mesh sizes [111,120]. Cell adhesion 2-D experiments on the surface of peptide-functionalized gels showed that the adhesive peptides RGD and GFOGER were active after conjugation and crosslinking in the hydrogel platform. Antibody blocking experiments showed that short term hMSC adhesion was largely mediated by integrin $\alpha 2\beta 1$ on GFOGER hydrogels and by integrin $\alpha v\beta 3$ on RGD hydrogels, consistent with previous reports [78,85]. As expected, RDG and GAOGER peptide control hydrogels supported little hMSC adhesion, similar to blank hydrogels. It is noteworthy to discuss the stiffness of our hydrogel formulation compared to many other hydrogel compositions in the field used for osteogenic differentiation. Although matrix stiffness and cell shape may play a role in determining cell fate *in vitro* [33,36,37], *in vivo*, the transplanted microenvironment must not only provide directional cues to the transplanted cells, but allow for their engraftment as well as the infiltration of host cells. Because the ultimate aim of this project was to engineer a microenvironment for cell delivery and tissue repair, the hydrogels used in this study were relatively soft ($G' = 60$ Pa) compared to other published studies ($G' = 100$ - 1000 Pa [121], $G' = 4$ - 7 kPa [39], $\sigma = 1$ - 50 kPa [122,123]). Previous work in our lab and others have shown that less cross-linked and more degradable hydrogels, result in better healing *in vivo* [32,50,80], thus we decided to move forward with *in vitro* characterization of hydrogels that would closely mimic what we used for cell delivery *in vivo*.

Encapsulation in adhesive RGD and GFOGER hydrogels resulted in high viability and spreading, as shown by Calcein AM uptake, cell area, and distinct cytoskeletal actin

fibers. Significantly less spreading and diffuse actin staining was observed in RDG and GAOGER hydrogels, consistent with the 2-D cell adhesion results in that RDG and GAOGER do not support cell adhesion. The levels of FAK phosphorylation were higher in GFOGER and RGD hydrogels as compared to their inactive control peptides, indicating that integrin activation and binding is occurring in 3-D. The nonzero values of FAK phosphorylation in the GAOGER and RDG control hydrogels may be due to an incomplete decrease in phosphorylation levels prior to seeding in the hydrogels. The low levels of cell growth and proliferation after encapsulation as shown by DNA content and EdU incorporation, combined with the high viability staining suggest that encapsulated hMSC are neither growing nor dying over 1 week in culture.

We did observe an increase in ALP activity for hMSC encapsulated in ligand functionalized hydrogels under osteogenic stimulation, although we did not see a significant difference between RGD and GFOGER hydrogels. The lack of increased differentiation in GFOGER functionalized materials differs from previous work from our lab showing GFOGER enhances hMSC osteogenic differentiation [78,79,85]. It is important to note that the previous work with the GFOGER ligand has been on 2-D surfaces or porous scaffolds (2-D surfaces with curvature). Most of the differentiation protocols in literature are for a confluent 2-D monolayer suggesting that cell-cell contacts are crucial for osteogenic differentiation. Because of the nature of the 3-D microenvironment, it is likely that the cell density or mechanical properties used in this aim may not have been ideal to support osteogenesis. As previously mentioned, the aim of this project was to engineer an environment ultimately for cell delivery, thus finding the optimal parameters for *in vitro* differentiation was not explored further.

In this aim, we have engineered an integrin-specific cell microenvironment using biomimetic adhesive ligands. We have shown that we were able to control material properties of the matrix which were independent of ligand peptide, and that we were able to tune material properties such as storage modulus by varying hydrogel parameters. The ligand peptides exhibited specificity to expected integrins and we were able to observe differences in cell morphology in 3-D, while maintaining high cell viability.

CHAPTER 4: THE ABILITY OF INTEGRIN-SPECIFIC HYDROGELS TO PROMOTE HMSC SURVIVAL AND BONE REPAIR IN VIVO

ABSTRACT

Cell-based therapies represent promising strategies for tissue repair, although current cell therapies fail to address long term engraftment or delivery timing and location resulting in engraftment rates of less than 1%. Although bone has the innate ability to remodel and regenerate, large, non-healing bone defects and non-union fractures remain a significant clinical problem. Mesenchymal stem cell (MSC) transplantation has been shown to enhance bone, cartilage, and intervertebral disc repair in preclinical and clinical models, but engraftment rates of delivered hMSC are extremely low (<3%). The lack of information regarding cell fate after transplantation, cell dose, cell source, and appropriate scaffold properties limits the therapeutic effect of hMSC for treatment of large musculoskeletal defects. Integrins are a family of cell surface receptors that primarily mediate adhesion of cells to ECM proteins and also transduce signals across the cell membrane to regulate cellular activities such as migration, proliferation, survival and differentiation. Therefore, as a major mediator of important cellular responses, engineering integrin binding activity within a 3D environment may improve transplanted cell survival and function.

In this study, we aimed to investigate the performance of a cell-mediated degradable hydrogel functionalized with integrin-specific ligands in supporting the survival of transplanted hMSC and tissue repair in a segmental bone defect. We

accomplished this by incorporating the cell-adhesive $\alpha 2\beta 1$ integrin-specific GFOGER peptide, cell-adhesive $\alpha v\beta 3$ integrin-specific RGD peptide, or non-adhesive RDG peptide combined with human mesenchymal stem cells in a protease-degradable PEG-maleimide hydrogel and tracked cell survival through transgenic luciferase expression. We hypothesized that hydrogel delivery vehicles that promote cell viability in combination with the pro-osteogenic properties of the carrier would result in superior bone repair. We found that $\alpha 2\beta 1$ -specific GFOGER-functionalized hydrogels promote enhanced hMSC survival and bone repair in vivo, compared to RGD- or RDG-functionalized hydrogels, highlighting integrin-specificity as a novel strategy for tissue-specific cell delivery and repair.

INTRODUCTION

Cell-based therapies represent promising strategies for tissue repair, particularly in cases in which host cells, due to disease, age, or excessive trauma, are unable to repair the defect or deficiency alone, even with additional delivered therapeutics. Current cell therapies fail to address long term engraftment or delivery timing and location resulting in engraftment rates of less than 3% as the majority of delivered cells die or are washed away as quickly as 1 hour post transplantation [1,2]. Long term cell engraftment has been shown to correlate with enhanced therapeutic outcomes [5-7], and has also been shown to be greater in cases in which cells are delivered in an appropriate biomaterial carrier versus in media alone [2,8].

Although bone has the innate ability to remodel and regenerate, large, non-healing bone defects and non-union fractures remain a significant clinical problem [124]. Current clinical treatments for large bone defects due to disease, injury or tumor resection include bone grafting using autografts or allografts, but these techniques exhibit high failure rates and limitations due to donor site morbidity and pain, tissue availability, risk of disease transmission and immune rejection, and reduced biologic activity or mechanical properties due to processing [9,125]. The protein therapeutics bone morphogenetic proteins- (BMP) 2 and 7 exhibit success rates similar to autografts for vertebral fusions, however, currently used biomaterial carriers of BMP-2, such as the collagen sponge-based INFUSE®, exhibit serious limitations in the control over release mechanisms and kinetics. The supraphysiological dose required for the stimulation of bone formation leads to complications such as neuropathy, ectopic bone formation [126], and severe inflammation

[10]. Carriers with controlled release functionality may decrease the dose and cost of BMP-2-based therapies thereby decreasing incidence of adverse side effects [46,80].

Mesenchymal stem cell (MSC) transplantation has been shown to enhance bone, cartilage, and intervertebral disc repair in preclinical and clinical models [15,16], but engraftment rates of delivered hMSC are extremely low (<3%) [12]. The lack of information regarding cell fate after transplantation, cell dose, cell source, and appropriate scaffold properties limits the therapeutic benefits of hMSC for treatment of large musculoskeletal defects.

An appropriate carrier must support the adhesion, migration, organization, and differentiation of the transplanted cells and host cells. These behaviors rely on an intricate interaction among various cues supplied by the extracellular environment which include insoluble molecules within the ECM such as proteins, soluble molecules such as growth factors, hormones, and cytokines, and cell-cell interactions.

Integrins are a family of cell surface receptors that primarily mediate adhesion of cells to ECM components and also transduce signals across the cell membrane to regulate cellular activities such as migration, proliferation, survival and differentiation [127]. Therefore, as a major mediator of important cellular responses, engineering integrin binding activity in addition to cell-mediated degradability within a 3D environment may improve transplanted cell survival and function.

In this study, we aimed to investigate the performance of a cell-mediated degradable matrix functionalized with integrin-specific ligands in supporting the survival of transplanted hMSC and tissue repair in a segmental bone defect. We incorporated the cell-adhesive $\alpha 2\beta 1$ integrin-specific GFOGER peptide, cell-adhesive $\alpha v\beta 3$ integrin-

specific RGD peptide, or non-adhesive RDG peptide combined with hMSC in a protease-degradable PEG-maleimide hydrogel. The effect of hMSC delivery and ligand specificity on tissue repair was assessed by newly formed bone volume after treatment. The effect of ligand on cell survival or persistence was studied through cell tracking by transgenic luciferase expression and *in vivo* imaging. Our lab has previously shown that GFOGER-functionalized degradable hydrogels promote enhanced bone repair in a murine segmental defect, and when combined with low doses of rhBMP-2, fully healed the defect [80]. We hypothesize that hydrogel delivery vehicles that promote cell viability in combination with the pro-osteogenic properties of the carrier will result in superior bone repair.

METHODS

Luciferase Lentiviral Production

Lentiviral production was performed by the Viral Vector Core in the Neuroscience NINDS Core Facilities at Emory University. HEK 293FT (Invitrogen) cells were maintained in complete medium (DMEM, 10% FBS and 1% Pen-Strep), incubated at 37 °C, 5% CO₂ and seeded at 70-80% confluence 1 day prior to transfection. HEK cells were incubated with transfection mixture (500 µg pLenti-UbC-RFLuc- tdtomato (Targeting Systems), 250 µg pMDLg/pRRE, 125 µg pRSV-REV187 and 150 µg pVSVG in ddH₂O with 125 mM CaCl₂ and 30 mM HEPES) for 7 hr before fresh medium change. Lentivirus was harvested 72 hr post transfection by centrifuging the supernatant at 500xg for 5 min at 40 °C, followed by passage through a 0.45 µm low protein binding filter. Filtered supernatant was then centrifuged at 91,000xg for 2 hr at 40 °C in a 45Ti rotor (Beckman). The virus pellets were re-suspended in 500 µL PBS, and after addition of 20% sucrose as a cushion, centrifuged at 91,000xg for 2 hr at 40 °C in a SW 41 rotor (Beckman). The virus pellet was resuspended in 100 µL PBS and stored at -80 °C.

Lentiviral Transduction

Transduction protocol was adapted from Lin et al [128]. Early passage hMSC (<3) were seeded at 60-70% confluence and allowed to attach overnight. Media was replaced with a small volume of complete media containing 100 µg/mL protamine sulfate or 8 µg/mL Polybrene. Lentivirus was thawed on ice and added to the cells at MOI 5-20. Eight hr after initial infection, additional complete media with protamine sulfate or Polybrene was added to the plate, and 24 hr after initial infection, media was replaced with fresh complete media. Six days after initial infection, transduction efficiency was measured by

tdtomato expression by flow cytometry (BD Accuri C6). A scatter plot comparing 533 nm and 585 nm fluorescence emission was used in order to gate out the high auto-fluorescent cell population found within hMSC.

hMSC^{FLuc} characterization

Cell growth capacity for hMSC transduced to express luciferase (hMSC^{FLuc}) compared to hMSC was measured by fold change in DNA content over 7 days. 1000 hMSC or hMSC^{FLuc} were seeded into wells of a 96 well plate and cultured in growth media. At days 1 and 7, cells were rinsed with PBS and plates were stored at -80 °C until analysis. DNA content was measured using the CyQuant kit (Thermo Fisher) according to the manufacturer's instructions. Differentiation capacity for hMSC^{FLuc} compared to hMSC was measured by alkaline phosphatase activity (ALP) and mineralization. hMSC were seeded at 10,000 cells/cm² on tissue culture plastic and cultured in osteogenic differentiation medium (basal media with dexamethasone, ascorbate, mesenchymal cell growth supplement, L-glutamine, penicillin/streptomycin, and β -glycerophosphate, Lonza). After 9 days of culture in osteogenic differentiation medium, cells were lysed and assayed for ALP by incubating with MUP substrate. hMSC were scraped in cold 50 mM Tris-HCl and sonicated to lyse the cells. The total protein content for each lysate sample was determined using a BCA assay kit (Thermo Scientific). Samples and ALP standards were loaded into a 96-well plate, then incubated with 60 μ g/mL MUP substrate at 37 °C for 1 hr and read at 360 nm excitation/465 nm emission. ALP activity was normalized to sample protein content. After 21 days in induction media, luciferase expression and mineralization were assessed. To visualize luciferase expression after differentiation, luciferin (150 μ g/mL) was added to the cells and bioluminescence imaged on an IVIS

Lumina II (Perkin Elmer). Mineral deposition was visualized by Alizarin red staining. Cells were fixed in 10% formalin, rinsed in water, incubated in 2% Alizarin red solution for 20 min, and washed 4 times with water.

Implant preparation

Implant hydrogels (3 μ L) were precast within 4-mm long polyimide tube sleeves (Microlumen) with laser machined 300 μ m diameter holes to improve nutrient transport and cell invasion into the defect (**Figure 14**). All hydrogels used for *in vivo* studies contained 4.0 - 4.5% (wt/v) PEG-maleimide and 1.0 mM adhesive peptide (unless otherwise stated). All implant and hydrogel components were tested for endotoxin contamination and were confirmed to be below 0.1 EU/mL (5-fold lower than the United States Food and Drug Administration's recommended 0.5 EU/mL) by Limulus Amebocyte Lysate colorimetric assay (Lonza). The hydrogel was prepared as previously mentioned and individual implant sleeves were filled. Hydrogels were allowed to cross-link and swell in complete media. Cell loading efficiency was quantified for sister implant samples by DNA content. Implants were incubated in 1 mg/mL collagenase, type I (Thermo Fisher) at 37 °C until fully degraded. Cells were lysed by sonication and freeze-thaw cycles. Whole cell lysate was assayed for DNA content and cell number using a CyQuant kit according to the manufacturer's instructions (Thermo Fisher) and compared to a cell standard curve.

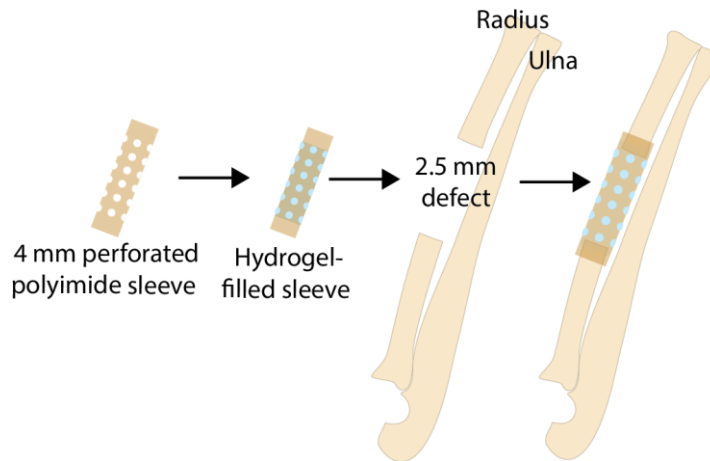


Figure 14. Murine radial segmental defect. A 4 mm polyimide sleeve laser machined with 300 μm diameter holes along its length is filled with hydrogel prior to implantation. A 2.5 mm defect is created in the radius and the implant sleeve is slipped over the ends of the defect holding the hydrogel in contact with the defect ends.

Radial Segmental Defect

All animal experiments were performed with the approval of the Georgia Tech Animal Care and Use Committee with veterinary supervision and within the guidelines of the Guide for the Care and Use of Laboratory Animals. NOD.Cg-*Prkdc*^{scid} *Il2rg*^{tm1Wjl}/SzJ (NSG) male mice (8–10 weeks old, Jackson Laboratories) were anesthetized under isoflurane, and fur was removed from both forelimbs. The right forelimb was then swabbed with chlorohexidine and alcohol, and a 1.5-cm incision was made in the skin. Muscle tissue overlying the ulna and radius were blunt dissected, and 2.5 mm defects were made in the right radius using a custom-built bone cutter, while leaving the ulna intact. Implants were placed into the defect by fitting the polyimide sleeve over the radius at the proximal and distal ends of the defect holding the hydrogel in contact with the defect ends (**Figure 14**). The incision was then closed with Vicryl suture. Mice were given a single dose of slow-release buprenorphine for pain relief and were monitored post-surgery for signs of distress, normal eating habits and movement.

Cell tracking in vivo

Bioluminescence of transplanted hMSC^{FLuc} was measured using an IVIS Spectrum CT (Perkin Elmer). Luciferin salt (Promega) was dissolved in physiological saline and sterile filtered through 0.22 μ m pore membranes. Mice received a 150 mg/kg luciferin dose injected into the intraperitoneal cavity. Time to maximum signal intensity was determined for each time point and 2D bioluminescence images were acquired 20-45 min post injection and analyzed with Living Image software (Perkin Elmer). Background bioluminescence of the unoperated arm was subtracted from the signal in the defect and signal is reported as photon flux which normalizes for acquisition settings and ROI area.

Faxitron and live animal μ CT

X-ray images and 3D μ CT images were acquired as previously described [80]. Briefly, radial defects were imaged with the MX-20 Radiography System (Faxitron). For μ CT scanning, a 3.2 mm length of the radius centered about the 2.5 mm radial defects was scanned in anesthetized, live subjects using a VivaCT system (Scanco Medical, 145 mA intensity, 55 kVp energy, 200 ms integration time, and 15 μ m resolution). Bone formation was evaluated by contouring 2D slices to include only the radius and applying a Gaussian filter. 3D μ CT reconstructions display the full 3.2 mm length of radius scanned. However, in order to ensure that only new bone formation was measured, quantification of bone volume and mineral density within the defect was performed by evaluating only the middle 2.0 mm of the original 2.5 mm defect (**Figure 15**).

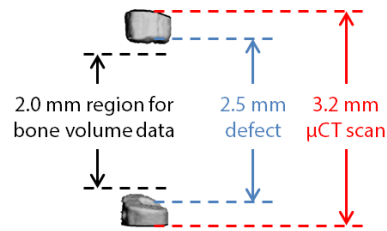


Figure 15. Representative 3-D microCT reconstruction of segmental defect at day 3. Dashed lines show schematic of bone volume quantification.

Histology and Immunostaining

Animals were euthanized 8 weeks after surgery by CO₂ inhalation and their radii and ulna were harvested. Soft tissue was removed carefully without disturbing the defect and the bones fixed in 10% neutral buffered formalin overnight. Samples were briefly rinsed in tap water and decalcified in formic acid for two days. The samples were processed for paraffin embedding and sectioned to a 5 μm thickness. For histological staining, sections were deparaffinized and hydrated. Sections were then stained with Weigert's Iron Hematoxylin, 0.02% Fast Green, and 1.0% Safranin-O. For human-specific staining, sections were deparaffinized and hydrated and treated with sodium citrate buffer, pH 6.0, at 60 °C overnight for antigen retrieval. Endogenous peroxidase was inhibited with 3% H₂O₂ followed by blocking with 2.5% horse serum for 1 hr at room temperature (Vector Labs). Sections were stained with human-specific anti-NuMa (Rabbit-anti-NuMa, Abcam, 1:100) or Rabbit IgG isotype control (1 μg/mL, Vector Labs) at 4 °C overnight, followed by ImmPRESS™ HRP Anti-Rabbit IgG (Vector labs) for 1 hour at room temperature. The stain was developed with ImmPACT™ DAB (Vector labs) and sections were dehydrated and mounted.

RESULTS

Luciferase-expressing hMSC

Red firefly luciferase catalyzes the oxidation of D-luciferin releasing a photon of light at 610 nm as a byproduct (**Figure 16A**). The emitted bioluminescence can then be detected using a charge-coupled device camera such as the IVIS. hMSC were transduced with a lentivirus carrying the red firefly luciferase and tdtomato genes under the ubiquitin C promoter (**Figure 16B**). Because ubiquitin C is constitutively expressed, red firefly luciferase and tdtomato are both stably, constitutively expressed in transduced hMSC, rendering bioluminescence after addition of the substrate D-luciferin a reliable marker of cell live cell presence. In addition, the signal intensity is proportional to cell number.

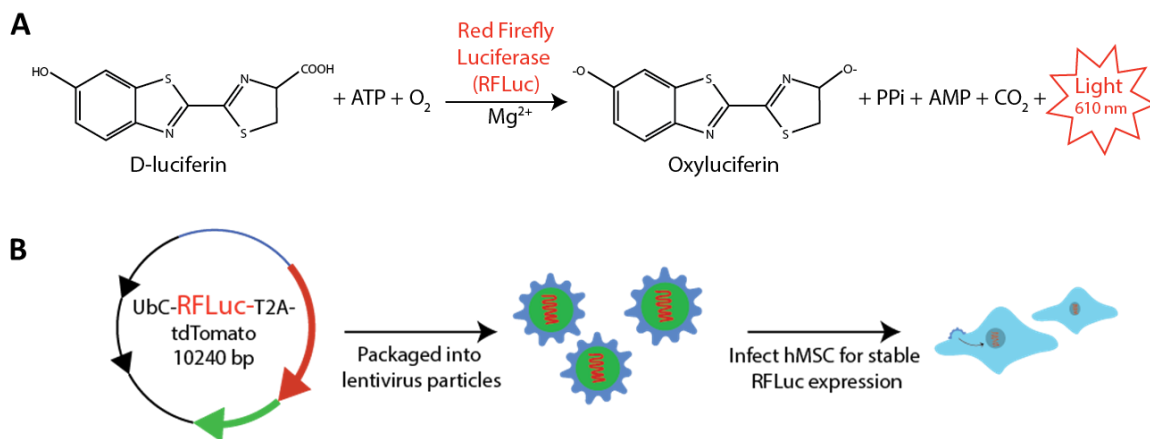


Figure 16. Schematic of luciferase reaction for bioluminescent cell tracking. A) In the presence of ATP and oxygen, firefly luciferase catalyzes the oxidation of D-luciferin releasing a photon of light as a byproduct. B) A plasmid carrying red firefly luciferase and tdtomato coexpressed under the ubiquitin C promoter is packaged into lentivirus particles which then transduce hMSC to constitutively express red firefly luciferase.

We first examined the effect of lentiviral transduction and luciferase/tdtomato expression on hMSC function. Using an adapted, published protocol [128], we transduced

hMSC and assessed transduction efficiency by expression of the fluorescent protein tdTomato and flow cytometry. Positive hMSC were gated comparing 533 nm and 585 nm fluorescence emission in order to gate out the high auto-fluorescent cell population found within hMSC. We were able to achieve high transduction efficiencies (>90%) at relatively low multiplicity of infection ratios (MOI=5-15, **Figure 17A**) when treated with protamine sulfate or Polybrene. Cell growth was examined by assessing cell number by DNA content over 1 week in culture for unmodified hMSC and transduced hMSC^{FLuc} (**Figure 17B**). The fold change in cell number for hMSC^{FLuc} treated with Polybrene was significantly lower than unmodified hMSC or hMSC^{FLuc} treated with protamine sulfate. To examine whether lentiviral transduction affected osteoblastic differentiation, hMSC and hMSC^{FLuc} were grown in osteogenic differentiation medium with hMSC in growth media as a negative control. After 9 days in culture, ALP, an early marker of osteogenic differentiation, was assessed and showed no significant difference between hMSC and hMSC^{FLuc} treated with protamine sulfate, whereas hMSC^{FLuc} treated with Polybrene resulted in significantly lower ALP levels compared to unmodified hMSC (**Figure 17C**). After 21 days of osteogenic induction, cells were stained with Alizarin red for visualization of mineral deposits (**Figure 17D**, top). To visualize luciferase expression after differentiation, luciferin was added to the culture medium and bioluminescence images were acquired (**Figure 17D**, bottom). The bioluminescent signal distribution correlated to the areas of high Alizarin red staining likely due to higher cell densities in areas of higher mineral density. We found no significant differences in cell functions such as growth or osteogenic differentiation between hMSC and hMSC^{FLuc} when treated with protamine sulfate to increase transduction efficiency. The luciferase gene also remained active after osteogenic differentiation.

Polybrene treatment during transduction resulted in significantly decreased levels of growth and differentiation of hMSC^{FLuc}, in agreement with previous reports [19], thus protamine sulfate was used in all subsequent transductions.

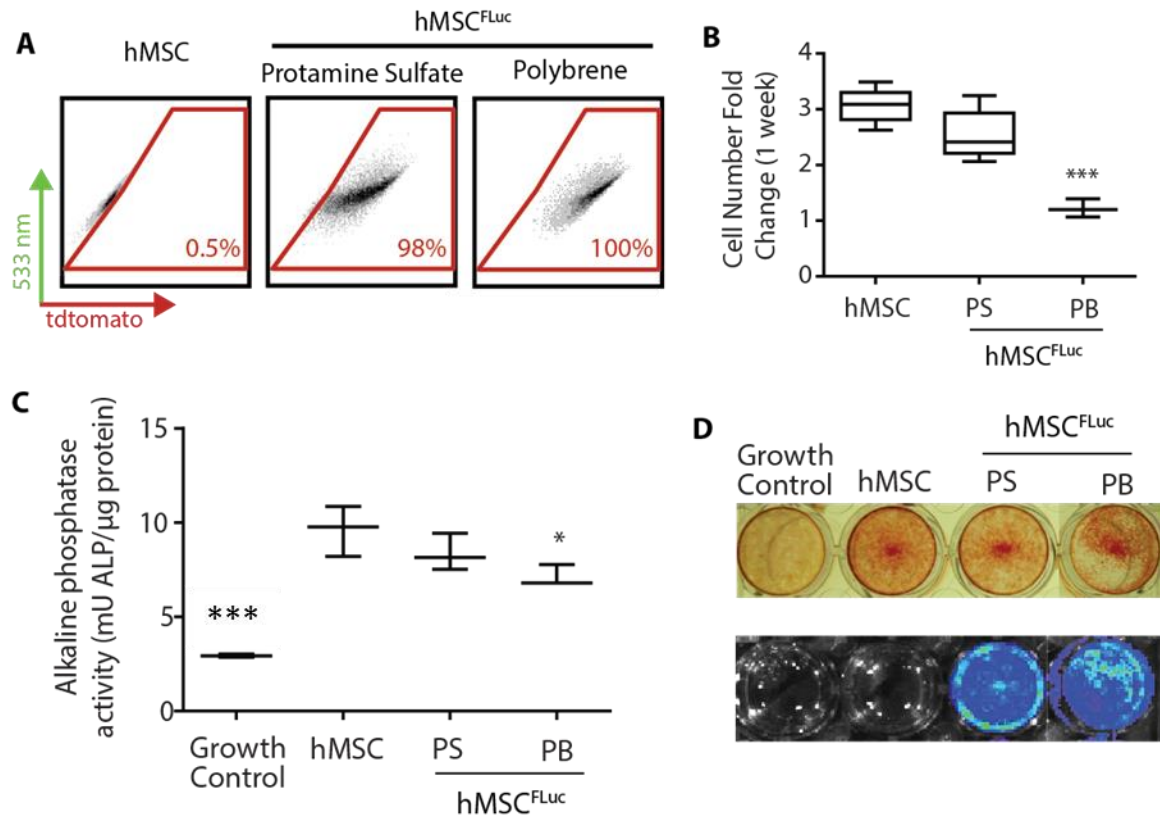


Figure 17. hMSC^{FLuc} exhibit normal growth and differentiation capacities. A) hMSC were transduced at high efficiency (>90%) with a lentivirus to co-express red firefly luciferase and tdtomato under the ubiquitin C promoter. B) Fold change in cell number by DNA content over 1 week for unmodified hMSC or hMSC^{FLuc} treated with protamine sulfate (PS) or Polybrene (PB). hMSC and hMSC^{FLuc} treated with protamine sulfate exhibited similar differentiation capacities as shown by C) ALP activity and D) mineral deposition by Alizarin red staining (top panel) in response to osteogenic stimulation and hMSC^{FLuc} continued to express luciferase after differentiation (bottom panel). (Whiskers represent min and max, box extends from 25th to 75th percentiles, line represents median. N=3-4; ANOVA: ***p<0.001; *p<0.05 compared to hMSC).

We next compared hMSC^{FLuc} to unmodified hMSC in their effect on bone repair after transplantation. The radial segmental defect surgery was performed as previously described [80]. Hydrogels for cell delivery were cast prior to surgery within a polyimide sleeve laser machined with holes to better support nutrient transport (**Figure 14**). Polyimide, a polymer used in FDA-approved devices, is currently used for applications such as encapsulation and insulation of active electrodes and retention sheaths for stents. The sleeve diameter is slightly larger than the diameter of the radius and is not fastened to the bone in any way, thus providing minimal mechanical fixation to the defect which is mainly stabilized by the intact ulna. The sleeve prevents the hydrogel from moving out of the defect space after wound closure and holds the hydrogel in contact with the defect ends. 15,000 hMSC or hMSC^{FLuc} were delivered to the radial segmental defect in 4.5% PEG (w/v) hydrogels functionalized with 1.0 mM GFOGER. Newly formed bone volume was measured at weeks 4 and 8. No significant differences in bone volume were found between hMSC modified to express luciferase and unmodified hMSC (**Figure 18**). The *in vitro* and *in vivo* results comparing hMSC and hMSC^{FLuc} taken together show no significant differences in cell function due to transgenic expression of luciferase.

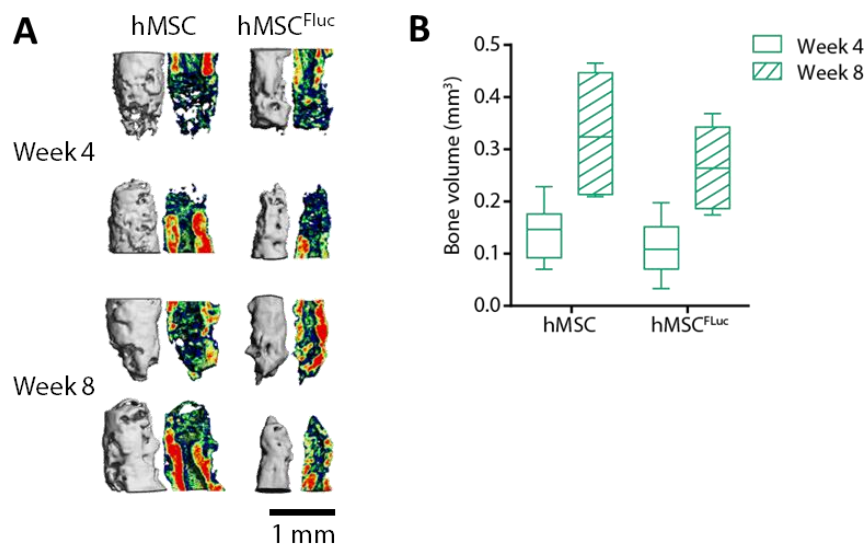


Figure 18. Effect of genetically modified hMSC on bone repair. Bone volume at weeks 4 and 8 after 15,000 hMSC or hMSC^{FLuc} delivery to the radial segmental defect in 4.5% PEG with 1.0 mM GFOGER hydrogels. (Whiskers represent min and max, box extends from 25th to 75th percentiles, line represents median. N=5-11; t-test for each time point: no differences).

Optimization of hydrogel formulation for subsequent bone repair studies

We next tested multiple hydrogel and cell dosing parameters to optimize the treatment formulation for cell delivery. To investigate the effect of hydrogel polymer weight percent on healing, 4.5%, 6.0%, or 8.0% PEG (w/v) hydrogels with 1.0 mM GFOGER and 15,000 hMSC were delivered to the radial segmental defect. Representative 3-D reconstructions are shown in **Figure 19A** of full 3.2 mm scans surrounding the original 2.5 mm defect at weeks 4 and 8. The extent of defect closure increased with decreasing weight percent as significantly higher bone volume was measured in the 4.5% PEG-treated defects compared to 6% or 8%, identifying 4.5% as a suitable polymer weight percent for subsequent studies.

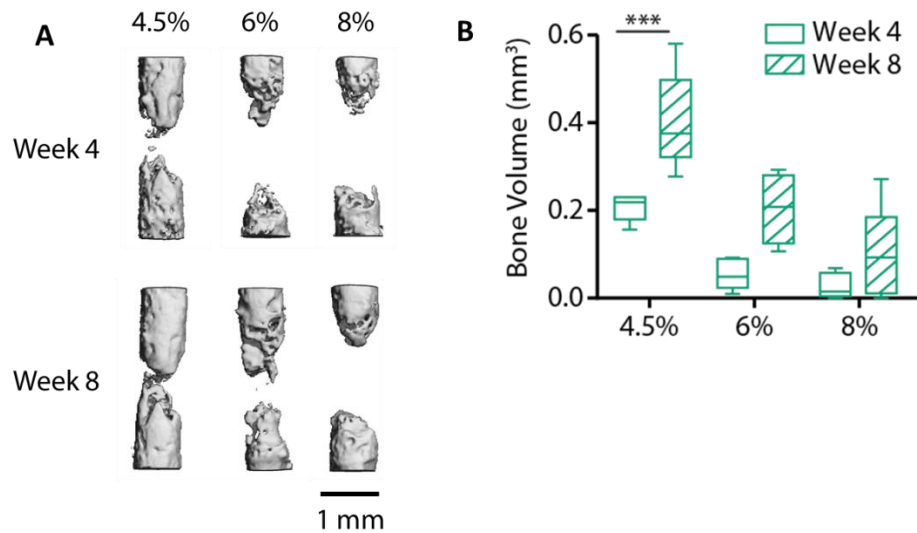


Figure 19. Effect of PEG weight percent and hMSC delivery on bone repair. A) Representative 3-D reconstructions and B) bone volume of defects treated with 4.5%, 6%, or 8% PEG w/v with 1.0 mM GFOGER and 15,000 hMSC. (Whiskers represent min and max, box extends from 25th to 75th percentiles, line represents median. N=5; 2-way ANOVA: ***p<0.0005).

To investigate the effect of cell dose on cell survival and healing, two doses of hMSC^{FLuc}, 15,000 or 30,000 per implant, were delivered to the radial segmental defect in 4.5% PEG (w/v) hydrogels functionalized with 0.3 mM GFOGER. Bioluminescent tracking showed a higher signal for the 30k cell dose, as expected (**Figure 20A**), but the signals for both doses followed a similar trend over the 8 week study increasing to week 4 and then declining gradually through week 8. When the bioluminescent signal was normalized to day 0 for each defect, there was no statistical difference in bioluminescence between the two cell doses (**Figure 20B**). Bone volume was measured by microCT at weeks 4 and 8 and showed no significant difference between 15,000 or 30,000 hMSC^{FLuc} doses at either time point (**Figure 21**). Because we see no significant difference in bone volume between cell doses of 15,000 or 30,000, we chose a cell dose of 15,000 for subsequent studies to reduce the number of cells needed for treatment.

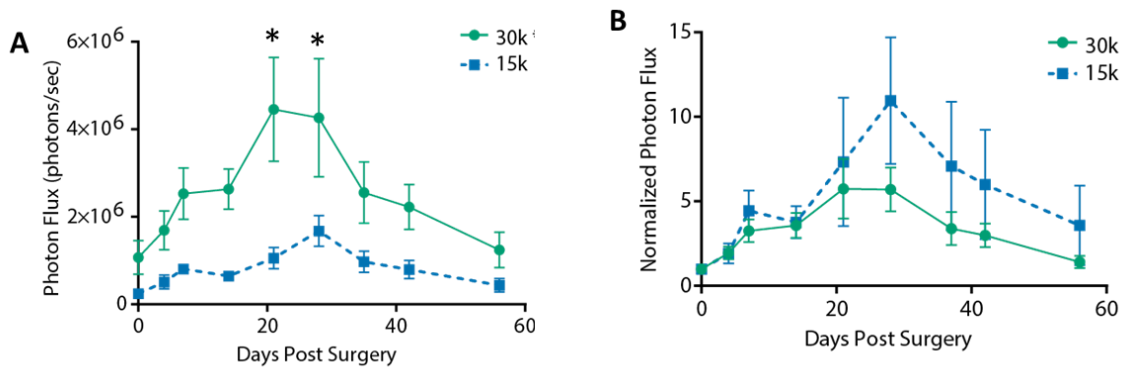


Figure 20. Effect of cell dose on cell survival. A) Bioluminescence after dose of 30,000 or 15,000 hMSC^{FLuc} delivered to the radial segmental defect in 4.5% PEG with 0.3 mM GFOGER hydrogels. B) Normalized bioluminescence to day 0 signals. (Bars represent SEM; N=7; Repeated measures ANOVA: * $p < 0.05$).

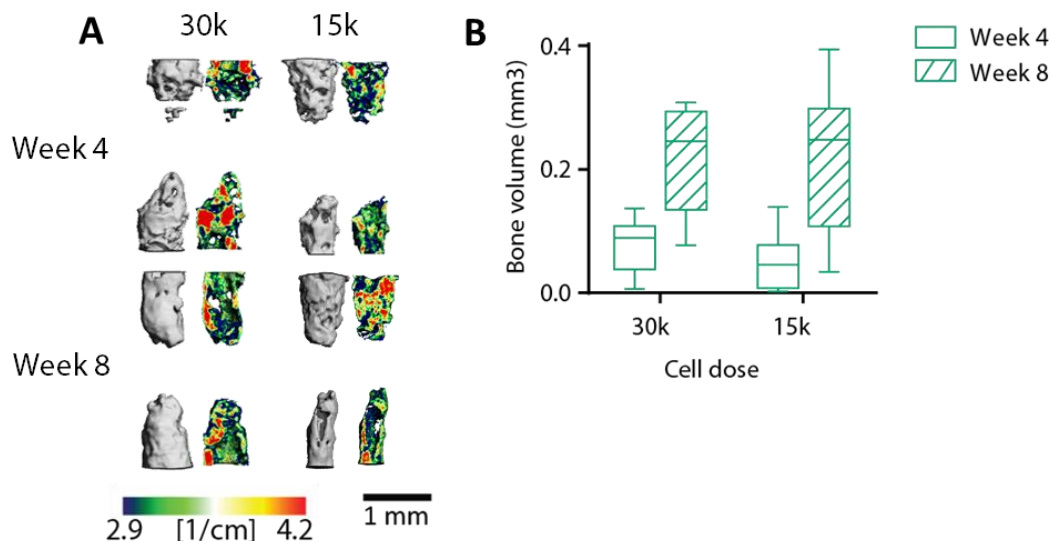


Figure 21. Effect of cell dose on bone repair. A) Representative 3-D reconstructions and B) bone volume at weeks 4 and 8 after delivery of 30,000 or 15,000 hMSC^{FLuc} to the radial segmental defect in 4.5% PEG with 0.3 mM GFOGER hydrogels. (Whiskers represent min and max, box extends from 25th to 75th percentiles, line represents median. N=7; Repeated measures ANOVA: no differences).

Finally, we examined the effect of ligand density in cell-free hydrogels on bone repair. Radial segmental defects were treated with 4.5% (w/v) hydrogels functionalized with 0.3 or 1.0 mM GFOGER *without* cells and newly formed bone volume was quantified

at weeks 4 and 8 (**Figure 22**). Significantly more bone was observed in defects treated with 1.0 mM GFOGER hydrogels. However, this effect cannot be simply attributed to higher ligand density. Because the coupling of ligand density and cross-link density in the present formulations, the increased healing could be due to lower cross-link density (and therefore faster degradation) of the 1.0 mM ligand hydrogels. Nevertheless, these pilot studies have identified a promising formulation (4.5% PEG (w/v) with 1.0 mM ligand and 15,000 hMSC) for investigating the effect of adhesive ligand type on hMSC survival and bone repair.

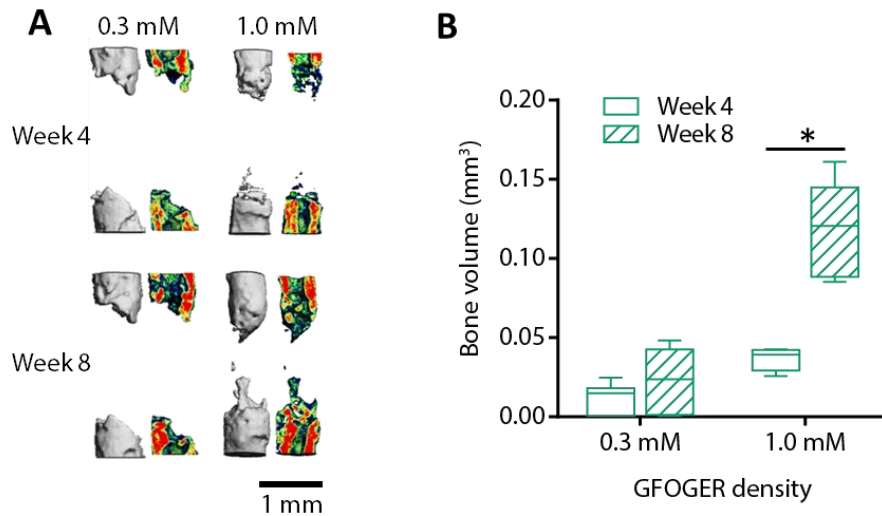


Figure 22. Effect of ligand density on bone repair. Bone volume at weeks 4 and 8 after radial segmental defect treatment with 4.5% PEG hydrogels functionalized with 0.3 mM or 1.0 mM GFOGER *without* cells. (Whiskers represent min and max, box extends from 25th to 75th percentiles, line represents median. N=5-6; Repeated measures ANOVA: *p<0.0001).

Effects of integrin-specific ligands on hMSC survival

To assess cell number loading in hydrogel implants, cell-laden hydrogel implants were degraded and DNA content was measured against a cell standard curve. **Figure 23A** shows cell number for hydrogel implants functionalized with GFOGER, RGD, or RDG. Each implant contained an average of 15,000 hMSC with no significant differences among hydrogel formulations. Integrin-specific hydrogels loaded with 15,000 early passage hMSC^{FLuc} were delivered into the radial segmental defect of male, NSG mice. Bioluminescence of transplanted hMSC was measured at multiple time points, as shown in **Figure 23B**. The bioluminescent signal for all groups increased 15-fold by week 2 and gradually declined through week 8. While all three groups exhibit similar bioluminescence trends through week 2, GFOGER maintained significantly higher bioluminescence between weeks 2 and 8, particularly at weeks 3, 4, and 6, while there were no significant differences between RGD and RDG.

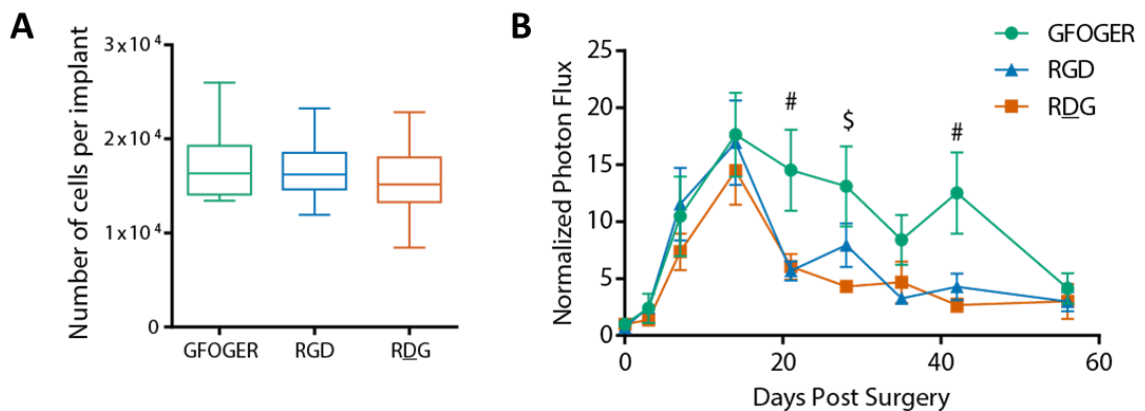


Figure 23. $\alpha 2 \beta 1$ -specific GFOGER hydrogel enhances hMSC survival. A) DNA content of pre-loaded implants shows about 15,000 cells per implant and no differences among groups. (Whiskers represent min and max, box extends from 25th to 75th percentiles, line represents median. N=6 for 3 independent experiments; ANOVA: no differences). B) Bioluminescence, quantified as photon flux, normalized to day 0 signal. (Error bars

represent SEM; N=8; 2-way ANOVA: #p<0.05 GFOGER compared to RGD and RDG, \$p<0.05 GFOGER compared to RDG).

Effect of integrin-specific ligands and hMSC on bone repair

Integrin-specific hydrogels with and without 15,000 early passage hMSC were delivered into the radial segmental defect of mice. Newly formed bone volume was monitored with live animal microcomputer tomography at weeks 4 and 8. **Figure 15** shows a representative micro-CT reconstruction of the segmental defect at day 3. Figure 24A presents representative 3-D reconstructions of the full 3.2 mm scan of the original 2.5 mm defect plus surrounding bone and sagittal cross-sections with a mineral density heat map overlay. Higher amounts of bone are visualized in the 3-D reconstructions for the GFOGER with hMSC group, whereas all other groups exhibited low levels of bone within the defect. Newly formed bone volume was quantified for the middle 2.0 mm of the 2.5 mm defect to avoid including bone from the defect ends. Defects treated with RGD or RDG exhibited very low levels of bone, with no significant difference between hydrogels containing hMSC and cell-free scaffolds (**Figure 24**). Defects treated with GFOGER-functionalized hydrogels without cells also exhibited low levels of bone volume, equivalent to levels in RGD and RDG groups, however, defects receiving hMSC in GFOGER-functionalized hydrogels resulted in significantly higher levels of bone formation at weeks 4 and 8 (**Figure 24**).

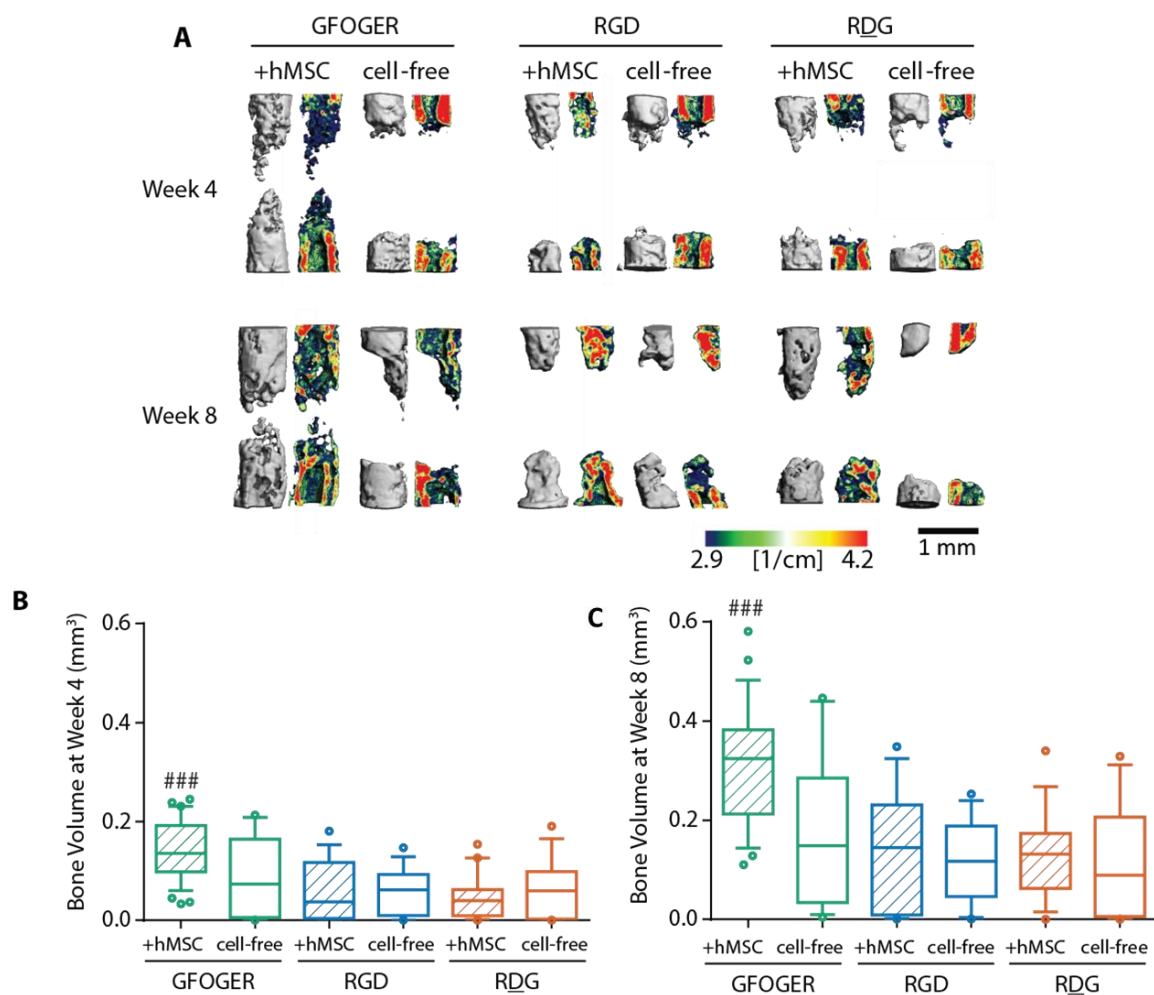


Figure 24. hMSC and $\alpha 2\beta 1$ -specific GFOGER enhance bone repair. GFOGER, RGD, or RDG-functionalized hydrogels with or without 15k encapsulated hMSC were implanted into the radial segmental defect in 8-10 week old male NSG mice and bone formation was monitored with micro-CT. B) Representative 3-D reconstructions of 3.2 mm bone section surrounding original 2.5 mm defect with sagittal mineral density heat maps. Bone volume was quantified in the middle 2.0 mm of the original 2.5 mm defect. GFOGER + hMSC resulted in significantly more bone formation compared to RGD + hMSC and RDG + hMSC at C) week 4 and D) week 8. (Whiskers represent 10th and 90th percentiles, box extends from 25th to 75th percentiles, line represents median. N=13-26; Kruskal-Wallis: ###p<0.0005 compared to RGD+hMSC and RDG+hMSC).

Histological sections of defects at week 8 were stained with Safranin-O/fast green to visualize histology of repaired bone (**Figure 25**). Bone marrow and lamellar bone can be seen in all defects, although defects treated with GFOGER hydrogels exhibit more

lamellar bone at the proximal and distal ends of the defect compared to RGD- and RDG-hydrogel treated defects with and without hMSC which show pockets lacking tissue attributed to un-degraded hydrogel. Defects treated with GFOGER-hydrogel without hMSC show more collagen rich matrix in the middle of the defect compared to RGD and RDG-treated defects, although un-degraded hydrogel is still observed. GFOGER and hMSC treated defects show the most bone-like histology compared to all other conditions with collage-rich unorganized bone matrix in the middle of the defect. Human-specific nuclear mitotic apparatus (NuMa) staining confirms the presence of human cells in the defect at weeks 4 and 8 (**Figure 26**). Increased positive staining can be seen in the GFOGER-treated defects compared to RGD or RDG, consistent with bioluminescence data. The majority of stained human cells seemed to be localized in the bone marrow, although some are detected in the hydrogel space.

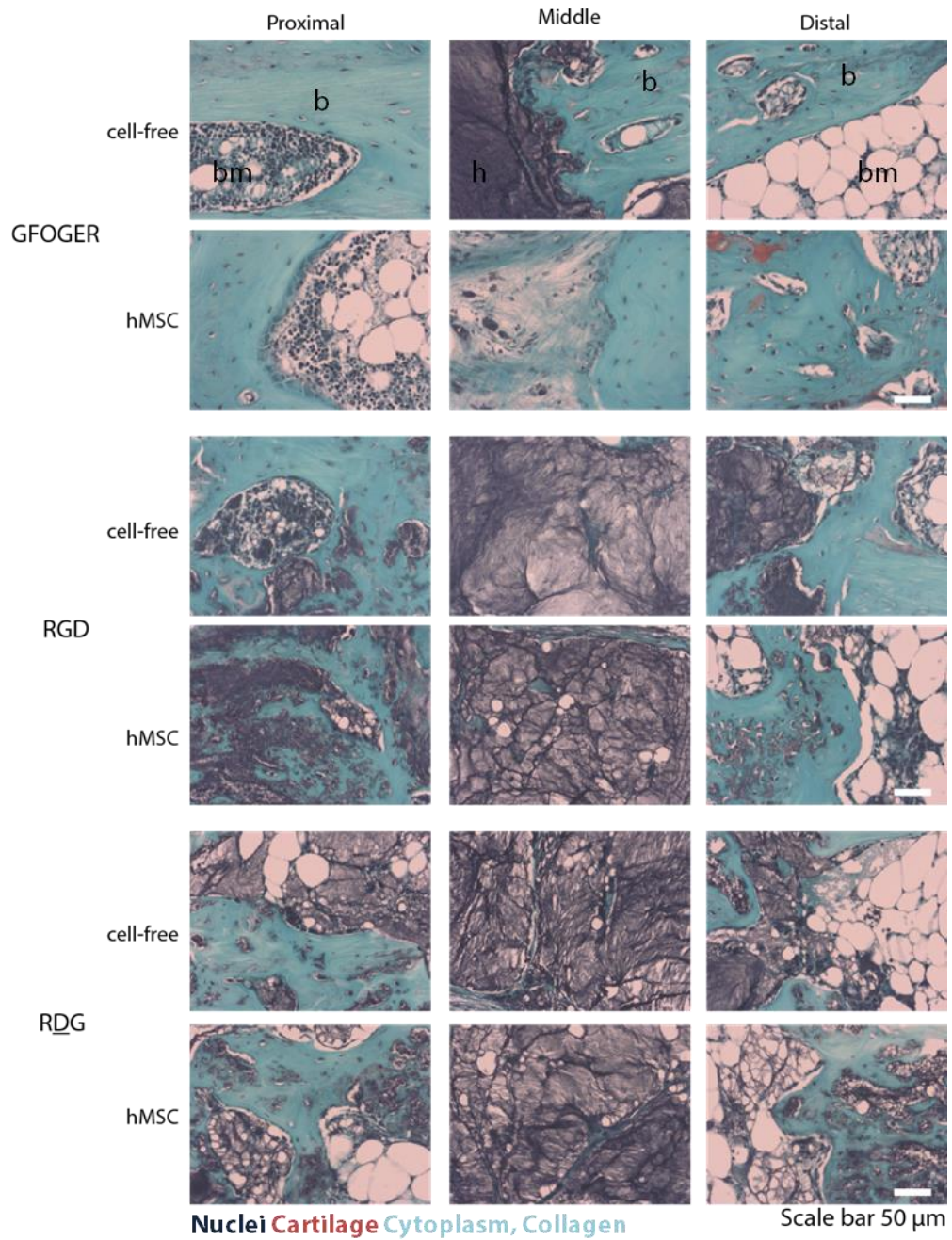


Figure 25. hMSC and $\alpha 2\beta 1$ -specific GFOGER result in improved tissue of repaired bone. Histological evaluation of defects after 8 weeks by Safranin-O/fast green.

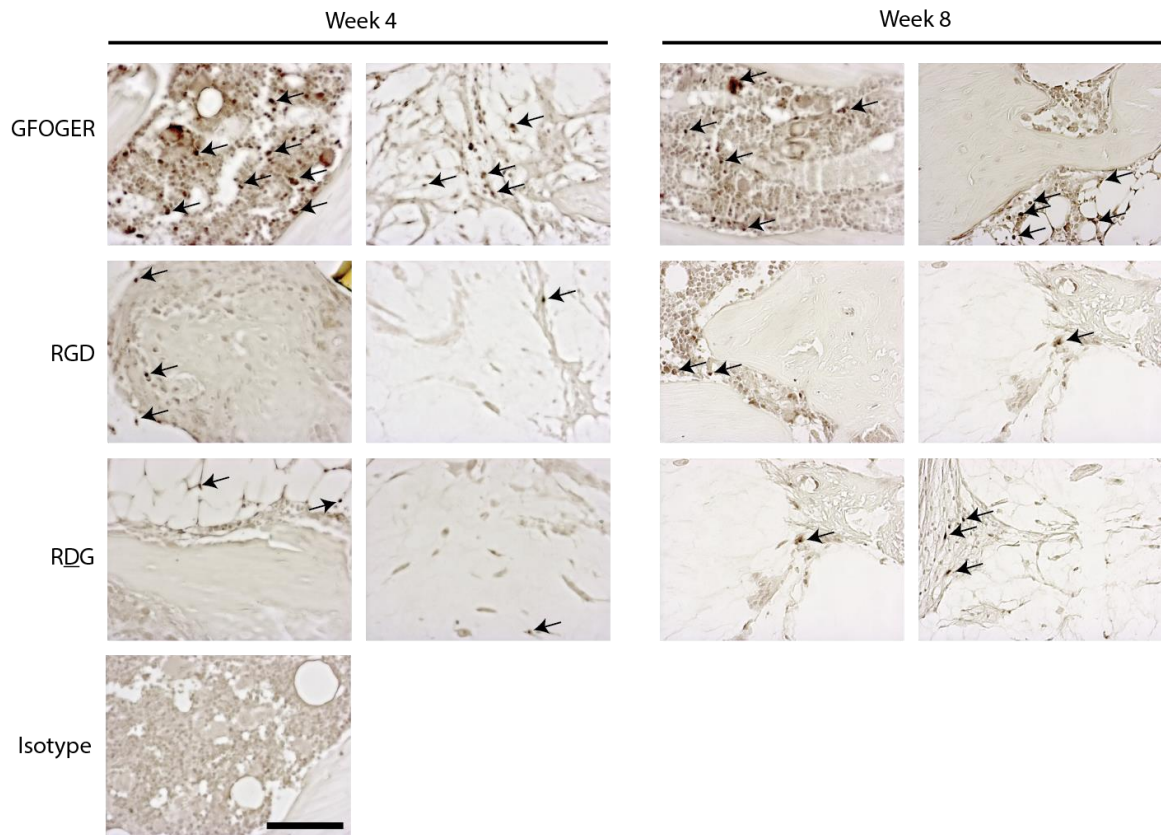


Figure 26. Human cells detected in defect by immunostaining. Human-specific NuMa stain (dark brown, black arrows) localizes in the nucleus and confirms presence of human cells in defect space of hMSC-treated defects at weeks 4 and 8. Staining with isotype control shows non-specific staining. Scale bar: 100 μ m.

DISCUSSION

In this study, we aimed to investigate the performance of a novel, cell-mediated degradable matrix functionalized with integrin-specific ligands in supporting the survival of transplanted hMSC and tissue repair in a segmental bone defect. We incorporated the adhesive $\alpha 2\beta 1$ integrin-specific GFOGER ligand, adhesive $\alpha v\beta 3$ integrin-specific RGD ligand, non-adhesive RDG peptide combined with hMSC in a protease-degradable PEG-maleimide hydrogel and tracked cell survival through transgenic luciferase expression. Our lab has previously shown that GFOGER-functionalized degradable hydrogels promote enhanced bone repair in a murine segmental defect, and when combined with low doses of rhBMP-2, fully healed the defect. We hypothesized that hydrogel delivery vehicles that promote cell viability in combination with the pro-osteogenic properties of the carrier would result in superior bone repair.

To track cell survival *in vivo*, we used transgenic expression of the luciferase gene which relies on the photonic byproduct of the reaction between luciferase and its substrate, luciferin. As luciferase is an enzyme, it can only be expressed by living cells, providing an advantage over quantum dot or nanoparticle based tracking which may confound results if materials are phagocytosed by other cell types [129]. Because there is no need for an excitation source, unlike fluorescence-based modalities, there is very little background allowing for sensitive measurements. Although bioluminescence exhibits many advantages, there are still limitations to this method. Stable, transgenic expression of the luciferase gene must be maintained, in our case by means of lentiviral transduction, which may have downstream effects due to genome insertion location or residual viral protein expression. Because most bioluminescent tracking schemes require the exogenous delivery

of the appropriate substrate, usually through a systemic injection into the intraperitoneal cavity, the kinetics of the substrate movement, first, to the defect site, and second, into the implant material to the transplanted cells, must be determined for each model. As with all cell tracking modalities, though, the signal must be validated as representative of actual cell number due to other possible confounding factors. We found no significant differences between hMSC and hMSC^{FLuc} with respect to *in vitro* cell function or *in vivo* bone repair. *In vitro*, hMSC^{FLuc} demonstrated equivalent levels of cell growth and osteogenic differentiation to unmodified hMSC. When both cell types were delivered to the mouse radial segmental defect, equivalent amounts of bone were observed in the defect, therefore luciferase expression did not affect *in vivo* bone repair.

The murine radial segmental defect provides many significant advantages over other bone defects – stabilization by the ulna eliminates the need for fixation hardware and the small model allows for *in vivo* imaging techniques such as bioluminescence or transgenic strains. However, the defect is not without its limitations – an unknown contribution from the ulna due to its close proximity, the small size of the defect does not present the same vascularization or diffusion challenges as larger defects, and the use of immunodeficient mice in our studies is not representative of a clinical therapy. Nevertheless, the relatively simple procedure (compared to more complex defects such as the cranial defect or femoral defect) lends itself as a useful screening model to identify candidate conditions for larger, more challenging injury models.

To identify an appropriate treatment formulation for subsequent studies on the effect of ligand on hMSC survival and bone repair, we first examined the effect of various hydrogel and construct parameters such as polymer weight percent, cell dose, and ligand

density on bone repair. We hypothesized that lower weight percent hydrogels would support better tissue repair due to lower cross-linking density, thereby allowing for faster tissue ingrowth. When we varied polymer weight percent from 4.5% to 8.0% (w/v) while holding ligand density and cell dose constant, we observed higher bone volumes in 4.5% hydrogels with lower bone volumes in 6% hydrogels and very little healing in 8.0% hydrogels, supporting our hypothesis that lower weight percent hydrogels, and therefore hydrogels with lower cross-linking densities, support increased tissue growth. For hydrogel systems, like the one employed in this study, in which degradation is primarily mediated by enzyme-degradable cross-linkers, there are three main strategies in which degradation can be tuned: 1. varying macromer molecular weight [32], 2. varying polymer weight percent [41,42], and 3. choice of cross-linker in terms of degradability [130]. Our lab and others have shown significantly increased tissue ingrowth and bone repair when MMP sensitivity is engineered into synthetic matrices compared to MMP insensitive matrices, confirming that matrix degradation is required for improved tissue ingrowth [32,50,80]. Lutolf et al. compared synthetic matrices of varying macromer molecular weights but equivalent polymer weight percentages in a calvarial defect. They found improved bone repair in defects treated with synthetic matrices of higher molecular weight and thus, lower cross-link density showing that tissue infiltration is greatly increased with lower cross-link densities [32]. In our hands, we observed the same trend, in which 4.5% hydrogels, with the lowest cross-linking density, exhibited greater tissue ingrowth compared to 6.0% and 8.0% hydrogels of higher cross-link densities. Although increasing matrix degradability by decreasing cross-link density supports better tissue repair, there is likely a balance between the rate of material degradation for tissue ingrowth and integrity of the material for

providing cell instructive cues and mechanical support. For example, a material that degrades too slowly may not allow for cell infiltration and vascularization, but a material that degrades too quickly may not persist long enough to provide structural support or repair cues, or retain transplanted cells at the defect site.

When we varied ligand density for *in vivo* bone repair (note that cells were *not* delivered for this study), we observed significantly more bone in defects treated with 1.0 mM GFOGER hydrogels compared to 0.3 mM GFOGER hydrogels. Due to the coupling of ligand density and cross-link density in the formulations examined, the increased healing cannot be solely attributed to a higher adhesive peptide density. It is likely that because of the lower cross-link density and faster degradation of the 1.0 mM ligand hydrogels, as more maleimides were conjugated to ligand and less were available for cross-linking in the 1.0 mM GFOGER hydrogels compared to the 0.3 mM GFOGER hydrogels, better bone repair was obtained. A more controlled experiment to decouple ligand density and cross-linking density is to use an inactive, mutated peptide, such as GAOGER, at varying ratios with the active peptide GFOGER, such that equal numbers of maleimides are reacted with ligand peptides resulting in equal number of maleimides remaining for cross-linking for hydrogels of varying active peptide density. Our lab has previously performed such an experiment to test the effect of RGD density on epithelial morphogenesis [44].

One of the limitations of the size of the radial defect and the method in which cells are encapsulated in the hydrogel is the number of cells that we were able to incorporate while maintaining hydrogel integrity. The two cell doses examined in this study, 30,000 and 15,000 (corresponding to about 15×10^6 and 7.5×10^6 cells/mL) per hydrogel, represent the maximum number of cells that we were able to encapsulate and half of the maximum

cell dose, respectively. We found no significant differences between the two cell doses in terms of normalized bioluminescent signal or bone repair. Thus, to decrease the number of cells needed, we chose to use the lower cell dose in subsequent studies. There is likely a balance between delivering enough cells to have a significant effect and delivering too many cells leading to adverse effects such as high competition for limited nutrients (with other transplanted cell or host cells) and significant cell death. The effective cell dose also depends on the efficacy of the delivery strategy in supporting and maintaining cell viability after transplantation. Other groups that have delivered cells to the murine radial defect have delivered $1 \times 10^6 - 3 \times 10^6$ cells on collagen scaffolds per defect, although the number of actual cells seeded on scaffolds and implanted into the defect was not quantified [71,131-135]. Interestingly, when BMP-2 overexpressing mouse MSC were delivered to the mouse radial segmental defect on a collagen sponge, a significant increase in bone formation was observed compared to control MSC [71]. Because cell survival and released BMP-2 amounts were not studied, it is unknown if the increase in bone formation (including large amounts of ectopic bone) was due to sustained release of BMP-2 over the course of healing or an initial, burst release of BMP-2 followed by significant cell death. The latter scenario may explain the very low amounts of healing and bone formation observed in the control MSC group on collagen scaffolds. A range of cell doses are reported in literature for other bone defects such as $1-3 \times 10^6$ cells in a rat femoral defect [129,136], $5 \times 10^4 - 2.5 \times 10^6$ cells in a mouse calvarial defect [51,137], 2×10^5 cells in a mouse femoral defect [67], 1×10^6 rat MSC in a rat femoral fracture [138], and 1.5×10^6 cells in a rat cranial defect [139].

When we implanted hMSC^{FLuc} in ligand-functionalized hydrogels, we found that integrin-specificity did have an effect on transplanted cell survival. Bioluminescence

increased after injury in all conditions, but GFOGER-treated defects exhibited significantly enhanced bioluminescence at later time points compared to RGD- and RDG-treated defects, suggesting an effect of integrin-specificity on cell survival. Interestingly, bioluminescence was still detectable above background at 8 weeks for all conditions, which represents a significant improvement over reports in the literature which document complete loss of signal by this time point [51,101,137,138,140-142]. We also found that the kinetics of injected luciferin distribution to the defect and time to maximum signal varied with time point, with shorter times to maximum signal at later time points and longer times to maximum at early time points, but no significance among groups (**Figure 43**). We also did not find a correlation between hMSC dose or bioluminescent signal and bone formation. Olivo et al reported a very strong, positive correlation ($r^2=0.98$) between hMSC seeding density on porous biphasic calcium phosphate scaffolds and bone deposition, however, their report studied ectopic bone formation in a subcutaneous pocket – a significantly different injury environment compared to the orthotopic radial defect model [140].

Bone repair after radial defect treatment with cell-free GFOGER, RGD, or RDG functionalized hydrogels was minimal and not significantly different among ligands. Bone volumes were equally low at weeks 4 and 8 with low levels of bone ingrowth into the defect space as visualized by microCT and histological staining. Bone volumes in cell-free GFOGER hydrogels were lower than previously observed in our lab [80], but mouse strain and hydrogel formulation have been changed for our study to better support cell encapsulation, thus bone volume results may not be directly comparable. Defects treated with hMSC in RGD or RDG hydrogels exhibited very low levels of bone, with no

significant difference between hydrogels containing hMSC and cell-free scaffolds. However, defects receiving hMSC in GFOGER-functionalized hydrogels resulted in significantly higher levels of bone formation at weeks 4 and 8 and improved morphology as visualized by histological staining. The significantly enhanced hMSC survival and bone repair observed in GFOGER-functionalized hydrogels suggest that integrin-specificity may be a novel strategy for enhancing tissue repair and transplanted cell survival.

Many groups have delivered MSC or bone marrow stromal cells for bone repair and have reported mixed therapeutic benefits of cell delivery. The use of an appropriate scaffold is necessary not only to provide the correct cues to transplanted and host cells, but to also retain cells at the site of injury. When Kodama et al injected a suspension of rat MSC to a rat femoral fracture, they observed little effect of cell delivery on bone repair, however, when an external magnetic targeting system was used to retain cells at the defect site, there was a moderate effect on bone repair [138]. Several groups have reported no effect of transplanted cells on various scaffolds on bone repair and required additional growth factors or genetic modifications for a significant effect. Degano et al reported no effect of hMSC compared to the cell-free RGD-PEG-vinylsulfone hydrogel scaffold in a mouse calvarial defect [51]. Watson et al also observed no effect of rat MSC in a rat cranial defect compared to cell-free methacrylated thermogelling hydrogels [139]. Vila et al found no significant differences in bone repair in a mouse calvarial defect for hMSC on a fibrin-BMP-2-PGDF-BB scaffold compared to the cell-free scaffold and untreated control [137]. Kanczler et al reported no effect of human bone marrow stromal cells on a poly(lactic acid) scaffold in a mouse femoral defect, and required the addition of VEGF for increased repair compared to the scaffold alone [67]. Dossier et al observed minimal bone repair after

treatment with rat bone marrow stromal cells in a RGD-alginate scaffold in a rat femoral segmental defect and required exogenous BMP-2 for a significant effect of cell delivery [136]. When 2×10^6 mouse MSC were delivered to the mouse radial defect on a collagen sponge (100x more cells than used in our studies in the same defect), minimal bone formation was observed, possibly due to an inappropriate cell dose or rapid cell death – neither of which were directly assessed [71]. However, when Dupont et al delivered hMSC or human amniotic fluid stem cells on a GFOGER and collagen I-coated polycaprolactone scaffold, they observed a significant effect of cell delivery on bone repair compared to the cell-free scaffold [129]. The mixed reports of therapeutic benefit of cells and scaffold delivery on bone repair in addition to the results we have reported here highlight the importance of the use of an appropriate scaffold to study the effect of cell delivery on bone repair. Our results are in agreement with the results from Degano and Dosier above in that we observed no significant benefit of hMSC delivery when hMSC were delivered in a RGD- or RDG- functionalized hydrogel. However, when delivered in an appropriate scaffold (GFOGER-functionalized hydrogel), we not only see enhanced cell survival, but a significant effect on bone repair compared to the cell-free scaffold.

Although we observed significant differences among ligands in bone repair and hMSC survival, it is important to consider the limitations of our study. The immunocompromised NSG mouse used in these studies was necessary to assess the effect of ligand on human cell survival after transplantation and the effect of hMSC on bone repair while avoiding massive xenograft rejection. The alternative, delivering mouse cells to an immunocompetent mouse limits the translational potential of this therapy, as significant differences have been reported in the susceptibility of mMSC to malignant

transformations and in the profiles of effector molecules needed for immunomodulation [143]. NSG mice lack mature T cells, B cells, or functional NK cells, and are deficient in cytokine signaling, thus the response that we have observed may be different from a fully competent host. The recent development of humanized mouse models which carry functional, completely engrafted human immune systems, may be a more relevant and useful model for studying the survival of transplanted human cells in a murine model [144]. The murine radial bone defect, while a useful tool for screening a number of parameters, does not present the same hurdles that a larger, more challenging defect presents, however, the small, simple animal model allowed for bioluminescent imaging and eliminated the need for external fixation hardware (reducing risk of infection and surgical complexity). Due to the size difference of 12 kDa GFOGER and 600 Da RGD, it is important to rule out the mere presence of the peptide or differences in the resulting hydrogel local structure as a contributing factor to the differences observed in cell survival and bone repair. Although we have included RDG as an inactive, non-adhesive control in these studies, we will examine the inactive, mutated GAOGER peptide in future in vivo studies as a better control for GFOGER. In this aim, we have engineered a novel PEG-mal cell delivery hydrogel system that supports hMSC survival through 8 weeks and bone repair and established a bioluminescent cell-tracking system. We have shown that integrin specificity may have an effect on transplanted cell survival, in addition to tissue-specific repair that our lab has previously shown [80]. Within the parameters that we studied, we observed that $\alpha 2\beta 1$ -specific GFOGER supports enhanced hMSC survival and bone repair in vivo, suggesting a role for integrin-specificity in improving transplanted cell survival and tissue repair.

CHAPTER 5: THE EFFECT OF INTEGRIN-SPECIFIC HYDROGELS AND HMSC ON THE REPAIR ENVIRONMENT IN VIVO

ABSTRACT

Mesenchymal stem cells (MSC) have emerged as a promising cell source for regenerative medicine applications for musculoskeletal deficiencies and exhibit immunosuppressive properties in response to allogeneic immune responses and anti-inflammatory effects after activation with pro-inflammatory cytokines. Recent work has shown that MSC can actively interact with components of the immune system and display both anti-inflammatory and pro-inflammatory effects.

In this study, we aimed to gain more insights into the differential effects of adhesive peptide ligand in PEG hydrogels and hMSC delivery on the *in vivo* bone repair environment. First, we analyzed gene expression *in vivo* to investigate which genes were regulated after hMSC delivery and whether adhesive peptide influenced that profile. We then investigated whether adhesive ligand has an effect on the cytokine secretome of encapsulated hMSC *in vitro*, with and without exogenous pro-inflammatory stimulation. We found significant differences in gene expression *in vivo* after transplantation of hMSC in GFOGER, RGD, or RDG hydrogels. We also found that GFOGER-functionalization resulted in significant differences in the secreted cytokines of encapsulated hMSC compared to RGD, RDG, or GAOGER. Taken together, this study shows that GFOGER-

functionalized hydrogels skew encapsulated hMSC toward an anti-inflammatory phenotype.

INTRODUCTION

Mesenchymal stem cells (MSC) have emerged as a promising cell source for regenerative medicine applications for musculoskeletal deficiencies [11,12]. In addition to their differentiation potential, hMSC have been reported to also provide anti-apoptosis, angiogenesis [17], growth factor production [18], neuroprotection [19], anti-fibrosis [2,20], and chemo-attraction functions [21]. They also exhibit immunosuppressive properties in response to allogeneic immune responses [22,23] and anti-inflammatory effects after activation with pro-inflammatory cytokines [24,25] secreted by inflammatory cells or through exogenous stimulation in culture. Recent work has shown that MSC can actively interact with components of the immune system and display both anti-inflammatory and pro-inflammatory effects [143]. MSC have the ability to interact with T cells, B cells, natural killer cells and dendritic cells [145] and to adopt a phenotype in response to the inflammatory environment which can then skew macrophage polarization [146].

Bone healing following injuries resulting in gaps larger than 0.5 mm involves overlapping phases of inflammation, renewal, and remodeling [147]. An initial inflammatory response is activated directly after injury initiating a well-orchestrated cascade of inflammatory mediators to recruit inflammatory cells and promote angiogenesis [148]. Activated platelets and osteoprogenitor cells release growth factors to recruit and guide endogenous MSC, and this phase is usually completed by the end of the first week [147]. A renewal phase follows in which chondrogenesis occurs forming a cartilaginous callus which is then mineralized into woven bone through growth factor signaling [147]. The latest stage of bone healing is the remodeling phase and is regulated by pro-

inflammatory signals to direct osteoblast and osteoclast differentiation and renewal and resorption of woven bone into lamellar bone [148].

In this study, we aimed to gain more insights into the differential effects of hydrogel adhesive peptide and hMSC delivery on the repair environment. First, we analyzed gene expression *in vivo* to investigate which genes were regulated after hMSC delivery and whether adhesive peptide ligand influenced that profile. We then investigated whether adhesive ligand has an effect on the cytokine secretome of encapsulated hMSC *in vitro*, with and without pro-inflammatory stimulation.

METHODS

RNA isolation and cDNA purification

Radial segmental defects in 8-10 week old male NSG mice (Jax) were treated with 4.5% hydrogels functionalized with 1.0 mM GFOGER, RGD, RDG, or GAOGER and cross-linked with 75:25 VPM:DTT with 15k hMSC (n=7-8). The tissue within the 2.5 mm defect space was explanted at 1 week post-transplantation and stored in RNAlater solution (Qiagen) until further processing. Samples were placed in Qiazol solution (Qiagen), lysed by probe sonication, and homogenized in QIAshredder columns (Qiagen). Total RNA was isolated using an RNAeasy Plus Micro kit (Qiagen), and RNA content and purity were measured by spectrophotometry (NanoDrop 1000). cDNA synthesis was performed on total RNA (100 ng) using the High-Capacity RNA-to-cDNA Kit (Thermo Fisher).

qPCR microarray

Quantitative PCR was performed using Fluidigm 96×96 nanofluidic arrays targeting a set of 96 transcripts (human or murine) to observe changes in bone, survival, inflammation, vascularization, and matrix markers. The genes were pre-amplified in a single 13-cycle PCR reaction for each sample with EvaGreen Mastermix (Fluidigm BioMark) following the manufacturer's protocol. Sixty-three gene targets resulted in detectable qPCR results and are listed in **Table 3**. All subsequent statistical analyses were carried out using JMP-Genomics (SAS Institute, Cary, NC, USA) using the basic gene expression workflow [149]. Raw Ct values were imported into JMP-Genomics and normalized to mean Ct values across all genes for each sample for principal components analysis (PCA), assessment of the biological principal variance component contributions (PVCA), and hierarchical clustering using Ward's method to identify sub-types of

expression profile. Finally, the estimate builder function in JMP-Genomics was used to perform analysis of variance (ANOVA) of pairwise contrasts of cluster differences with a false discovery rate (FDR) of 5% cutoff for inclusion in downstream analysis. Results are presented as raw Ct values normalized to mean Ct values across all genes for a sample.

Cytokine analysis *in vitro*

Early passage (< 6) hMSC were encapsulated in 25 μ L 4.5% hydrogels functionalized with 1.0 mM GFOGER, RGD, RDG, or GAOGER and cross-linked with 75:25 VPM:DTT. Hydrogels were cultured in complete media overnight followed by stimulation with 50 ng/mL (1000 U/mL) recombinant human IFN- γ and 20 ng/mL (1520 U/mL) recombinant human TNF- α (R&D Systems) or no stimulation for 48 hours. Conditioned medium was collected, supplemented with Halt protease inhibitor (Thermo Fisher), and centrifuged at 10,000xg for 10 min at 4 °C to remove debris. Supernatant was frozen in liquid nitrogen and stored at -80 °C until analysis. Conditioned media were analyzed using the Bio-Plex Pro Human Cytokine 27-plex Assay (Bio-Rad) on a Magpix multiplexing machine (Luminex) according to the manufacturer's instructions. Multiple comparisons for secretion levels for each cytokine were performed using Fisher's LSD test as only 3 comparisons were considered: GFOGER vs. RGD, GFOGER vs. GAOGER, and RGD vs RDG. Multivariate analyses were performed in JMP Pro v11.

Table 3. Gene targets for qPCR microarray.

Human Targets		Murine Targets	
Gene Symbol	Gene Name	Gene Symbol	Gene Name
ANGPTL4	angiopoietin-like 4	ACTA2	actin, alpha 2, smooth muscle, aorta
BAX	BCL2-associated X protein	ANGPT1	angiopoietin 1
Bcl2	B-cell CLL/lymphoma 2	BGLAP3	Bone gamma-carboxyglutamate protein 3
BMP2	bone morphogenetic protein 2	CCL2	chemokine (C-C motif) ligand 2
CCND1	cyclin D1	CCR2	chemokine (C-C motif) receptor 2
CDKN1A	cyclin-dependent kinase inhibitor 1A	CSF2	colony stimulating factor 2
coll1a2	collagen, type I, alpha 2	CX3CR1	chemokine (C-X3-C motif) receptor 1
col3a1	collagen, type III, alpha 1	CXCL12	chemokine (C-X-C motif) ligand 12
CXCL5	chemokine (C-X-C motif) ligand 5	CXCL15	chemokine (C-X-C motif) ligand 15
CYGB	cytoglobin	CXCL2	chemokine (C-X-C motif) ligand 2
DAPK3	death-associated protein kinase 3	EPO	erythropoietin
Dlx5	distal-less homeobox 5	FGFR1	fibroblast growth factor receptor 1
EGF	epidermal growth factor	FGFR2	fibroblast growth factor receptor 2
FGF7	fibroblast growth factor 7	FLT1	FMS-like tyrosine kinase 1
FGFR1	fibroblast growth factor receptor 1	HGF	hepatocyte growth factor
FN1	fibronectin 1	IBSP	integrin binding sialoprotein
GPX1	glutathione peroxidase 1	IFNg	interferon gamma
HGF	hepatocyte growth factor	IL1a	interleukin 1 alpha
HIF1a	hypoxia inducible factor 1, alpha subunit	IL1b	interleukin 1 beta
IGF1	insulin-like growth factor 1	KDR	kinase insert domain protein receptor
ITGa5	integrin, alpha 5	MMP9	matrix metalloproteinase 9
ITGav	integrin, alpha V	NFkB1	nuclear factor of kappa light polypeptide gene enhancer in B-cells 1
ITGb1	integrin, beta 1	RUNX2	runt-related transcription factor 2
KITLG	KIT ligand	TNF	tumor necrosis factor
MMP1	matrix metalloproteinase 1	VEGFA	vascular endothelial growth factor A
MMP13	matrix metalloproteinase 13		
MMP14	matrix metalloproteinase 14		
MMP2	matrix metalloproteinase 2		
NES	nestin		
NFkB1	nuclear factor of kappa light polypeptide gene enhancer in B-cells 1		
PPARg	peroxisome proliferator-activated receptor gamma		
TGFBI	transforming growth factor, beta-induced		
TIMP1	TIMP metalloproteinase inhibitor 1		
TIMP2	TIMP metalloproteinase inhibitor 2		
TP53	tumor protein p53		
VEGFA	vascular endothelial growth factor A		
Wnt5a	wingless-type MMTV integration site family, member 5A		
YAP1	Yes-associated protein 1		

RESULTS

Effect of ligand on gene expression after hMSC delivery *in vivo*

To gain more insights into the effect of adhesive peptide ligand presented in the delivery hydrogel on the repair environment *in vivo*, we first examined gene expression at an early time point, as others have shown differential gene expression at 1 week or earlier [150]. 15,000 hMSC were delivered to the murine radial segmental defect in GFOGER-, RGD, or RDG-functionalized hydrogels. Tissue within the defect space was explanted 1 week after transplantation and processed for RNA extraction. We identified 96 human or mouse gene targets of interest that were related to vascularization, bone, inflammation, wound healing, matrix proteins, and cell survival (**Table 3**). Of the initial 96 gene targets, approximately 60 resulted in a detectable signal after microfluidic PCR analysis on the Fluidigm system. When we analyze the entire data set of detectable genes, discriminant analysis shows clear separation of the samples grouped together based on adhesive peptide (**Figure 27**). Discriminant analysis aims to classify observations described by values on continuous variables (covariates) into groups. The canonical plot visually represents this analysis and shows the sample points and multivariate means in the two dimensions, or canonical variables, that best separate the groups. The “+” plus marker corresponds to each multivariate mean and ellipses represent a 95% confidence level – thus groups that differ significantly tend to not intersect. The canonical plot in **Figure 27** shows the adhesive peptide groups GFOGER and RGD closer together and more removed from RDG along the canonical 1 axis, but with no overlap among the groups. Along canonical 2, RGD and RDG exhibit slight overlap and GFOGER is more removed from the other two peptide

groups, indicating more similarity between RGD and RDG than GFOGER and RGD or GFOGER and RDG.

Hierarchical clustering based on adhesive peptide shows GFOGER samples tightly clustered, while RGD and RDG samples cluster together without much separation between the two (**Figure 27**). Clustering with respect to gene expression levels shows two clear clusters – cluster 1 solely consisting of human genes and cluster 2 primarily consisting of mouse genes (**Figure 28**). This clustering is not surprising as the different species targets likely exhibit different variances. From the cluster expression map, we can clearly observe areas of differential gene expression. We then split the genes according to cluster (cluster 1 (human) vs. cluster 2 (mouse)), and compared ligands by multivariate ANOVA (MANOVA) with a sum combination across genes, essentially transforming the multivariate data set into a univariate data set. The MANOVA revealed significant differences in each cluster with respect to adhesive peptide ($p < 0.05$), and the centroid canonical plot shows that while the centroids for RGD and RDG exhibit considerable overlap, suggesting high similarity, the centroid for GFOGER is the farthest removed with minimal overlap, signifying that both hMSC delivered in GFOGER hydrogels and defects treated with hMSC in GFOGER-functionalized hydrogels exhibit significantly different gene expression patterns compared to RGD and RDG ($p < 0.05$) (**Figure 29**).

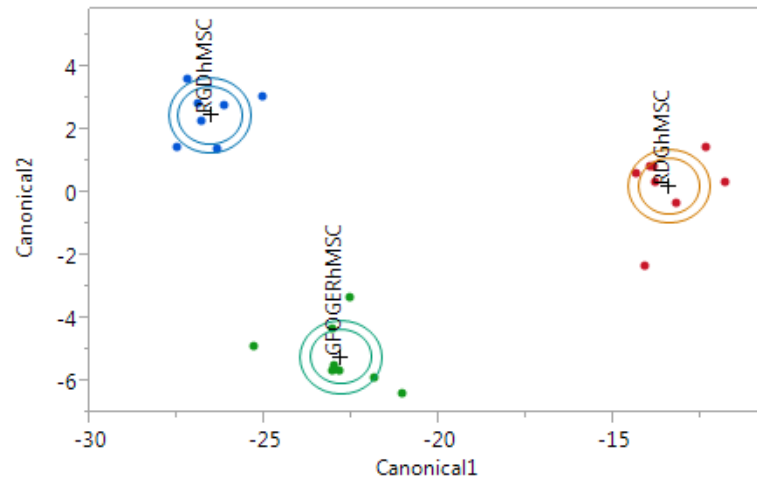


Figure 27. Discriminant analysis of gene expression. Linear discriminant analysis of gene expression after 1 week. Each point represents a sample and each multivariate mean is a labeled circle corresponding to a 95% confidence limit for the mean. Groups that are significantly different tend to have non-intersecting circles.

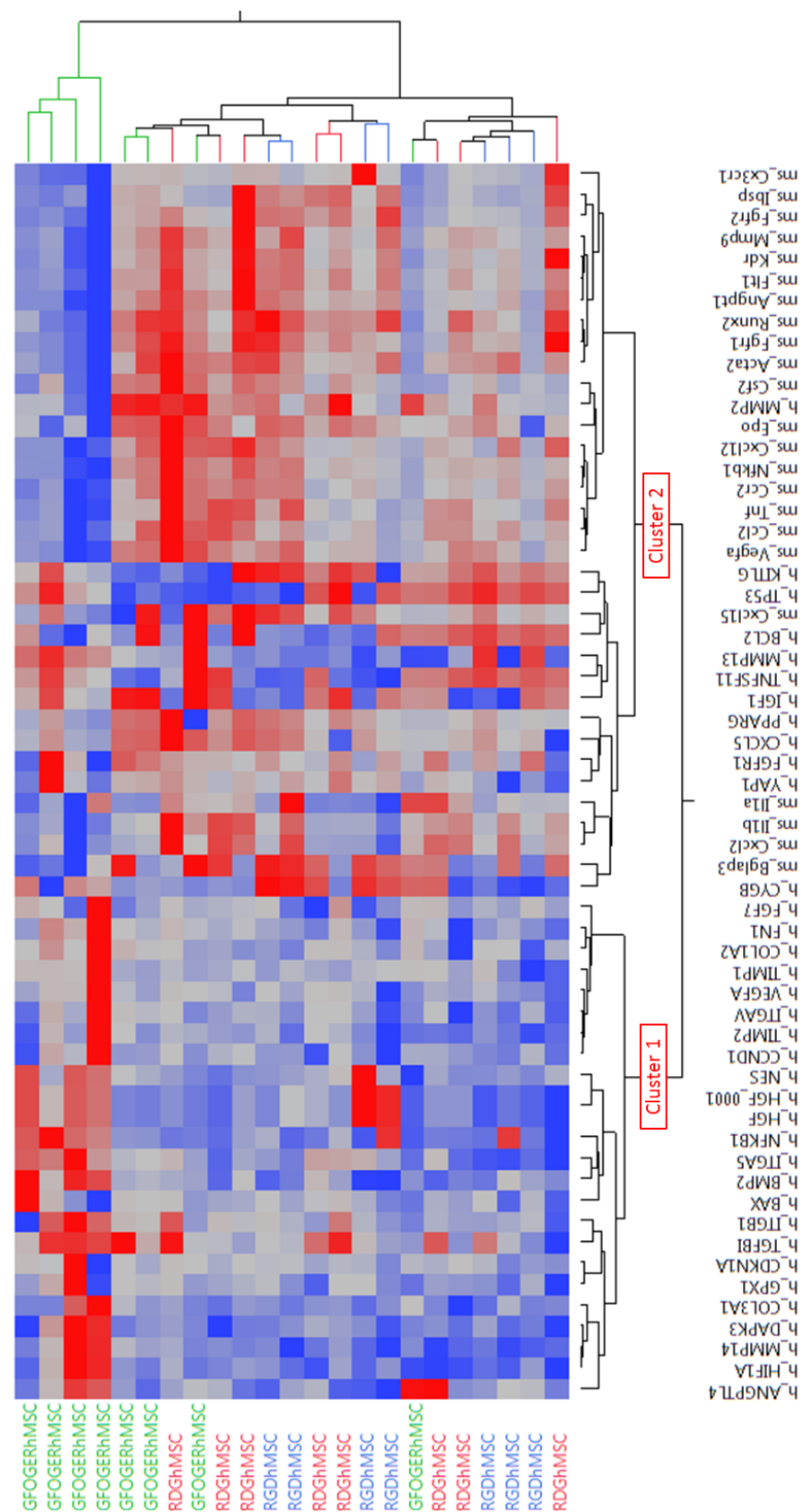


Figure 28. Hierarchical clustering of in vivo gene expression using Ward's method.

Red = high expression, blue = low expression.

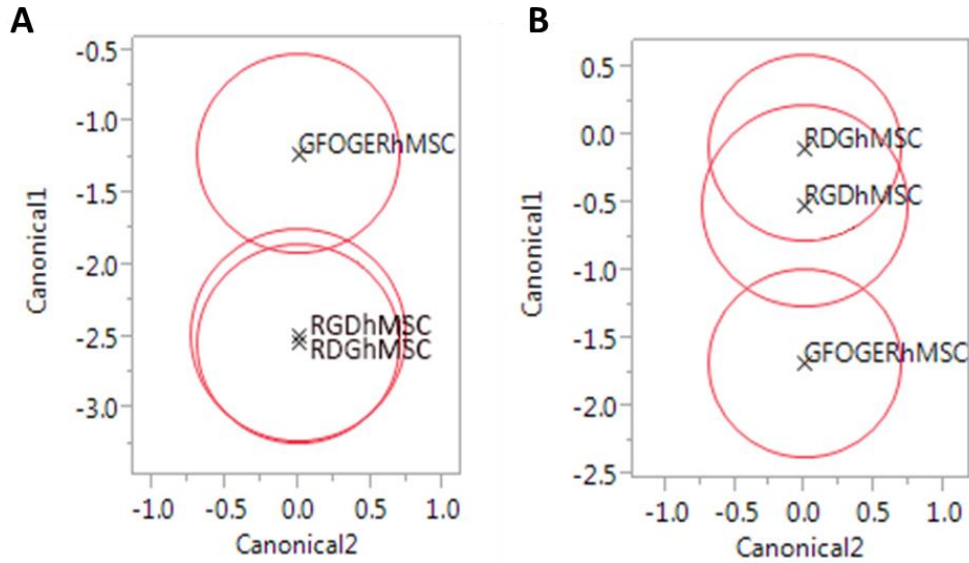


Figure 29. Defects treated with hMSC in GFOGER hydrogels exhibit differential gene expression profile compared to other ligands. Multivariate ANOVA with a sum combination across genes for A) cluster 1 (human genes) and B) cluster 2 (mouse genes) indicates that hMSC encapsulated in GFOGER-functionalized hydrogels and defects receiving hMSC in GFOGER hydrogels exhibit significantly different gene expression profiles *in vivo* at 1 week as shown by centroid canonical plots. (N=7-8; MANOVA: $p < 0.05$ for cluster 1 and cluster 2).

Figure 30 shows genes sorted by categorical function with red indicating higher normalized expression and blue representing lower normalized expression. We can see clear differences among adhesive peptides in expression of vascularization, inflammation and bone related genes. Using ANOVA to detect significant differences among ligands for each gene, relative expression levels of genes displaying differential expression with respect to ligand are shown in **Figure 31**, **Figure 32**, and **Figure 33**.

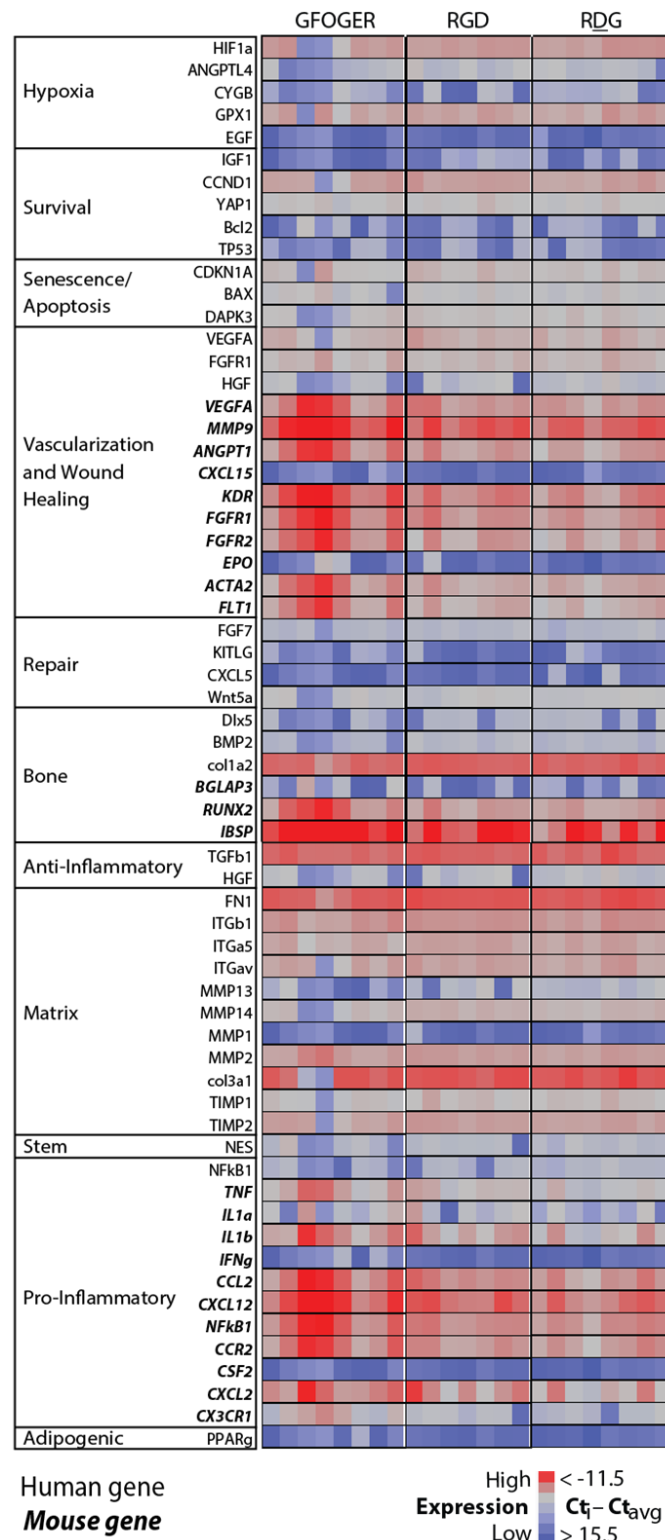


Figure 30. Gene expression heat map. hMSC transplantation in $\alpha 2\beta 1$ -specific GFOGER hydrogels resulted in upregulation of inflammation, vascularization and bone genes *in vivo* after 1 week compared to RGD and RDG. Tissue was explanted from the defect space after 1 week and total RNA was extracted and standardized across all samples. 96 total genes were screened using gene chip technology resulting in differential expression of about 60...

Inflammation genes with differences among hydrogel adhesive peptides are shown in **Figure 31**. *Mouse* host genes tumor necrosis factor (TNF), interleukin 1-beta (IL-1 β), stromal cell-derived factor 1 (SDF-1/CXCL12), monocyte chemoattractant protein-1 receptor (CCR2), macrophage inflammatory protein 2-alpha (MIP-2 α /CXCL2), and nuclear factor kappaB (NF κ B) were upregulated in GFOGER- compared to RDG-hydrogels. Interestingly, *human* NF κ B was upregulated in RDG compared to GFOGER. SDF-1/CXCL12 is a chemokine for lymphocytes and endothelial progenitor cells and plays an important role in vascular development. Using CXCR4 knockout mice (the receptor for SDF-1), Kawakami et al demonstrated that SDF-1 plays an important role in bone fracture healing [151], and SDF-1 can be induced by both TNF and IL-1 [152]. TNF, IL-1 β , and MIP-2 α /CXCL2, pro-inflammatory cytokines, have been shown to be upregulated during the early inflammation phase and then decrease to baseline levels during normal fracture healing and tooth extraction socket healing [153,154], however IL-1 β is translated as pro-IL-1 β and must be processed by caspase-1 for biological activity [155]. MCP-1, the ligand for CCR2, plays a critical role in the recruitment and activation of leukocytes, including a subpopulation of macrophages critical for angiogenesis, and is specifically regulated during activation of skeletal repair and remodeling [156,157]. NF κ B, a transcription factor, requires activation through one of two distinct pathways for translocation to the nucleus and can interact with over 200 genes depending on the stimuli and cell type regulating cellular stress [158]. The classical pathway can be activated TNF- α and other inflammatory

Figure 30 continued. ...genes. Mean normalized Ct values were used for the analysis and are represented in the heat map where red is high expression and blue is low expression.

mediators [159]. The inflammatory mediators upregulated in the GFOGER group are important in the early phase of healing and recruit inflammatory cells which promotes angiogenesis. Prolonged expression of these molecules may lead to abnormal healing and persistent inflammation, however, upregulated expression at 1 week after injury is in line with the fracture healing cascade.

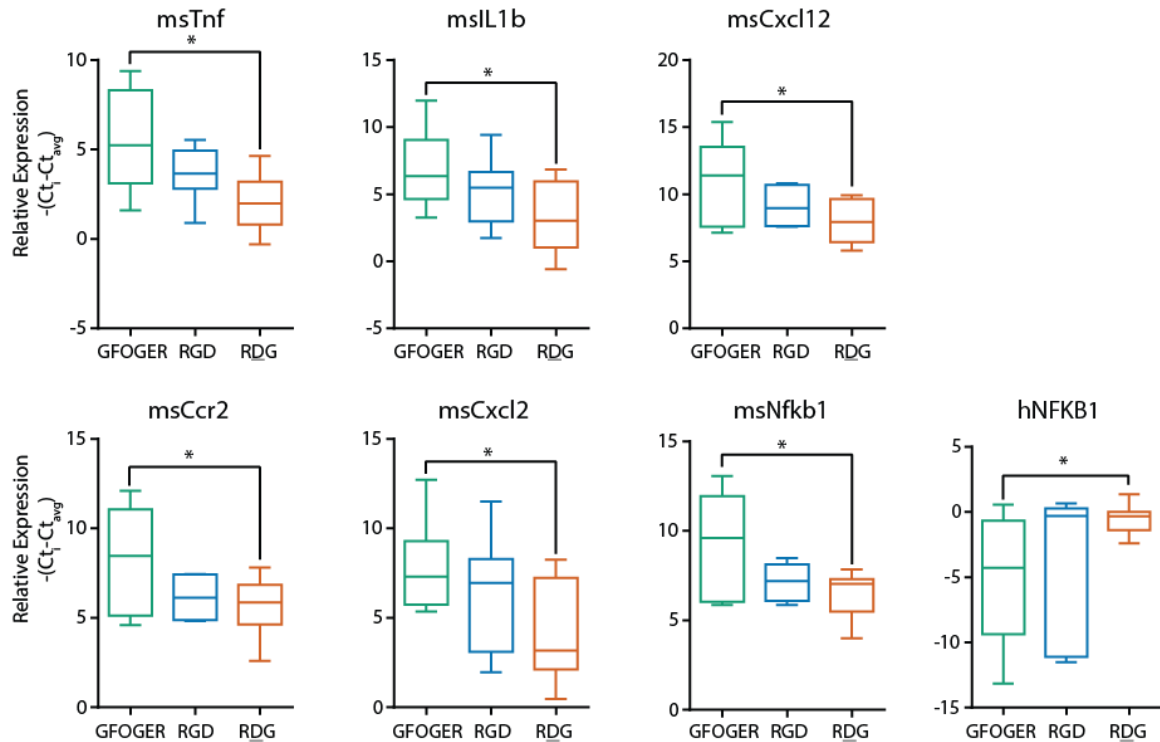


Figure 31. Differentially expressed inflammation genes *in vivo* at 1 week. (Whiskers represent min and max, box extends from 25th to 75th percentiles, line represents median. N=7-8; ANOVA: *FDR<0.05).

Vascularization genes showing differences among groups are shown in **Figure 32**.

Mouse genes matrix metalloproteinase 9 (MMP), angiopoietin 1 (Angpt1), VEGF receptor 2 (VEGFR2/KDR), alpha actin 2 (ACTA2), VEGF receptor 1 (VEGFR1/FLT1), and fibroblast growth factor receptor 2 (FGFR2) were upregulated in GFOGER compared to

RGD and RDG. *Human* hypoxia inducible factor 1 α (HIF1 α) was upregulated in RGD and RDG and *human* hepatocyte growth factor was upregulated in RDG. VEGF, the ligand for VEGFR2/KDR and VEGFR1/FLT1, is involved in endothelial cell migration, mitogenesis, sprouting, and tube formation, and upregulated VEGF and VEGFR have been detected in the tips of angiogenic sprouts [160]. FGF, the pro-angiogenic ligand for FGFR2, is upregulated during angiogenesis and is stored in the basement membrane as a reservoir supply. It enhances VEGF production and induces placental growth factor expression in the presence of VEGF, exhibiting cross talk with other growth factor pathways [161]. ANGPT1 functions primarily during vascular remodeling and angiogenesis to stabilize new blood vessels and regulate endothelial cell survival. It acts as a competitive agonist for ANGPT2 which is involved in the disruption of the endothelial monolayer promoting sprouting and angiogenesis [162]. MMP9 is critical in vascular remodeling, cell migration, and sprout formation as protein inhibitors of MMP9 have been shown to attenuate the migration of endothelial cells [160]. ACTA2 is a marker of pericytes, a cell type required for the maturation and stabilization of new blood vessels [163]. The HIF-1 α pathway is activated in response to hypoxia, and overexpression has been linked to increases in osteogenesis and angiogenesis [60]. HGF, a paracrine factor reported to be secreted by apoptotic cells, stimulates endothelial cell motility and growth and activates the NF κ B pathway which can then regulate HIF-1 α expression [164,165] – interestingly, human HGF, NF κ B, and HIF-1 α were all upregulated in RDG hydrogels compared to hydrogels presenting adhesive peptides. Many critical angiogenic mediators were found to be upregulated in the host in the GFOGER group, whereas hypoxic and apoptotic markers were upregulated in RGD and RDG groups.

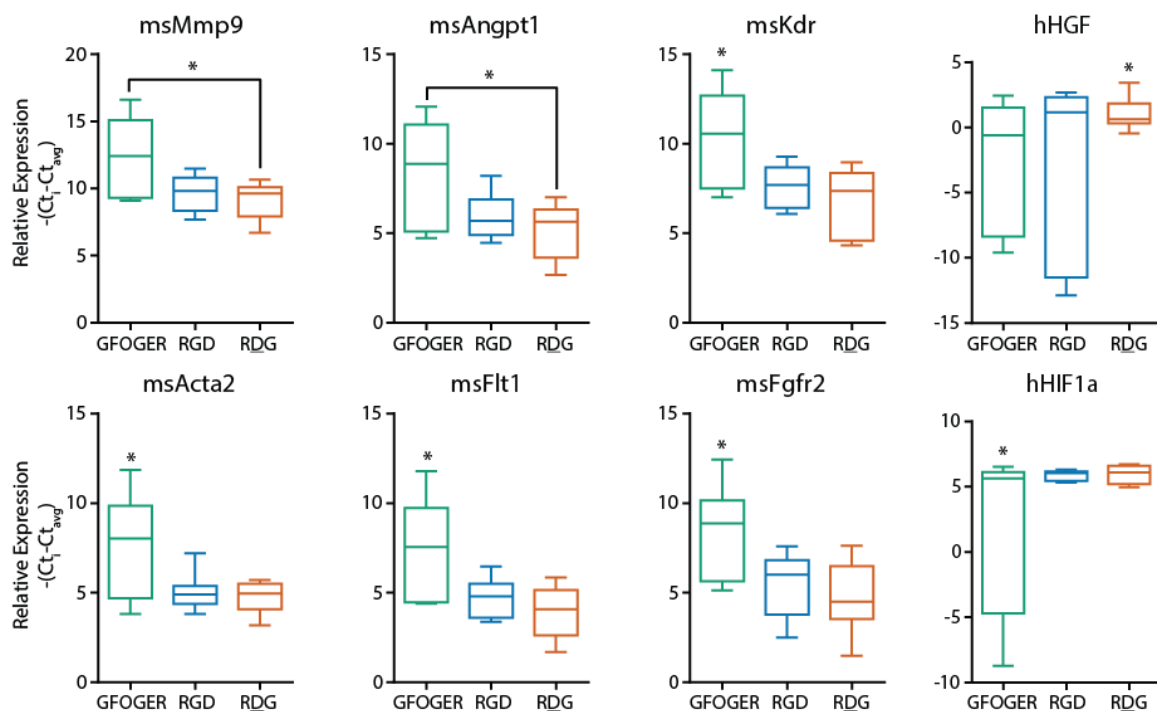


Figure 32. Differentially expressed vascularization genes *in vivo* at 1 week. (Whiskers represent min and max, box extends from 25th to 75th percentiles, line represents median. N=7-8; ANOVA: *FDR<0.05).

Figure 33 shows bone related genes with significant differences among groups. Runt-related transcription factor 2 (RUNX2) and bone sialoprotein (IBSP) *mouse* genes were upregulated in GFOGER hydrogels whereas *human* bone morphogenetic protein 2 (BMP2) was upregulated in RGD and RDG. RUNX2 is a master transcription factor and regulator of bone matrix genes, including IBSP, a significant component of the bone ECM [166]. BMP2 initiates the bone healing cascade and is critical for osteogenic differentiation and chondrocyte proliferation and maturation during endochondral bone development [167,168]. However, RUNX2 is essential for the execution and completion of BMP2 signaling for osteoblast differentiation [169]. Gonzalez-Gil et al reported that hypoxia triggered BMP2 expression in human periosteum explants, supporting the upregulation of human HIF-1 α and BMP2 that we observe in RGD- and RDG-hydrogel treated defects.

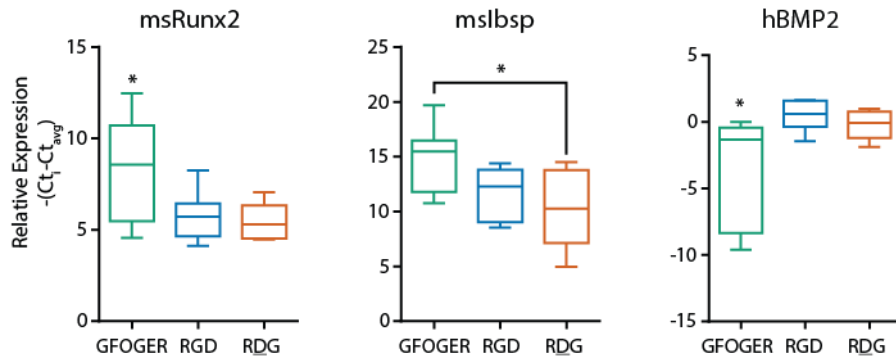


Figure 33. Differentially expressed bone genes *in vivo* at 1 week. (Whiskers represent min and max, box extends from 25th to 75th percentiles, line represents median. N=7-8; ANOVA: *FDR<0.05).

Effect of adhesive ligand on cytokine secretion profiles of encapsulated hMSC *in vitro*

hMSC were encapsulated in GFOGER-, GAOGER-, RGD-, or RDG-functionalized hydrogels. After 24 hours in culture, encapsulated hMSC were either stimulated or not stimulated with rhTNF- α and rhIFN- γ to mimic the inflammatory environment *in vivo*, and cultured for another 48 hours. Conditioned media was collected after the 48 hour stimulation period and assayed for cytokine content. We observed a significant effect of stimulation on all cytokine levels across hydrogel groups, except for IL-12p70 which was insensitive to stimulation (**Table 4**).

Table 4. Secreted cytokine levels of hMSC encapsulated in ligand-functionalized hydrogels. Encapsulated hMSC were either stimulated with TNF- α and IFN- γ or maintained unstimulated and conditioned medium was analyzed. Table below shows average cytokine level across ligands. All cytokine levels were significantly affected by stimulation except IL-12p70. ND: Below detection limit, * significant differences in cytokine level among ligands, N=16.

Cytokine	No stimulation (pg/mL)	With stimulation (pg/mL)
Basic FGF	57.5 \pm 5.3*	78.7 \pm 6.1*
Eotaxin	ND	91.2 \pm 15.9
G-CSF	ND	98.1 \pm 7.9
GM-CSF	24.8 \pm 8.1	55.3 \pm 8.6
IFN-g	630.9 \pm 280.5*	-
IL-1b	3.8 \pm 0.6	20.4 \pm 1.9
IL-1ra	65.5 \pm 2.8*	156.1 \pm 13.3
IL-2	7.3 \pm 7.6	22.6 \pm 2.5
IL-4	2.4 \pm 0.4	10 \pm 1
IL-5	ND	14.3 \pm 1
IL-6	1356.8 \pm 175.2*	26790.5 \pm 5416.7
IL-7	5.5 \pm 1.1	10 \pm 2.4
IL-8	12 \pm 3.3*	1622.8 \pm 337.2*
IL-9	19.1 \pm 3.6*	32.6 \pm 2.7
IL-10	65.4 \pm 16.3	76.8 \pm 16
IL-12p70	98.2 \pm 11.8	91.7 \pm 11.8
IL-13	3.1 \pm 0.6	5 \pm 1
IL-15	ND	104.1 \pm 6.2
IL-17a	18.8 \pm 4.4	64.8 \pm 5.4
IP-10	19.4 \pm 1.5	37025.7 \pm 2911.3
MCP-1	213.3 \pm 46.7*	1034.9 \pm 91.7
MIP-1a	1.7 \pm 0.1	3 \pm 0.2
MIP-1b	4.5 \pm 1.1	10.3 \pm 1
PDGF-bb	0.4 \pm 0.4	13.8 \pm 3.4
RANTES	5.1 \pm 3	3860.2 \pm 1342
TNF-a	15.8 \pm 7.2	-
VEGF	5550.2 \pm 1300.6*	3279 \pm 1112.2

When we analyze the entire data set of cytokines, discriminant analysis, as described previously, shows clear separation of the samples based on adhesive ligand (**Figure 34**). Separation along canonical parameter 1 resulted in cytokine profiles separated based on adhesive peptide with the adhesive GFOGER- and RGD-hydrogels separated from the inactive GAOGER- and RDG-hydrogels. Separation along canonical parameter 2 resulted in separation between GFOGER- and GAOGER-hydrogels and between RGD- and RDG-hydrogels, although to a lesser degree than adhesive vs. non-adhesive groups. Hierarchical clustering based on adhesive ligand shows separation similar to canonical parameter 1 in that adhesive samples GFOGER- and RGD-hydrogels form one main cluster, and non-adhesive RDG- and GAOGER-hydrogels form the other (**Figure 35**). We then compared adhesive ligands by multivariate ANOVA (MANOVA) with a sum combination across cytokines, essentially transforming the multivariate data set into a univariate data set. The MANOVA revealed significant differences in cytokine secretion level with respect to adhesive ligand ($p < 0.001$). The centroid canonical plot shows high similarity and overlap between GAOGER- and RDG-hydrogels and a slightly different profile for RGD-hydrogel (however not significant, **Figure 36**). The centroid for GFOGER-hydrogel is the farthest removed with minimal overlap, signifying hMSC in GFOGER hydrogels exhibited significantly different cytokine profiles whereas there was no significant difference among hMSC in RGD-, RDG-, or GAOGER-hydrogel profiles.

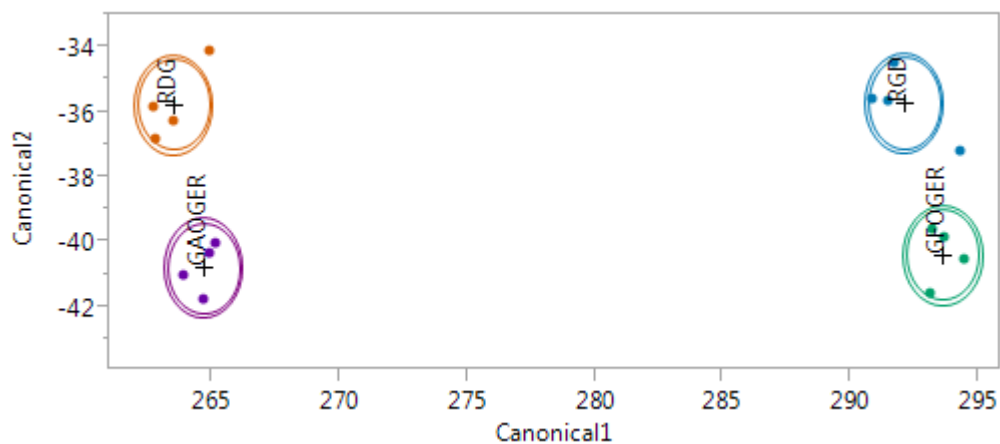


Figure 34. Discriminant analysis of cytokine secretion from encapsulated hMSC without IFN- γ /TNF- α stimulation. Linear discriminant analysis of cytokine secretion of hMSC encapsulated in ligand-functionalized hydrogels over 2 days in growth conditions. Each point represents a sample and each multivariate mean is a labeled circle corresponding to a 95% confidence limit for the mean. Groups that are significantly different tend to have non-intersecting circles (N=4).

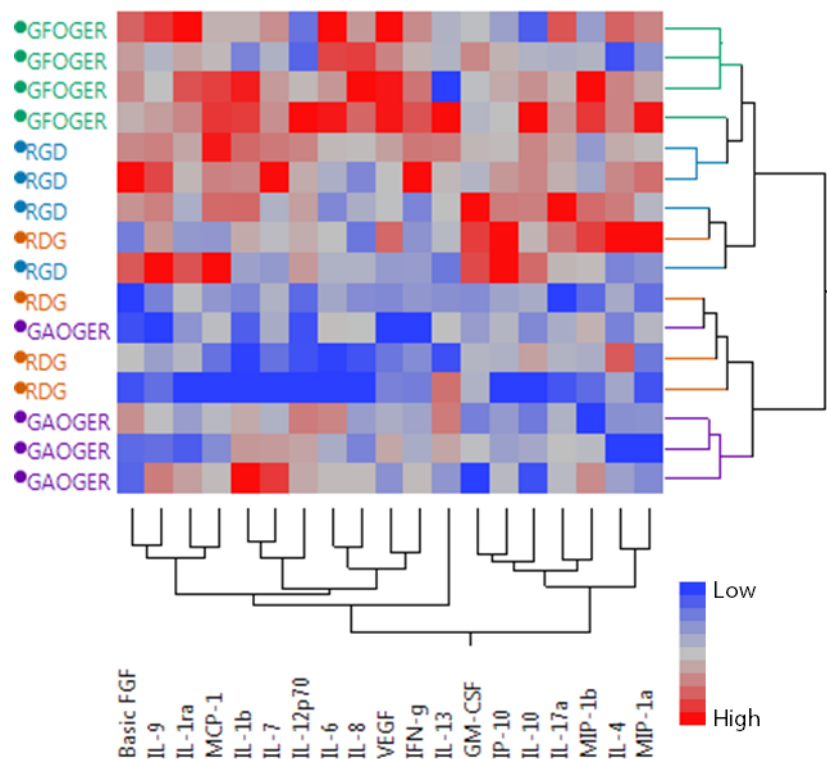


Figure 35. Hierarchical clustering of cytokine secretion from encapsulated hMSC without IFN- γ /TNF- α stimulation. Ward's method shows clustering between adhesive and non-adhesive hydrogels, and further clustering by ligand for secreted cytokine levels of hMSC in growth conditions.

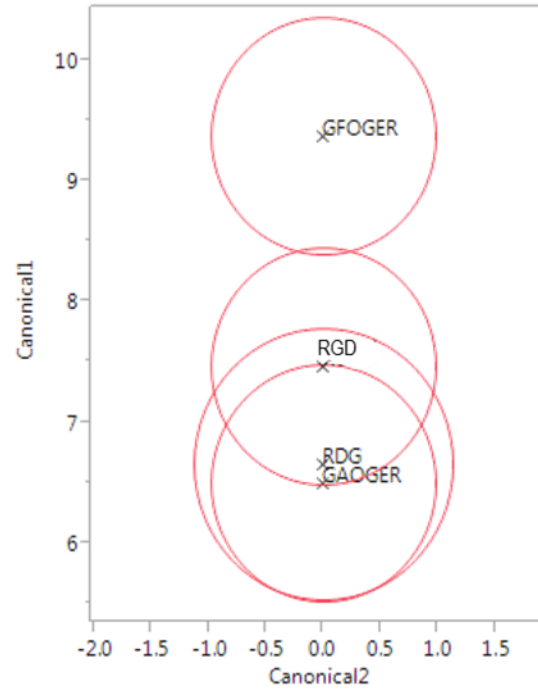


Figure 36. hMSC in GFOGER hydrogels exhibit differential secretory cytokine profile compared to other hydrogels without exogenous stimulation. Multivariate ANOVA with a sum combination across cytokines shows hMSC encapsulated in GFOGER-functionalized hydrogels exhibit significantly different cytokine profile under growth conditions. (N=4; MANOVA: $p < 0.001$).

Figure 37 shows individual cytokines that exhibited significant differences among adhesive ligands without rhTNF- α and rhIFN- γ stimulation. Interleukin 1 receptor antagonist (IL-1ra) and interferon gamma (IFN- γ) were upregulated in GFOGER-hydrogels compared to its inactive GAOGER-hydrogel control. Interleukins 8 and 9 (IL-8 and IL-9) were upregulated in RGD-hydrogels compared to RDG gels. Basic fibroblast growth factor (Basic FGF/FGF2) and monocyte chemotactic protein (MCP-1) were upregulated in both GFOGER- and RGD-hydrogels compared to their inactive controls. IL-8, Interleukin 6 (IL-6) and vascular endothelial growth factor (VEGF) were all upregulated in GFOGER hydrogels compared to RGD- and GAOGER-hydrogel control. FGF and VEGF are both angiogenic mediators that exhibit crosstalk in their signaling

[161]. IL-1ra binds the IL-1 receptor inhibiting pro-inflammatory IL-1 signaling [155]. IL-9 is a potent, antigen-independent growth factor for T cells and mast cells and affects many cell types to regulate inflammation [170]. IL-6 is constitutively expressed by hMSC and polarizes monocytes toward an anti-inflammatory IL-10 producing phenotype [143]. The major effector function of IL-8 is the recruitment and activation of neutrophils to the site of injury [155]. MCP-1 induces CCR2-dependent migration of monocytes, particularly a subset of macrophages important for vascularization [155-157]. IFN- γ is a pro-inflammatory cytokine mainly secreted by activated T cells and macrophages and activates the inflammatory cascade. Duque et al reported autocrine regulation of IFN- γ in hMSC, which regulated cell processes such as osteoblastic differentiation [171]. In our study, IFN- γ may have an autocrine feedback effect, regulating the cytokine secretion of encapsulated hMSC. It is noteworthy to mention that the interaction between IFN- γ and its receptor is species specific, and thus, hMSC cannot be activated by mouse IFN- γ and vice versa [143,155].

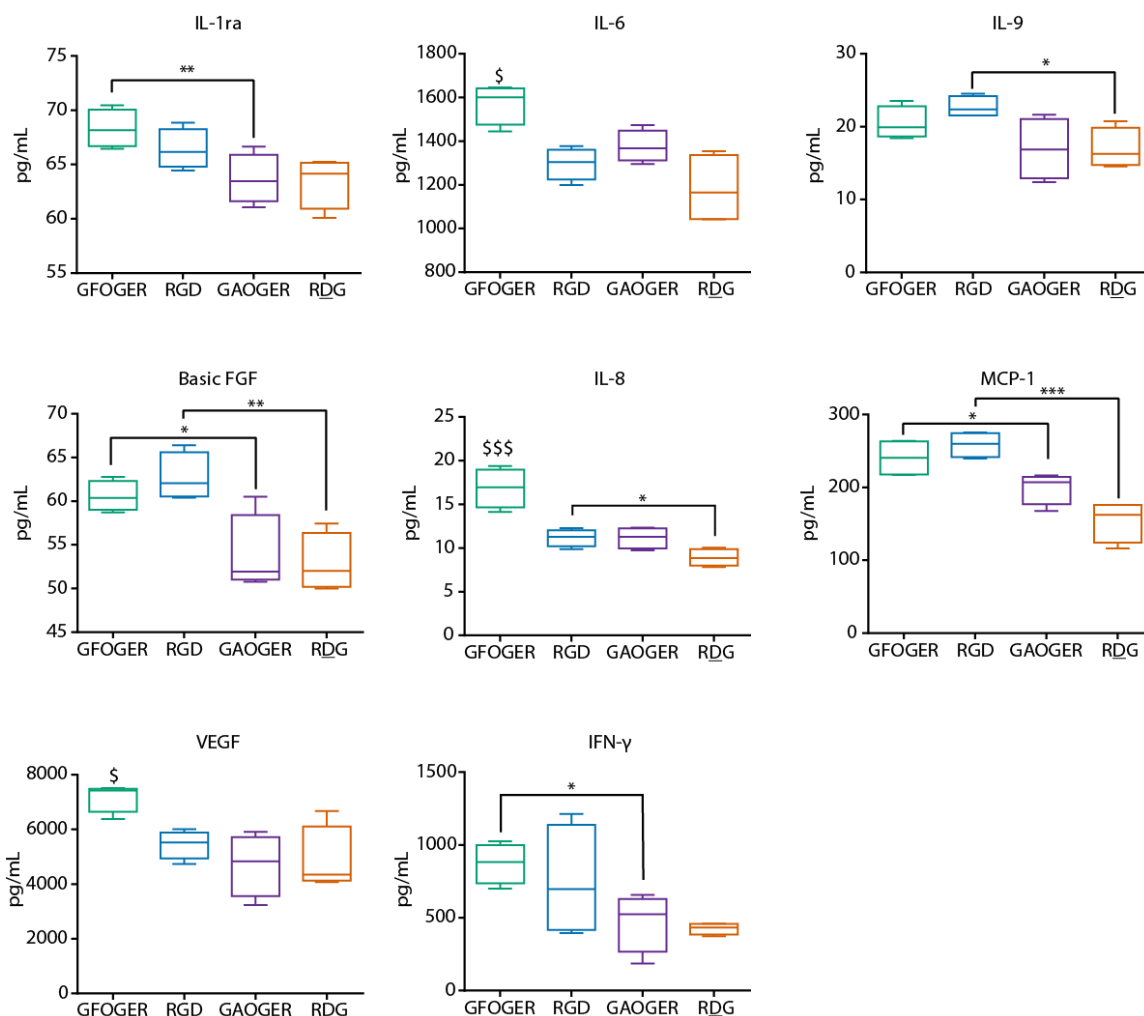


Figure 37. Cytokines with significant secretion levels for encapsulated hMSC without IFN- γ /TNF- α stimulation. Concentrations of secreted levels were significantly different for cytokines showed above from hMSC encapsulated in ligand-functionalized hydrogels in growth conditions. (Whiskers represent min and max, box extends from 25th to 75th percentiles, line represents median. N=4; ANOVA: * $p < 0.05$, ** $p < 0.005$, *** $p < 0.0005$, \$ $p < 0.05$ vs. GAOGER and RGD, \$\$\$ $p < 0.0005$ vs. GAOGER and RGD).

When we stimulated hMSC in ligand-functionalized hydrogels with TNF- α and IFN- γ , we saw a significant effect of stimulation on the secretion levels of almost all of the cytokines tested in the conditioned medium. Discriminant analysis shows some separation of samples by adhesive ligand (**Figure 38**). Along canonical parameter 1, GFOGER- and RDG-hydrogels are slightly farther from the GAOGER and RGD groups. Along canonical

parameter 2, the GFOGER, GAOGER, and RGD groups overlap with RDG slightly removed. Cluster analysis shows no clear pattern with respect to adhesive ligand (**Figure 39**). Multivariate ANOVA, as described previously, shows no significant effect of ligand on cytokine secretion profiles after stimulation with IFN- γ and TNF- α (**Figure 40**). Upon analysis of individual cytokines, no cytokines exhibited differences among adhesive ligand, except for basic FGF which is upregulated in RDG hydrogels after stimulation (**Figure 41**). We did not detect an effect of adhesive ligand on cytokine secretion profiles of hMSC encapsulated in ligand-functionalized hydrogels after stimulation with IFN- γ and TNF- α . This is likely due to the highly potent effects of IFN- γ and TNF- α on hMSC activation masking any possible effects of adhesive ligand.

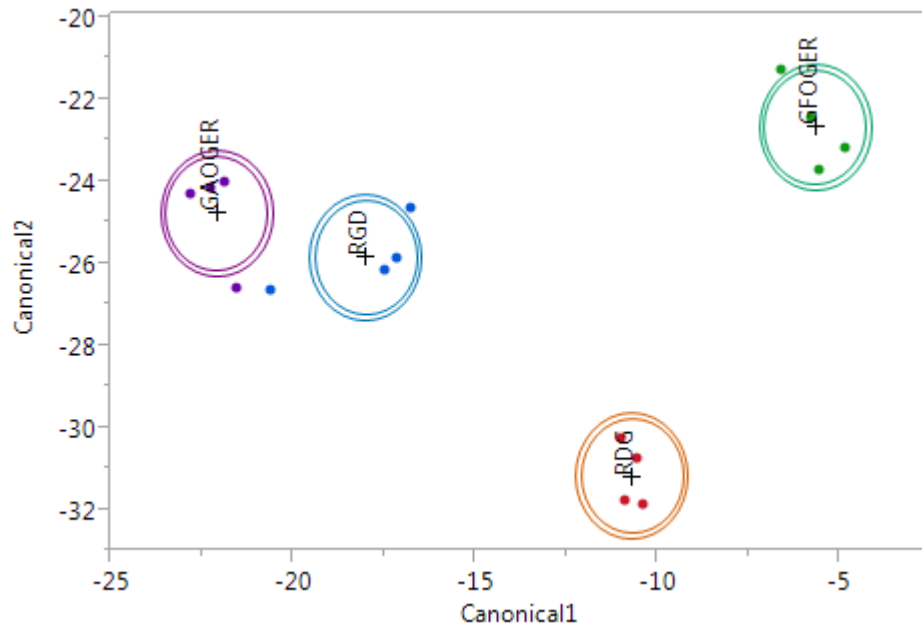


Figure 38. Discriminant analysis of cytokine secretion from encapsulated hMSC with IFN- γ /TNF- α stimulation. Linear discriminant analysis of cytokine secretion of hMSC encapsulated in ligand-functionalized hydrogels with cytokine stimulation over 2 days in culture. Each point represents a sample and each multivariate mean is a labeled circle corresponding to a 95% confidence limit for the mean. Groups that are significantly different tend to have non-intersecting circles (N=4).

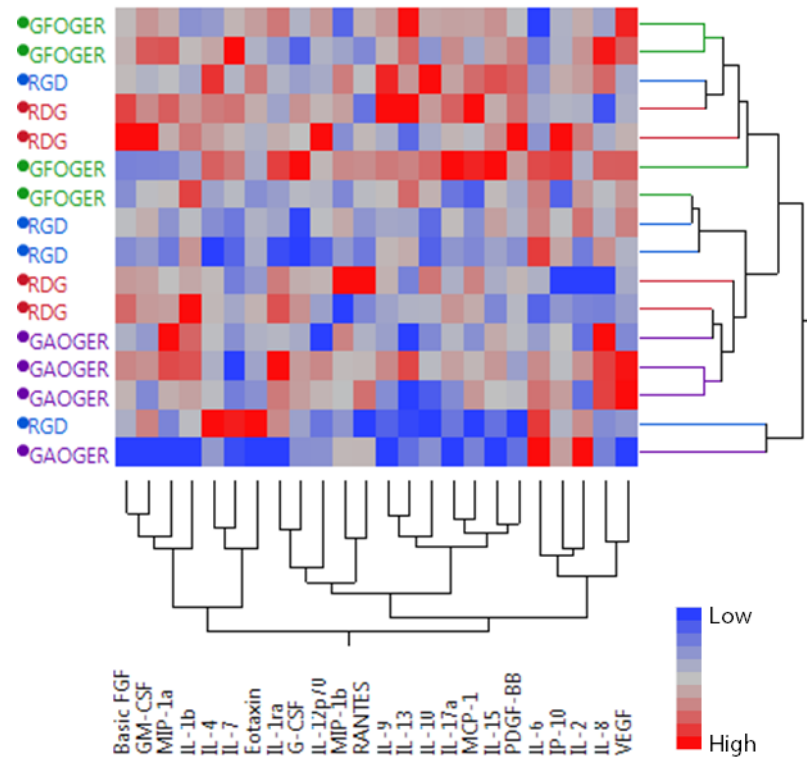


Figure 39. Hierarchical clustering of cytokine secretion from encapsulated hMSC with IFN- γ /TNF- α stimulation. Ward's method shows no clear clustering among ligands when stimulated with TNF- α and IFN- γ .

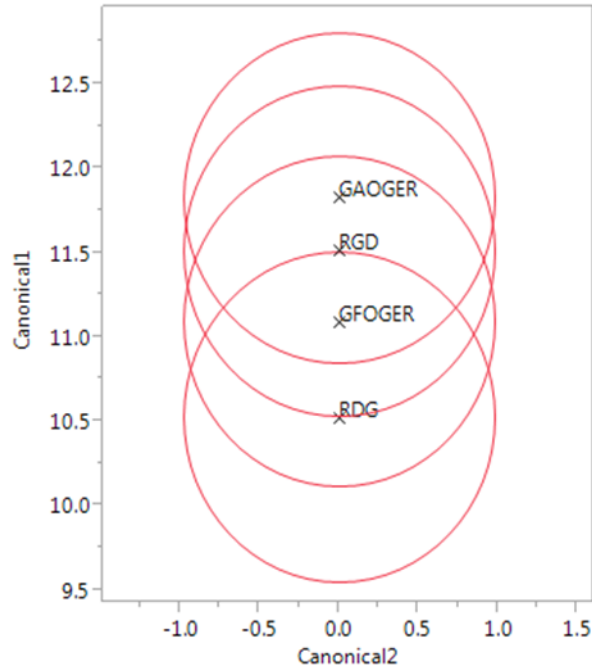


Figure 40. Stimulation masks effect of ligand on cytokine secretion profile. Multivariate ANOVA with a sum combination across cytokines shows no significant differences among ligands when stimulated with TNF- α and IFN- γ . (N=4; MANOVA: $p=0.3281$).

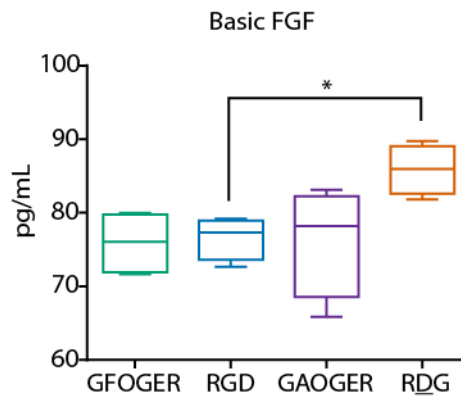


Figure 41. Cytokines with significant secretion levels for hMSC encapsulated in ligand-functionalized hydrogels when stimulated with TNF- α and IFN- γ . (Whiskers represent min and max, box extends from 25th to 75th percentiles, line represents median. N=4; ANOVA: * $p<0.05$).

DISCUSSION

In this study, we aimed to gain more insights into the differential effects of adhesive ligand and hMSC delivery on the repair environment. Given the significantly increased bone repair and hMSC survival observed in radial segmental defects after delivery of hMSC in GFOGER-functionalized hydrogels, we hypothesized that the early gene expression profile *in vivo* would vary among ligands. First, we analyzed gene expression *in vivo* to investigate which types of genes were regulated after hMSC delivery and whether adhesive ligand influenced that profile. We then investigated whether adhesive peptide ligand has an effect on the cytokine secretome of encapsulated hMSC *in vitro*.

To investigate the gene expression profiles of bone defects treated with hMSC in GFOGER-, RGD-, or RDG-hydrogels, 96 genes were chosen to cover a number of functional areas specific to mouse or human. The wide array of genes screened is a large advantage to the microfluidic, high throughput PCR platform that was employed in this study. Multivariate analysis indicated no significant difference between hMSC/RGD and hMSC/RDG treated defects, however, the overall gene expression pattern in hMSC/GFOGER hydrogel-treated defects was statistically significant compared to RGD and RDG gels. Upon analysis of mRNA expression from explanted tissue, we found significant differences in gene expression related to inflammation, vascularization, and bone. All of the genes upregulated in GFOGER hydrogel-treated defects were specific to the host response, and many have been reported to play a significant role in the normal fracture healing cascade. The inflammation genes upregulated in GFOGER hydrogel-treated group are responsible for immune cell recruitment and activation, critical in initiating the repair cascade and vascularization. We also observed significant upregulation

of vascularization genes, namely angiogenic growth factor receptors and mediators of vessel remodeling. The upregulation of host bone genes in hMSC/GFOGER defects suggests that the transplanted hMSC serve as paracrine support rather than differentiation into the target tissue, in agreement with recent thinking [172]. Vascularization is a vital component to bone development and repair [173], and due to the high amounts of cross-talk between inflammatory and angiogenic mediators, the upregulation of inflammatory, angiogenic, and bone related genes in hMSC/GFOGER treated defects is consistent with the survival and bone repair outcomes previously described. The human genes, HGF, NF κ B, HIF-1 α , and BMP-2 were found to be upregulated in hMSC/RGD and hMSC/RDG compared to hMSC/GFOGER-treated defects, and may indicate a lack of vascularization and hypoxic and apoptotic hMSC. HGF, which has been reported to be secreted by apoptotic cells [165], can activate NF κ B which then regulates HIF-1 α [164] and BMP-2 signaling [174,175], is one possible explanation for the pattern of genes upregulated in RGD and RDG gels. Our result that the delivery of hMSC in an appropriate carrier modulates the tissue repair environment is consistent with other reports of MSC delivery. Seebach et al observed higher gene expression of VEGF, IL-6, and MIP-2 *in vivo* after delivery of fibrin-encapsulated rat MSC to a femur defect compared to fibrin alone [176]. Swartzlander et al observed a diminished fibrous capsule when mMSC-laden hydrogels were implanted subcutaneously compared to cell-free scaffolds, or scaffolds containing osteogenically differentiated mMSC, suggesting mMSC modulation of macrophage activation [177].

The murine radial segmental defect provides many significant advantages over other bone defects – stabilization by the ulna eliminates the need for fixation hardware and

the small model allows for *in vivo* imaging techniques such as bioluminescence or transgenic strains. However, the defect is not without its limitations – an unknown contribution from the ulna due to its close proximity, the small size of the defect does not present the same vascularization or diffusion challenges as larger defects, and the use of immunodeficient NSG mice in our studies is not representative of a clinical therapy. The NSG mouse lacks B cells, T cells, natural killer cells and complement, and has defective dendritic cells and macrophages [178,179]. The alternative model, delivering murine cells to a fully competent host, diminishes translational capacity of this therapy and may not correspond to a human cell-based therapy. Although murine and human MSC share multi-lineage differentiation capacity, murine MSC have been shown to exhibit high susceptibility to malignant transformation and carry cytogenic abnormalities [180,181]. The recent development of humanized mouse models which carry functional, completely engrafted human immune systems, may be a more relevant and useful model for studying the immunomodulation potential of hMSC in a murine model, however, the reports of eventual graft versus host disease in humanized mice warrant further characterization [144]. Nevertheless, the relatively simple procedure (compared to more complex defects such as the cranial defect or femoral defect) lends itself as a useful screening model to identify candidate conditions for larger, more challenging injury models.

Although we observed significant differences in gene expression patterns *in vivo* due to ligand, the complex environment and multiple factors at play make interpretations complicated. Thus, we aimed to investigate whether the simple presentation of various integrin-specific ligands could alter the secretome of encapsulated hMSC in a more controlled environment and if the differences in transcription that we observed *in vivo* are

present *in vitro*. Using multiplex technology, we screened 27 cytokines in the conditioned media of encapsulated hMSC without exogenous stimulation. Discriminant and cluster analysis revealed a large separation in cytokine profile based on adhesive versus non-adhesive peptide functionalization, and a slightly smaller, but still significant, separation based on integrin specificity. Multivariate analysis indicated high similarity between RDG and GAOGER groups, a slight, but not significant, difference due to RGD gels, and a significant difference in cytokine profile in GFOGER hydrogels compared to RGD, RDG, or GAOGER hydrogels. We observed significant increases in the secretion levels of trophic factors, FGF and VEGF, and inflammatory mediators, IL-6, IL-8, IL-1ra, IFN- γ , and MCP-1 in $\alpha 2\beta 1$ -specific GFOGER hydrogels compared to other groups. When encapsulated hMSC were stimulated with exogenous TNF- α and IFN- γ , no major effect of adhesive ligand was detected, which may be due to the high, sustained levels of inflammatory stimulation. hMSC have the ability to secrete a number of immunomodulatory factors, but to the best of our knowledge, no one has shown that integrin-specificity can tailor the secretome profile, although groups have shown effects of encapsulation, aggregation, and material. Rustad et al reported that mMSC encapsulated in pullulan-collagen hydrogels secreted higher amounts of VEGF and MCP-1 compared to plated mMSC [182]. Cantu et al showed that hMSC encapsulated in collagen gels secreted higher levels of IL-6 compared to PEG-gelatin (whose main adhesive site is RGD) [183]. Seib et al and Sumanasinghe et al showed that mechanical stimuli such as substrate stiffness and cyclic strain, respectively, can alter cytokine secretion [184,185].

Interestingly, upon comparison of *in vivo* gene expression and the *in vitro* cytokine profile, we observe consistent upregulation of several targets that support a differential

effect of GFOGER peptide on immunomodulation compared to RGD or RDG ligands. Higher secreted levels of the growth factors FGF and VEGF were detected for hMSC in GFOGER hydrogels *in vitro* and gene transcripts for their receptors, FGFR2, VEGFR2/KDR and VEGFR1/FLT1, were significantly upregulated in the host mouse tissue *in vivo*. Although mouse IL-1 β gene was upregulated *in vivo* in GFOGER defects, IL-1ra levels were higher from hMSC in GFOGER *in vitro*, suggesting modulation of the important balance of IL-1 and IL-1ra in tissue homeostasis [186]. MCP-1, which plays a critical role in the recruitment and activation of leukocytes [156,157], was more highly secreted from hMSC in GFOGER *in vitro* and gene transcripts for its receptor, CCR2, was also upregulated in host mouse tissue *in vivo*.

Waterman et al recently proposed a paradigm for hMSC in which hMSC can be polarized into two homogenously acting phenotypes – MSC1, a pro-inflammatory phenotype, and MSC2, an anti-inflammatory phenotype, summarized in **Figure 42** [187]. Our data, particularly the upregulation of IL-6, VEGF, FGF, and CXCL12 of hMSC encapsulated in GFOGER-functionalized hydrogels, is consistent with the anti-inflammatory MSC2 phenotype which may help to polarize monocytes towards a more reparative macrophage. Regardless of phenotype, this study combined with the enhanced bone repair and transplanted hMSC survival *in vivo*, shows that targeting $\alpha 2\beta 1$ integrin during hMSC encapsulation and cell delivery has a beneficial effect on the repair environment and overall repair outcomes.

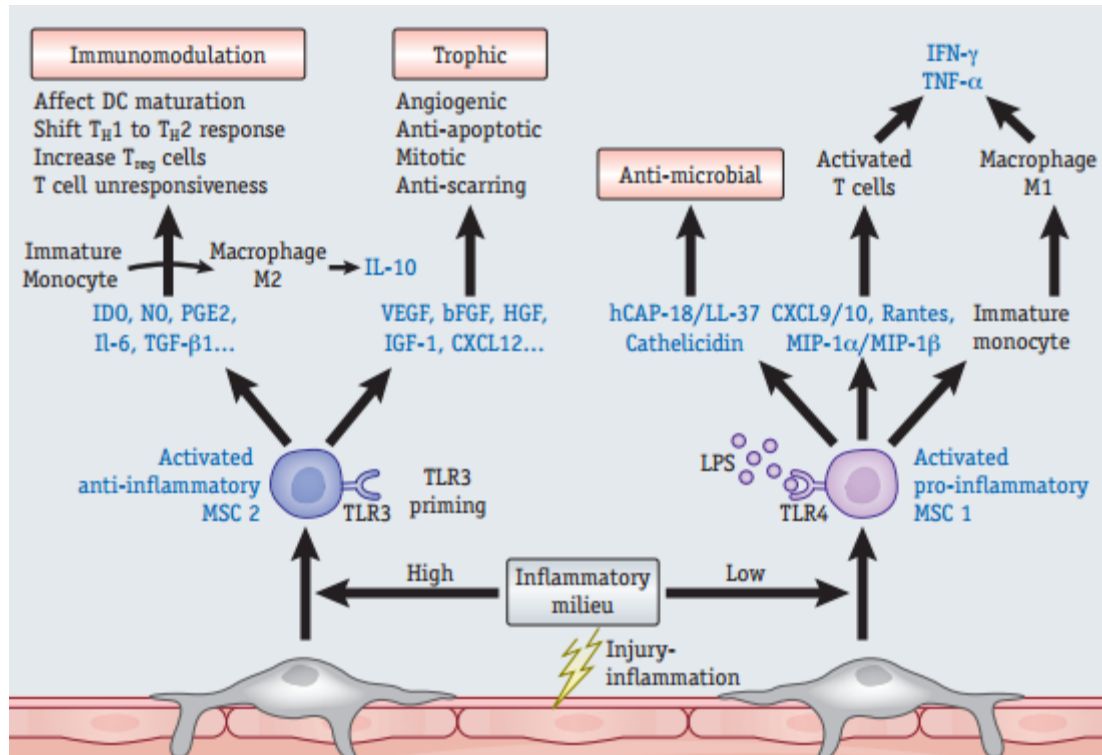


Figure 42. Roles for mesenchymal stem cells as medicinal signaling cells. [188]

CHAPTER 6: FUTURE CONSIDERATIONS

This thesis presents a significant contribution to the field of biomaterials research by demonstrating the novelty of an integrin-specific, protease-degradable hydrogel in cell delivery and tissue repair. We have demonstrated the effect of integrin-specificity on transplanted cell survival, bone repair, and hMSC immunomodulatory phenotype.

In Aim 1, we engineered an integrin-specific cell microenvironment using biomimetic adhesive ligands. We showed that we were able to control material properties of the matrix independent of ligand peptide, and that material properties such as storage modulus can be tuned by varying hydrogel parameters. The ligand peptides exhibited specificity to targeted integrins and we observed differences in cell morphology in 3-D, while maintaining high cell viability.

In Aim 2, we demonstrated that the novel PEG-mal cell delivery hydrogel system supports hMSC survival through 8 weeks and bone repair. We have shown that integrin specificity has an effect on transplanted cell survival, in addition to tissue-specific repair that our lab has previously shown [80]. We observed that $\alpha 2\beta 1$ -specific GFOGER supports enhanced hMSC survival and bone repair *in vivo*, suggesting a role for integrin-specificity in improving transplanted cell survival and tissue repair.

In Aim 3, we gained additional insights into how integrin-specificity may be modulating the repair environment. First, we observed significant differences due to adhesive peptide in the gene expression profiles *in vivo* with respect to bone, inflammation, and vascularization. Second, we observed a significant effect of integrin-specificity on the *in vitro* cytokine secretion profiles of encapsulated hMSC. Interestingly, upon comparison

of *in vivo* gene expression and the *in vitro* cytokine profile, we observed some consistent upregulations that support a differential effect of GFOGER on immunomodulation compared to RGD or RDG, specifically in growth factor signaling and immune cell recruitment and activation. Taken together, these observations suggest that GFOGER hydrogels may be polarizing hMSC toward an anti-inflammatory MSC2 phenotype, which may help to polarize monocytes towards a more reparative macrophage phenotype [187]. Regardless of phenotype, this study combined with the enhanced bone repair and transplanted hMSC survival *in vivo*, shows that targeting $\alpha 2\beta 1$ integrin during hMSC encapsulation and cell delivery has a beneficial effect on the repair environment and overall repair outcomes.

Future studies as follow up to this thesis include studying the effect of encapsulated hMSC and adhesive peptide on a wider array of secreted cytokines and immunomodulatory factors or monocyte migration and polarization. Investigating the cytokine profile *in vivo* after hMSC delivery would shed additional light on the effects of ligand on the repair environment. There is also room for improvement of our cell delivery strategy as our most therapeutic condition, hMSC in GFOGER-functionalized hydrogels, fails to achieve full healing of the defects. Modifying hydrogel parameters such as macromer size and thus mesh size, cross-link degradation kinetics, or ligand density may have an effect on tissue repair. The limitations of our bone injury model such as size, ulna proximity, and the use of an immunocompromised host, warrants investigation of the performance of our cell therapy in additional bone repair models, such as the larger femoral defect or the use of humanized mice.

There is growing evidence that MSC exhibit great potential beyond multipotent differentiation and that they actually lose their immunomodulatory properties after differentiation [177]. Swartzlander et al showed that delivery of encapsulated mMSC reduced fibrous capsule formation compared to cell free scaffolds, thus it would be interesting to study the effect of adhesive peptide and hMSC on fibrous capsule given the differences in behavior of mouse versus human MSC [143]. Immunomodulation provided by hMSC encapsulated in GFOGER hydrogels may also be therapeutic in tissue injury models such as after myocardial infarction or after islet transplantation for type 1 diabetes.

Ultimately, these studies provide insight into the effects of integrin-specificity on transplanted hMSC survival, bone repair, and hMSC immunomodulation. A novel, highly defined, integrin-specific hydrogel system was evaluated for cell encapsulation *in vitro*, as well as in a relevant segmental bone defect model *in vivo*. These studies demonstrated the potential of integrin-specificity, specifically, targeting the $\alpha 2\beta 1$ integrin with GFOGER, in augmenting cell survival after transplantation, enhancing tissue repair, and modulating the immunomodulatory properties of hMSC. Altogether, this thesis provides integrin-specificity as a novel strategy for enhancing transplanted hMSC survival, tissue repair, and immunomodulation.

APPENDIX

KINETICS OF TIME TO MAXIMUM SIGNAL FOR BIOLUMINESCENT IMAGING

15,000 hMSC^{FLuc} were delivered in ligand-functionalized hydrogels to the radial segmental defect. Mice received a luciferin dose of 150 mg/kg delivered intraperitoneally prior to imaging. At each time point, images were acquired every 2 minutes until maximum signal was reached to establish kinetic curves. Signal was maintained between 90%-100% of maximum for roughly 15 min.

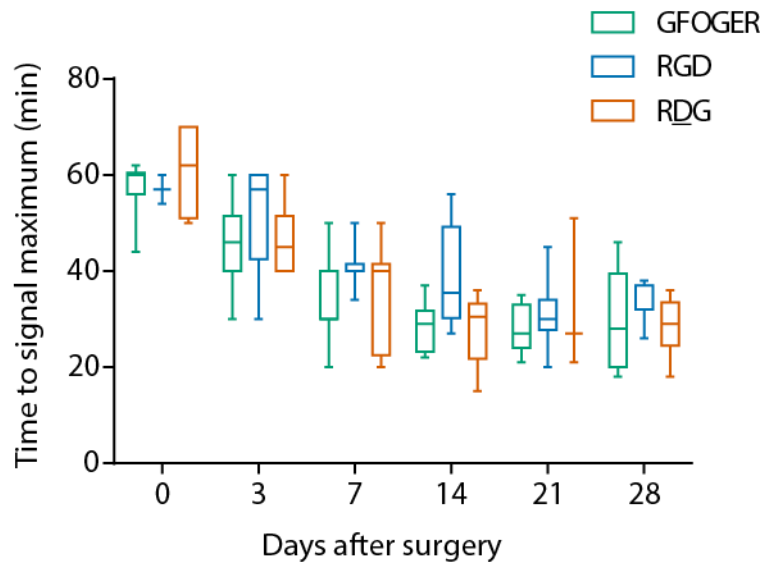


Figure 43. Time to maximum signal for individual time points after transplantation.

Well-defined Poly(lactic acids) Containing Poly(ethylene glycol) Side-chains. Macromolecules.

Macromolecules

ARTICLE

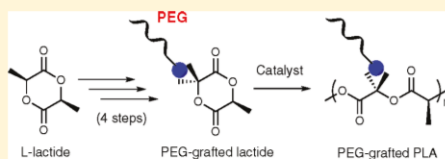
pubs.acs.org/Macromolecules

Well-Defined Poly(lactic acid)s Containing Poly(ethylene glycol) Side Chains

José A. Castillo,[†] Dorothee E. Borchmann,[†] Amy Y. Cheng,[‡] Yufeng Wang,[‡] Chunhua Hu,[‡] Andrés J. García,^{*,‡} and Marcus Weck^{*,†}[†]Molecular Design Institute and Department of Chemistry, New York University, New York, New York 10003, United States[‡]Woodruff School of Mechanical Engineering and Institute for Bioengineering and Bioscience, Georgia Institute of Technology, Atlanta, Georgia 30332-0400, United States

Supporting Information

ABSTRACT: Poly(ethylene glycol) (PEG) side-chain functionalized lactide analogues have been synthesized in four steps from commercially available L-lactide. The key step in the synthesis is the 1,3-dipolar cycloaddition between PEG-azides and a highly strained spiro lactide–heptene monomer, which proceeds in high conversions. The PEG-grafted lactide analogues were polymerized via ring-opening polymerization using triazabicyclodecene as organocatalyst to give well-defined tri- and hepta(ethylene glycol)–poly(lactide)s (PLA) with molecular weights above 10 kDa and polydispersity indices between 1.6 and 2.1. PEG–poly(lactide) (PLA) with PEG chain M_n 2000 was also prepared, but GPC analysis showed a bimodal profile indicating the presence of starting macromonomer. Cell adhesion assays were performed using MC3T3-E1 osteoblast-like cells demonstrating that PEG-containing PLA reduces cell adhesion significantly when compared to unfunctionalized PLA.



INTRODUCTION

Poly(lactic acid) (PLA), a poly(2-hydroxypropionic acid), is a biodegradable and biocompatible polymer from biorenewable feedstock. Following today's trend of minimizing the impact of chemicals on the environment as well as searching for alternatives to depleting petrochemical resources, PLA is the candidate of choice for polymeric commodities (e.g., packaging materials for food and beverages, plastic bags, and thin film coatings) as well as in the medical field (e.g., for medical devices, sutures, and tissue replacement and as delivery vehicle).^{1,2} PLA can be obtained via the polycondensation of lactic acid or the ring-opening polymerization (ROP) of cyclic lactides.³ One drawback of PLA is its lack of functional side-chain diversity, which limits the possibilities for chemical modification.^{2,4} To overcome this limitation, syntheses of modified lactide monomers with functionalized side chains have been reported in the past decade.^{2,4–8} We have published the synthesis of cyclic lactides bearing protected alcohols, amines, and carboxylic acid functionalities starting from commercially available amino acids.^{9,10} Another versatile synthetic approach has been reported by Yang and co-workers, who have synthesized functional hemilactides through a Passerini-type condensation.¹¹

Our ultimate goal is to develop polymeric scaffolds for bone tissue engineering with adequate mechanical properties and controlled architectures that support osteoblast function. Recently, we have reported the synthesis of poly(lactic acid) (PLA)-*block*-poly(norbornene) (PNB) copolymers that bear photo-cross-linkable cinnamate side chains to enhance mechanical strength.¹²

In order to improve the properties of these scaffolds further, herein we report the preparation of poly(ethylene glycol) (PEG)-functionalized PLA. We rationalize that this modification should reduce nonspecific protein adsorption, a prerequisite to our scaffold design.¹³ It has also been reported that surface PEGylation increases the mechanosensitivity of osteoblasts, i.e., the specific response to mechanical stimulation, and accelerates growth and development of osteoblasts for bone repair and tissue engineering.^{14,15}

Several groups have grafted PEG in a random fashion onto PLA. Baker and co-workers reported a postpolymerization modification of propargylglycolide polymers with PEG-azides via Huisgen cycloaddition.¹⁶ Hildgen and co-workers have prepared randomly PEG-grafted PLA to prepare stealth nanoparticles for drug delivery. They initially polymerized D,L-lactide in the presence of allyl glycidyl ether followed by subsequent PEG functionalization.¹⁷ Baker and co-workers have also reported the synthesis of well-defined PEG-grafted PLA based on the condensation of hydroxyacids with PEG side chains. However, this synthetic route consisted of several steps in moderate yields.¹⁸ Despite these elegant approaches, a general approach to prepare well-defined PLA containing PEG side chains still remains a synthetic challenge. In this contribution we report a short and efficient functionalization of L-lactide monomer with PEG side chains and the subsequent

Received: July 17, 2011

Revised: November 14, 2011

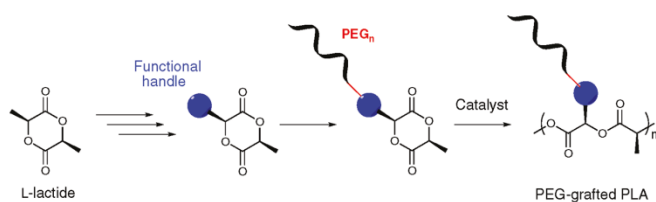
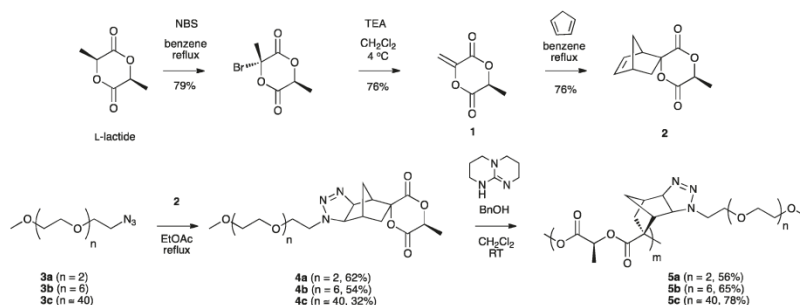


Figure 1. Schematic approach to the preparation of well-defined PEG-grafted PLA from L-lactide.

Scheme 1. General Synthetic Approach To Prepare PEG_n-PLA



polymerization. Furthermore, since cell adhesion to polymeric surfaces is primarily mediated by adhesive proteins adsorbed from serum such as vitronectin and fibronectin,¹⁹ cell adhesion assays were performed using MC3T3 $\times 10^{-1}$ as osteoblast-like cells in order to investigate the reduction of nonspecific protein adsorption caused by the new PEG-grafted polymers.

RESEARCH DESIGN

The main requirement for our research design is that we can functionalize cyclic L-lactide monomers with PEG side chains of different sizes in high yields and in a straightforward fashion in order to prepare well-defined PEG-grafted PLA (Figure 1). Our design is based on some recent work by Jing and Hillmyer, who have reported the synthesis of *exo*-methylene-lactide **1** and spiro-lactide-heptene **2** (Scheme 1).²⁰ We rationalized that **2** due to its high ring strain can serve as dipolarophile in cycloaddition reactions. Knowing that azides react readily with strained alkenes such as norbornenes via 1,3-dipolar cycloadditions,^{21–23} our hypothesis is that the cycloaddition between PEG-azides and **2** which contains a norbornene moiety might be an easy entranceway toward PEG functionalized cyclic lactides.

EXPERIMENTAL SECTION

Materials. Compounds **1** and **2** were synthesized as described by Jing and Hillmyer.²⁰ Poly(ethylene glycol) monomethyl ether tosylates **6**, **10**, and **11** were prepared as reported by Ouchi and co-workers.²⁴ Azido-poly(ethylene glycol) monomethyl ethers **3a**, **3b**, and **3c** were obtained using a methodology reported by Saha and Ramakrishnan.²⁵ Triethylene glycol monomethyl ether (97%), poly(ethylene glycol)

methyl ether ($M_n \sim 2000$), L-lactide (98%), dicyclopentadiene (97%), 1,5,7-triazabicyclo[4.4.0]dec-5-ene (97%), benzyl alcohol (99.8%), and 1-azidoadamantane (97%) were purchased from Sigma-Aldrich. Tetraethylene glycol (99.5%) was purchased from Acros Organics. Benzene was distilled over sodium and benzophenone under nitrogen before use. Dichloromethane was dried over calcium hydride and distilled under nitrogen prior to use. ¹H and ¹³C NMR spectra were recorded on a Bruker AC 400 spectrometer (400 and 100 MHz for ¹H and ¹³C, respectively). All chemical shifts are reported in parts per million (ppm) with reference to solvent residual peaks. Gel permeation chromatography (GPC) was performed using an HPLC from Agilent Technologies 1200 series and two columns (gel type: AM GPC gel, porosities: 100, 1000, 100 000 Å, linear mixed bed from American Polymer Standards) connected in series with an Optilab rEX refractive index detector from Wyatt Technology. Experiments were performed at room temperature using CHCl₃/triethylamine/isopropanol 94:4:2 as eluent, flow rate of 1 mL/min, and molecular weights are reported versus PEG standards (M_n from 1050 to 30 000). Electrospray ionization (ESI) mass spectra were obtained on an Agilent 1100 Series capillary LCMSD trap XCT spectrometer using MeOH/H₂O and ACN/H₂O as eluents. Microwave-assisted reactions were performed using a CEM Discovery microwave reactor. IR spectra were recorded using KBr tablets or poly(ethylene) sample cards on a Nicolet 550 Magna-IR spectrometer. Elemental analysis was performed on a Perkin-Elmer 2400 Series II CHNSO analyzer and by Intertek-QTI. Melting points were determined using a Fisher-Johns apparatus. The MALDI-TOF spectrum of **4c** was recorded on a Bruker UltrafleXtreme using dithranol as matrix and NaCl as doping salt. The sample was prepared following the multiple-layer spotting technique reported by Meier and Schubert.²⁶ Thermogravimetric analyses were recorded on a Perkin-Elmer Pyris 1 TGA from 25 to 550 °C with a heating/cooling rate of 10 °C min⁻¹ under N₂. Differential scanning calorimetry (DSC) measurements were acquired

using a Perkin-Elmer DSC Pyris 1. Samples were run under a nitrogen atmosphere from -10 to 100 °C with a heating/cooling rate of 10 °C min^{-1} . Dialysis membrane Spectra/Por 6, MWCO 1000 and 3500 (38 mm flat width), was purchased from SpectrumLabs and rinsed with water prior to use. About 10 cm of dialysis membrane was used per purification. For **4c** and polymers **5a–c**, a dichloromethane solution of product was introduced inside the dialysis bag (MWCO 1000 for monomer **4c** and polymers **5a,b** and MWCO 3500 for polymer **5c**) that was then introduced to 0.5 L of dichloromethane and gently stirred for about 12 h. Four cycles were performed for each dialysis.

Single Crystal Structure Determination. A colorless block crystal **4d** with the size of $0.12 \times 0.22 \times 0.30$ mm³ was selected for geometry and intensity data collection with a Bruker SMART APEXII CCD area detector on a D8 goniometer at 100 K. The temperature during the data collection was controlled with an Oxford Cryosystems Series 700 plus instrument. Preliminary lattice parameters and orientation matrices were obtained from three sets of frames. Data were collected using graphite-monochromated and 0.5 mm MonoCap-collimated Mo K α radiation ($\lambda = 0.71073$ Å) with the ω scan method.²⁷ Data were processed with the INTEGRATE program of the APEX2 software²⁷ for reduction and cell refinement. Multiscan absorption corrections were applied by using the SCALE program for area detector. The structure was solved by the direct method and refined on F^2 (SHELXTL).²⁸ Non-hydrogen atoms were refined with anisotropic displacement parameters, and hydrogen atoms on carbons were placed in idealized positions (C–H = 0.99 or 1.00 Å) and included as riding with $U_{\text{iso}}(\text{H}) = 1.2$ or $1.5 U_{\text{eq}}(\text{non-H})$.

Synthesis of Triethylene Glycol Methyl Ether–1,2,3- Δ^2 -Triazoline-spiro[6-methyl-1,4-dioxane-2,5-dione-3,2'-bicyclo[2.2.1]heptane], PEG₃-Spirolactide (4a**).** Azidoethylene glycol methyl ether, PEG₃-N₃, **3a** (684 mg, 3.62 mmol), and spiro[6-methyl-1,4-dioxane-2,5-dione-3,2'-bicyclo[2.2.1]hepta-5-ene], **2** (753 mg, 3.62 mmol), were dissolved in EtOAc (20 mL). The reaction was refluxed under nitrogen for 3 days, and the conversion was monitored by ¹H NMR spectroscopy. The crude reaction was concentrated under reduced pressure to give a brown oil. This crude product was purified by silica chromatography using EtOAc/hexane 7:3 as eluent to afford the titled triazoline as a yellow oil (897 mg, 62%). ¹H NMR (CDCl₃, 400 MHz, data shown for major isomer): δ = 5.18 (q, J = 4.9 Hz, 1H, –CH– of LA unit), 4.92 (d, J = 9.8 Hz, 1H, –CH– of triazoline unit), 3.81 (m, 2H), 3.75–3.60 (PEG chain, 12H), 3.57 (m, 3H), 3.37 (s, 3H, CH₃–PEG–), 3.08 (s, 1H), 2.76 (dd, J = 14.3 Hz, J = 5.0 Hz, 1H), 2.63 (d, J = 4.9 Hz, 1H), 1.76 (dt, J = 11.7 Hz, J = 1.5 Hz, 1H), 1.69 (d, J = 6.7 Hz, 3H, CH₃– of LA unit), 1.53 (dd, J = 14.1 Hz, J = 3.5 Hz, 1H), 1.28–1.25 (m, 1H). ¹³C NMR (CDCl₃, 100 MHz, data shown for major isomer): δ = 167.9, 167.1, 85.7, 78.7, 73.0, 72.1, 70.8 ($\times 2$), 70.7, 70.3, 62.7, 59.2, 49.0, 48.3, 38.3, 31.6, 16.8. ESI-mass: 420.1 (M^+ +Na⁺). MS-ESI ($M + H$)⁺ m/z calcd for C₁₈H₂₈N₃O₇: 398.42; found 398.1. Elemental analysis: calcd for C₁₈H₂₇ON₃O₇: C 54.40, H 6.85, N 10.57; found: C 54.78, H 6.83, N 10.08. IR (KBr) ν (cm^{−1}): 2920.3, 2881.5, 1759.0, 1466.5, 1352.2, 1281.6, 1228.3, 1199.3, 1105.7, 1062.2, 1020.5, 986.9, 851.4, 647.1.

Synthesis of Heptaethylene Glycol Methyl Ether–1,2,3- Δ^2 -Triazoline-spiro[6-methyl-1,4-dioxane-2,5-dione-3,2'-bicyclo[2.2.1]heptane], PEG₇-Spirolactide (4b**).** Azidoheptaethylene glycol methyl ether, PEG₇-N₃, **3b** (1.30 g, 3.56 mmol), and spiro[6-methyl-1,4-dioxane-2,5-dione-3,2'-bicyclo[2.2.1]hepta-5-ene], **2** (741 mg, 3.56 mmol), were dissolved in EtOAc (20 mL). The reaction was refluxed under nitrogen for 4 days. The conversion after 4 days was measured by ¹H NMR spectroscopy to be 78%. The crude reaction was concentrated under reduced pressure to give a brown oil. This solid was purified by silica chromatography using EtOAc/hexane 7:3 as eluent to afford the titled triazoline as a yellow oil (1.10 g, 54%). ¹H NMR (CDCl₃, 400 MHz, data shown for major isomer): δ = 5.18 (q, J = 6.7 Hz, 1H, –CH– of LA unit), 4.90 (d, J = 9.8 Hz, 1H, –CH– of triazoline unit), 3.82 (m, 2H), 3.75–3.61 (PEG chain, 34H), 3.53 (m, 3H), 3.35

(m, 3H, CH₃–PEG–), 3.09 (s, 1H), 2.75 (dd, J = 14.0 Hz, J = 4.9 Hz, 1H), 2.63 (d, J = 4.7 Hz, 1H), 1.78 (m, 1H) (dd, J = 11.6 Hz, J = 1.5 Hz, 1H), 1.69 (d, J = 6.7 Hz, 3H, CH₃– of LA unit), 1.54 (dd, J = 14.1 Hz, J = 3.6 Hz, 1H), 1.26–1.23 (m, 1H). ¹³C NMR (CDCl₃, 100 MHz, data shown for major isomer): δ = 167.9, 167.1, 85.7, 78.7, 73.0, 72.1, 70.8, 70.7 ($\times 2$), 70.2, 62.7, 59.2, 48.9, 48.3, 41.0, 38.2, 31.5, 16.7. MS-ESI ($M + H$)⁺ m/z calcd for C₂₆H₄₄N₃O₁₁: 574.63; found 574.2. Elemental analysis: calcd for C₂₆H₄₃N₃O₁₁: C 54.44, H 7.56, N 7.33; found: C 54.85, H 7.76, N 7.12. IR (KBr) ν (cm^{−1}): 2922.3, 2870.3, 2105.6, 1957.5, 1757.7, 1466.3, 1350.9, 1282.0, 1140.8, 1062.6, 986.7, 937.0, 851.7, 743.7, 685.7, 649.0, 571.1.

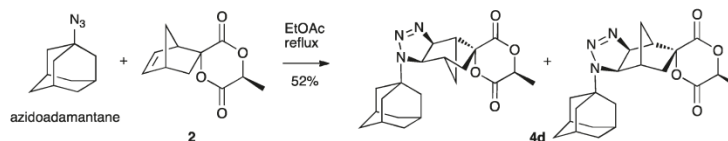
Synthesis of Poly(ethylene glycol methyl ether)–1,2,3- Δ^2 -Triazoline-spiro[6-methyl-1,4-dioxane-2,5-dione-3,2'-bicyclo[2.2.1]heptane] ($M_n \sim 2200$), PEG₄₀-Spirolactide (4c**).** Azido-poly(ethylene glycol methyl ether) ($M_w \sim 2000$), PEG₄₀-N₃, **3c** (3.35 g, 1.67 mmol), and spiro[6-methyl-1,4-dioxane-2,5-dione-3,2'-bicyclo[2.2.1]hepta-5-ene], **2** (1.26 mg, 6.0 mmol, 3.6 equiv), were dissolved in EtOAc (40 mL). The reaction was refluxed under nitrogen for 3 days. The crude reaction was concentrated under reduced pressure to afford a dark green solid. The crude product was dissolved in CH₂Cl₂ (~15 mL), and diethyl ether was added (~30 mL). The suspension was refluxed for 20 min and cooled down to room temperature, affording a white suspension and a green oil. The layers were separated, and the white suspension was cooled down to 4 °C when a white solid precipitated. This solid was washed with diethyl ether. The crystallization was repeated two more times, affording the title compound as a white solid (1.17 g, 32%). The monomer was dialyzed in CH₂Cl₂ using a cellulose membrane (MWCO 1000). Finally, compound **4c** was lyophilized twice from distilled benzene (3 times distilled) prior to polymerization. ¹H NMR (CDCl₃, 400 MHz, data shown for major isomer): δ = 5.17 (q, J = 6.6 Hz, 1H, –CH– of LA unit), 4.92 (d, J = 9.7 Hz, 1H, –CH– of triazoline unit), 3.73–3.45 (PEG chain), 3.45 (m, 3H), 3.36 (m, 3H, CH₃–PEG–), 3.08 (s, 1H), 2.75 (dd, J = 14.0 Hz, J = 4.9 Hz, 1H), 2.62 (d, J = 4.6 Hz, 1H), 1.87 (dd, J = 11.6 Hz, J = 1.3 Hz, 1H), 1.68 (d, J = 6.7 Hz, 3H, CH₃– of LA unit), 1.53 (dd, J = 14.1 Hz, J = 3.7 Hz, 1H), 1.24 (m, 1H). ¹³C NMR (CDCl₃, 100 MHz, data shown for major isomer): δ = 167.9, 167.0, 88.6, 85.7, 78.7, 77.4, 70.3 (PEG chain), 62.7, 59.2, 56.1, 49.0, 48.3, 44.9, 41.0, 40.0, 39.5, 38.3, 31.6, 27.3, 16.8. Melting point: 45–46 °C. Elemental analysis: calcd for C₉₄H₂₁₈N₃O₄₅: C 53.55, H 10.3, N 2.0; found: C 53.79, H 8.61, N 1.08. IR (KBr) ν (cm^{−1}): 2921.3, 2882.4, 2242.3, 2098.6, 2058.5, 1954.3, 1758.6, 1467.0, 1343.2, 1280.6, 1241.9, 1112.8, 963.0, 843.0, 742.8, 569.8.

Synthesis of Adamantyl-1,2,3- Δ^2 -triazoline–Spiro[6-methyl-1,4-dioxane-2,5-dione-3,2'-bicyclo[2.2.1]heptane] (4d**).** 1-Azidoadamantane (255 mg, 1.44 mmol) and spiro[6-methyl-1,4-dioxane-2,5-dione-3,2'-bicyclo[2.2.1]hepta-5-ene], **2** (300 mg, 1.44 mmol), were dissolved in EtOAc. The reaction was refluxed overnight under nitrogen. The crude reaction was concentrated under reduced pressure to afford an orange solid. The crude product was purified by silica chromatography using EtOAc/hexane 8:2 as eluent to afford the titled triazoline as a white solid (290 mg, 52%). ¹H NMR (CDCl₃, 400 MHz, data shown for major isomer): δ = 5.22 (q, J = 6.7 Hz, 1H, –CH– of LA unit), 4.84 (d, J = 9.9 Hz, 1H, –CH– of triazoline unit), 3.65 (d, J = 9.9 Hz, 1H, –CH'– of triazoline unit), 3.13 (s, 1H), 2.73 (dd, J = 14.1 Hz, J = 4.9 Hz, 1H), 2.42 (d, J = 5.2 Hz, 1H), 2.15–2.08 (m, 7H), 1.86–1.79 (m, 4H), 1.78–1.66 (m, 10H, CH₃– of LA unit and adamantane unit), 1.56 (dd, J = 14.1 Hz, J = 4.6 Hz, 1H), 1.30–1.27 (m, 1H). ¹³C NMR (CDCl₃, 100 MHz, data shown for major isomer): δ = 168.0, 167.2, 86.1, 78.2, 73.0, 58.4, 57.4, 49.1, 43.8, 42.2, 36.4, 31.7, 29.6, 16.8. Melting point: 214–215 °C. MS-ESI ($M + H$)⁺ m/z calcd for C₂₁H₂₈N₃O₄: 386.46; found 386.2. Elemental analysis: calcd for C₂₁H₂₇N₃O₄: C 65.44, H 7.06, N 10.9; found: C 65.53, H 7.00, N 10.9. IR (KBr) ν (cm^{−1}): 3533.7, 3497.0, 2997.3, 2917.6, 2851.5, 2680.6, 2333.5, 1750.1, 1482.3, 1454.8, 1360.3, 1313.2, 1242.6, 1147.6, 1086.6, 1020.0, 987.4, 928.6, 855.7, 826.2, 787.1, 737.5, 693.1, 647.5, 582.3, 485.7.

C

dx.doi.org/10.1021/ma2016387 | Macromolecules XXXX, XXX, 000–000

Scheme 2. 1,3-Dipolar Cycloaddition between 1-Azidoadamantane and Spirolactide 2



General Procedure for Microwave-Assisted 1,3-Dipolar Cycloaddition. PEG_n-azide (1 equiv) and spirolactide (1 equiv) were mixed in a tube reactor in the absence of solvent. The reaction mixture was irradiated using microwave irradiation at 70 °C for 3 cycles (each 1 h) at 150 W. The conversion was followed by ¹H NMR spectroscopy.

Polymerization. All L-lactide analogues were stored under nitrogen in a freezer to ensure stability. Prior to polymerization, monomers 4a,b were triply recrystallized from EtOAc/hexane while monomer 4c was triply recrystallized from CH₂Cl₂/diethyl ether. Then, each monomer was frozen in benzene (triply distilled) and lyophilized (3×). The polymerization of 4a is described as an example. In a nitrogen-filled glovebox, a catalyst/initiator solution was prepared by combining 1,5,7-triazabicyclo[4.4.0]dec-5-ene (TBD, 18 mg, 0.126 mmol), benzyl alcohol (26 μL, 0.251 mmol), and anhydrous CH₂Cl₂ (25 mL) in a 25 mL volumetric flask. The freshly prepared catalyst/initiator solution (730 μL) was added to the Schlenk flask containing 4a (290 mg, 0.73 mmol). The initial concentrations were 4a 1 M (100 equiv), TBD 0.5 equiv, and BnOH 1 equiv. After 24 h, the crude reaction was concentrated under reduced pressure and purified by dialysis (MWCO 1000) from CH₂Cl₂. Polymer 5a was isolated as a yellow oil (255 mg, 56%). ¹H NMR (acetone-*d*₆, 400 MHz): δ = 5.34–4.70 (m, 2H, –CH– of LA unit and –CH– of triazoline unit), 3.81 (m, 1H), 3.71 (m, 3H), 3.60 (PEG chain, 8H), 3.48 (m, 2H), 3.30 (s, 3H, CH₃–PEG–), 3.23–2.78 (m, 2H), 2.62–2.47 (m, 2H), 1.75 (m, 1H), 1.56 (m, 4H, including CH₃– of LA unit), 1.36 (m, 1H), 1.09 (m, 1H). ¹³C NMR (acetone-*d*₆, 100 MHz): δ = 170.8, 170.6, 85.0, 80.7, 72.7, 71.1, 70.5, 63.0, 59.0, 50.0, 48.9, 42.4, 37.8, 29.9, 17.1. Elemental analysis: calcd for C₁₈H₂₇N₃O₇: C 54.40, H 6.85, N 10.57; found: C 55.12, H 7.27, N 9.65.

PEG₇-Grafted PLA (5b). Polymer 5b was prepared as described above and isolated as a yellow oil (454 mg, 65%). ¹H NMR (acetone-*d*₆, 400 MHz): δ = 5.35–4.55 (m, 2H, –CH– of LA unit and –CH– of triazoline unit), 3.85 (m, 1H), 3.72 (m, 4H), 3.59 (PEG chain, 30H), 3.48 (m, 3H), 3.30 (s, 4H, including CH₃–PEG–), 3.24–2.95 (m, 1H), 2.75–2.54 (m, 2H), 1.75 (m, 1H), 1.59 (m, 5H, including CH₃– of LA unit), 1.36 (m, 1H), 1.11 (m, 1H). ¹³C NMR (acetone-*d*₆, 100 MHz): δ = 170.9, 170.7, 85.2, 80.6, 70.6, 63.0, 55.1, 48.9, 42.4, 41.9, 29.9, 17.0. Elemental analysis: calcd for C₂₆H₄₃N₃O₁₁: C 54.44, H 7.56, N 7.33; found: C 53.57, H 7.72, N 6.90.

PEG₄₀-Grafted PLA (5c). Polymer 5c was prepared as described above; in this case the initial concentration of monomer 4c was 0.33 M (100 equiv), TBD 1.5 equiv, and BnOH 3.0 equiv. Polymer 5c was purified by dialysis (MWCO 3500) from CH₂Cl₂, resulting in a white solid (454 mg, 78%). Melting point: 45–46 °C. ¹H NMR (acetone-*d*₆, 400 MHz): δ = 5.27 (m, 1H, –CH– of LA unit), 3.91–3.51 (PEG chain, 349H), 3.46 (m, 5H), 3.29 (s, 6H, including CH₃–PEG–), 3.10 (m, 2H), 2.81 (m, 11H), 2.63 (m, 2H), 2.50 (m, 1H), 1.65–1.47 (m, 5H, including CH₃– of LA unit), 1.41 (m, 1H), 1.29 (m, 1H), 1.08 (m, 1H). ¹³C NMR (acetone-*d*₆, 100 MHz): δ = 162.1, 170.7, 94.8, 86.5, 77.7, 71.4, 69.6, 63.7, 60.6, 58.9, 49.9, 49.0, 39.0, 29.5, 16.7. Elemental analysis: calcd for C₉₄H₂₁₈N₃O₄₅: C 53.55, H 10.3, N 2.0; found: C 54.08, H 9.01, N 1.11.

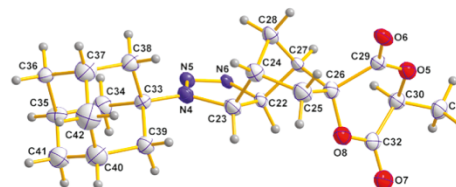


Figure 2. Crystal structure of one isomer of azidomantane–spirolactide 4d.

Cell Adhesion Assay. Glass slides were spin-coated with polymer solutions (100 mg/5 mL CHCl₃) at 500 rpm for 10 s and then at 3000 rpm for 30 s. After air drying, the slides were rinsed with deionized water, 70% ethanol, and Dulbecco's phosphate-buffered saline (DPBS, Invitrogen). MC3T3-E1 osteoblast-like cells (RIKEN Cell Bank) at passage 12 were seeded on coated slides at a cell density of 10 000 cells/cm² in serum-containing media (α-MEM supplemented with 10% fetal bovine serum). At 4 h, cells were permeabilized for 3 min in DPBS containing 0.5% Triton X-100 and fixed in 4% paraformaldehyde for 10 min. Slides were blocked in complete DPBS containing 5% goat serum and 0.01% NaN₃ for 1 h and subsequently incubated with antivinculin antibodies (1:400, Upstate Biotechnology V284) and 4',6-diamidino-2-phenylindole (DAPI, Sigma) in blocking buffer for 1 h. AlexaFluor488-conjugated secondary antibody (Invitrogen) was then incubated for 1 h. Slides were mounted with antifade reagent and viewed with a Nikon E400 fluorescence microscope using 10× and 40× objectives. Images were acquired with SPOT Advanced Software (Diagnostic Instruments, Inc.). To quantify cell adhesion, fluorescence images were analyzed with the ImageJ software (v1.44, NIH) to determine average cell numbers. Cell counts were analyzed using ANOVA with Tukey's test for pairwise comparisons.

RESULTS AND DISCUSSION

Our synthetic strategy to functionalize L-lactide with PEG side chains started with the preparation of spirolactide–heptene 2 according to literature procedures, which was prepared as a mixture of diastereomers (Scheme 1).²⁰

We investigated initially whether 2 can react as a dipolarophile in 1,3-dipolar cycloadditions. Since the 1,3-dipolar cycloaddition between 1-azidoadamantane and norbornene has been reported in the literature,²³ we studied, as a proof of concept, the 1,3-dipolar cycloaddition between 1-azidoadamantane and 2 (Scheme 2). The reaction was carried out in EtOAc at reflux. Within 12 h, high conversions of the 1,2,3-Δ²-triazoline isomers were obtained as characterized by TLC analyses. ¹H NMR spectroscopy analysis showed the disappearance of the alkene signals of 2 as well as the formation of two new doublets at 4.84 and 3.65 ppm, which is in good agreement with the chemical shifts of the Δ¹-1,2,3-triazoline

D

dx.doi.org/10.1021/ma2016387 | Macromolecules XXXX, XXX, 000–000

Table 1. Polymer Characterization Data

polymer	M_n (10^{-3}) ^a	PDI ^a	t_R (min) ^a	X_n ^b	M_n (10^{-3}) ^c	conv ^d (%)	yield ^e (%)
PEG ₃ -PLA 5a	12	2.1	18.3	30	44	99	60
PEG ₇ -PLA 5b	14	1.6	18.3	24	270	82	54
PEG ₄₀ -PLA 5c	11	1.4	18.3	5	3200	50	78 ^f

^a GPC in CHCl₃/TEA/isopropanol 94:4:2 with PEG standards using refractive index for detection. ^b Degree of polymerization (X_n) calculated from GPC analyses. ^c Number-average molecular weight determined based on ¹H NMR end-group analysis. ^d Conversion of polymerization measured by ¹H NMR spectroscopy. ^e Isolated yield of polymerization after purification by dialysis in CH₂Cl₂. ^f Polymer 5c was contaminated with starting macromonomer 4c.

ring protons reported for the corresponding norbornene adduct with azidoadamantane.²³ The crude reaction was purified by silica gel column chromatography and recrystallized from EtOAc/hexane, affording a mixture of two isomers in a ratio of 1.0:0.4. Single crystal X-ray analysis confirmed the formation of two isomers of 4d (Scheme 2, Figure 2, and Supporting Information).

After our model reaction afforded the desired cycloaddition product, we investigated the functionalization of 2 with poly(ethylene glycol) moieties. With this aim, we synthesized the three PEG-azides 3a and 3c via tosylation and azidation of the corresponding commercially available poly(ethylene glycol) methyl ether using standard conditions (i.e., p-TsCl and NaOH in H₂O/THF and NaN₃/DMF, respectively).²⁵ In the case of PEG-azide 3b, we previously synthesized the starting heptaethylene glycol methyl ether (see Scheme S1 in the Supporting Information). The 1,3-dipolar cycloaddition between PEG₃-N₃ 3a and 2 carried out in EtOAc under reflux for 12 h gave the desired PEG₃-spirolactide 4a. ¹H NMR spectroscopy analyses showed the formation of a new doublet at 4.91 ppm, corresponding to one of the two Δ^1 -1,2,3-triazoline ring protons, with similar chemical shift and coupling constants to those reported above for the triazoline 4d. The second doublet overlapped with the PEG chain signal in the ¹H NMR spectrum. However, it could be observed easily at 3.65 ppm in the COSY NMR spectrum (Supporting Information). The doublet at 4.91 ppm served as criterion for us to monitor the progress of the reaction by NMR spectroscopy. After 3 days at reflux, the observed conversion was 94%. Based on ¹H NMR spectroscopy analyses of the crude reaction mixture, two triazoline isomers were obtained in a ratio of 1.0:0.45. In addition, ¹³C NMR spectroscopy analysis showed two signals at 168.0 and 167.1 ppm corresponding to the two carbonyl groups on the lactide ring, indicating that the ring was conserved during the cycloaddition and the purification process. The IR spectrum of 4a does not show a signal corresponding to the starting azide, and the ESI mass spectrum of 4a showed one signal at 398.1 *m/z* (*M* + H)⁺.

After preparing 4a successfully (62% yield after silica chromatography), we applied our methodology to azides 3b, PEG₇-N₃, and 3c, PEG₄₀-N₃, $M_w \sim 2000$. The 1,3-dipolar cycloadditions between PEG₇-N₃ 3b and PEG₄₀-N₃ 3c with 2 in EtOAc at reflux for 3–4 days afforded PEG₇-spirolactide 4b and PEG₄₀-spirolactide 4c, respectively, in high conversions (75–80% by ¹H NMR spectroscopy). Monomer 4b was purified by silica chromatography (54% isolated yield), and monomer 4c was triply recrystallized from a 1:5 mixture of CH₂Cl₂/diethyl ether (32% isolated yield). The MALDI-TOF spectrum for 4c showed masses from 1713 to 2595 (theoretical $M_n \sim 2200$) (Supporting Information). The 1,3-dipolar cycloaddition was also investigated using microwave irradiation to explore whether microwave irradiation can result in

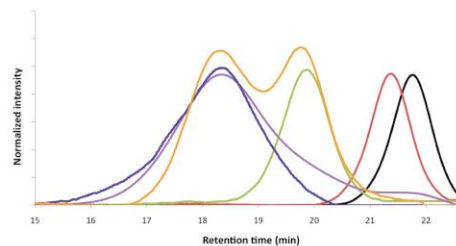


Figure 3. GPC curves of all monomers and polymers in CHCl₃/TEA/isopropanol 94:4:2. GPC trace of 4a (black trace), 4b (red trace), 4c (green trace), 5a (purple trace), 5b (blue trace), and 5c (orange trace). All molecular weights are reported versus PEG standards using refractive index for detection.

shorter reaction times. The microwave-assisted cycloaddition between 3a and 2 in an equimolar ratio reached a maximum of 86% conversion after 3 h at 70 °C as observed by ¹H NMR spectroscopy. In the case of the cycloaddition between 3c and 2 in equimolar ratio, the conversion observed was 68% after 3 h at 70 °C. When using the spirolactide 2 in slight excess (3c:2 ratio of 1:1.5 equiv), the reaction proceeded to full conversion.

After the successful synthesis of our three target monomers, we investigated the ring-opening polymerization of 4a–c. The monomers were obtained as a mixture of diastereomers, and we assume that they might possess slightly different reactivities. It is well-known that the ROP of lactides requires high monomer purity,^{9,20} and each monomer was purified and dried extensively as can be seen from the Experimental Section. Initially, we investigated the ROP of 4a using the polymerization conditions reported by us: SnOct₂ as catalyst and benzyl alcohol as initiator without solvent under N₂ at 140 °C overnight.⁹ Unfortunately, 4a was not stable under these reactions conditions. Next, we investigated the conditions employed by Hillmyer and co-workers to polymerize 2 (100 equiv) using triazabicyclodecene (TBD, 0.5 equiv) as organocatalyst and benzyl alcohol (1 equiv) as co-initiator.²⁰ This methodology ensures the preparation of PLA without any metal impurities, which is crucial for the use of our materials in regenerative medicine.²⁹ The polymerization of 4a at room temperature after 24 h using the Hillmyer procedure was almost quantitative as measured by ¹H NMR spectroscopy. We hypothesize that BnOH attacks the less sterically hindered carbonyl group of the lactide ring, i.e., the carbonyl next to the methyl group.

The kinetics of the polymerization of 4b was investigated by ¹H NMR spectroscopy, showing a maximum of 82% conversion

E

dx.doi.org/10.1021/ma2016387 | Macromolecules XXXX, XXX, 000–000

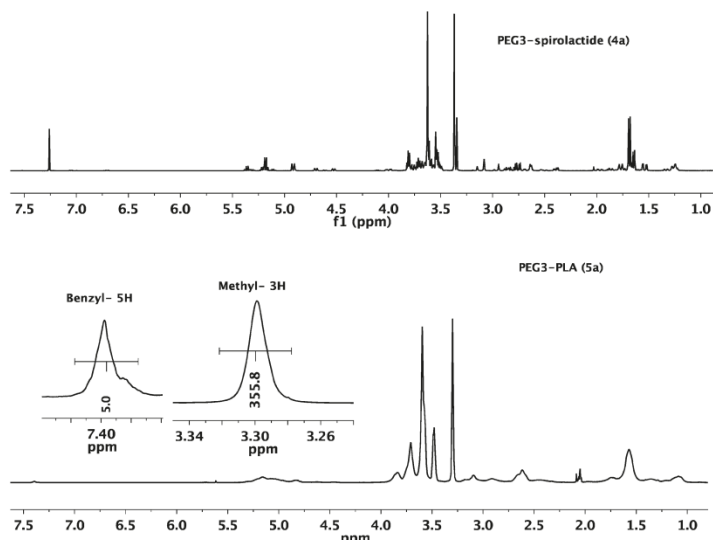


Figure 4. ^1H NMR spectrum of PEG₃-spirolactide **4a** in CDCl_3 (top) and end-group analysis of PEG₃-PLA **5a** by the ^1H NMR spectrum in acetone- d_6 (bottom).

after 20 h. In the case of monomer **4c**, which is a solid at room temperature and contains a long PEG chain ($M_n \sim 2200$), we decided to dilute the reaction mixture to increase the solubility of the monomer as well as the concentration of the catalyst and co-initiator. The initial concentrations used were **4c** 0.33 M (100 equiv), TBD 1.5 equiv, and BnOH 3 equiv. The polymerization of **4c** was followed by ^1H NMR spectroscopy, showing a maximum conversion ($\sim 50\%$) after 36 h. The spectrum of the crude reaction showed two similar and overlapping singlets at 3.29 and 3.30 ppm corresponding to the terminal methyl group of the CH_3 -PEG chain (Supporting Information). These two singlets suggest that **4c** and **5c** were present in the crude reaction in similar ratios. We hypothesize that the long PEG chain hinders the polymerization process. Since **4c** is a macromonomer, the long PEG side chain could adopt a random coil conformation that could “internalize” the lactide unit. This conformation would limit catalyst accessibility and thus significantly impede polymerization. Furthermore, the long PEG side chains of the monomers might entangle with the polymer PEG side chains, limiting monomer diffusion.

Isolated yields of all polymers ranged from 54 to 78% (Table 1) after extensive purification by dialysis in CH_2Cl_2 and lyophilization. All polymers were characterized by ^1H NMR and ^{13}C NMR spectroscopies, gel-permeation chromatography (GPC), and thermogravimetric analysis (TGA) (Table 1 and Supporting Information). In case of polymer **5c**, after purification by dialysis (MWCO 3500), the ^1H NMR spectrum showed again both singlets at 3.3 ppm in similar ratio, indicating that the dialysis process was unsuccessful in removing **4c**.

GPC analyses of the polymers show number-average molecular weights between 11 and 14 kDa and PDI values between 1.4 and 2.1. All values are reported versus PEG standards. We cannot

exclude trace contamination of monomers with water due to the hydrophilic PEG side chains despite careful repurifications and lyophilizations using distilled benzene as solvent. The presence of these water molecules might compete with BnOH as co-initiator and would explain the higher than expected PDI values. As expected, GPC analyses of polymers **5a–c** show lower retention times (t_R 18.3 min for all three polymers) than monomers **4a–c** (Figure 3). The GPC chromatogram of PEG₄₀-PLA **5c** shows a bimodal profile with a second peak at 19.7 min. This peak overlaps with the signal of the monomer **4c**. Therefore, in the case of polymer **5c**, the PDI value 1.4 was measured in the region of the GPC curve centered at 18 min. That result is in agreement with the NMR spectroscopy data, suggesting that polymer **5c** was still contaminated with the macromonomer **4c** (M_n 2200) after dialysis using a membrane bag MWCO 3500.

Molecular weights of **5a–c** were also determined by ^1H NMR end-group analysis comparing the integration of the methyl ether group (CH_3 -PEG chain) to the benzyl group of the co-initiator (Figure 4). The disagreement between the molecular weights determined by ^1H NMR end-group analysis (44 kDa for **5a**, 270 kDa for **5b**, and 3200 kDa for **5c**) and GPC might be due to the high error measuring the small signal in the ^1H NMR spectrum corresponding to the co-initiator (benzyl group). Besides, the average molecular weights measured by GPC are not accurate since linear PEG standards were used for calibration while the PEG-grafted polymers **5a–c** are brush polymers. The PEG-grafted PLAs have smaller hydrodynamic volumes than linear PEG standards, and consequently, the apparent molecular weight measured by GPC are smaller than that estimated by ^1H NMR spectroscopy. Hillmyer and co-workers have recently reported that the polymerization of aliphatic spirolactide derivatives affords polyesters with higher glass transition temperatures than

F

dx.doi.org/10.1021/ma2016387 | Macromolecules XXXX, XXX, 000–000

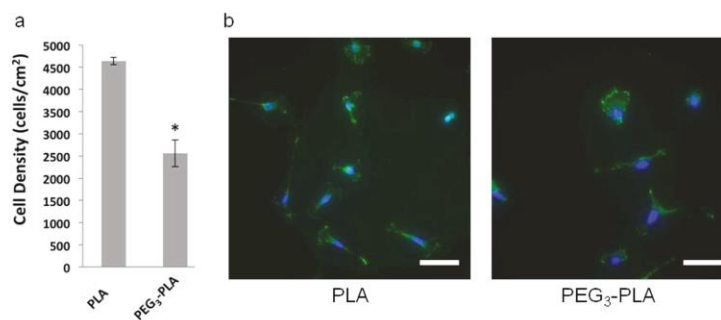


Figure 5. MC3T3-E1 cell adhesion and spreading on spin-coated polymer films. (a) Average density of adherent cells on polymer coatings. Error bars represent standard error of the mean. * $P < 0.01$ compared to PLA. (b) Representative images of adherent cells on polymer films with stained nuclei (DAPI, blue) and focal adhesion protein vinculin (vinc, green). Scale bars are 50 μm .

PLA ($T_g \sim 50^\circ\text{C}$).³⁰ In contrast, differential scanning calorimetry (DSC) measurements of PEG₃-PLA **5a** and PEG₇-PLA **5b**, which are oils at room temperature, did not show any transition between -10 and 100°C (Supporting Information). PEG₄₀-PLA **5c** showed a sharp transition around 50°C , which corresponds to its melting point. Thermogravimetric analysis (TGA) was used to evaluate the thermal stability of polymers **5a–c** (Supporting Information). The degradation of **5a** starts at 215°C , **5b** at 285°C , and **5c** at 332°C . Hence, the length of the PEG side chain slightly increases the thermal stability of PEG-grafted polymers.

Cell adhesion studies were performed in order to investigate the capability of the new PEG-grafted PLAs to reduce nonspecific protein adsorption and cell adhesion. Hence, MC3T3 $\times 10^{-1}$ cells were seeded in the presence of serum-containing media on PLA (control) and PEG₃-PLA films to examine initial cell adhesion responses. We only examined adhesion to the shorter PEG₃-PLA polymer because the longer PEG chain polymers (PEG₇-PLA and PEG₄₀-PLA) exhibited high water solubility and were rapidly lost from the surface in aqueous solutions. We note that the increased water solubility of the longer PEG chain polymers will be advantageous in future studies dealing with cross-linked scaffolds. The osteoblast-like cells adhered and spread on both PLA and PEG₃-PLA films, but clear differences between PEG-functionalized and control PLA can be seen in cell density and cell morphology. Figure 5a shows that the number of adhered cells was significantly decreased for the PEG-functionalized PLA compared to PLA. Although cells assembled vinculin-containing focal adhesions on both polymer films, differences in morphology were evident (Figure 5b). Cells on PLA were more spread and polarized with focal adhesions localized to the cell tips, whereas cells on PEG₃-PLA showed less spread cells. The differences in cell adhesion and spreading are likely due to differences in protein adsorption between the polymeric films due to the protein adsorption-resistant nature of PEG. The cell adhesion results demonstrate that the addition of PEG chains to PLA modulates biological responses to the base PLA. These results are consistent with previous reports demonstrating changes in cell adhesion following grafting of PEG. Future studies will examine cellular responses within PEG-functionalized PLA scaffolds.

CONCLUSIONS

In this contribution, we have presented a short and general approach to prepare PEG side-chain functionalized L-lactide monomers and their subsequent polymerization. The PEG-spirolactide-based monomers were prepared readily in four steps from commercially available L-lactide in good yields. The key step is the 1,3-dipolar cycloaddition between PEG-azides and the spiro-lactide–heptene precursor. The monomers were polymerized using TBD as organocatalyst yielding well-defined oligo-(ethylene glycol)-functionalized poly(lactic acid) with molecular weights above 10 kDa and polydispersity indices between 1.6 and 2.1. In the case of PEG₄₀-PLA, the measured PDI was 1.4, but the GPC analysis showed a bimodal profile indicating the presence of starting macromonomer despite purification by dialysis. Preliminary biological studies showed that PEG₃-grafted PLA reduces cell adhesion when compared to PLA.

ASSOCIATED CONTENT

Supporting Information. Detailed spectroscopic data and crystallographic data. This material is available free of charge via the Internet at <http://pubs.acs.org>.

AUTHOR INFORMATION

Corresponding Author

*E-mail: marcus.weck@nyu.edu (M.W.); andres.garcia@me.gatech.edu (A.J.G.).

ACKNOWLEDGMENT

Financial support has been provided by the National Institute of Health (SR01EB008069). The MALDI instrument was purchased with a grant from the National Science Foundation (CHE-0958457).

REFERENCES

- (1) Auras, R.; Lim, L.-T.; Selke, S. E. M.; Tsuji, H. *Poly(Lactic Acid): Synthesis, Structures, Properties, Processing, and Applications*; John Wiley & Sons, Inc.: Hoboken, NJ, 2010.
- (2) Becker, J. M.; Pounder, R. J.; Dove, A. P. *Macromol. Rapid Commun.* **2010**, *31*, 1923–1937.

G

dx.doi.org/10.1021/ma2016387 | Macromolecules XXXX, XXX, 000–000

- (3) Platel, R. H.; Hodgson, L. M.; Williams, C. K. *Polym. Rev.* **2008**, *48*, 11–63.
- (4) Pounder, R. J.; Dove, A. P. *Polym. Chem.* **2010**, *1*, 260–271.
- (5) Edlund, U.; Kallrot, M.; Albertsson, A.-C. *J. Am. Chem. Soc.* **2005**, *127*, 8865–8871.
- (6) Voegelé, N. J.; Baker, G. L.; Smith, M. R., III. *Polym. Prepr. (Am. Chem. Soc., Div. Polym. Chem.)* **2005**, *46*, 336.
- (7) Leemhuis, M.; van Nostrum, C. F.; Kruijtzter, J. A. W.; Zhong, Z. Y.; ten Breteler, M. R.; Dijkstra, P. J.; Feijen, J.; Hennink, W. E. *Macromolecules* **2006**, *39*, 3500–3508.
- (8) Cohen-Arazi, N.; Katzhendler, J.; Kolitz, M.; Domb, A. J. *Macromolecules* **2008**, *41*, 7259–7263.
- (9) Gerhardt, W. W.; Noga, D. E.; Hardcastle, K. L.; García, A. J.; Collard, D. M.; Weck, M. *Biomacromolecules* **2006**, *7*, 1735–1742.
- (10) Noga, D. E.; Petrie, T. A.; Kumar, A.; Weck, M.; García, A. J.; Collard, D. M. *Biomacromolecules* **2008**, *9*, 2056–2062.
- (11) Rubinshtein, M.; James, C. R.; Young, J. L.; Ma, Y. J.; Kobayashi, Y.; Gianneschi, N. C.; Yang, J. *Org. Lett.* **2010**, *12*, 3560–3563.
- (12) Wang, Y.; Noga, D. E.; Yoon, K.; Wojtowicz, A. M.; Lin, A. S. P.; García, A. J.; Collard, D. M.; Weck, M. *Adv. Funct. Mater.* **2008**, *18*, 3638–3644.
- (13) Heuberger, M.; Drobek, T.; Spencer, N. D. *Biophys. J.* **2005**, *88*, 495–504.
- (14) Subramani, K.; Birch, M. A. *Biomed. Mater.* **2006**, *1*, 144–154.
- (15) Hamamura, K.; Weng, Y.; Zhao, J.; Yokota, H.; Xie, D. *Biomed. Mater.* **2008**, *3*, 025017–025023.
- (16) Jiang, X.; Vogel, E. B.; Smith, M. R.; Baker, G. L. *Macromolecules* **2008**, *41*, 1937–1944.
- (17) Sant, S.; Nadeau, V.; Hildgen, P. *J. Controlled Release* **2005**, *107*, 203–214.
- (18) Jiang, X.; Milton, R.; Smith, M. R.; Baker, G. L. *Macromolecules* **2008**, *41*, 318–324.
- (19) García, A. J. *Biomaterials* **2005**, *26*, 7525–7529.
- (20) Jing, F.; Hillmyer, M. A. *J. Am. Chem. Soc.* **2008**, *130*, 13826–13827.
- (21) Dahl, R. S.; Finney, N. S. *J. Am. Chem. Soc.* **2004**, *126*, 8356–8357.
- (22) Bräse, S.; Friedrich, A.; Gartner, M.; Schröder, T. *Top. Heterocycl. Chem.* **2008**, *12*, 45–115.
- (23) Sasaki, T.; Eguchi, S.; Yamaguchi, M.; Esaki, T. *J. Org. Chem.* **1981**, *46*, 1800–1804.
- (24) Ouchi, M.; Inoue, Y.; Liu, Y.; Nagamune, S.; Nakamura, S.; Wada, K.; Hakushi, T. *Bull. Chem. Soc. Jpn.* **1990**, *63*, 1260–1262.
- (25) Saha, A.; Ramakrishnan, S. *Macromolecules* **2009**, *42*, 4956–4959.
- (26) Meier, M. A. R.; Schubert, U. S. *Rapid Commun. Mass Spectrom.* **2003**, *17*, 713–716.
- (27) APEX2 (version 2009.11-0). Program for Bruker CCD X-ray Diffractometer Control; Bruker AXS Inc.: Madison, WI, 2009.
- (28) Sheldrick, G. M. *SHELXTL, version 6.14. Program for solution and refinement of crystal structures*; Universität Göttingen: Göttingen, Germany, 2000.
- (29) Pratt, R. C.; Lohmeijer, B. G. G.; Long, D. A.; Waymouth, R. M.; Hedrick, J. L. *J. Am. Chem. Soc.* **2006**, *128*, 4556–4557.
- (30) Fiore, G. L.; Jing, F.; Young, J. V. G.; Cramer, C. J.; Hillmyer, M. A. *Polym. Chem.* **2010**, *1*, 870–877.
- (31) Göpferich, A.; Peter, S. J.; Lucke, A.; Lu, L.; Mikos, A. G. *J. Biomed. Mater. Res.* **1999**, *46*, 390–398.
- (32) Iguerb, O.; Poleunis, C.; Mazeas, F.; Compere, C.; Bertrand, P. *Langmuir* **2008**, *24*, 12272–12281.

Bone regeneration using an alpha 2 beta 1 integrin-specific hydrogel as a BMP-2 delivery vehicle. Biomaterials.

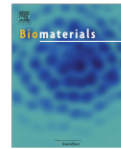
Biomaterials 35 (2014) 5453–5461



Contents lists available at ScienceDirect

Biomaterials

journal homepage: www.elsevier.com/locate/biomaterials



Bone regeneration using an alpha 2 beta 1 integrin-specific hydrogel as a BMP-2 delivery vehicle



Asha Shekaran^{a,b,1}, José R. García^{b,c}, Amy Y. Clark^{b,c}, Taylor E. Kavanaugh^a, Angela S. Lin^{b,c}, Robert E. Guldberg^{b,c}, Andrés J. García^{b,c,*}

^a Department of Biomedical Engineering, Georgia Institute of Technology and Emory University, 313 Ferst Drive, Atlanta, GA 30332, USA

^b Petit Institute for Bioengineering and Biosciences, Georgia Institute of Technology, 315 Ferst Drive, Atlanta, GA 30332, USA

^c School of Mechanical Engineering, Georgia Institute of Technology, 801 Ferst Drive, Atlanta, GA 30332, USA

ARTICLE INFO

Article history:

Received 23 January 2014

Accepted 21 March 2014

Available online 13 April 2014

Keywords:

Integrin-specific

Hydrogel

Polyethylene glycol

Bone healing

BMP-2

Protein delivery

ABSTRACT

Non-healing bone defects present tremendous socioeconomic costs. Although successful in some clinical settings, bone morphogenetic protein (BMP) therapies require supraphysiological dose delivery for bone repair, raising treatment costs and risks of complications. We engineered a protease-degradable poly(ethylene glycol) (PEG) synthetic hydrogel functionalized with a triple helical, $\alpha 2 \beta 1$ integrin-specific peptide (GFOGER) as a BMP-2 delivery vehicle. GFOGER-functionalized hydrogels lacking BMP-2 directed human stem cell differentiation and produced significant enhancements in bone repair within a critical-sized bone defect compared to RGD hydrogels or empty defects. GFOGER functionalization was crucial to the BMP-2-dependent healing response. Importantly, these engineered hydrogels outperformed the current clinical carrier in repairing non-healing bone defects at low BMP-2 doses. GFOGER hydrogels provided sustained *in vivo* release of encapsulated BMP-2, increased osteoprogenitor localization in the defect site, enhanced bone formation and induced defect bridging and mechanically robust healing at low BMP-2 doses which stimulated almost no bone regeneration when delivered from collagen sponges. These findings demonstrate that GFOGER hydrogels promote bone regeneration in challenging defects with low delivered BMP-2 doses and represent an effective delivery vehicle for protein therapeutics with translational potential.

© 2014 Elsevier Ltd. All rights reserved.

1. Introduction

Over 1 million bone grafting, bone excision and fracture repair surgeries are performed annually in the US at a cost of approximately \$5 billion [1–4]. While autografts are the gold-standard therapy for non-healing bone defects, these grafts are limited by low availability as well as donor site pain and inflammation [5]. More recently, bone morphogenetic protein (BMP) therapies have emerged as promising alternatives to autografts and allografts. While BMP therapy has been successful in stimulating bone repair, the BMP doses used clinically are orders of magnitude higher [6]

than physiological concentrations of BMP, resulting in high costs of treatment and complications such as ectopic bone formation, nerve injuries and inflammation [5,7–10]. Therefore, there is an unmet clinical need for improved BMP delivery vehicles which promote bone healing at low delivered BMP doses to enable safe, cost-effective and efficacious BMP treatments.

Hydrogels, water-swollen cross-linked polymer networks, offer tremendous advantages as vehicles for protein delivery due to their high cytocompatibility, low inflammatory profile, tailorable mechanics and biofunctionality, and injectable delivery method [11–13]. In particular, poly(ethylene glycol) (PEG) hydrogels are attractive because they resist non-specific protein adsorption, providing a 'clean-slate' background onto which desired biofunctionalities may be incorporated [14]. In addition, PEGs are widely used in FDA-approved therapeutic products as covalent modifiers of proteins and lipids [15], indicating a history of safety in patients. This has led to increasing research interest in delivering protein therapeutics such as BMP-2 and BMP-7 from synthetic and natural hydrogels to improve bone healing [16–19].

* Corresponding author. Petit Institute for Bioengineering and Biosciences, Georgia Institute of Technology, 315 Ferst Drive, Atlanta, GA 30332, USA.

E-mail address: andres.garcia@me.gatech.edu (A.J. García).

¹ Current address: Bioprocessing Technology Institute, 20 Biopolis Way, #06-01 Centros, Singapore 138668.

We have recently established PEG hydrogels cross-linked via maleimide groups as an alternative cross-linking chemistry to address limitations associated with other widely used PEG hydrogel polymerization chemistries such as free-radical polymerization [20]. The maleimide reactive group is extensively used in peptide bioconjugate chemistry because of its fast reaction kinetics and high specificity for thiols at physiological pH. Maleimide-based cross-linking of PEG hydrogels has significant advantages over other cross-linking chemistries, namely well-defined hydrogel structure, stoichiometric incorporation of bioligands, increased cytocompatibility, improved cross-linking efficiency, and reaction time scales appropriate for *in situ* gelation for *in vivo* applications [20]. Additionally, the base macromer exhibits minimal toxicity and inflammation *in vivo* and is rapidly excreted via the urine [21] – important considerations in establishing the safety and translational potential of these hydrogels.

A critical consideration in the design of protein delivery systems for regenerative medicine is the incorporation of extracellular matrix (ECM)-mimetic adhesive ligands. Many orthopedic biomaterials utilize ECM-inspired peptides which promote integrin–ECM interactions to direct desired host cell responses [16,22,23] as these interactions regulate cell survival, proliferation, migration and differentiation [24–26]. In particular, the interaction of $\alpha 2\beta 1$ integrin with collagen I is a crucial signal for osteoblastic differentiation and mineralization [27–32]. The hexapeptide sequence Gly–Phe–Hyp–Gly–Glu–Arg (GFOGER), residues 502–507 of the $\alpha 1(I)$ chain of type I collagen, serves as the major recognition site for $\alpha 2\beta 1$ integrin binding [33–35]. Our group has previously engineered a synthetic collagen I-mimetic GFOGER-containing peptide, GYGGGP(GPP)₃GFOGER(GPP)₃GPC, which recapitulates the triple helical structure of native collagen (Fig. S1) and binds $\alpha 2\beta 1$ integrin with high affinity and specificity [36]. GFOGER peptide coatings on plastic, titanium and poly(ϵ -caprolactone) support equivalent levels of $\alpha 2\beta 1$ integrin-mediated cell adhesion as native collagen I [36], promote osteoblastic differentiation *in vitro* [22,37], improve fixation of metal implants to rat cortices [22], and enhance bone healing in rat femur defects [38]. In contrast to the collagen I-mimetic GFOGER peptide, the widely used bioadhesive RGD peptides bind primarily to the $\alpha v\beta 3$ integrin and do not have intrinsic osteogenic properties [39–41].

We hypothesized that presentation of the pro-osteogenic $\alpha 2\beta 1$ integrin-specific GFOGER peptide to host cells combined with sustained release of low doses of BMP-2 would direct endogenous stem cell differentiation *in vivo* and promote bone healing. Therefore, we synthesized matrix metalloproteinase (MMP)-degradable PEG-maleimide hydrogels functionalized with GFOGER and incorporating recombinant human BMP-2. In order to test this hypothesis, we implanted protease-degradable GFOGER-modified PEG hydrogel BMP-2 carriers within critical-sized, non-healing murine radial bone defects in order to evaluate their effects on bone regeneration.

2. Materials and methods

2.1. GFOGER-modified PEG hydrogel synthesis

GFOGER peptide, GYGGGP(GPP)₃GFOGER(GPP)₃GPC (Activotec), four-arm, maleimide-end functionalized (>95%) PEG macromer (PEG-MAL, 20 kDa, Laysan Bio), GRGDSPC (RGD adhesive peptide), and GCRDVPMSMRGGDRCG (VPM) cross-linker peptide (AAPTEC), and rhBMP-2 (R&D Biosystems) were used. PEG-MAL hydrogels (4% wt/v) were synthesized by reacting PEG-MAL with adhesive peptides (RGD or GFOGER) followed by mixing in BMP-2 and VPM cross-linker at a volume ratio of 2:1:1 at the required concentrations to obtain the desired final concentrations of the adhesive peptide (0.5–2.0 mM) and BMP-2 (0.03, 0.06 or 0.3 μ g per 1.5 μ L hydrogel implant). The concentration of VPM used for the synthesis of each hydrogel was calculated to match the number of cysteine residues on the peptide cross-linker with the number of free (unreacted) maleimide groups remaining in the adhesive peptide-functionalized PEG-maleimide solution. The mixture of peptide-functionalized PEG-maleimide, BMP-2 and VPM cross-linker was

incubated at 37 °C for 2–6 h to allow for cross-linking before adding PBS to the hydrogels. For *in vitro* studies, thin gel discs were fabricated by covering polymerizing gel solutions with sterile Sigmacote-treated coverslips. For *in vivo* studies, hydrogel (1.5 μ L) was cast within 4-mm long polyimide tube sleeves with laser machined 200 μ m diameter holes to improve nutrient transport and cell invasion into the defect. All hydrogels used for *in vivo* studies contained 4% (wt/v) PEG-maleimide and 2.0 mM adhesive peptide. Collagen sponges were cut with a 1 mm diameter biopsy sponge and placed within the polyimide sleeves, injected with a BMP-2 solution at an equivalent dose as was loaded in the GFOGER hydrogels and incubated for 10 min at room temperature to allow for adsorption to the collagen sponge prior to implantation.

2.2. *In vitro* assays

hMSCs (Lonza) were cultured in MSCGM (Lonza) and seeded (10,000 cells/cm²) on hydrogel surfaces. Cells were cultured for up to 21 days in osteogenic media (Lonza). After 3 days of culture in osteogenic media, cells were incubated in 2 μ M calcein and 4 μ M ethidium homodimer for 30 min for Live/Dead staining and imaged on a Zeiss fluorescence microscope. At 14 days hMSCs were lysed and assayed for alkaline phosphatase activity (ALP) by incubating with MUP substrate. hMSCs were scraped in PBS, transferred to cold 50 mM Tris–HCl and sonicated to lyse the cells. The total protein content for each lysate sample was determined using a BCA assay kit (Thermo Scientific). Samples were diluted to the same total protein content before assaying for ALP. Samples and ALP standards were loaded into a 96-well plate, then incubated with MUP substrate at 37 °C for 1 h and read at 360 nm excitation/465 nm emission. Mineral deposition at 21 days post-induction was assayed by Alizarin Red staining and extraction. Cells were fixed in 10% formalin, rinsed in water and incubated in 2% Alizarin Red solution for 20 min. After 4 washes in water, the stained cells were scraped in 10% acetic acid and heated to 85 °C for 10 min. The supernatant was collected after centrifugation, neutralized with 10% ammonium hydroxide and read at 405 nm.

2.3. Radial defect surgery

All animal experiments were performed with the approval of the Georgia Tech Animal Care and Use Committee with veterinary supervision and within the guidelines of the Guide for the Care and Use of Laboratory Animals. B6129SF2/J wild-type male mice (8–10 week old, Jackson Laboratories) were anesthetized under isoflurane, and fur was removed from the right forelimb. The forelimb was then swabbed with chlorhexidine and alcohol and a 1.5-cm incision was made in the skin. Muscle tissue overlying the ulna and radius were bluntly dissected, and 2.5 mm defects were made in the right radius using a custom-machined bone cutter, while leaving the ulna intact. Hydrogel or collagen sponge placed within polyimide sleeves were implanted into the defect by fitting the sleeve over the radius at the proximal and distal ends of the defect, so that the hydrogel or collagen sponge filled the defect space. The incision was then closed with vicryl suture and wound clips. Mice were provided with a single dose of slow-release buprenorphine for pain relief and were monitored post-surgery for signs of distress, normal eating habits and movement.

2.4. BMP-2, GFOGER *in vivo* retention

GFOGER and BMP-2 were labeled with Vivotag 680 and Vivotag 800 IR dyes, respectively. Labeled GFOGER and BMP-2 were incorporated into PEG hydrogels and implanted into mice as described earlier. GFOGER peptide and BMP-2 retention within the defect site ($n = 6$) was analyzed by scanning mouse forelimbs (FMT 4000) on the 680 or 790 laser channels (Perkin Elmer, 1 mm source density, 65 source points per scan). The signal was quantified by placing 3D regions of interest markers around the forelimb, using a 0.0 nM IR dye threshold and normalizing to the day 0 value.

2.5. Faxitron/ μ CT imaging and mechanical testing

Radial defects were imaged with the MX-20 Radiography System (Faxitron, 23 kV energy setting, 15 s scan time). For μ CT scanning, a 3.2 mm length of the radius centered around the 2.5 mm radial defects was scanned in anesthetized, live subjects using a VivaCT system (Scanco Medical, 145 μ A intensity, 55 kVp energy, 200 ms integration time, and 15 μ m resolution). Bone formation was evaluated by contouring 2D slices to include only the radius and applying a Gaussian filter (sigma = 1, support = 1, threshold = 540 mg HA/ccm). 3D μ CT reconstructions display the full 3.2 mm length of radius scanned. However, in order to ensure that only new bone formation was measured, quantification of bone volume and mineral density within the defect was performed by evaluating only the middle 2.0 mm of defect.

Torsion to failure testing was performed on 8-week radial defects ($n = 5–9$) as described [42] with modifications. The radii and ulnae were excised post-euthanasia, wrapped in PBS-soaked gauze and stored at –20 °C. On the day of testing, the bones were thawed and potted in woods–metal within potting blocks. After the ulna was cut, the potting blocks were tested using a Bose Electroforce ELF 3200 system. The radius was torqued to failure at a rate of 3° per second and the torque was measured using a 0.07 N·m torque sensor (Transducer Techniques) (Fig. S3).

2.6. Histology and stem cell recruitment

For histology, bones were fixed in 10% neutral-buffered saline, decalcified and embedded in Immunobond or MMA. Sections (2 μm thick) were deplasticized and stained with Safranin-O/Fast Green. To quantify osteoprogenitor cell recruitment, radii were excised 7 days post-surgery. Cells were harvested by a 45 min collagenase I incubation of tissue and stained with anti-CD45 (FITC) and anti-CD 90 (APC) antibodies (Biolegend) and analyzed by flow cytometry (Accuri C6 cytometer, Flowjo software) to determine the proportion CD45⁺/CD90⁺ cells in the defect.

2.7. Statistical analyses

Error bars graphs represent SEM. Statistical comparisons between multiple groups were made by one-way ANOVA with post-hoc Tukey tests for parametric data, by Kruskal Wallis test with Dunn's post-hoc test for non-parametric data (bridging scores), and by t-test for comparisons of two groups in Graphpad. A *p* value of <0.05 was considered significant.

3. Results

3.1. Synthesis of GFOGER/BMP-2 hydrogels

We synthesized MMP-degradable, GFOGER-functionalized hydrogels with encapsulated BMP-2 in a facile two-step reaction (Fig. 1). The terminal maleimide groups on the 4-armed PEG macromer (Fig. 1A and B) underwent a Michael addition reaction with free sulfhydryl groups on the cysteine residues of the GFOGER peptide, resulting in a GFOGER-tethered PEG-maleimide precursor (Fig. 1B). The subsequent reaction of the GFOGER-functionalized PEG-maleimide macromer with a bi-cysteine cross-linking peptide (VPM) [43,44], containing an MMP cleavage site, resulted in the formation of an insoluble cross-linked PEG hydrogel network (Fig. 1B). In this modular system, BMP-2 can be incorporated into the hydrogel by physical entrapment during network cross-linking. In the presence of cell-secreted proteases, the VPM cross-linker is cleaved, disrupting the PEG network and releasing the entrapped BMP-2 (Fig. 1B). We chose a peptide cross-linker which undergoes rapid degradation in response to MMP in order to tailor the *in vivo* degradation rate of the PEG hydrogels to obtain a half-life of 1–2 weeks. To determine the efficiency at which GFOGER ligand was covalently tethered to PEG-maleimide, we measured the free sulfhydryl groups in reaction mixtures of GFOGER and PEG-maleimide at varying maleimide:GFOGER molar ratios. At a molar ratio higher than 5, ~100% of added GFOGER was tethered to PEG-maleimide

(Fig. S2), providing precise control of GFOGER density within the hydrogel.

3.2. *In vitro* cell activities on engineered hydrogels

We first evaluated the potential of GFOGER-functionalized PEG hydrogels to direct osteoblastic differentiation in human mesenchymal stem cells (hMSCs). GFOGER-functionalized hydrogels were compared to hydrogels modified with RGD peptides as RGD is the most commonly used adhesive peptide in the biomaterials field. We tested the levels of *in vitro* osteoblastic differentiation of hMSCs cultured on hydrogel surfaces. GFOGER- and RGD-functionalized hydrogels supported dose-dependent levels of hMSC adhesion and spreading (Fig. 2A), while significantly fewer cells adhered to PEG-only (no ligand) gels or scrambled RGD peptide-modified gels and these cells remained rounded (Fig. 2A). hMSCs exhibited high viability on both GFOGER- and RGD-tethered hydrogels at 3 days in culture (Fig. 2B). Despite comparable levels of adhesion and viability on GFOGER- and RGD-functionalized gels, hMSCs on GFOGER-functionalized hydrogels exhibited 94% and 40% increases in alkaline phosphatase activity and Alizarin Red staining, respectively, compared to RGD-presenting gels (Fig. 2C).

3.3. Repair of non-healing bone defects

We evaluated the potential of GFOGER-functionalized hydrogels to promote bone repair in a murine non-healing radial bone defect model [45]. If left untreated, this critical-sized defect does not heal over the experimental period and provides a stringent bone repair model analogous to non-healing, long bone defects in humans. To improve the ease of handling, we pre-cast hydrogels within polyimide tube sleeves. The sleeve walls were laser machined with holes to improve nutrient transport and cell migration across the sleeve walls as including perforations within a mesh sleeve surrounding a BMP-containing hydrogel has been shown to improve healing outcomes [46]. We implanted hydrogel constructs into 2.5 mm-long unilateral murine radial critical-sized defects (Fig. 2D) and evaluated bone healing by radiography and micro-computed tomography (μCT) at 4 and 8 weeks post-surgery. Defects treated with GFOGER-functionalized hydrogels exhibited significantly improved bone healing compared to those treated with no

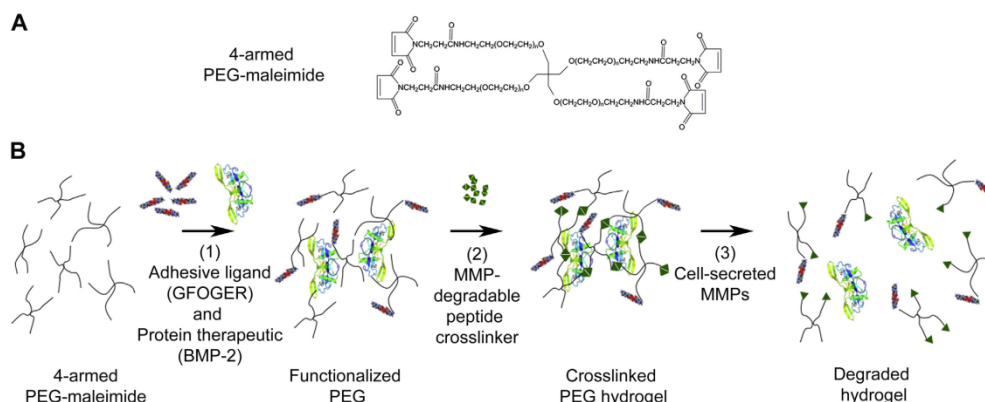


Fig. 1. Protease-degradable integrin-specific GFOGER-modified PEG hydrogels are synthesized with precise control of GFOGER density. (A) Chemical structure of branched 4-armed PEG-maleimide. (B) Synthesis of GFOGER- and BMP-2-functionalized hydrogels.

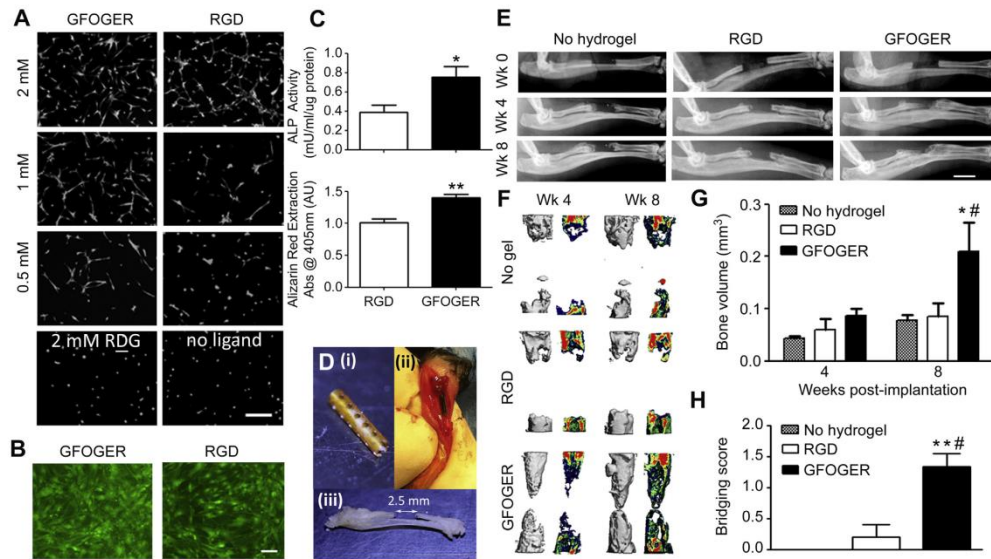


Fig. 2. GFOGER-functionalized hydrogels promote differentiation and bone healing. (A) Calcein-stained hMSCs on GFOGER- and RGD-tethered gels at varying densities of ligand and non-adhesive controls 1 day after seeding, scale bar 50 μ m, $n = 3$. (B) Live/dead stained hMSCs on 2.0 mM GFOGER- and 2.0 mM RGD-presenting hydrogels 3 days after osteogenic induction, scale bar 20 μ m, $n = 3$. (C) ALP activity at 14 days, $n = 4$ (top) and Alizarin Red stain for mineralization of hMSCs at 21 days, $n = 4$ (bottom). Hydrogels were pre-cast in a polyimide sleeve with 200 μ m diameter holes along tube walls. (D) Pictures indicate (i) a polyimide tube sleeve, (ii) radial defect with hydrogel-sleeve implant, hydrogel stained blue, and (iii) excised radius and ulna with 2.5 mm radial defect (iii). (E) Radiographic images of radial defects treated with hydrogel, scale bar 2 mm. (F) 3D μ CT reconstructions (left) and mineral density mappings on sagittal sections of the defects (right), scale bar 1 mm, $n = 5-6$. (G) μ CT measures of bone volume within defects, $n = 5-6$. (H) Bridging scores for defects receiving implants containing no hydrogel, or hydrogels functionalized with RGD or GFOGER, $n = 5-6$, 0: < half bridged, 1: > half bridged, and 2: completely bridged – 8 weeks post-surgery. * $p < 0.05$, ** $p < 0.01$ compared to RGD, # $p < 0.05$, ## $p < 0.01$ compared to No hydrogel.

hydrogel (defects received an empty polyimide sleeve implant) and RGD-modified gel implants (Fig. 2E–H). Bone volume at 8 weeks for defects treated with GFOGER-functionalized gel was 140% and 150% higher than no hydrogel and RGD-presenting gel-treated defects, respectively (Fig. 2FG). There was no difference in bone volume between RGD-modified gels and empty defects. Furthermore, while minimal bone formation and no defect bridging was observed in all subjects treated with RGD-functionalized gel and empty defect controls, several defects treated with GFOGER-functionalized hydrogels were close to full bridging after 8 weeks (Fig. 2E–F). We scored the degree to which defects were bridged 8 weeks after implantation according to the following criteria: 0 – defect is less than half bridged, 1 – defect is more than half bridged, and 2 – defect is fully bridged. Bridging scores for GFOGER-functionalized hydrogels were higher than RGD-presenting gels and empty defects (Fig. 2H). These results demonstrate that $\alpha 2 \beta 1$ integrin-specific GFOGER-functionalized hydrogels promote hMSC osteogenic differentiation and enhance bone repair compared to conventional RGD-tethered gels or treatment with no hydrogel.

3.4. Dose response of BMP-2 in hydrogels in bone repair

Because GFOGER-modified PEG hydrogels supported great enhancements in bone healing, we explored whether combining GFOGER gels with low doses of BMP-2 could yield further improvements in bone healing and bridge critical-sized segmental defects. Five groups were tested: implants containing no hydrogel (empty sleeve) as a negative control and GFOGER-functionalized

hydrogels lacking BMP-2 (0 μ g) or incorporating increasing BMP-2 doses (0.03, 0.06 and 0.3 μ g, referred to as low, medium and high doses respectively). There was minimal bone healing in defects treated with no hydrogel and high levels of bone formation and almost complete bridging with treatment with GFOGER-functionalized hydrogels without BMP-2 (Fig. 3A–D). For the medium and high BMP-2 doses, defect bridging was observed by week 4 (Fig. 3B(i)), and for all BMP-2 doses, bone volumes were increased compared to no hydrogel implants, and bridging occurred by week 8 (Fig. 3A–C). Even within defects treated with the low BMP-2 dose, bone volume was 200% higher than defects which received no hydrogel (Fig. 3C). Treatment with all GFOGER-functionalized hydrogels including those lacking BMP-2 resulted in increased bridging scores compared to the no hydrogel treatment (Fig. 3D). Histological analysis revealed that PEG hydrogels were completely degraded by week 8, facilitating cell invasion into the defects (Fig. 3E). In addition, non-woven bone containing marrow compartments was formed in defects treated with GFOGER-functionalized hydrogels but not in the no hydrogel group (Fig. 3E). Importantly, low dose BMP-2 treatment within GFOGER-functionalized hydrogels induced bone defect bridging after 8 weeks without any structural change to the adjacent ulna (Fig. 3B(ii)). In mice receiving implants with the medium and high BMP-2 doses, radial defect bridging also occurred, but was accompanied by unintended alterations to the ulna (Fig. 3B(ii)). Treatment with medium dose BMP-2 resulted in expansion of the ulna around the radius, while for the high dose BMP-2 group, the ulna completely encircled the radius and fused with the radius

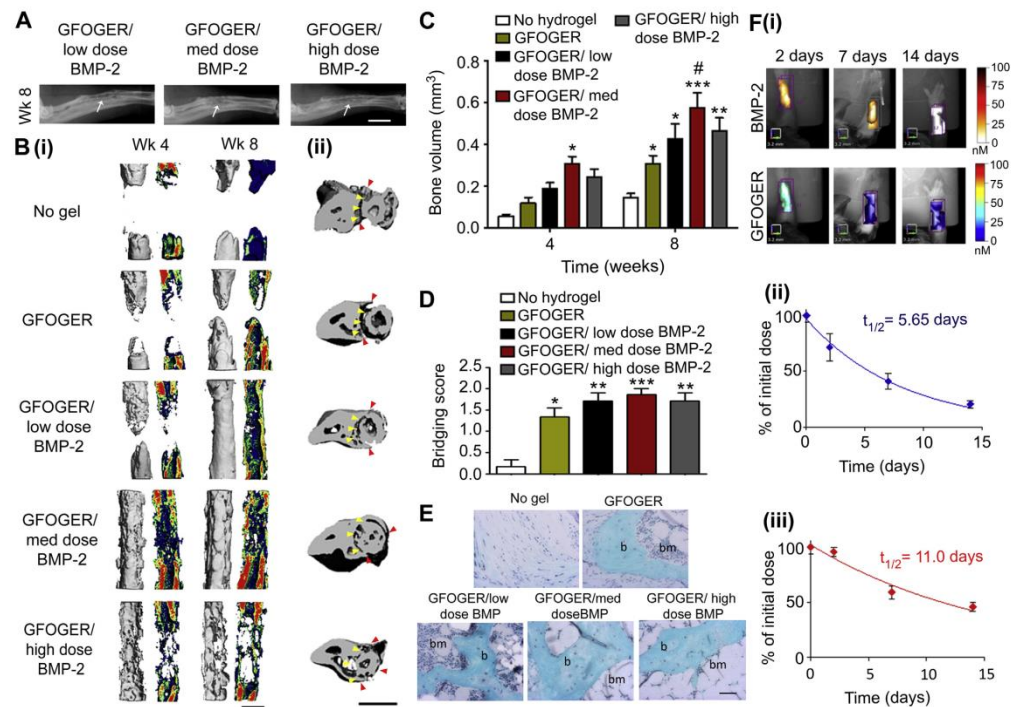


Fig. 3. GFOGER-functionalized PEG hydrogels with low dose BMP-2 bridge radial segmental defects without altering ulnar structure. (A) Radiographic images, white arrows indicate space between ulna and radius which is not present in the high BMP-2 dose image, scale bar 2 mm. (B) 3D μ CT reconstructions of (i) radius in sagittal view (left) with mineral density mapping (right), and (ii) radius and ulna in transverse view. Yellow arrowheads indicate boundary between the ulna and radius prior to implantation, red arrowheads indicate the position of the ulna closest to the radius at 8 weeks, scale bar 1 mm. (C) μ CT measures of bone formation, $n = 6-7$. (D) Scoring of defect bridging at 8 weeks, $n = 6-7$. (E) Sections stained with Safranin-O/Alizarin Red at the center of defect, scale bar 50 μ m; b – bone, bm – bone marrow. (F) (i) Representative FMT images and FMT quantification of % implanted dose retained in radial defect space over time *in vivo* for (ii) high dose BMP-2 labeled with Vivotag 800 and (iii) GFOGER peptide labeled with Vivotag 680, $n = 6$. * $p < 0.05$, ** $p < 0.01$, *** $p < 0.001$ compared to defect receiving no hydrogel implant, * $p < 0.05$ compared to GFOGER hydrogel. (For interpretation of the references to color in this figure legend, the reader is referred to the web version of this article.)

(Fig. 3B(ii)). These results highlight the adverse effects of excessive BMP-2 delivery, recapitulating off-target clinical results in humans [47], and underscore the importance of precise control of the dose and release mechanism of BMP-2.

Because BMP-2 release kinetics as well as scaffold degradation and cell invasion are important factors which contribute to tissue healing in response to implantable biomaterials, we examined the retention times of near infrared (IR) dye-labeled GFOGER peptide and BMP-2 in PEG hydrogels within the radial defect site using fluorescence molecular tomography (FMT). BMP-2 was localized within the defect site over a prolonged period of time (Fig. 3F). The half-life for BMP-2 was 5.65 days and more than 20% of the initial BMP-2 dose remained 14 days after surgery, indicating sustained release of BMP-2 from GFOGER hydrogels *in vivo* (Fig. 3F(ii)). The half-life of GFOGER peptide within the defect site was considerably longer than BMP-2 at 11.0 days and is an indication of the retention time of the bulk PEG polymer to which the peptide was tethered (Fig. 3D (iii)). This result confirms our targeted *in vivo* hydrogel degradation rate of 1–2 week half-life using the MMP-cleavable VPM cross-linker. Because GFOGER-functionalized hydrogels incorporating low dose BMP-2 supported localized bone formation

and bridging within the radial defect without inducing any off-target alterations to bone volume or structure in the ulna, we used GFOGER gels with low BMP-2 dose (GFOGER/low BMP-2) delivery in subsequent analyses.

3.5. Contributions of GFOGER and BMP-2 to bone healing

A major advantage of the PEG-maleimide hydrogel platform is the ability to independently control its modular components to examine their relative contributions to tissue repair. We therefore systematically tested combinations of implants containing GFOGER peptide, low BMP-2 dose, or the combination of both. Four groups were tested (Fig. 4A): GFOGER/low BMP-2 (PEG/GFOGER/BMP-2), GFOGER/no BMP-2 (PEG/GFOGER), no ligand/low dose BMP-2 (PEG/BMP-2), and no ligand/no BMP-2 (PEG). GFOGER/low BMP-2 hydrogels supported robust healing and defect bridging within 8 weeks, while GFOGER/no BMP-2 gels induced significant bone formation and almost complete bridging (Fig. 4B–D, Fig. S2). GFOGER/low BMP-2 gels displayed enhancements in bone volume, defect bridging and maximum torque compared to groups lacking GFOGER (Fig. 4B–E). BMP-containing implants that lacked GFOGER

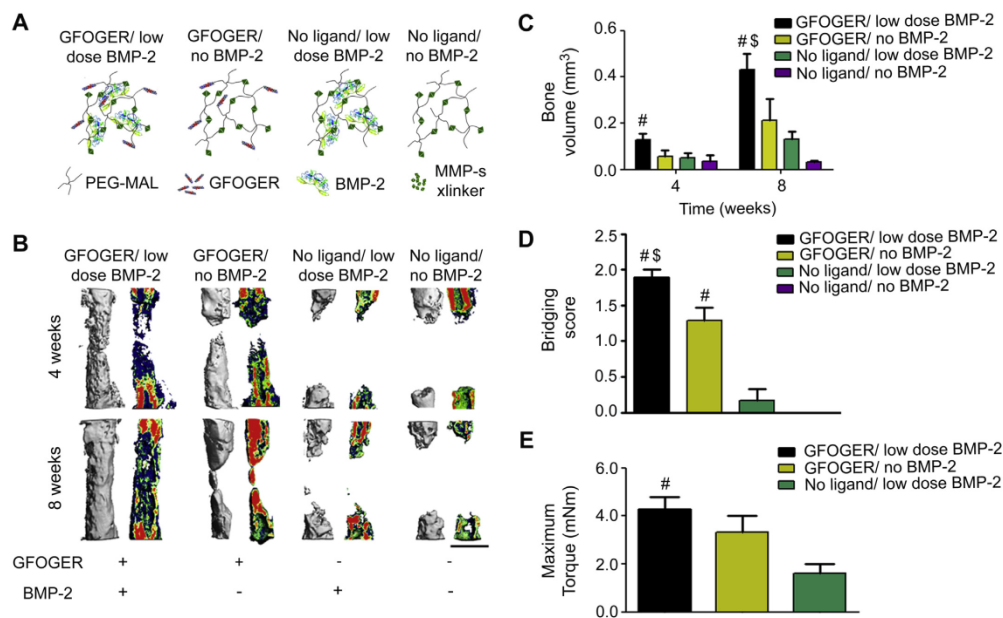


Fig. 4. GFOGER ligand is crucial to and BMP-2 improves bone healing in response to engineered hydrogel. (A) Cartoon of hydrogel formulations tested in this study, MMP x-linker – MMP-sensitive cross-linker. (B) 3D μ CT reconstructions (left) and mineral density mappings on sagittal sections of the same defects (right), scale bar 1 mm. (C) μ CT measures of bone formation at 4 and 8 weeks post-surgery. (D) Bridging scores for defects 8 weeks post-surgery. (E) Maximum torque values for radial samples 8 weeks after surgery. * $p < 0.05$ compared to No ligand/no BMP-2 gels, # $p < 0.05$ compared to No ligand/low dose BMP-2 gels. $n = 5$ for No ligand/no BMP-2 and $n = 6-7$ for other groups.

(no ligand/low dose BMP-2) gels supported no defect bridging and exhibited ~70% lower bone volume than GFOGER/low dose BMP-2 gels and 30% less bone volume than GFOGER/no BMP-2 gels (Fig. 4C), indicating that the GFOGER peptide is critical to the bone repair activity of the engineered hydrogel. Taken together, these results demonstrate that GFOGER is critical to bone repair and BMP-2 further enhances the osteoreparative properties of these hydrogels.

3.6. Bone repair and osteoprogenitor recruitment compared to the standard carrier

In current clinical practice, BMP-2 is delivered by injecting a BMP-2 solution into collagen foams prior to implantation. Therefore, in order to compare our engineered biomaterial to the clinical standard, we examined the role of the delivery vehicle on bone formation in response to 0.03 μ g BMP-2 dose, the lowest dose tested in the dose response study. Two groups were compared: GFOGER hydrogels and collagen sponges loaded with 0.03 μ g BMP-2. μ CT evaluation of bone volume within defects revealed that GFOGER/BMP-2 hydrogel implants improved bone healing compared to collagen sponge/BMP-2 implants by 200% and >300% at 4 and 8 weeks, respectively (Fig. 5A and B). Defects treated with GFOGER/BMP-2 hydrogels bridged consistently, whereas collagen sponge/BMP-2 treated defects exhibited minimal bone healing (Fig. 5A and B) with no bridging (Fig. 5C). Importantly, GFOGER/BMP-2 treated defects were mechanically robust and showed a 100% increase in maximum torque at 8 weeks compared to defects treated with collagen sponge/BMP-2 (Fig. 5D). Notably, the

maximum torque levels for the defects treated with GFOGER/BMP-2 were equivalent to the maximum torque of intact radii (3.2 ± 0.3 mNm), demonstrating that the quality of the repair tissue is similar to native bone. Histological analysis at 8 weeks showed fibrous tissue with almost no bone tissue formation for collagen sponge/BMP-2, whereas defects treated with GFOGER/BMP-2 hydrogels exhibited abundant bone formation as well as establishment of bone marrow in the center of the defect (Fig. 5E). Both the collagen sponge and PEG hydrogel were fully degraded by 8 weeks after implantation (Fig. 5E).

Because BMP-2 release kinetics greatly impact bone healing, we compared the release rates of BMP-2 from GFOGER gels and collagen sponges in the bone defect using Vivotag 800-labeled BMP-2. GFOGER-functionalized hydrogels exhibited 30% higher levels of BMP-2 retained within the radial defect space at 1 day and 90% higher levels at 5 days post-implantation compared to the collagen sponge (Fig. 5F) by fluorescence molecular tomography. Because BMP-2 is known to have chemotactic effects on mesenchymal stem cells and osteoprogenitor cells [48], we evaluated the recruitment of CD45⁺/CD90⁺ osteoprogenitor stem cells to the defect site following the implantation of GFOGER/BMP-2 hydrogels or collagen sponge/BMP-2 (Fig. 5G). At 7 days post-implantation, there was a 300% increase in CD45⁺/CD90⁺ cells in defects treated with GFOGER/BMP-2 gels compared to collagen/BMP-2 (Fig. 5G). These results demonstrate that GFOGER-functionalized PEG hydrogels delivering BMP-2 outperform the current clinical standard delivery vehicle in terms of bone repair and provide sustained release of BMP-2 and enhanced osteoprogenitor stem cell recruitment.

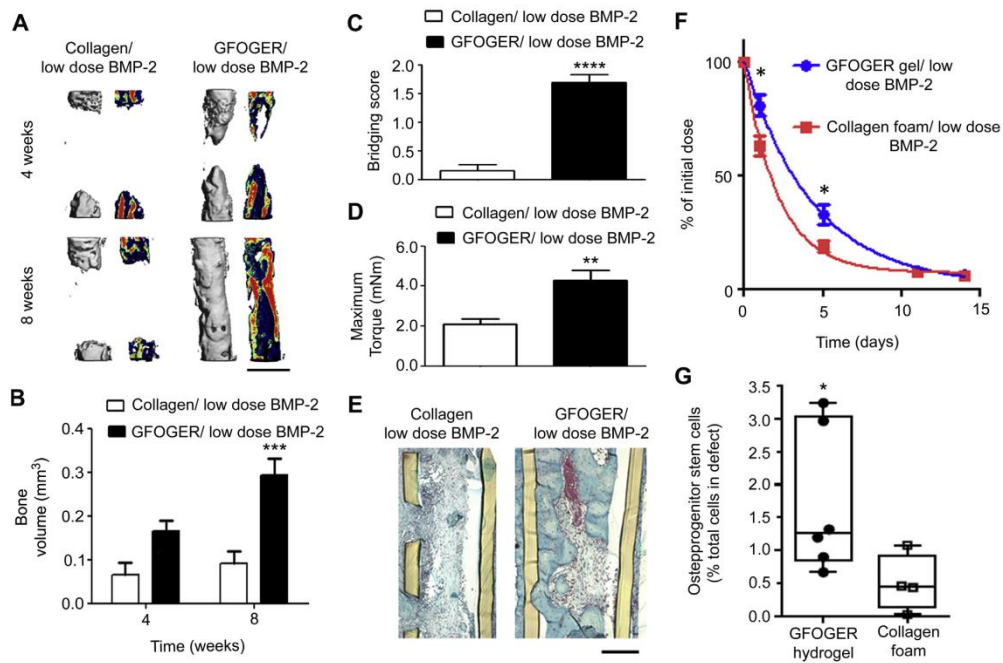


Fig. 5. BMP-2 delivery from GFOGER-functionalized gels improves bone regeneration compared to collagen foams. (A) 3D μ CT reconstructions of radii (left) and mineral density sagittal sections (right), scale bar 1 mm. (B) μ CT measures of bone volume in radial defects. (C) Bridging score at 8 weeks post-implantation $n = 13$. (D) Maximum torque values for 8 week radial samples subjected to torsion mechanical testing to failure $n = 5-9$. (E) Sections of 8 week radial samples stained with Safranin-O/Fast Green, scale bar 200 μ m. (F) Retention of infrared dye-labeled BMP-2 at implanted defect site *in vivo* $n = 6$. (G) Quantification of CD45⁺/CD90⁺ osteoprogenitor cells present in defect 7 days post-implantation, $n = 4-6$. * $p < 0.05$, *** $p < 0.001$ and **** $p < 0.0001$ compared to Collagen foam/low dose BMP-2.

4. Discussion

Bone grafts are widely used in clinical practice for spinal, foot and ankle fusions, revision arthroplasties, and treating large, non-healing bone defects. Because the gold-standard autograft treatments cause donor pain and are in limited supply [5] and processed allografts exhibit limited bioactivity or risks of infection [2,5,49,50], protein therapeutics are becoming extensively used in the clinic. However, BMP treatments present cost limitations [7] and clinical safety concerns [5,8–10], primarily because suboptimal growth factor carriers require BMP-2 to be delivered at supraphysiological doses. Therefore, there is a strong motivation to engineer protein therapeutic delivery systems which offer greater safety and cost-effectiveness by reducing the therapeutic dose of growth factors required for healing of critical-sized bone defects.

Here, we engineered a hydrogel carrier functionalized with a collagen-mimetic, triple helical, integrin-specific peptide (GFOGER) which significantly enhanced bone healing compared to collagen sponges, the current clinical BMP-2 carrier. GFOGER-modified gels incorporating low doses of BMP-2 promoted osteoprogenitor cell recruitment to the defect site and produced robust repair and bridging of segmental bone defects within 8 weeks. Importantly, the repair tissue had equivalent mechanical strength to native bone. Furthermore, this result was achieved with GFOGER gels loaded with a low dose of BMP-2 which supported almost no bone

formation within clinical standard collagen foam vehicles. These results show that GFOGER gels produce superior healing outcomes compared to current carriers for protein therapeutics. Follow-up studies with large animal models are required to fully establish the translational potential of these delivery vehicles.

The improved healing induced by the GFOGER-tethered PEG gels compared to collagen foams can be attributed to a combination of factors. First, in contrast to collagen foams [51], GFOGER-functionalized materials enhance bone formation without cell or protein co-delivery due to the intrinsic osteogenic bioactivity of the $\alpha 2 \beta 1$ integrin-specific GFOGER peptide. Simple presentation of GFOGER within the hydrogel significantly enhanced bone formation, outperforming other adhesive peptides such as RGD. Second, GFOGER gels provided sustained release of encapsulated BMP-2 compared to the clinical collagen sponge carrier. This improvement in BMP-2 release kinetics from GFOGER gels is due to effective entrapment of BMP-2 within the tightly cross-linked hydrogel network and MMP-dependent gel degradation. In contrast, collagen foams have large micron-scale pores and release BMP-2 through protein desorption from scaffold surfaces, diffusion of BMP-2 from solution trapped in the pores, and collagenase-mediated degradation of the foams. Third, GFOGER-functionalized hydrogels support rapid MMP-mediated hydrogel degradation and cell invasion that allows for replacement of the carrier with repair tissue. Indeed, we demonstrated a 3-fold enhancement in

the recruitment of osteoprogenitor cells for GFOGER gels compared to collagen sponges.

The $\alpha 2 \beta 1$ integrin-specific PEG hydrogel BMP-2 carrier described in this study has potential for clinical translation because it demonstrates superior bone healing compared to the commonly used adhesive RGD peptide and collagen sponges and is a purely synthetic, well tolerated, and tunable system. GFOGER gels supported 150% more bone formation than RGD gels. Notably, the well-defined, synthetic nature of the GFOGER-functionalized PEG hydrogel carrier makes it amenable to scale-up in production and well-regulated quality control. Furthermore, the modularity of the PEG-maleimide hydrogels allows key properties such as degradation rate as well as the density or combinations of adhesive ligands and therapeutic proteins to be tuned to optimize or adapt the material for other applications.

5. Conclusion

This study highlights the bone regeneration potential of a synthetic PEG-maleimide hydrogel functionalized with the $\alpha 2 \beta 1$ integrin-specific GFOGER peptide as a BMP-2 carrier. GFOGER-functionalized hydrogels displayed intrinsic osteogenic activity, provided sustained release of BMP-2, underwent rapid degradation *in vivo*, bridged critical-sized bone defects at low BMP-2 doses, and exhibited improved bone repair compared to the collagen foams which are the clinical standard carriers. These findings underscore the effectiveness of targeting pro-osteogenic integrins to enhance bone regeneration and establish the GFOGER-modified PEG-maleimide hydrogel as an effective BMP-2 delivery vehicle with significant translational potential.

Author contributions

A.S. and A.J.G. designed all experiments. A.S., T.E.K., J.R.G. and A.Y.C. performed research and performed data analysis. A.S.L. and R.E.G. provided critical input on μ CT and mechanical testing. A.S. and A.J.G. wrote the paper and all co-authors edited the manuscript.

Acknowledgments

We thank Ningtao Cheng for his assistance with mechanical testing and Aby Thyparambil and Robert Latour at Clemson University for CD analysis. The facilities at Clemson University were supported by NIH Grants 5P20RR021949 and 8P20GM103444. This work was funded by the National Institutes of Health (_100000002), USA (R01 AR062920, R01 AR062368). A.S. was supported by the Singaporean Agency for Science, Technology and Research (_501100001348).

Appendix A. Supplementary data

Supplementary data related to this article can be found at <http://dx.doi.org/10.1016/j.biomaterials.2014.03.055>.

References

- [1] Bucholz RW. Nonallograft osteoconductive bone graft substitutes. *Clin Orthop Relat Res* 2002;395:44–52.
- [2] Finkemeier CG. Bone-grafting and bone-graft substitutes. *J Bone Joint Surg Am* 2002;84-A(3):454–64.
- [3] Giannoudis PV, Dinopoulos H, Tsiridis E. Bone substitutes: an update. *Injury* 2005;36(Suppl. 3):S20–7.
- [4] Kretlow JD, Mikos AG. Review: mineralization of synthetic polymer scaffolds for bone tissue engineering. *Tissue Eng* 2007;13(5):927–38.
- [5] De Long Jr WG, Einhorn TA, Koval K, McKee M, Smith W, Sanders R, et al. Bone grafts and bone graft substitutes in orthopaedic trauma surgery. A critical analysis. *J Bone Joint Surg Am* 2007;89(3):649–58.
- [6] Schmidmaier G, Schwabe P, Strobel C, Wildemann B. Carrier systems and application of growth factors in orthopaedics. *Injury* 2008;39(Suppl. 2):S37–43.
- [7] Desai BM. Osteobiologics. *Am J Orthop (Belle Mead NJ)* 2007;36(4 Suppl.):8–11.
- [8] Carragee EJ, Hurwitz EL, Weiner BK. A critical review of recombinant human bone morphogenetic protein-2 trials in spinal surgery: emerging safety concerns and lessons learned. *Spine J* 2011;11(6):471–91.
- [9] Yoon ST, Boden SD. Osteoinductive molecules in orthopaedics: basic science and preclinical studies. *Clin Orthop Relat Res* 2002;395:33–43.
- [10] Bishop GB, Einhorn TA. Current and future clinical applications of bone morphogenetic proteins in orthopaedic trauma surgery. *Int Orthop* 2007;31(6):721–7.
- [11] Mikos AG, Herring SW, Ochareon P, Elisseeff J, Lu HH, Kandel R, et al. Engineering complex tissues. *Tissue Eng* 2006;12(2):3307–39.
- [12] Salinas CN, Anseth KS. Mesenchymal stem cells for craniofacial tissue regeneration: designing hydrogel delivery vehicles. *J Dent Res* 2009;88(8):681–92.
- [13] Lutolf MP, Hubbell JA. Synthetic biomaterials as instructive extracellular microenvironments for morphogenesis in tissue engineering. *Nat Biotechnol* 2005;23(1):47–55.
- [14] Ratner BD, Hoffman AS. Non-fouling surfaces. In: Buddy DR, Allan SH, Frederick JS, Jack EL, editors. *Biomaterials science: an introduction to materials in medicine*. Academic Press; 2013. pp. 241–7.
- [15] Bailon P, Won CY. PEG-modified biopharmaceuticals. *Expert Opin Drug Deliv* 2009;6(1):1–16.
- [16] Lutolf MP, Weber FE, Schmoekel HG, Schense JC, Kohler T, Muller R, et al. Repair of bone defects using synthetic mimetics of collagenous extracellular matrices. *Nat Biotechnol* 2003;21(5):513–8.
- [17] Mariner PD, Wudell JM, Miller DE, Genova EE, Streubel SO, Anseth KS. Synthetic hydrogel scaffold is an effective vehicle for delivery of INFUSE (rhBMP2) to critical-sized calvaria bone defects in rats. *J Orthop Res* 2013;31(3):401–6.
- [18] Reichert JC, Cipitria A, Epari DR, Saifzadeh Z, Krishnakanth P, Berner A, et al. A tissue engineering solution for segmental defect regeneration in load-bearing long bones. *Sci Transl Med* 2012;4(141):141ra93.
- [19] Boerckel JD, Kolamunnage YM, Dupont KM, Uhrig BA, Phelps EA, Stevens HY, et al. Effects of protein dose and delivery system on BMP-mediated bone regeneration. *Biomaterials* 2011;32(22):5241–51.
- [20] Phelps EA, Enemchukwu NO, Fiore VF, Sy JC, Murthy N, Sulchek TA, et al. Maleimide cross-linked bioactive PEG hydrogel exhibits improved reaction kinetics and cross-linking for cell encapsulation and *in situ* delivery. *Adv Mater* 2012;24(1):64–70.
- [21] Phelps EA, Headen DM, Taylor WR, Thule PM, Garcia AJ. Vascularized bio-synthetic hydrogel for enhancement of pancreatic islet engraftment and function in type 1 diabetes. *Biomaterials* 2013;34(19):4602–11.
- [22] Reyes CD, Petrie TA, Burns KL, Schwartz Z, Garcia AJ. Biomolecular surface coating to enhance orthopaedic tissue healing and integration. *Biomaterials* 2007;28(21):3228–35.
- [23] Martino MM, Tortelli F, Mochizuki M, Traub S, Ben-David D, Kuhn GA, et al. Engineering the growth factor microenvironment with fibronectin domains to promote wound and bone tissue healing. *Sci Transl Med* 2011;3(100):100ra89.
- [24] Bourdoulous S, Orend G, MacKenna DA, Pasqualini R, Ruoslahti E. Fibronectin matrix regulates activation of RHO and CDC42 GTPases and cell cycle progression. *J Cell Biol* 1998;143(1):267–76.
- [25] Chen CS, Mrksich M, Huang S, Whitesides GM, Ingber DE. Geometric control of cell life and death. *Science* 1997;276(5317):1425–8.
- [26] Giancotti FG, Ruoslahti E. Integrin signaling. *Science* 1999;285(5430):1028–32.
- [27] Mizuno M, Fujisawa R, Kuboki Y. Type I collagen-induced osteoblastic differentiation of bone-marrow cells mediated by collagen- $\alpha 2$ $\beta 1$ integrin interaction. *J Cell Physiol* 2000;184(2):207–13.
- [28] Jikko A, Harris SE, Chen D, Mendrick DL, Damsky CH. Collagen integrin receptors regulate early osteoblast differentiation induced by BMP-2. *J Bone Min Res* 1999;14(7):1075–83.
- [29] Mizuno M, Kuboki Y. Osteoblast-related gene expression of bone marrow cells during the osteoblastic differentiation induced by type I collagen. *J Biochem* 2001;129(1):133–8.
- [30] Suzawa M, Tamura Y, Fukumoto S, Miyazono K, Fujita T, Kato S, et al. Stimulation of Smad1 transcriptional activity by Ras-extracellular signal-regulated kinase pathway: a possible mechanism for collagen-dependent osteoblastic differentiation. *J Bone Min Res* 2002;17(2):240–8.
- [31] Takeuchi Y, Suzawa M, Kikuchi T, Nishida E, Fujita T, Matsumoto T. Differentiation and transforming growth factor- β receptor down-regulation by collagen- $\alpha 2 \beta 1$ integrin interaction is mediated by focal adhesion kinase and its downstream signals in murine osteoblastic cells. *J Biol Chem* 1997;272(46):29309–16.
- [32] Xiao G, Wang D, Benson MD, Karsenty G, Franceschi RT. Role of the $\alpha 2 \beta 1$ -integrin in osteoblast-specific gene expression and activation of the *Osf2* transcription factor. *J Biol Chem* 1998;273(49):32988–94.
- [33] Morton LF, Peachey AR, Zijenah LS, Goodall AH, Humphries MJ, Barnes MJ. Conformation-dependent platelet adhesion to collagen involving integrin $\alpha 2 \beta 1$ mediated and other mechanisms: multiple $\alpha 2 \beta 1$ recognition sites in collagen type I. *Biochem J* 1994;299(Pt 3):791–7.

- [34] Knight CG, Morton LF, Peachey AR, Tuckwell DS, Farndale RW, Barnes MJ. The collagen-binding A-domains of integrins $\alpha(1)\beta(1)$ and $\alpha(2)\beta(1)$ recognize the same specific amino acid sequence, GFOGER, in native (triple-helical) collagens. *J Biol Chem* 2000;275(1):35–40.
- [35] Knight CG, Morton LF, Onley DJ, Peachey AR, Messent AJ, Smethurst PA, et al. Identification in collagen type I of an integrin $\alpha(2)\beta(1)$ -binding site containing an essential GER sequence. *J Biol Chem* 1998;273(50):33287–94.
- [36] Reyes CD, Garcia AJ. Engineering integrin-specific surfaces with a triple-helical collagen-mimetic peptide. *J Biomed Mater Res A* 2003;65(4):511–23.
- [37] Reyes CD, Garcia AJ. $\alpha(2)\beta(1)$ integrin-specific collagen-mimetic surfaces supporting osteoblastic differentiation. *J Biomed Mater Res A* 2004;69(4):591–600.
- [38] Wojtowicz AM, Shekaran A, Oest ME, Dupont KM, Templeman KL, Hutmacher DW, et al. Coating of biomaterial scaffolds with the collagen-mimetic peptide GFOGER for bone defect repair. *Biomaterials* 2010;31(9):2574–82.
- [39] Miljkovic ND, Cooper GM, Hott SL, Disalle BF, Gawalt ES, Smith DM, et al. Calcium aluminate, RGD-modified calcium aluminate, and beta-tricalcium phosphate implants in a calvarial defect. *J Craniofac Surg* 2009;20(5):1538–43.
- [40] Hennessy KM, Clem WC, Phipps MC, Sawyer AA, Shaikh FM, Bellis SL. The effect of RGD peptides on osseointegration of hydroxyapatite biomaterials. *Biomaterials* 2008;29(21):3075–83.
- [41] Jager M, Boge C, Janissen R, Rohrbeck D, Hulsen T, Lensing-Hohn S, et al. Osteoblastic potency of bone marrow cells cultivated on functionalized biomaterials with cyclic RGD-peptide. *J Biomed Mater Res A* 2013;101(10):2905–14.
- [42] Duvall CL, Taylor WR, Weiss D, Wojtowicz AM, Guldberg RE. Impaired angiogenesis, early callus formation, and late stage remodeling in fracture healing of osteopontin-deficient mice. *J Bone Min Res* 2007;22(2):286–97.
- [43] Patterson J, Hubbell JA. SPARC-derived protease substrates to enhance the plasmin sensitivity of molecularly engineered PEG hydrogels. *Biomaterials* 2011;32(5):1301–10.
- [44] Patterson J, Hubbell JA. Enhanced proteolytic degradation of molecularly engineered PEG hydrogels in response to MMP-1 and MMP-2. *Biomaterials* 2010;31(30):7836–45.
- [45] Kimelman-Bleich N, Pelled G, Zilberman Y, Kallai I, Mizrahi O, Tawackoli W, et al. Targeted gene-and-host progenitor cell therapy for nonunion bone fracture repair. *Mol Ther* 2011;19(1):53–9.
- [46] Kolambkar YM, Boerckel JD, Dupont KM, Bajin M, Huebsch N, Mooney DJ, et al. Spatiotemporal delivery of bone morphogenetic protein enhances functional repair of segmental bone defects. *Bone* 2011;49(3):485–92.
- [47] Lehman Jr RA, Kang DG. Symptomatic ectopic intracanal ossification after transforaminal lumbar interbody fusion with rhBMP-2. *Spine J* 2012;12(6):530–1.
- [48] Fiedler J, Roderer G, Gunther KP, Brenner RE. BMP-2, BMP-4, and PDGF-bb stimulate chemotactic migration of primary human mesenchymal progenitor cells. *J Cell Biochem* 2002;87(3):305–12.
- [49] Sorger JJ, Hornicek FJ, Zavatta M, Menzner JP, Gebhardt MC, Tomford WW, et al. Allograft fractures revisited. *Clin Orthop Relat Res* 2001;382:66–74.
- [50] Mankin HJ, Hornicek FJ, Raskin KA. Infection in massive bone allografts. *Clin Orthop Relat Res* 2005;432:210–6.
- [51] Azad V, Breitbart E, Al-Zube I, Yeh S, O'Connor JP, Lin SS. rhBMP-2 enhances the bone healing response in a diabetic rat segmental defect model. *J Orthop Trauma* 2009;23(4):267–76.

Microphysical space of a liver sinusoid device enables simplified long-term maintenance of chimeric mouse-expanded human hepatocytes. Biomedical Microdevices.

Biomed Microdevices (2014) 16:727–736
DOI 10.1007/s10544-014-9877-x

Microphysical space of a liver sinusoid device enables simplified long-term maintenance of chimeric mouse-expanded human hepatocytes

Steven P. Maher · Richard B. Crouse · Amy J. Conway · Emilee C. Bannister ·
Anil Kumar H. Achyuta · Amy Y. Clark · Francly L. Sinatra · Joseph D. Cui ffi ·
John H. Adams · Dennis E. Kyle · Wajeeh M. Saadi

Published online: 7 June 2014
© The Author(s) 2014. This article is published with open access at Springerlink.com

Abstract While many advanced liver models support hepatic phenotypes necessary for drug and disease studies, these models are characterized by intricate features such as co-culture with one of more supporting cell types or advanced media perfusion systems. These systems have helped elucidate some of the critical biophysical features missing from standard well-plate based hepatocyte culture, but their advanced designs add to their complexity. Additionally, regardless of the culture system, primary hepatocyte culture systems suffer from reproducibility issues due to phenotypic variation and expensive, limited supplies of donor lots. Here we describe a microfluidic bilayer device that sustains primary human hepatocyte phenotypes, including albumin production, factor IX production, cytochrome P450 3A4 drug metabolism and bile canaliculi formation for at least 14 days in a simple monoculture format with static media. Using a variety of channel architectures, we describe how primary cell phenotype is promoted by spatial confinement within the microfluidic channel, without the need for perfusion or co-

culture. By sourcing human hepatocytes expanded in the Fah, Rag2, and Il2rg-knockout (FRGTM-KO) humanized mouse model, utilizing a few hundred hepatocytes within each channel, and maintaining hepatocyte function for weeks *in vitro* within a relatively simple model, we demonstrate a basic primary human hepatocyte culture system that addresses many of the major hurdles in human hepatocyte culture research.

Keywords Organ microenvironment · Microfluidics · Human hepatocytes · Factor IX · CYP3A4 · Albumin

1 Introduction

The liver is involved in the course of many infectious and non-infectious diseases as it maintains hundreds of biological functions and is the primary organ responsible for activation and clearance of most therapeutic drugs. While some studies, such as hepatic drug metabolism and hepatotoxicity screening, can utilize short-term hepatocyte cultures or liver microsomes, long-term culture technologies are needed to model most liver diseases and their potential therapies (Donato et al. 2008). Previous liver culture studies with the causative agents of viral hepatitis and malaria have demonstrated that such models require at least three weeks of continuous host cell culture (Mazier et al. 1984, Ploss et al. 2010, March et al. 2013). Also, despite their limited availability and lot-to-lot variation, these and other studies have found human hepatocytes essential in order to properly model both the disease and the human response to potential therapeutics. Thus, a complete infectious disease liver model for drug discovery should incorporate a renewable source of human hepatocytes in a simple, long term, and flexible culture system.

Electronic supplementary material The online version of this article (doi:10.1007/s10544-014-9877-x) contains supplementary material, which is available to authorized users.

S. P. Maher · R. B. Crouse · A. J. Conway · E. C. Bannister ·
A. K. H. Achyuta · A. Y. Clark · F. L. Sinatra · J. D. Cui ffi ·
W. M. Saadi (✉)
Bioengineering Center at USF, Charles Stark Draper Laboratory,
3802 Spectrum Blvd ste 201, Tampa, FL 33612, USA
e-mail: wsaadi@draper.com

S. P. Maher · J. H. Adams · D. E. Kyle (✉)
Department of Global Health, University of South Florida,
3720 Spectrum Blvd ste 304, Tampa, FL 33612, USA
e-mail: dkyle@health.usf.edu

Many seeding techniques, culture methods, and microfluidic culture systems have been developed to accomplish long-term hepatocyte culture (reviewed in Soldatow et al. 2013). Media perfusion has been shown to be central for maintenance of sufficient oxygen transport and appropriate cytokine gradients, and results in enhanced phenotypic gene expression from hepatic cell lines (Domansky et al. 2010; Prot et al. 2011). Primary hepatocyte vesicular transport functions require cuboidal cell morphology with proper apical and basolateral surface domains; these domains are established, in part, by proper interaction with extracellular matrix proteins. Culturing hepatocytes with specific extracellular matrix compositions significantly affects hepatic phenotypes, and an overlay of extracellular matrix can help maintain cuboidal morphology and hepatocyte polarization (Flaim et al. 2005; LeCluyse 2001). Cuboidal cell architecture is also affected by the culture microenvironment; compaction within a small channel leads to extended viability (Lee et al. 2007). To enable multiplexing, maintenance of primary hepatocyte phenotype in a multiwell format has been achieved and utilized by patterning hepatocytes in a co-culture with fibroblasts, demonstrating the importance of cell-cell interaction in the design of high-order culture systems (Bhatia et al. 1997; Khetani and Bhatia 2008).

While these elements are critical for the development of a high-order liver model, they also carry drawbacks. Perfusion often requires integrated pumps and custom-fabricated fluidic lines. Cells cultured on single component extracellular matrices show matrix lot-specific phenotypes and multicomponent matrices are often difficult to mix and deposit on surfaces; requiring additional technologies. Co-cultures require specific, often proprietary sub-clones of supporting cells and require much trial and error to optimize seeding logistics and media compositions. These characteristics make it difficult to incorporate several functionalities into one culture system to take advantage of the additive effects of each mechanism.

To address the challenges of integrating multiple mechanisms into one system for long-term, stable culture of human hepatocytes, we have designed a microfluidic bilayer device (MBD) featuring two microfluidic channels separated by a polydimethylsiloxane (PDMS) membrane. While this MBD is capable of media perfusion, zonal deposition of extracellular matrix, and cell co-culture, we describe how static culture of hepatocytes in the MDB is sufficient to maintain hepatocyte phenotype for three weeks, without the need for perfusion or co-culture. We demonstrate that this phenotype is dependent on spatial confinement of hepatocytes into a collagen and fibronectin-coated microphysical space, which is relevant to a liver sinusoid. To enable comparisons between studies, to model the human response to novel compounds, and to take advantage of their potentially unlimited production, we selected commercially available FRGTM-KO mouse-expanded human hepatocytes (FHH's) as host cells (Azuma et al. 2007,

Strom et al. 2010). This new technology shows promise for mitigation of risks associated with primary human hepatocyte lots, particularly their limited availability and reproducibility. Here we describe an optically accessible and simple, yet highly adaptable and reproducible liver model. This model provides a testbed to measure the incremental advantages of adding important factors such as media perfusion, complex extracellular matrices, and co-cultures to create an even more effective liver model. Our overarching goal is to develop and optimize a platform that recapitulates key hepatocyte phenotypes for long-term studies of multiple liver-associated diseases, such as hepatitis and malaria, and enables testing of potential therapies.

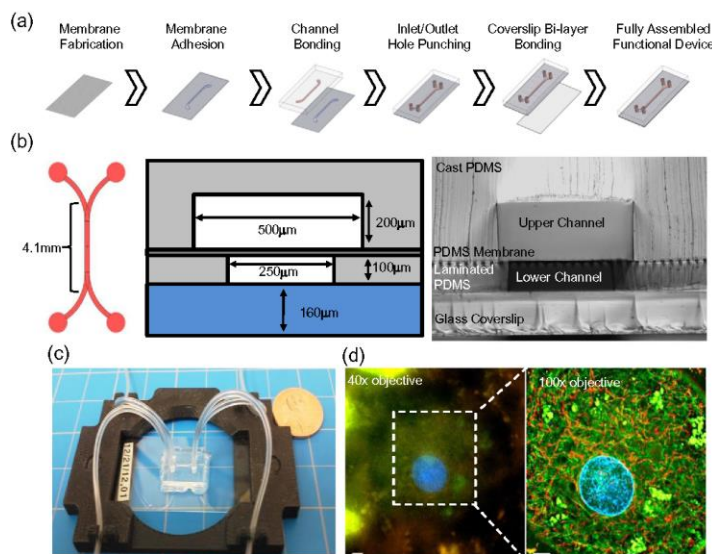
2 Materials and methods

2.1 Fabrication

In summary, the MBD consists of a No. 1 glass coverslip bonded to a 100 μm -thick slab of PDMS featuring a 250- μm -wide, 7.4-mm-long laminated channel. A 10- μm -thick spun PDMS membrane, with a 7.25 % total porosity of evenly-patterned 10- μm -diameter holes, separates the lower and upper layers, thus forming bilayer channels. The upper layer consists of a 500- μm -thick PDMS slab featuring a 500- μm -wide, 7.4-mm-long cast channel. The two channels originate in separate areas and run together for 4.1 mm, forming the bilayer (Fig. 1).

The MBD is assembled by first fabricating the membrane, upper channel, and lower channel out of PDMS, followed by plasma bonding of the layers to each other and then to a glass coverslip. The membrane is fabricated by mixing PDMS base and curing agent at 10:1 w/w (PDMS, Sylgard[®] 184, Dow Corning, Midland, MI, U.S.A.), then degassing the mixture for 30 min before pouring approximately 1 g onto an SU8 mold featuring 10- μm -tall, evenly spaced posts. The wafer (treated after initial lithography with (tridecafluoro-1,1,2,2-tetrahydroxy) trichlorosilane (Gelest, Morrisville, PA) for 2 days) is then spun at 500 rpm for 60 s, then 6000 rpm for 250 s (10 s ramp). The spun wafer is placed on a 100 °C hot plate for 10 min, covered in Kapton[®] and soaked in IPA before the PDMS membrane is cut and pulled off the wafer. The lower layer is fabricated from modified protocols previously described (Epshteyn et al. 2011). Briefly, the lower, laminated layer is manufactured by pouring 1.2–1.5 g of degassed PDMS (mixed as above) onto an SU8 wafer with inverse channel features. The wafer is placed in a laminator with Kapton above the PDMS, needed for handling the thin and fragile laminated layer after pressurizing at 35 psi, 60 °C for 30 min. The upper layer is fabricated by seating an SU8 wafer with inverse channel features into a petri dish and then pouring

Fig. 1 MBD fabrication and features. (a) A spun PDMS membrane is bonded to a cast PDMS upper channel and a laminated PDMS lower channel before being bonded to a glass coverslip. (b) Schematic top-view of channel layout (left); cross-sectional schematic (middle) and microscope image (right) showing device dimensions and arrangement of the different layers. Scale bar represents 100 μm . (c) Complete device is seated into a 3D-printed microscope stage adapter. (d) Device dimensions are thin enough for high resolution, individual tubulin strands and mitochondrion within FHH's are noticeable by imaging with a 100x objective but not a 40x objective. Green: tubulin, red: mitochondria, blue: DNA. Scale bars represent 5 μm



degassed PDMS (mixed as above) onto the wafer to a height of 2 mm and allowing it to cure at 65 °C for 90 min. Once cured, the upper layer containing the cast channel feature is cut away and inlet/outlet holes are punched with a 1 mm biopsy punch (Fig. 1).

Final assembly of the microfluidic MBD begins by activating the lower laminated layer and membrane in a plasma asher under the following conditions: time: 10 s, RF power: 300 W, vacuum set point: 0.180 torr. The lower laminated layer and membrane are then pressed together under a weight at 65 °C for 20 min. The inlet/outlet holes for these layers are punched with a 1 mm biopsy punch. Then, the upper cast layer and reverse side of the membrane-lower layer are activated in a plasma asher (conditions above), channels and inlet/outlet holes are aligned, and the layers are pressed together under a weight at 65 °C for 20 min. Lastly, the PDMS layer stack and a No. 1 glass coverslip (Dow Corning, Midland, MI, U.S.A.) are activated in a plasma asher (conditions above) and pressed together. A thin layer of silicon glue is applied to the outside interface between PDMS and glass in order to improve MBD ruggedness during handling. Completed MBD's are ethylene oxide sterilized for 12 h.

2.2 Cell seeding and culture

Stocks of human liver cell line HC-04 (Sattabongkot et al. 2006) were maintained in media consisting of a 1:1 mixture of

F12 and MEM alpha (Life Technologies™, Grand Island, NY, U.S.A.) supplemented with 0.03 mM Hepes, 551 mg/L L-Glutamine, and 10 % FBS (Thermo Scientific® Hyclone®, Waltham, MA, U.S.A.). FHH's (Yecuris™, Tualatin, OR, U.S.A.) of the same human donor but from two lots (two engraftments and harvestings from FRG™-KO mice), were maintained in Hepatocyte Culture Medium supplemented with a SingleQuot™ kit (Lonza, Walkersville, MD, U.S.A.) containing ascorbic acid, fatty acid free BSA, transferrin, insulin, hEGF and hydrocortisone, prepared per manufacturer's instructions. Human Liver Sinusoidal Endothelial Cells (HLSEC's, ScienCell™, Carlsbad, CA, U.S.A.) were thawed per manufacturer's instructions onto a 2 $\mu\text{g}/\text{cm}^2$ fibronectin-coated flask (Sigma-Aldrich®, St. Louis, MO, U.S.A.) and cultured in manufacturer's complete medium. HLSEC's were allowed grow to 90 % confluence in the flask before being shaken in an orbital shaker at 1000 rpm overnight, to align the cells and adapt them to shear stress (Fig. S5). All cells were maintained in a 5 % CO₂ incubator at 37 °C.

The net volume of the upper and lower channels of the MBD is less than 4 μL and cannot be directly accessed by pipette tips. To enable liquid handling, 0.02 in ID, 0.06 in OD Tygon® Tubing (US Plastics®, Lima, Ohio, U.S.A.) is inserted into the slightly smaller diameter inlets and outlets, creating a tight but temporary seal. A 50 μL HPLC syringe with a 22 gauge blunt needle is used to perfuse extracellular matrix solution, media, and cells into the MBD by inserting the blunt tip into the opposite end of the Tygon tubing. For

static culture, the tubing is removed from a seeded MBD and the lower 1 cm of a 1 mL pipette tip (Eppendorf, Hauppauge, NY, U.S.A.) is cut, sterilized, and inserted into the MBD to serve as a media reservoir. Four tips, one inserted into each of the four inlets/outlets, hold about 120 μL of media. Alternatively, for perfused culture, after cell seeding an extended piece of Tygon tubing is connect to a syringe by a 22 gauge blunt needle tip. The syringe sits in a syringe pump (Harvard Apparatus, Holliston, MA, U.S.A.) and a flow rate of 137 $\mu\text{L}/\text{h}$ is equivalent to a shear stress of 0.1 dyn/cm^2 at the cell surface is applied in the lower channel (Fig S3).

The MBD can support long-term culture of either cell lines, such as HepG2 and HC-04, or FHH's. Additionally, the MBD supports both direct and indirect co-cultures when cells are seeded together in one channel or separately in either channel (Fig. 5). Because fibronectin-coated surfaces are recommended for endothelial cells and collagen-coated surfaces are recommended for hepatocytes, MBD's were coated at a calculated concentration of 5 $\mu\text{g}/\text{cm}^2$ collagen and 2 $\mu\text{g}/\text{cm}^2$ fibronectin by injecting a solution 1.4 $\mu\text{g}/\mu\text{L}$ rat tail collagen I (BD™, Waltham, MA, U.S.A.) and 0.6 $\mu\text{g}/\mu\text{L}$ bovine fibronectin (Sigma) diluted in 0.01 N acetic acid into the upper and lower channels, allowing it to adsorb onto the surface overnight. For hepatocyte seeding, a vial of cryopreserved human FHH's was thawed according to manufacturer's protocols; for hepatocyte cell lines, cells are trypsin-released from a flask, pelleted, and resuspended in complete hepatocyte culture media to a concentration of 15000 cells/ μL (for cell lines) or 8000 cells/ μL (for FHH's). The cell slurry is perfused into the MBD lower channel with a 50 μL syringe and allowed to adhere over 3 h before initiation of static culture, described above. For HLSEC-FHH co-culture experiments, hepatocyte seeding was preceded by trypsin-releasing aligned HLSEC's, concentrating them to 2400 cells/ μL , injecting them into the upper channel, and allowing them to grow to confluence over 2 days under static media. During static MBD culture, media is changed daily with the appropriate hepatocyte culture medium (for hepatocyte-only cultures) or a 1:1 mixture of hepatocyte culture media and endothelial culture media (for HLSEC and hepatocyte co-cultures). FHH's were seeded at a concentration of 100,000 cells/well into 8-chamber slides (BD) coated with 5 $\mu\text{g}/\text{cm}^2$ rat tail collagen I and 2 $\mu\text{g}/\text{cm}^2$ fibronectin, serving as control cultures for albumin production, factor IX and bile canaliculi experiments.

2.3 Imaging, sampling, and phenotyping assays

For high-resolution imaging of FHH's within the MBD, hepatocytes cultured for 12 days within the MBD were stained with 10 $\mu\text{g}/\text{mL}$ Hoechst 33342 (Life Technologies), 10 μM Vybrant Celltracker Red (Life Technologies) and 250 nM Tubulin Tracker Green (Life Technologies) for 30 min. Live, stained cells were imaged with a 40x and 100x objective

on a Deltavision Elite (Applied Precision, Issaquah, WA, U.S.A.) and, for 100x images, were deconvoluted using the softWoRx® image processing software (Applied Precision). Assessing bile production was performed by incubating MBD cultures with 2 $\mu\text{g}/\text{mL}$ 5-(and-6)-Carboxy-2',7'-Dichlorofluorescein Diacetate (Carboxy-DCFDA, Life Technologies) and 10 $\mu\text{g}/\text{mL}$ Hoechst 33342 for 10 min, washing the MBD with complete medium, and imaging live cells on a Deltavision Elite (Khetani and Bhatia 2008). HLSEC-hepatocyte co-cultures within the MBD were imaged by first seeding the MBD with HLSEC's and allowing them to grow to confluence over 2 days before staining with 10 μM Vybrant® Celltracker Red. Simultaneously, HC-04 hepatocytes were stained with 10 μM Vybrant Celltracker Green within a culture flask before being trypsin-released and seeded into the vascularized MBD. After attachment, the MBD was imaged by a Deltavision Elite from coverslip to upper channel at 1 μm intervals to make a Z-stack; which was further modeled into polygons in 3D space by the softWoRx image processing package. Viability staining of cell lines and FHH's after long term-flow and static culture was performed with the Live/Dead® Calcein AM/Ethidium Homodimer kit (Life Technology) per manufacturer's protocol.

For albumin and factor IX production assays, media was collected from the pipette tip reservoirs or 8 chamber slide wells during daily media changes and frozen at -80°C until needed for the ELISA. Samples were loaded into an ELISA specific for human albumin (Bethyl Labs, Montgomery, TX, U.S.A.) or human factor IX (Assaypro, St. Charles, MO, U.S.A.) after diluting 1:10 v/v (for albumin) or 1:5 v/v (for factor IX) in kit-supplied dilution buffer. ELISA labeling and washing was performed per manufacturer's protocols, and final concentrations were corrected for dilution factor. For CYP3A4 assays, MBD cultures were induced with 25 mM Rifampicin (MP Biomedical™, Santa Ana, CA, U.S.A.) or DMSO for 3 days. The assay was performed with a CYP3A4 P450-Glo™ kit (Promega, Madison, WI, U.S.A.) using a slight modification to manufacturer's lytic protocol: MBD's were treated with 100 μL of the luciferin reagent for 45 min and then collected into an opaque plate, followed by 100 μL of cell lysis reagent injected through the MBD before being mixed with the previously collected luciferin reagent, to collect both intracellular and extracellular luciferin from the MBD. Statistics were performed with Prism (Graphpad, La Jolla, CA, U.S.A.) using multiple student's t-tests.

3 Results and discussion

3.1 Device design and optimization

Channel materials and dimension were designed around several considerations for optimization. First, functional liver

research is hindered by the cost of primary human hepatocytes, regardless of sourcing from human cadavers or further propagation within the FRGTM-KO mouse. Thus, we designed the MBD to hold only 200 hepatocytes per sample, versus 10,000 or more for conventional well plate-based culture, such that a single cryovial of hepatocytes could populate dozens of devices at once. Second, the device was optimized to allow static culture without perfusion, thus simplifying device implementation by eliminating the need for syringe pumps. To minimize diffusion limitations, we shortened the MBD channel length, compared to a precursor channel described in Epshteyn et al. (2011), such that no part of the channel was more than 5 mm from an inlet. Cells cultured beyond a threshold of 5 mm from an inlet die; presumably due to lack of media exchange by diffusion alone during static culture (Fig. S2). Third, the MBD is meant to represent the functional unit of the liver. At the cellular level, the liver is organized into single or double layered sheets of hepatocytes separated by endothelial cell-lined sinusoids. The lower channel of the device is approximately 100 μm tall, 250 μm wide and 4 mm long in the overlapping area. Upon seeding, a monolayer of primary hepatocytes about four to five cells wide occupies the length of the channel across from the vascular upper channel, similar to the liver sinusoid (Fig. 2). Lastly, long-term culture within a complex, non-well platform is challenging because the various materials and interfaces used to manufacture the device are exposed to water for extended timelines; increasing the opportunity for delamination. To facilitate lamination by plasma bonding, which results in much stronger bonds than those obtained with either glue or silane treatment, a PDMS membrane was developed to yield an entirely glass and PDMS device (Fig. 1). This membrane was fabricated using a well-known soft-lithographic molding process (Jackman et al. 1999); surface treatment and spin-speeds were optimized to ensure a reproducible fabrication process with >90 % yield. Successful fabrication of open holes was verified with SEM (Fig. S1), and the number of open holes estimated to be ~98 %. PDMS is useful as a prototyping substrate but is not recommended for studies involving small molecules because PDMS is known to absorb hydrophobic molecules; a potential confounder in drug dosing experiments (Regehr et al. 2009). This model is a prototype and as the exact architectures and cell types needed for a long-term liver model are better understood, a future device composed of non-PDMS plastics and manufactured via rapid prototyping or injection molding would circumvent the negative properties of a PDMS-based device.

3.2 Long-term maintenance of primary human hepatocyte phenotypes

Four of the many fundamental roles of hepatocytes are the production of serum albumin and clotting factor IX,

production and excretion of bile salts, and activation of the cytochrome P450 enzymes. These phenotypes are lost within a few days of typical *in vitro* well-plate culture (Guguen-Guillouzo et al. 1983; Miao et al. 2000). On the contrary, primary hepatocytes can maintain their phenotype for ≥ 3 weeks in the MBD in static culture (no perfusion, with daily refreshing of the media), without any other supporting cells in the device. Upon seeding in the lower MBD channel, FHH's adhere to the glass coverslip in a monolayer. Over the course of several days hepatocyte groups ranging from five to twelve or more cells remodel into multicellular structures, becoming more cuboidal as observed by microscopy (Figs. 2 & 3). This remodeling phenomenon appears essential for function, as it is accompanied with a simultaneous rise in albumin and factor IX production during the first ten days post seed, which then stabilizes (Fig. 2). This production level remained stable until we stopped the experiment 21 days post-seed. Formation of extracellular bile canaliculi progressed in tandem with the formation of cuboidal multicellular structures over ten or more days within the MBD. Bile canaliculi are representative of hepatocytes maintaining proper polarization, with two basolateral surfaces separated by an apical belt featuring transporters for bile salts into canaliculi between neighboring hepatocytes (Dunn et al. 1991). FHH's cultured in standard wells spread and do not produce bile canaliculi (data not shown, Nakao et al. 2011) but FHH's cultured within the MBD formed bile networks visualized by Carboxy-DCFDA; a dye which fluoresces upon cleavage by hepatic esterases and is subsequently pumped into bile networks (Fig. 3)

A valid *in vitro* liver model, especially one designed to model both the disease and potential treatments, must demonstrate sustained cytochrome P450 activity to project drug activation and clearance rates. Quantitative gene expression measured by RT-PCR is often used to measure many of the P450 induction levels as many of the dozens of P450 enzymes can be quantified simultaneously, but this method does not reveal actual metabolism (Rodríguez-Antona et al. 2001). Therefore, metabolism of FHH's within MBD's was measured by cleavage of luciferin from a CYP3A4 substrate after induction with Rifampin over three days. While in standard well cultures metabolism rapidly drops and becomes non-existent within days of hepatocyte seeding, expression and function of CYP3A4 was maintained for at least two weeks in MBD culture (Fig. 3). While more studies are needed to validate other P450 enzymes, CYP3A4 is responsible for metabolism of over 30 % of FDA approved drugs and is representative of *in vitro* hepatic drug metabolism (Guengerich 1999).

Many alternative culture methods utilizing co-cultures, gel overlays, and perfused channels have demonstrated these phenomena. However, only the MBD promotes hepatocyte culture with key hepatocyte phenotypes without co-culture or perfusion. While unexpected, this result is consistent with

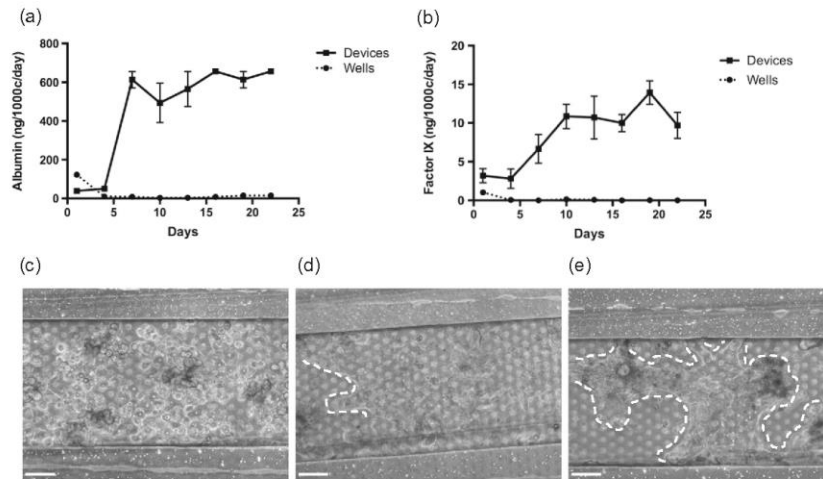


Fig. 2 Three-week maintenance of albumin secretion and morphology. (a, b) FHH wellplate and MBD albumin and factor IX output over three weeks in static culture show a stabilization of primary phenotype in devices but not wells. Error bars represent standard error of the mean

(SEM) ($n=4$). (c, d, e) MBD-cultured FHH's imaged at 5 h, 13 days, and 21 days post-seed, respectively, showing that FHH's become more cuboidal and form multicellular structures, outlined by dotted lines. Scale bars represent 100 μm

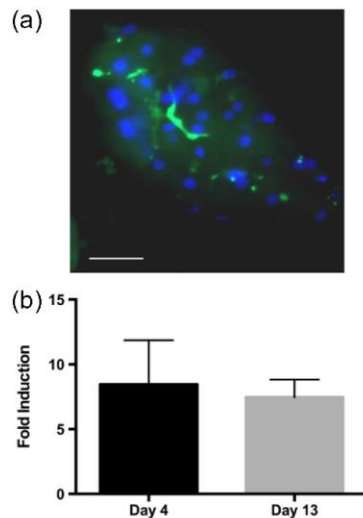


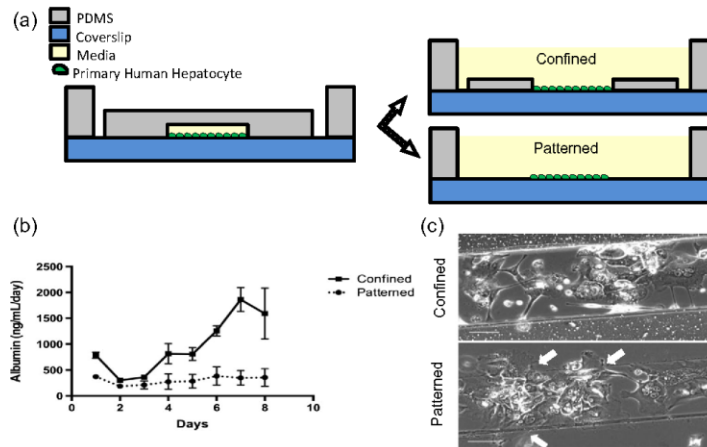
Fig. 3 Hepatocyte P450 expression and bile canaliculi formation. (a) At two weeks post seed of FHH's in the MBD, bile production identified by Carboxy-DCFDA dye, which fluoresces upon cleavage by intercellular esterases and is subsequently pumped into extracellular bile networks, green: CDF, blue: DNA. (b) Rifampin-induced CYP3A4 expression is maintained for at least two weeks in MBD culture. Error bars represent SEM ($n=2$). Scale bar represents 50 μm

studies showing that hepatocytes seeded within tubes or cords demonstrate extended viability (Lee et al. 2007). These models, however, also feature media perfusion or other advanced culture methods, confounding the true functional effect on hepatocytes. Elucidating the essential elements responsible for maintenance of primary phenotype is critical to the development of a simple yet effective liver model.

3.2.1 Spatial confinement leads to long-term maintenance of primary hepatocyte phenotypes

The MBD possesses two key attributes that differ from well plates, which may be critical for hepatocyte culture: the microphysical environment provide by the microfluidic channel (250 μm wide, 100 μm tall), and the small volume of media available to the cells within the channel. To investigate if one or both of these differences contribute to maintenance of hepatic phenotypes, partial devices were constructed with decreasing complexity. Cells were seeded in a simple channel architecture, which was subsequently modified to yield either an open channel with walls but no top ("Confined") or a patterned line of cells with no walls ("Patterned") (Fig. 4a). A disparity in albumin and factor IX production resulted when hepatocytes were seeded into a confined space defined by walls, compared to hepatocytes seeded into a patterned line without confinement (Fig. 4b). Both device-like cultures featured 500 μL of media, thus the small volumes of the MBD do not seem to be sufficient to induce this effect.

Fig. 4 Spatial confinement is necessary to maintain hepatocyte phenotype. (a) Devices with decreasingly complex architecture were seeded with FHH's, and then modified post-seed to yield either a patterned strip of cells ("patterned") or cells confined in an open channel within a well ("confined"). (b) Confined hepatocytes achieve stable albumin expression, but patterned hepatocytes produce much less albumin. Error bars represent SEM (n=3). (c) Hepatocytes within the walled device are spatially confined to the channel, but line-patterned hepatocytes are able to spread beyond their initial seeding pattern (white arrow). Scale bars represent 100 μ m



Microscopy revealed that hepatocytes within the patterned line were able to spread beyond their initial seeding pattern (despite the fact that the ECM coating was confined to the patterned area by the removable channel), in contrast to their wall-confined counterparts (Fig. 4c). This demonstrates the primary hepatocyte phenotype is dependent on physical confinement of the cells.

Cell concentration and compaction is a well-documented prerequisite to prevent flattening of primary hepatocytes in short-term well-based culture (LeCluyse 2001). Likewise, forming tight cords of hepatocytes within a perfused microchannel and patterning hepatocyte islands with surrounding fibroblasts has been shown to maintain proper phenotypes for long-term culture (Bhatia et al. 1998). Compaction allows for proper spacing of hepatocytes to mimic the cellular structure of a liver acinus. To supply the liver, the portal vein and hepatic artery branch 8–10 times to feed hexagonal structures called Kieman lobules. Inside lobules, blood flows from portal venules and hepatic arterioles to the central vein of a lobule through sinusoids as plasma is filtered by sinusoidal endothelial cells before being engulfed by hepatocytes. Within the lobules are single layers of hepatocytes, often one cell thick. Fifty percent of the hepatocytes cell surface is shared with other hepatocytes. Tight junctions coordinated from cell to cell form bile canaliculi, which aggregate into a bile ductile (Arias et al. 2009). By culturing hepatocytes in a microenvironment that prevents them from spreading, and instead encouraging formation of units several cells across and 50–100 cells long, it is possible the MBD is effectively re-creating the spatial features of a liver acinus. While the exact mechanism of action of the MBD requires further investigation, this demonstrates that the spatial constriction of the channel alone, without perfusion, co-cultures, elaborate

extracellular matrices or media components, is sufficient to prevent hepatocyte spreading. This understanding, especially its simplicity, is invaluable in the design of both micro-scale liver models, as well as larger liver-assist type devices.

It is important to note that the cell density was kept constant between the different conditions, to eliminate the role of cell-aggregation as a contributing factor to the phenotype. The cell density in well cultures and different device architectures was kept constant at 150,000 cells/cm². Moreover, cells seeded in the MBD spread out and adhered well to the collagen-coated glass substrate, and only began to form aggregates a few days after seeding, as result of active remodeling by the cells (Fig. 2e). Though this remodeling resulted in a discontinuous layer of cells that do not appear closely packed, their cuboidal morphology appears key to their phenotype, consistent with previous data (Evenou et al. 2010). It is possible that high enough cell densities can lead to a sustained phenotype (Dembélé et al. 2014). In our hands, higher cell densities up to 300,000 cells/cm² phenotypes did not improve cell phenotype in well cultures (Fig. S4). While much higher densities can maintain stable phenotypes, as in the case of spheroids (Kikuchi et al. 2009; Lee et al. 2004; Miranda et al. 2009; Thoma et al. 2005; Evenou et al. 2010), such systems can be difficult to produce, image and handle, and pose practical challenges for multiplexing. Our MBD offers a substitute for well-based attached hepatocyte culture and is simple to implement and analyze.

3.3 HLSEC-hepatocyte co-culture under static and perfused media

As there are at least seven distinct cell types in liver (hepatocytes, cholangiocytes, endothelial cells, Kupffer cells,

lymphocytes, dendritic cells, and stellate cells) and hepatocytes alone are not able to complete all the functions of the liver (Arias et al. 2009), the ability to co-culture multiple liver cells types is important to achieve a more complete liver model that reproduces many of the essential functions of the liver. To demonstrate the ability of the device to support multiple cell types, we employed the bilayer architecture to investigate juxtaposing the hepatocytes with human liver sinusoidal endothelial cells (HLSEC's). Endothelial cells have been shown to support both hepatocyte cell line and primary hepatocyte phenotypes (Ohno et al. 2008; Lee et al. 2004). The addition of endothelial cells would also aid in developing a perfused system, as they would (along with the membrane) serve as a barrier that discourages flow from crossing from the top to the bottom channel, protecting the hepatocytes from excessive shear. To develop this vascularized device, we used the HC-04 hepatoma cell line, as cell lines are an efficient cell source for prototyping (Mateme et al. 2013). Donor-specific lots of HLSEC's were confirmed for primary phenotypes via characterization for LDL uptake and Tumor Necrosis Factor alpha-induced expression of ICAM and E-selectin. HLSEC culture was optimized to include shaking the starter flask of HLSEC's overnight in an orbital shaker, having the effect of aligning the cells to shear stress before being seeded into the upper channel (Fig. S5).

While HC-04 cultured by themselves did not survive under perfusion for more than 3 days, the presence of vascular channels increased the ability of HC-04 to tolerate flow (Fig. 5). This investigation allow us to us to establish three

basic requirements for HC-04 survival under flow, which were extrapolated for FHH. First, hepatocytes were perfused with media harvested from a culture flask, such that necessary cytokines or other extracellular factors can be maintained at appropriate concentration during perfusion. Second, establishing a monolayer of HLSEC's in the upper, perfused channel prior to hepatocyte seeding contributed to culture longevity under flow. It is worth noting that post-experiment staining revealed no HLSEC's remaining in the upper channel. The endothelial layer likely served to protect the hepatocytes from shear stress, gradually pulling off from the membrane while hepatocytes simultaneously were adapting to steadily increasing shear (Fig. 5b). This points to the challenges associated with culturing microvascular endothelial cells (which are generally less robust than other endothelial cells) in microfluidic channels, particularly on porous PDMS membranes. More studies are required to elucidate proper conditions for culturing these cells under shear. Third, we established the upper limit for flow rates that the hepatocytes can tolerate. This was exceptionally low in the case of HC-04 (2.5 $\mu\text{L/h}$, equivalent to a shear stress of 0.003 dyn/cm^2 at the cell surface), indicating a loss of shear tolerance, likely due to the HC-04 cell line being adapted to static conditions over many passages. FHH's were more tolerant, and were able to be perfused at 137 $\mu\text{L/h}$ (equivalent to a shear stress of 0.1 dyn/cm^2 at the cells surface), provided they were first cultured under static conditions to allow them enough time to attach and remodel their microenvironment prior to experiencing shear from perfusion.

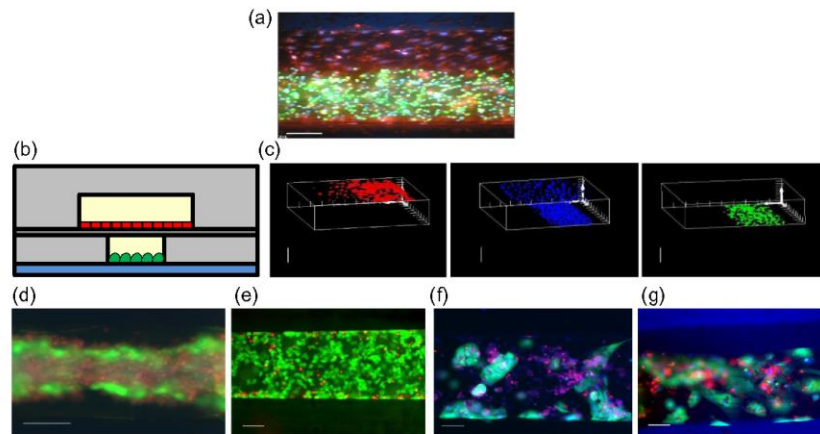


Fig. 5 Device co-culture and perfusion. (a) Merged Z-stack through the co-culture device, green: HC-04, red: HLSEC, blue: DNA. (b) Schematic of (a) showing HLSEC's in the upper channel co-cultured with HC-04 hepatocytes in the lower channel. (c) Three-dimensional rendering of (a). (d) HC-04 cultured in static media in the lower chamber for three weeks show overgrowth and death, but many live cells in the periphery of the cell

mass in the channel. (e) HC-04 cultured in the lower channel under media perfusion at 2.5 $\mu\text{L/h}$ for one week. HLSEC were seeded in the top channel at the start of the experiment (not imaged). (f) FHH's cultured in the lower channel for three weeks under static media. (g) FHH's after 12 days under static media followed by 10 days under perfusion at 137 $\mu\text{L/h}$. (d–g) Green: live, red: dead, blue: DNA. All bars represent 100 μm

A liver culture model featuring media perfusion is inherently more phenotypic because the liver is not a static organ. Previous research has shown the importance of flow for both the parenchymal and non-parenchymal aspects of the liver culture model. Healthy hepatocytes require a relatively large influx of oxygen difficult to achieve by diffusion alone, highlighting the importance of perfused oxygen-rich media (Domansky et al. 2010). Additionally, primary liver sinusoidal endothelial cells lose important phenotypes and features, such as sieve plates, after a few days in culture (Danecker et al. 1998). Efforts to maintain endothelial structure and phenotypes *in vitro* have focused on identifying proper perfusion, extracellular matrix, and cytokine gradients (Kim et al. 2013, Sato and Ohashi 2005). While our MBD is capable of perfused cell culture, much more optimization is needed to obtain *in vivo*-like vascular structures within the MBD. We have estimated the oxygen flux through the MBD to be greater than that in a typical wellplate culture, negating the need for flow to meet oxygen demands. Moreover, static culture is advantageous because there is no need for syringe pumps and tubing. The MBD's compatibility with different cell types and flow conditions is important for assessing which biological and mechanical components are necessary for a fully optimized liver model.

4 Conclusion

Here we present a simple and flexible liver model capable of supporting human hepatocytes and their phenotypes for at least three weeks of continuous culture. When hepatocytes are cultured in the MBD alone in static media, spatial confinement provided by the channel walls promotes albumin production, factor IX production, expression of cytochrome P450 enzymes, and formation of functional bile canaliculi, indicating that hepatocytes are maintaining functionality and demonstrating the potential of this liver model. As organ-on-a-chip models are often complex and tailored for specific cell types or organ models, this device demonstrates flexibility in that either hepatic cell lines or primary hepatocytes can be seeded into the parenchymal chamber, and if needed, additional cell types such as sinusoidal endothelial cells, stellate cells, or Kupffer cells can be utilized for co-culture effects and as potential cues for improved long-term liver culture. Furthermore, the MBD can be perfused or kept static, depending on the ideal culture conditions for each cell type within the MBD. Further studies with different media perfusion rates, supporting cell types, and complex extracellular matrices can elucidate and measure the incremental improvement each has on *in vitro* liver models. These findings are essential to development of a long-term, phenotypic, reproducible and multiplexed liver disease model.

Acknowledgments This work is funded by the Bill and Melinda Gates Foundation Grant OPP1023601 and a Draper Laboratory Fellowship awarded to SPM. Special thanks to Dr. Jeffrey Borenstein at Draper Laboratory for valuable guidance and discussions, Dr. Jetsumon Sattabongkot, Mahidol Vivax Research Unit, Mahidol University for HC-04 hepatocyte lines and Prof. Stephen Duncan, Medical College of Wisconsin, for valuable discussions and advice. Thanks also to Lisa Wilson of Yecuris Corporation for helpful discussion regarding FHH.

Conflict of interest The authors have no conflict of interest to declare.

Open Access This article is distributed under the terms of the Creative Commons Attribution License which permits any use, distribution, and reproduction in any medium, provided the original author(s) and the source are credited.

References

- I.M. Arias, H.J. Alter, J.L. Boyer, D.E. Cohen, D.E. Fausto, D.A. Shafritz, A.W. Wolkoff, *The Liver*, 5th edn. (John Wiley & Sons, West Sussex, 2009), pp. 3–13
- H. Azuma, N. Paulk, A. Ranade, C. Dorrell, M. Al-Dhalimy, E. Ellis, S. Strom, M. Kay, M. Finegold, M. Grompe, *Nat. Biotechnol.* **25**, 8 (2007)
- S.N. Bhatia, U.J. Balis, M.L. Yarmush, M. Toner, *Biotechnol. Prog.* **14**, 3 (1998)
- S.N. Bhatia, M.L. Yarmush, M. Toner, *J. Biomed. Mater. Res.* **34**, 2 (1997)
- G.W. Danecker, S.A. Lund, S.W. Caughman, R.A. Swerlick, A.H. Fischer, C.A. Staley, E.W. Ades, *In Vitro Cell. Dev. Biol. Anim.* **34**, 5 (1998)
- L. Dembélé, J. Franetich, A. Lorthiois, A. Gego, A. Zeeman, C.H.M. Kocken, R. Le Grand, N. Dereuddre-Bosquet, G. van Gemert, R. Sauerwein, J. Vaillant, L. Hannoun, M. Fuchter, T.T. Diagana, N.A. Malmquist, A. Scherf, G. Snounou, D. Mazier, *Nat. Med.* (2014). doi:10.1038/nm.3461
- K. Domansky, W. Inman, J. Serdy, A. Dash, M.H. Lim, L.G. Griffith, *Lab Chip* **10**, 1 (2010)
- M.T. Donato, A. Lahoz, J.V. Castell, M.J. Gómez-Lechón, *Curr. Drug Metab.* **9**, 1 (2008)
- J.C. Dunn, R.G. Tompkins, M.L. Yarmush, *Biotechnol. Prog.* **7**, 3 (1991)
- A.A. Epshteyn, S.P. Maher, A.J. Taylor, A.B. Holton, J.T. Borenstein, J.D. Cuijff, *Biomeicrofluidics* **5**, 4 (2011)
- F. Evenou, T. Fujii, Y. Sakai, *Biomed. Microdevices* **12**, 3 (2010)
- C.J. Flaim, S. Chien, S.N. Bhatia, *Nat. Methods* **2**, 2 (2005)
- F.P. Guengerich, *Annu. Rev. Pharmacol. Toxicol.* **39** (1999)
- C. Guguén-Guillouzo, B. Clément, G. Baffet, C. Beaumont, E. Morel-Chany, D. Glaise, A. Guillouzo, *Exp. Cell Res.* **143**, 1 (1983)
- R.J. Jackman, D.C. Duffy, O. Cherniavskaya, G.M. Whitesides, *Langmuir* **15**, 1999
- S.R. Khetani, S.N. Bhatia, *Nat. Biotechnol.* **26**, 1 (2008)
- K. Kikuchi, K. Sumaru, J.-I. Edahiri, Y. Ooshima, S. Sugiura, T. Takago, T. Kanamori, *Biotechnol. Bioeng.* **103**, 3 (2009)
- S. Kim, H. Lee, M. Chung, N.L. Jeon, *Lab Chip* **13**, 8 (2013)
- E.L. LeCluyse, *Eur. J. Pharm. Sci.* **13**, 4 (2001)
- D.H. Lee, H.H. Yoon, J.H. Lee, K.W. Lee, S.K. Lee, S.K. Kim, J.E. Choi, Y.J. Kim, J.K. Park, *Biochem. Eng. J.* **20**, 2–3 (2004)
- P.J. Lee, P.J. Hung, L.P. Lee, *Biotechnol. Bioengineering* **97**, 5 (2007)
- S. March, S. Ng, S. Velmurugan, A. Galstain, J. Shan, D.J. Logan, A.E. Carpenter, D. Thoma, B. Kim Lee, Sim, M. M. Mota, S. L. Hoffman, S. N. Bhatia, *Cell Host Microbe* **14**, 1 (2013)
- E.M. Materna, A.G. Tonevitsky, U. Marx, *Lab Chip* **13**, 18 (2013)

- D. Mazier, I. Landau, P. Druilhe, F. Miltgen, C. Guguen-Guillouzo, D. Baccam, J. Baxter, J.P. Chigot, M. Gentilini, *Nature* **307**, 5949 (1984)
- C.H. Miao, K. Ohashi, G.A. Patijn, L. Meuse, X. Ye, A.R. Thompson, M.A. Kay, *Mol. Ther.* **1**, 6 (2000)
- J.P. Miranda, S.B. Leite, U. Muller-Vieira, A. Rodrigues, M.J.T. Carrondo, P.M. Alves, *Tissue. Eng. Pt. C-Meth.* **15**, 2 (2009)
- Y. Nakao, H. Kimura, Y. Sakai, T. Fujii, *Biomicrofluidics* **5**, 2 (2011)
- M. Ohno, K. Motojima, T. Okano, A. Taniguchi, *Tissue Eng. Pt. A* **14**, 11 (2008)
- A. Ploss, S.R. Khetani, C.T. Jones, A.J. Syder, K. Trehan, V.A. Gaysinskaya, K. My, K. Ritola, C.M. Rice, S.N. Bhatia, *Proc. Natl. Acad. Sci. U. S. A.* **107**, 7 (2010)
- J.M. Prot, C. Aninat, L. Griscom, F. Razan, C. Brochot, C.G. Guillouzo, C. Legallais, A. Corlu, E. Leclerc, *Biotechnol. Bioeng.* **108**, 7 (2011)
- K.J. Regehr, M. Domenech, J.T. Koepsel, K.C. Carver, S.J. Ellison-Zelski, W.L. Murphy, L.A. Schuler, E.T. Alarid, D.J. Beebe, *Lab Chip* **9**, 15 (2009)
- C. Rodríguez-Antona, M.T. Donato, E. Pareja, M.J. Gómez-Lechón, J.V. Castell, *Arch. Biochem. Biophys.* **393**, 2 (2001)
- M. Sato, T. Ohashi, *Biorheology* **42**, 6 (2005)
- J. Sattabongkot, N. Yimamnuaychoke, S. Leelaudomlapi, M. Rasameesoraj, R. Jenwithisuk, R.E. Coleman, R. Udomsangpetch, L. Cui, T.G. Brewer, *Am. J. Trop. Med. Hyg.* **74**, 5 (2006)
- V.Y. Soldatow, E.L. LeCluyse, L.G. Griffith, *Toxicol. Res. (Camb)* **2**, 1 (2013)
- S. C. Strom, J. Davila, M. Grompe, *Methods Mol. Biol.* 640 (2010)
- R.J. Thoma, D.A. Bhandari, A.J. Barrett, J.R. Fry, D. Power, B.J. Thomson, K.M. Shakesheff, *Cells Tissues. Organs* **181**(2) (2005)

Integrin-specific hydrogels functionalized with VEGF for vascularization and bone regeneration of critical-size bone defects. Journal of Biomedical Materials Research Part A.



Integrin-specific hydrogels functionalized with VEGF for vascularization and bone regeneration of critical-size bone defects

José R. García,^{1,2} Amy Y. Clark,^{1,2} Andrés J. García^{1,2}

¹Woodruff School of Mechanical Engineering, Georgia Institute of Technology, Atlanta, Georgia

²Petit Institute for Bioengineering and Bioscience, Georgia Institute of Technology, Atlanta, Georgia

Received 12 October 2015; revised 26 November 2015; accepted 10 December 2015

Published online 00 Month 2015 in Wiley Online Library (wileyonlinelibrary.com). DOI: 10.1002/jbm.a.35626

Abstract: Vascularization of bone defects is considered a crucial component to the successful regeneration of large bone defects. Although vascular endothelial growth factor (VEGF) has been delivered to critical-size bone defect models to augment blood vessel infiltration into the defect area, its potential to increase bone repair remains ambiguous. In this study, we investigated whether integrin-specific biomaterials modulate the effects of VEGF on bone regeneration. We engineered protease-degradable, VEGF-loaded poly(ethylene glycol) (PEG) hydrogels functionalized with either a triple-helical, $\alpha_2\beta_1$ integrin-specific peptide GGYGGGP(GPP)₆GFOGER(GPP)₆GPC (GFOGER) or an $\alpha_v\beta_3$ integrin-targeting peptide GRGDSPC (RGD). Covalent incorporation of VEGF into the PEG hydrogel allowed for protease degradation-dependent release of the protein while maintaining VEGF bioactivity. When applied to critical-size segmental defects in the murine radius, GFOGER-functionalized VEGF-free hydrogels exhibited significantly increased vascular volume and density and resulted in a larger

number of thicker blood vessels compared to RGD-functionalized VEGF-free hydrogels. VEGF-loaded RGD hydrogels increased vascularization compared to VEGF-free RGD hydrogels, but the levels of vascularization for these VEGF-containing RGD hydrogels were similar to those of VEGF-free GFOGER hydrogels. VEGF transiently increased bone regeneration in RGD hydrogels but had no effect at later time points. In GFOGER hydrogels, VEGF did not show an effect on bone regeneration. However, VEGF-free GFOGER hydrogels resulted in increased bone regeneration compared to VEGF-free RGD hydrogels. These findings demonstrate the importance of integrin-specificity in engineering constructs for vascularization and associated bone regeneration. © 2016 Wiley Periodicals, Inc. *J Biomed Mater Res Part A*: 00A:000–000, 2015.

Key Words: vascularization, cell adhesion, mesenchymal stem cells

How to cite this article: García JR, Clark AY, García AJ. 2015. Integrin-specific hydrogels functionalized with VEGF for vascularization and bone regeneration of critical-size bone defects. *J Biomed Mater Res Part A* 2015:00A:000–000.

INTRODUCTION

Vascularization is a crucial factor in bone development as well as the repair of bone defects.^{1–3} In the developing skeleton, long bones are formed through endochondral ossification, which involves the invasion and sprouting of blood vessels into the intermediate cartilage tissue followed by osteoprogenitor cell migration and mineralization of the cartilaginous anlage.⁴ Blocking infiltration of blood vessels into cartilage causes enlarged hypertrophic zones associated with incomplete and delayed onset of ossification and sub-optimal bone formation.⁵ In terms of bone repair, large bone defects arising from trauma or cancer resection suffer from poor vascularization and impaired healing.⁶ Co-induction of a tibial fracture and vascular injury in the form of hind limb ischemia in a mouse model increases the chances of a non-union compared to the fracture alone.⁷ Anti-angiogenic treatment to inhibit the initial revascularization response following a critical-size segmental defect also

results in lower levels of bone formation and a higher prevalence of non-union.⁸ Although current gold-standard of autografts and allografts are extensively used in the clinic, these constructs are significantly limited by donor-site morbidity, supply, bioactivity, and risk of infection.⁹ Additionally, the revascularization of these grafts remains limited without micro-surgical procedures which often results in high degrees of local tissue morbidity.^{10,11} Therefore, incorporating cues to augment the vascularization response can greatly enhance the efficacy of these treatments while diminishing their limitations.

Vascular endothelial growth factor (VEGF) has routinely been delivered to increase vascularization *in vivo*. By interacting with two main tyrosine kinase receptors, VEGFR1 and VEGFR2, VEGF destabilizes existing blood vessel walls and allows endothelial cells to proliferate and migrate in the direction of highest VEGF concentration.¹² VEGF is instrumental in bone development as blocking VEGF activity results in reduced angiogenesis, massive chondrocyte death,

Correspondence to: A. J. García, e-mail: andres.garcia@me.gatech.edu

Contract grant sponsor: National Institutes of Health (NIH); contract grant number: R01-AR062368 and R01-AR062920

Contract grant sponsor: Cell and Tissue Engineering NIH Biotechnology Training Grant (to J.R.G.); contract grant number: T32-GM008433

and severely under-developed bone.^{13,14} However, in terms of bone repair, the efficacy of exogenous VEGF in increasing vascularization and associated bone regeneration remains ambiguous. One of the first studies utilizing VEGF for bone treatment demonstrated that continuous delivery of VEGF to a rabbit critical-size defect through an osmotic pump resulted in increased bone formation compared to no VEGF treatment.⁸ Subsequent efforts have focused on engineering scaffolds to deliver VEGF through more practical methodologies. VEGF incorporated into β -tricalcium phosphate and poly(lactic-co-glycolic acid) (PLGA) scaffolds increased blood vessel invasion and bone formation in critical-size defects.^{15,16} Other reports, however, have shown VEGF to induce minimal bone formation despite enhanced blood vessel formation.^{17–21}

Synergistic interactions between VEGF receptors and integrin adhesion receptors provide signals regulating vascularization. For example, blocking antibodies against the α_2 subunit of the collagen-binding $\alpha_2\beta_1$ integrin inhibits VEGF-dependent endothelial cell chemotaxis.²² Consistent with these results, deletion of the β_1 integrin subunit using the Cre-lox system negatively impacts angiogenic sprouting.²² VEGF has also been shown to upregulate endothelial cell surface expression of $\alpha_2\beta_1$.²³ In addition to the $\alpha_2\beta_1$ integrin, the $\alpha_v\beta_3$ integrin plays a central role in angiogenesis and vascularization.^{24–26} While the mechanism of integrin-dependent angiogenesis remains unclear, antagonists to $\alpha_v\beta_3$ have been used to prevent abnormally active angiogenesis within tumors as activated endothelium within these environments exhibit greatly enhanced expression of $\alpha_v\beta_3$.^{27–31} Extensive cross-talk also exists between $\alpha_v\beta_3$ and VEGF as expression of VEGF is in part induced through $\alpha_v\beta_3$ ligation, clustering, and association of the β_3 subunit with phosphorylated p66 Shc.³² The β_3 subunit is also involved in the activation of VEGFR2 in response to VEGF.^{33,34}

Because of the interplay between VEGF and integrins $\alpha_2\beta_1$ and $\alpha_v\beta_3$, the objective of this study was to investigate whether presentation of integrin-specific peptides within a hydrogel in combination with exogenous VEGF modulates vascularization and bone formation in a murine segmental bone defect model. We synthesized protease-degradable poly(ethylene glycol)-based hydrogels functionalized with VEGF and either the collagen I-mimetic $\alpha_2\beta_1$ -targeting GFOGER peptide or the fibronectin-derived $\alpha_v\beta_3$ -targeting RGD peptide. We then implanted these constructs within critical-size murine radial bone defects and evaluated blood vessel formation and newly formed bone tissue. Based on previous studies showing that GFOGER-functionalized biomaterials promote osteoblastic differentiation *in vitro*³⁵ and enhance osseointegration of metal implants in rat tibiae,³⁶ we hypothesized that VEGF-functionalized GFOGER hydrogels would increase vascularization and subsequent bone regeneration compared to VEGF-functionalized RGD hydrogels.

MATERIALS AND METHODS

Poly(ethylene glycol) (PEG) hydrogel synthesis and VEGF release kinetics

Four-arm maleimide-end functionalized poly(ethylene glycol) (PEG) macromer (PEG-MAL 20 kDa MW, Laysan Bio,

>95% purity) was functionalized with recombinant human VEGF-A165 (Invitrogen) for 15 min at room temperature in 10 mM HEPES buffer pH = 7.4 followed by functionalization with either GFOGER peptide, GGYGGGP(GPP)₅GFOGER(GPP)₅GPC (AAPPTec), or RGD peptide (GRGDSPC) (AAPPTec). Functionalized macromers were cross-linked using the bi-cysteine peptide VPM (GCRDVPMSMRGGDRCG) (AAPPTec). The PEG-MAL hydrogels were synthesized to obtain a final concentration of 1.0 mM adhesive peptide and 10 μ g/mL VEGF unless otherwise noted. The concentration of cross-linker used for the synthesis of each hydrogel was calculated by matching the number of cysteine residues on the cross-linker to the number of residual maleimides on the PEG-MAL macromer following adhesive peptide and VEGF functionalization. Hydrogels were allowed to gel at 37°C for 15 min before swelling in phosphate-buffered saline (PBS). For verification of VEGF tethering to the PEG-MAL macromer, the VEGF-PEG-MAL product was run on sodium dodecyl sulfate-polyacrylamide gel electrophoresis (SDS-PAGE) gel followed by protein visualization with Sypro Red (Life Technologies) staining.

To assess VEGF release kinetics, VEGF was labelled with NHS-AlexaFluor 488 (Life Technologies), purified, and incorporated into hydrogels as described. Hydrogels were incubated in either PBS or 50 μ g/mL collagenase (Worthington Biomedical). At specified time points, supernatant was collected and analyzed for fluorescence.

Rheology

The storage and loss moduli of hydrogels were assessed by dynamic oscillatory strain and frequency sweeps performed on a MCR 302 stress-controlled rheometer (Anton Paar, Austria) with a 9 mm diameter, 2° cone, and plate geometry. The hydrogels were synthesized as described and loaded between the cone and plate, after which the measuring system was lowered to a 39 μ m gap. Initial strain amplitude sweeps were performed at an angular frequency of 10 rad s⁻¹ to determine the linear viscoelastic range of the hydrogel. Oscillatory frequency sweeps were then used to examine the storage and loss moduli (ω = 0.5–100 rad s⁻¹) at a strain of 1%.

Bioactivity of PEGylated VEGF

Human umbilical vein endothelial cells (HUVECs, Lonza) were grown in complete endothelial growth media, EGM-2 (Lonza). Cells were synchronized in growth factor-free basal media (endothelial basal medium-2 (EBM-2), Lonza) with 1% fetal bovine serum (FBS) for 8 hr followed by addition of soluble VEGF, VEGF-conjugated PEG-MAL macromer, or control (VEGF-free) media for 48 hr. Cell metabolic activity was measured using CellTiter 96 Aqueous One Solution Cell Proliferation Assay (Promega). To assess the activity of endothelial cells on VEGF-functionalized hydrogels, GFOGER-modified hydrogels were synthesized with or without incorporated VEGF. HUVECs were seeded at 10,000 cells/cm² and incubated for 4, 8 or 15 hr. Samples were fixed in 3.7% paraformaldehyde, stained with AlexaFluor 488-conjugated phalloidin and 4',6-diamidino-2-phenylindole (DAPI), and

imaged on a Nikon C2 confocal microscope. Endothelial cell network length and cell numbers were quantified using a custom macro in ImageJ.

3D endothelial cell network formation. To study 3D endothelial cell network assembly, a co-culture of green fluorescent protein (GFP)-expressing HUVECs (Angioprotemie) and mouse embryo 10T1/2 cells (ATCC) was used. GFP-expressing HUVECs and 10T1/2 cells were encapsulated in PEG-MAL hydrogels presenting either GFOGER or RGD at final cell densities of 4×10^6 cells/mL for 10T1/2 cells and 15×10^6 cells/mL for HUVECs. For gels containing VEGF, gels were incubated in EGM-2 media without supplemented VEGF. For gels synthesized without VEGF, gels were incubated in EGM-2 media with or without soluble VEGF. The cell-laden hydrogels were cultured for 48 hr, rinsed, and fixed in 3.7% paraformaldehyde. GFP-expressing HUVECs were imaged on a Nikon C2 confocal microscope and 3D network formation analyzed using a custom ImageJ macro.

Bone defect surgery

A critical-size bone defect model in the mouse radius was used to evaluate bone formation as previously described.³⁷ All animal experiments were performed with the approval of the Georgia Tech Animal Care and Use Committee within the guidelines of the Guide for the Care and Use of Laboratory Animals. C57BL/6J wild-type male mice (8–10 weeks old, Jackson Laboratories) were anesthetized under isoflurane and fur was removed from the right forelimb. Prior to surgery, mice were administered a single dose of slow-release buprenorphine for pain relief. The right forelimb was then swabbed with chlorhexidine and alcohol, and a 1.5 cm incision was made in the skin. Muscle tissue surrounding the ulna and radius was dissected away, and a 2.5 mm complete excision in the radius was made using a custom-built bone cutter. 3.0 μ L of hydrogel was cast within a 4-mm long polyimide sleeve with four rows of laser machined holes spaced 200 μ m apart to improve cell invasion and nutrient transport. This sleeve was used to hold the hydrogel within the defect, and we previously showed that the sleeve does not interfere with the bone healing process.³⁷ The hydrogel-containing sleeve was then carefully inserted over the ends of the defect, the soft tissue repositioned over the bone and the incision was closed using Vicryl sutures. Mice were monitored post-surgery for lethargy, weight loss, normal eating habits, and signs of distress.

Micro computed tomography (MicroCT) angiography

Animals were euthanized by CO₂ inhalation at 8 weeks post-surgery. Radiopaque contrast agent-enhanced microCT angiography was performed using a protocol modified from Phelps et al.^{38–40} Briefly, an incision was made across the lower abdomen of the mouse followed by a continuing incision up the midline of the mouse exposing the entire abdominal cavity. The thoracic cavity was cut to carefully expose the heart. A butterfly needle was inserted into the left ventricle followed by cutting of the lower vena cava. Mice were then sequentially perfused with saline, 10% neutral buffered

formalin, saline, and lead chromate-based radiopaque contrast agent at a 30:60:10 v/v mixture of MV-122 Yellow: MV-diluent: MV curing agent (Microfill MV-122, Flow Tech). Samples were kept at 4°C overnight to allow the contrast agent to polymerize, and the forearms were then incubated for 72 hr in Krajan decalcification solution (Ricca Chemical), rinsed with PBS, and scanned using a μ CT50 scanning system (7 μ m resolution, 55 kVp, 145 μ A, Scanco Medical).

Immunohistochemistry

Following euthanasia by CO₂ inhalation, the ulna and radius were excised and fixed in 10% neutral-buffered formalin, decalcified using Krajan decalcification solution, processed for paraffin embedding and embedded in paraffin wax. Sections (5 μ m thick) were deparaffinized and incubated in antigen retrieval solution (10 mM sodium citrate buffer, pH = 6.0) overnight at 60°C. Sections were then stained with either rabbit anti-endomucin or rat anti-CD31 antibodies overnight at 4°C followed by secondary staining with AlexaFluor 488- and AlexaFluor 555-conjugated goat antibodies for 1 hr at room temperature. Sections were imaged on a Nikon C2 confocal microscope.

VEGF and fibroblast growth factor-2 (FGF-2) secretion

Human mesenchymal stem cells (hMSCs, Texas A&M University) were grown in alpha-minimum essential media (α -MEM) containing 16% FBS, 2 mM L-glutamine, 100 U/mL penicillin, and 100 μ g/mL streptomycin. hMSCs were encapsulated in VEGF-free integrin-specific hydrogels at a concentration of 5×10^6 cells/mL and cultured for 24 hr in growth media. After 24 hr, the media was exchanged for osteogenic media (growth media with 10 nM dexamethasone, 20 mM Na- β -glycerolphosphate, and 50 μ M L-ascorbic acid 2-phosphate). After 7 days in culture, the conditioned media was collected and assayed for VEGF and FGF-2 levels using enzyme-linked immunosorbent assay (ELISA) (Life Technologies).

MicroCT imaging of bone formation

In vivo microCT imaging was performed on anesthetized mice using a VivaCT imaging system (Scanco Medical) at a voltage of 55 kVp and a current of 142 μ A. Mice were centered such that the 2.5 mm radial defect was scanned within a 3.2 mm scan length window. Bone volume was evaluated as previously described.³⁷ Briefly, 2D slices were contoured to solely include the radius followed by application of a Gaussian filter (sigma = 1, support = 1, and threshold = 540 mg HA/ccm). While 3D reconstructions displayed the full 3.2 mm scanned length, only the middle 2.0 mm of the defect was analyzed for bone volume.

Statistics

Error bars on graphs represent standard error of the mean (SEM). Comparisons among multiple groups were performed by one-way analysis of variance (ANOVA) with post-hoc Tukey tests. Comparisons between two groups were done through a *t* test in GraphPad Prism 6. A *p* values of <0.05 was considered significant.

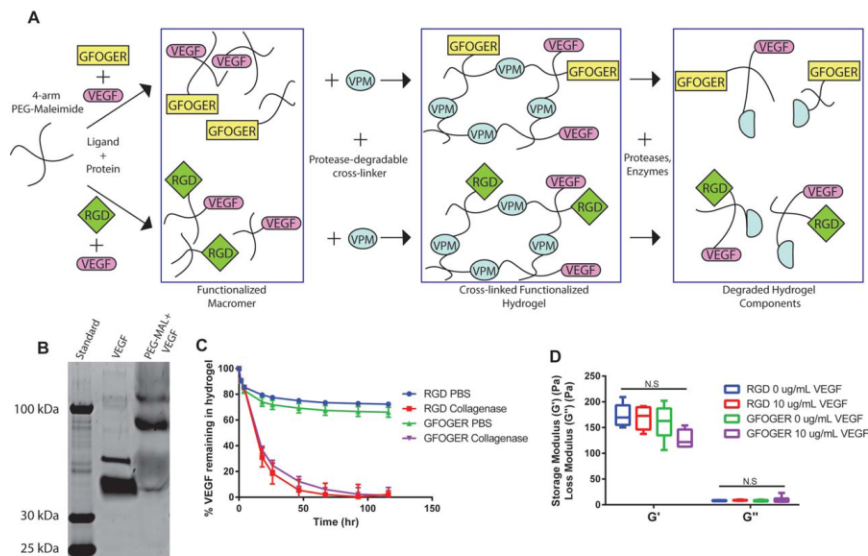


FIGURE 1. Protease-degradable integrin-specific PEG-MAL hydrogels for degradation-dependent release of covalently-tethered VEGF. (A) Schematic detailing PEG-MAL synthesis, stoichiometric ligand functionalization, and growth factor incorporation. (B) Gel electrophoresis of VEGF and PEG-MAL + VEGF demonstrating increased MW of VEGF tethered onto PEG-MAL macromer. (C) VEGF release profile from integrin-specific hydrogels treated in PBS or collagenase as measured through fluorescence (Mean \pm SEM $n = 4$). (D) Rheological properties of integrin-specific hydrogels measured through storage and loss moduli from dynamic oscillatory frequency tests (Box-whisker plot show min-max, $n = 6$). N.S.: not significant.

RESULTS

Synthesis and characterization of VEGF-releasing PEG-MAL hydrogels

We engineered hydrogels based on a maleimide-functionalized 4-arm PEG macromer, which allows for peptide tethering onto the polymer precursor via a Michael-type addition reaction between the terminal-maleimide group and free thiols present on the biomolecules. Subsequent reaction with bi-cysteine cross-linking peptides (VPM) containing a protease cleavage site resulted in the formation of a cross-linked PEG hydrogel network sensitive to protease degradation [Fig. 1(A)]. Prior to cross-linking, the PEG-MAL macromer was functionalized with VEGF by reacting the cysteine available for conjugation on VEGF₁₆₅ to the maleimide moiety on the PEG macromer.⁴¹ The VEGF-functionalized macromer was further reacted with either the RGD or GFOGER cell adhesion peptides in order to investigate the coupled effects of biomaterials-based VEGF delivery and integrin-specificity on vascularization and bone regeneration. By design, covalent incorporation of VEGF onto the hydrogel backbone provides for cell-demanded release of VEGF as the construct degrades. Covalent tethering of VEGF to the PEG-MAL macromer was verified through the expected increase in molecular weight for VEGF reacted with PEG-MAL macromer [Fig. 1(B)].

To determine the kinetics of VEGF release from integrin-specific hydrogels *in vitro*, VEGF was fluorescently labelled and incorporated into RGD- or GFOGER-functionalized hydrogels. Hydrogels subjected to collagenase treatment degraded within the first 48 hr and released 100% of the incorporated VEGF [Fig. 1(C)]. The high collagenase concentration used was selected to fully degrade the gel by 2–3 days; we expect slower *in vivo* protease-dependent degradation kinetics. In contrast, hydrogels incubated in PBS remained intact and, following an initial burst release due to hydrogel swelling, retained approximately 70% of the loaded VEGF over a period of 5 days. The loss of approximately 30% of loaded VEGF is attributed to incomplete covalent tethering of VEGF onto the PEG-MAL macromer as shown by the low intensity band on the SDS-PAGE gel at the molecular weight (MW) of unconjugated VEGF in the PEG-MAL + VEGF lane [Fig. 1(B)]. To investigate whether adhesive peptide or VEGF incorporation influences the hydrogel's mechanical properties, we performed dynamic oscillatory rheological testing to assess the storage (G') and loss (G'') moduli of the different hydrogel conditions [Fig. 1(D)]. Importantly, no significant differences in moduli were detected among the hydrogel conditions tested (average storage and loss moduli equal to 160 ± 6.3 and 8.1 ± 0.69 Pa, respectively).

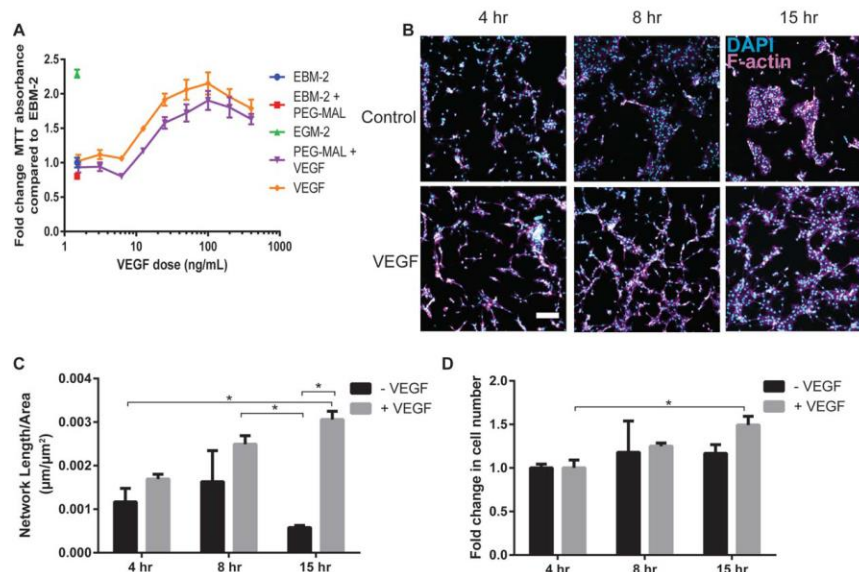


FIGURE 2. Bioactivity of PEGylated VEGF. (A) Endothelial cell metabolic assay for VEGF versus PEG-MAL-VEGF (Mean \pm SEM $n = 6$). (B) Images of endothelial cell networks on top of GFOGER-functionalized hydrogels either functionalized with (VEGF) or lacking VEGF (Control) over 15 hr (Scale bar = 200 μ m, DAPI = cyan, F-actin = magenta). (C) Quantification of endothelial cell network length measured through custom ImageJ macro. (Mean \pm SEM $n = 4$). (D) Quantification of endothelial nuclei count (Mean \pm SEM $n = 4$) * $p < 0.05$.

Bioactivity of PEGylated and hydrogel-tethered VEGF

We next investigated the bioactivity of VEGF tethered to the PEG-MAL macromer. HUVECs cultured in media containing either PEG-MAL-conjugated or unmodified VEGF displayed similar dose-dependent responses in metabolic activity over the course of 48 hr [Fig. 2(A)]. This result indicates that VEGF tethered to the PEG-MAL macromer retains bioactivity and that the PEG macromer does not interfere with VEGF-dependent signaling.

We further examined the bioactivity of VEGF tethered to hydrogels by assessing the proliferation and network formation of endothelial cells cultured on top of hydrogels with either soluble or tether VEGF. GFOGER-functionalized hydrogels supported cell adhesion regardless of VEGF incorporation [Fig. 2(B)]. By 8 and 15 hr after seeding, endothelial cells adhering to VEGF-containing hydrogels exhibited elevated levels of network formation compared to hydrogels lacking VEGF [Fig. 2(B,C)]. By quantifying the number of nuclei, we also found a significant increase in the number of endothelial cells on VEGF-containing hydrogels compared to VEGF-free gels [Fig. 2(D)]. Taken together, these results show that tethering VEGF to the PEG-MAL macromer either in soluble form or after incorporation into a hydrogel network maintains the bioactivity of VEGF in regards to endothelial cell activity.

Integrin-dependent 3D endothelial cell tubulogenesis

After confirming the biological activity of PEGylated VEGF, we examined the effect of different integrin ligands in conjunction with VEGF presentation on the vasculogenic response to these materials. We used a model for 3D vascular tubulogenesis consisting of GFP-expressing HUVECs encapsulated with 10T1/2 cells, which act as a supporting pericyte-like cell, in hydrogels functionalized with either the GFOGER or RGD adhesive peptide. For both adhesive peptides, endothelial cells encapsulated within VEGF-free hydrogels and cultured in VEGF-free media exhibited minimal tubulogenesis as the cells remained largely rounded and failed to form protrusions to adjacent cells [Fig. 3(A)]. In contrast, endothelial cells cultured in the presence of soluble VEGF in the media showed increased network formation in both RGD and GFOGER hydrogels [Fig. 3(B)]. Importantly, VEGF-containing hydrogels cultured in VEGF-free media displayed enhanced endothelial cell-based network formation compared to hydrogels in VEGF-free conditions for both RGD- and GFOGER-functionalized hydrogels [Fig. 3(B)]. For GFOGER-functionalized hydrogels, VEGF containing hydrogels exhibited similar levels of increased network formation compared to that of GFOGER-functionalized hydrogels cultured in VEGF-containing media. VEGF-containing RGD-functionalized hydrogels displayed elevated network formation

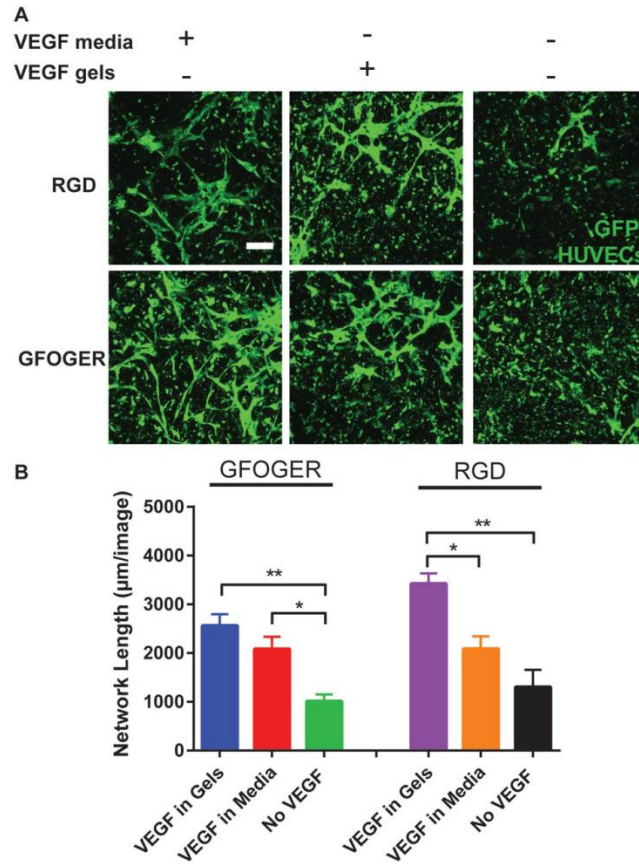


FIGURE 3. Integrin-specific hydrogels demonstrate VEGF-dependent increases in 3D endothelial cell network formation. (A) Projected Z-stack images of GFP-HUVECs cultured in either media containing VEGF, hydrogels containing VEGF or VEGF-free conditions for 3 days (scale bar = 200 μm). (B) Quantification of 3D network length in varying conditions (Mean ± SEM $n=5$). * $p < 0.05$, ** $p < 0.01$.

compared to RGD hydrogels in VEGF-free conditions and RGD hydrogels cultured in media with VEGF [Fig. 3(B)]. Taken together, the data demonstrates that hydrogels containing VEGF induce similar levels of endothelial cell tubulogenesis *in vitro* compared to soluble VEGF present in the media. Furthermore, this increase in tubulogenesis is independent of the adhesive peptide presented in the hydrogel.

Effects of integrin specificity and VEGF incorporation on vascularization

We evaluated the potential of VEGF-functionalized hydrogels presenting integrin-specific peptides to enhance vascularization in a murine critical-size radial bone defect model. We

tested two different VEGF doses (50 and 250 ng, referred to as low and high doses, respectively) as well as hydrogels lacking VEGF (0 ng) for both RGD and GFOGER-functionalized hydrogels. Hydrogels were implanted into 2.5 mm long unilateral murine radial defects and evaluated for vascular morphometric parameters within the bone defect area at 8 weeks via micro-computed tomographic (microCT) analysis of a perfused radiopaque polymer [Fig. 4(A)]. Importantly, this technique measures functional vasculature connected to the host vasculature as the radiopaque polymer is perfused through the left ventricle and exits out the inferior vena cava to perfuse the vasculature. VEGF-free, RGD hydrogels exhibited very low levels of

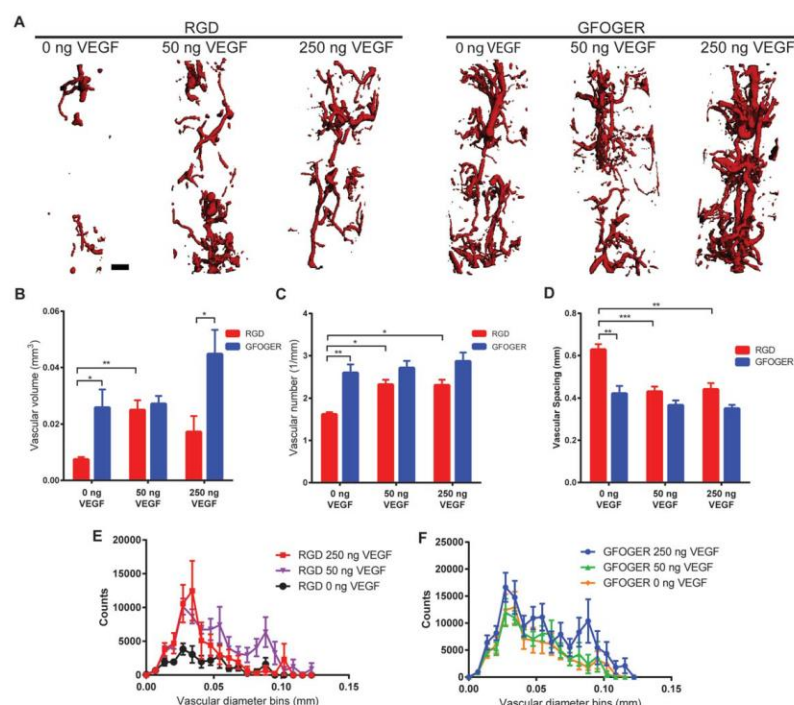


FIGURE 4. Vascularization of bone defects. (A) Representative 3D reconstructions of vascular structures within the bone defect for different adhesive peptides and VEGF doses (scale bar = 200 μ m). (B-D) Vascular volume, number, and spacing in bone defect respectively. (E,F) Vascular diameter histogram indicating blood vessel size distribution. (Mean \pm SEM $n = 5-8$). * $p < 0.05$, ** $p < 0.01$, *** $p < 0.001$.

vascularization [Fig. 4(A)]. With low and high doses of VEGF, RGD hydrogels exhibited significantly increased vessel number as well as significantly decreased vessel spacing denoting a higher density of vessels for both VEGF doses [Fig. 4(C,D)]. Low doses of VEGF also significantly increased the total blood vessel volume and resulted in higher frequency of both small diameter (25–50 μ m) and larger diameter vessels (80–100 μ m) compared to VEGF-free RGD hydrogels [Fig. 4(B,E)].

Remarkably, VEGF-free GFOGER hydrogels displayed significantly increased vascularization across all quantified parameters (vessel volume, number, and spacing) compared to VEGF-free RGD hydrogels [Fig. 4(B–D)]. The levels of vascularization present within VEGF-free GFOGER hydrogels were equivalent to those of VEGF-containing RGD hydrogels. Furthermore, at high VEGF doses, while GFOGER and RGD hydrogels showed similar levels of vascular number and spacing, GFOGER hydrogels demonstrated elevated levels of total vascular volume compared to those of RGD hydrogels. The high levels of vascularization exhibited in GFOGER

hydrogels were insensitive to delivery of either dose of exogenous VEGF as shown by the equivalent levels of vessel volume, spacing, and number [Fig. 4(B–D)]. Whereas, no differences were seen in these parameters, high doses of VEGF did increase the frequency of larger diameter vessels for GFOGER hydrogels compared to VEGF-free and low VEGF dose conditions [Fig. 4(F)]. Taken together, the microCT vascular analysis shows that for growth-factor free conditions, RGD hydrogels result in poor vascularization; however, addition of VEGF to these hydrogels increases vascularization of these bone defects. In contrast, GFOGER hydrogels show elevated levels of vascularization regardless of delivery of exogenous VEGF. The observation that VEGF-free GFOGER hydrogels show significantly increased vascularization compared to VEGF-free RGD hydrogels and similar levels of vascularization compared to low dose VEGF-delivering RGD hydrogels emphasizes the importance of integrin-specificity in these biomaterials. By simply functionalizing scaffolds with differing integrin-specific ligands, robust increases in vascularization can be achieved.

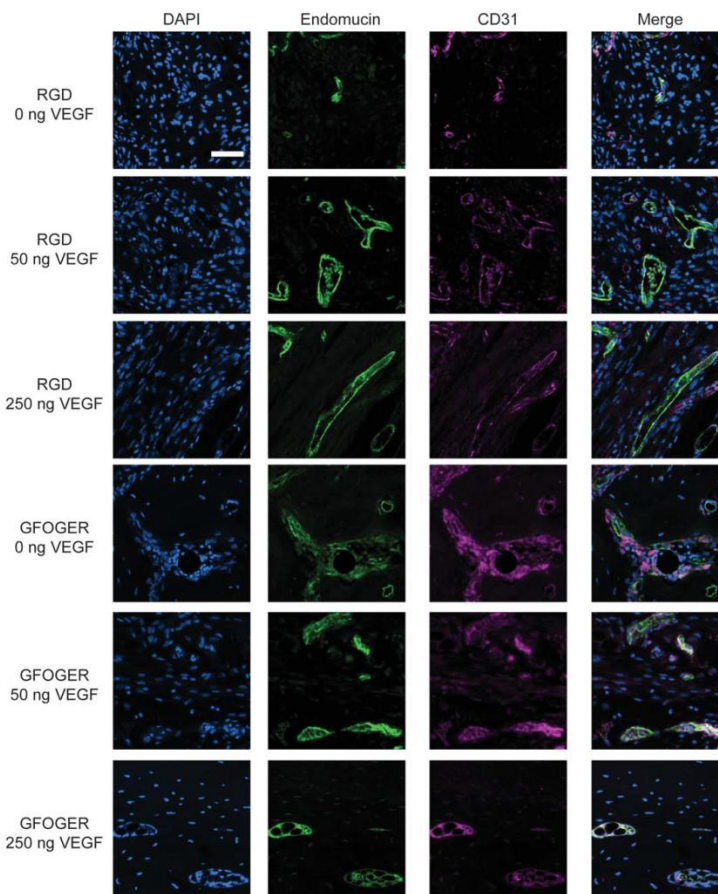


FIGURE 5. Representative images of endomucin and CD31 staining in bone defect samples. (scale bar – 50 μ m).

We also performed immunostaining for CD31 and endomucin, which are specific markers for endothelial cells within capillary networks⁴² (Fig. 5). RGD hydrogels having low and high doses of VEGF exhibited increased levels of CD31 and endomucin staining compared to VEGF-free RGD hydrogels. The staining also showed the presence of larger diameter vessels in the low dose group compared to the high dose group and VEGF-free gels, in agreement with the microCT vascular analyses. GFOGER hydrogels displayed robust staining for CD31 and endomucin independent of the VEGF dose. The histological analysis is fully consistent with the microCT results showing VEGF dose-dependent increases in endothelial markers for RGD hydrogels and no

VEGF-dependence in GFOGER hydrogels, underscoring the importance of integrin-specificity in the vascularization response to these biomaterials.

Effects of integrin-specificity on vasculogenic protein secretion by hMSCs

A major finding from the *in vivo* vascularization study is the enhancement in vascularization for defects treated with GFOGER-functionalized hydrogels compared to RGD-presenting gels. The network formation assay showed no differences in endothelial cell tubulogenesis between these two integrin-specific ligands (Fig. 3). Therefore, we investigated whether integrin binding specificity could influence

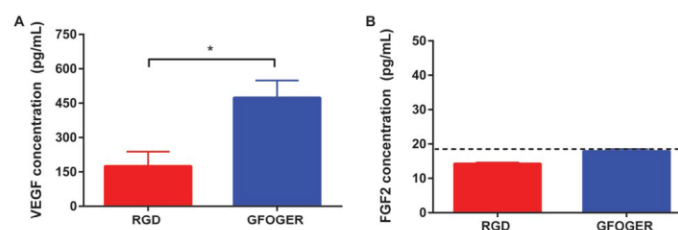


FIGURE 6. hMSCs encapsulated within GFOGER-functionalized hydrogels exhibit enhanced secretion of VEGF compared to hMSCs encapsulated within RGD-functionalized hydrogels. (A,B) Quantification of VEGF or FGF-2 in the supernatant of hMSCs encapsulated within integrin-specific hydrogels in osteogenic differentiation conditions (Mean \pm SEM $n=4$). Dotted line indicates reliable limit of detection. * $p < 0.05$.

the vasculogenic potential of non-endothelial cells such as mesenchymal stem cells (MSCs). During bone repair, MSCs secrete paracrine factors that increase the recruitment and proliferation of endothelial cells to form functional neovessels.^{43,44} Due to the influx of MSCs and osteoprogenitors immediately after bone injury,⁴⁵ we speculated that differential integrin binding could result in differences in secreted factors by MSCs. We thus investigated the effect of integrin-specificity on the secretion of angiogenic proteins from MSCs encapsulated within GFOGER or RGD-functionalized hydrogels. Integrin-specific hydrogels containing human MSCs were cultured in osteogenic media for 7 days after which the conditioned media was analyzed for VEGF and FGF-2 levels. Conditioned media from GFOGER hydrogels showed a significantly elevated concentration of VEGF when compared to that of RGD hydrogels [Fig. 6(A)]. The GFOGER-dependent upregulation in angiogenic factor secretion was specific to VEGF, as secretion of FGF-2 was below the limit of detection of the assay for both GFOGER and RGD hydrogels [Fig. 6(B)]. These results demonstrate that MSCs cultured within hydrogels presenting the $\alpha_2\beta_1$ -specific GFOGER secrete higher levels of VEGF compared to that of MSCs cultured in RGD hydrogels. This finding provides an explanation for the enhancements in vascularization observed in bone defects treated with GFOGER-functionalized hydrogels compared to defects treated with RGD-presenting hydrogels.

Effect of VEGF-delivering hydrogels on bone repair

We next analyzed the effects of VEGF delivery within integrin-specific hydrogels on the repair of non-healing bone defects. Hydrogel conditions and surgical procedures were consistent with the vascularization study, and bone healing was evaluated by microCT at 4 and 8 weeks post-surgery. Bone defects treated with VEGF-free GFOGER-modified hydrogels exhibited 3–4 fold higher bone volume compared to those treated with VEGF-free RGD-modified hydrogels at 4 and 8 weeks post-surgery [Fig. 7(B,D)]. For GFOGER hydrogels, VEGF had no significant effect on bone formation at 4 and 8 weeks post-surgery, consistent with the vascularization analyses. For RGD hydrogels, low doses of VEGF significantly increased bone volume at 4 weeks,

whereas high doses of VEGF showed similar levels of bone volume compared to VEGF-free RGD hydrogels. However, by 8 weeks post-surgery, there were no differences among VEGF-containing and VEGF-free RGD hydrogels [Fig. 7(B,D)]. These results demonstrate that in VEGF-free conditions, GFOGER hydrogels exhibit significantly increased bone formation compared to RGD hydrogels. Additionally, although increases in vascularization are noted, especially within RGD hydrogels, delivery of exogenous VEGF does not enhance bone repair in this murine critical-size defect for either integrin-specific hydrogel.

DISCUSSION

Non-healing bone defects and fractures represent a serious clinical problem with over 1 million surgical procedures necessitating bone grafts performed annually in the USA alone and costing over \$5 billion.⁴⁶ While the creation of a functional vascular network is considered a crucial factor in successful regeneration of bone defects, it is still unclear whether delivery of vasculogenic factors such as VEGF enhances bone repair.^{8,16,17,47} Additionally, while the role that integrins play in the progression of angiogenesis in tumors has been of particular interest recently,⁴⁸ the ability of integrin binding to direct vascularization in the context of biomaterial-directed tissue repair has not been investigated. In this study, we examined whether incorporation of VEGF into synthetic hydrogels functionalized with either the $\alpha_2\beta_1$ integrin-targeting GFOGER ligand or the RGD peptide that mainly binds to $\alpha_v\beta_3$ integrin modulates both the vascularization and bone regeneration of critical-size bone defects.

Controlled and sustained delivery of VEGF constitutes an important parameter in the design of the hydrogel. In the strategy described here, VEGF is covalently tethered to the hydrogel precursor thus allowing for high retention efficiency once cross-linked. The protease-sensitive nature of the cross-linked material provides for controlled release of VEGF based on cell-mediated invasion and degradation of the hydrogel. Another crucial parameter when designing a growth-factor based release system is retaining the biological activity of the protein. For delivery vehicles based on the encapsulation of proteins within solid matrices such as microparticles, the bioactivity of the protein is likely

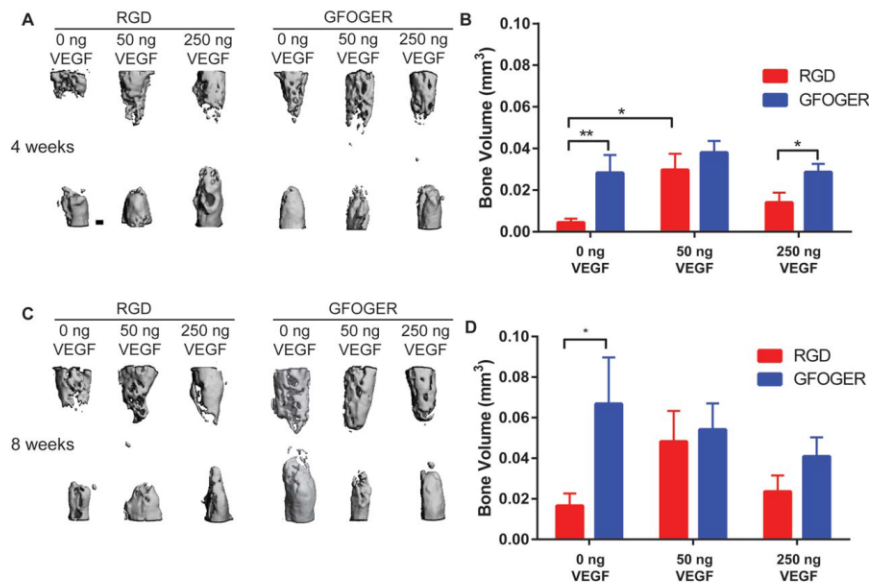


FIGURE 7. Bone volume for bone defects treated with VEGF-containing hydrogels. (A,C) Representative 3D reconstructions of radial defect at 4 and 8 weeks, respectively, with differing ligand and VEGF doses (scale bar = 200 μ m). (B,D) Quantification of bone volume of defects at 4 and 8 weeks, respectively. (Mean \pm SEM $n = 7-9$). * $p < 0.05$, ** $p < 0.01$.

reduced.⁴⁹ In the described system, VEGF remains in a hydrated state throughout gelation. Furthermore, the conjugation of the PEG macromer to free thiols within VEGF does not affect the protein's biological activity as endothelial cells exhibited heightened 3D network formation when encapsulated within VEGF-tethered hydrogels compared to those in VEGF-free conditions.

Whereas no differences were observed for *in vitro* endothelial network formation between integrin-specific hydrogels, significant differences were observed in the vascularization of bone defects *in vivo* for hydrogels presenting different adhesive peptides. For VEGF-free conditions, GFOGER-functionalized hydrogels exhibited significantly increased vascular volume and density compared to RGD-functionalized hydrogels. This difference may be attributed to multiple factors. Activation of the $\alpha_2\beta_1$ integrin has been reported to increase osteogenic activity resulting in increased pro-angiogenic signals as osteoblasts and osteoprogenitors secrete large quantities of VEGF to support the survival and proliferation of surrounding endothelial cells.⁵⁰⁻⁵² This observation potentially explains the findings that VEGF-free GFOGER-functionalized hydrogels produce higher bone regeneration *in vivo* compared to VEGF-free RGD-functionalized hydrogels. Additionally, while the $\alpha_v\beta_3$ integrin has often been implicated in angiogenesis, more recent studies have shown that the role of this integrin in vascularization is con-

text-dependent.⁵³ Depending on the environment, cell type, and which molecules the integrin interacts with, the $\alpha_v\beta_3$ integrin can play either a pro- or anti-angiogenic role.⁵⁴⁻⁵⁶

For hydrogels incorporating VEGF, RGD hydrogels exhibited increases in blood vessel volume, number, and density within the bone defect area compared to VEGF-free controls. This result is consistent with the well-established cross-talk between the β_3 integrin subunit and VEGFR2. Mutation of the cytoplasmic tail of the β_3 integrin results in impaired interactions with VEGFR2, which leads to inefficient phosphorylation of the dimerized VEGFR2 complex.³³ Downstream activation of focal adhesion kinase (FAK) and c-Jun N-terminal kinase (JNK) signaling pathways from VEGFR2 activity is also dependent on the co-activation of the $\alpha_v\beta_3$ integrin.⁵⁷ The ability for RGD hydrogels to activate the $\alpha_v\beta_3$ integrin could thus cause heightened sensitivity to the presence of VEGF within the defect microenvironment. In contrast, the level of vascularization for GFOGER-functionalized hydrogels was independent of VEGF dose, with VEGF-free as well as low and high doses of VEGF exhibiting high levels of vascularization. Notably, when MSCs were encapsulated within GFOGER hydrogels *in vitro*, the cells exhibited increased secretion of VEGF compared to those encapsulated within RGD hydrogels. This finding provides an explanation as to why *in vivo* vascularization in GFOGER hydrogels was elevated and insensitive to

exogenous VEGF as the interaction between the hydrogel and invading MSCs may provide abundant levels of endogenous VEGF. Overall, the finding that VEGF-free, GFOGER hydrogels show elevated levels of *in vivo* vascularization compared to VEGF-free, RGD hydrogels and similar levels of vascularization compared to VEGF-containing RGD hydrogels is noteworthy. The ability for integrin-specificity alone to instruct and guide levels of vasculogenesis and regulate biological activity of vasculogenic proteins highlights the importance of exploiting integrin-specificity in regenerative medicine applications. With the expensive and often significant regulatory issues associated with growth factor therapies, the ability to engineer scaffolds to reduce or completely eliminate the need for growth factors through simple functionalization techniques can greatly enhance the clinical efficacy of future regenerative medicine constructs.

In addition to differences in vascularization for the integrin-specific hydrogels, integrin specificity also played a role in the regeneration of bone within the critical-size defects. VEGF-free, GFOGER-functionalized hydrogels exhibited higher bone repair at both 4 and 8 weeks in comparison to VEGF-free RGD-presenting hydrogels. Addition of VEGF, however, had no effect on bone formation at 8 weeks indicating that exogenously delivered VEGF is not sufficient to repair critical-size bone defects in this model. This conclusion does not rule out an important role for VEGF in bone repair. On the contrary, endogenous VEGF is necessary for bone repair as treatment with VEGF blocking antibodies inhibits the healing of bone defects.⁸ Furthermore, mice lacking the VEGF₁₆₅ and VEGF₁₈₈ isoforms show abnormal vascular patterning along with significant decreases in trabecular bone volume and bone growth.⁵⁸ However, in terms of delivering exogenous VEGF to regenerate bone defects, studies demonstrate conflicting results with some reports showing enhanced bone formation while others showing no effect after delivery of VEGF.^{15–18,59,60} The inconsistencies between these reports could be related to the *in vivo* model, scaffold, or delivery kinetics. Exploration into strategies utilizing VEGF in conjunction with other stimuli such as other growth factors (e.g., BMP-2), further scaffold engineering, cell therapy or gene therapy could enhance its effects.

CONCLUSION

While endogenous VEGF is known to be essential to osteogenesis, the ability of exogenously delivered VEGF to significantly repair bone defects remains ambiguous. In this study, we investigated whether integrin-specific biomaterials could constitute a crucial, yet, up to now, unexplored role in vascularization and osteogenesis in bone defects. VEGF-free GFOGER-presenting hydrogels exhibited significantly increased vascularization and bone formation in a non-healing segmental bone defect compared to RGD-functionalized hydrogels. Furthermore, RGD-presenting hydrogels exhibited exogenous VEGF dose dependent increases in vascularization. Nevertheless, addition of VEGF to these hydrogels did not enhance bone repair in this bone defect model. This study demon-

strates interplay between biomaterial integrin specificity and VEGF in tissue vascularization.

ACKNOWLEDGMENT

The authors thank Dr. Nick Willet for his assistance with the Microfill perfusion technique.

REFERENCES

- Garcia JR, Garcia AJ. Biomaterial-mediated strategies targeting vascularization for bone repair. *Drug Deliv Transl Res* 2015; 1–19, doi:10.1007/s13346-015-0236-0.
- Rao RR, Stegemann JP. Cell-based approaches to the engineering of vascularized bone tissue. *Cytotherapy* 2013;15:1309–1322.
- Nguyen LH, Annabi N, Nickbarg M, Bae H, Binan L, Park S, Kang Y, Yang Y, Khademhosseini A. Vascularized bone tissue engineering: Approaches for potential improvement. *Tissue Eng Part B Rev* 2012;18:363–382.
- Mackie EJ, Ahmed YA, Tatarczuch L, Chen KS, Mirams M. Endochondral ossification: How cartilage is converted into bone in the developing skeleton. *Int J Biochem Cell Biol* 2008;40:46–62.
- Zhou Z, Apte SS, Soininen R, Cao R, Baaklini GY, Rauser RW, Wang J, Cao Y, Tryggvason K. Impaired endochondral ossification and angiogenesis in mice deficient in membrane-type matrix metalloproteinase 1. *Proc Natl Acad Sci USA* 2000;97:4052–4057.
- Carano RA, Filvaroff EH. Angiogenesis and bone repair. *Drug Discov Today* 2003;8:980–989.
- Lu C, Miclau T, Hu D, Marcucio RS. Ischemia leads to delayed union during fracture healing: A mouse model. *J Orthop Res* 2007;25:51–61.
- Street J, Bao M, deGuzman L, Bunting S, Peale FV, Jr, Ferrara N, Steinmetz H, Hoeffel J, Cleland JL Daugherty A, van Bruggen N, Redmond HP, Carano RA, Filvaroff EH. Vascular endothelial growth factor stimulates bone repair by promoting angiogenesis and bone turnover. *Proc Natl Acad Sci USA* 2002;99:9656–9661.
- Giannoudis PV, Dinopoulos H, Tsiridis E. Bone substitutes: An update. *Injury* 2005;36(Suppl 3):S20–S27.
- Finkemeier CG. Bone-grafting and bone-graft substitutes. *J Bone Joint Surg Am* 2002;84A:454–464.
- Frohlich M, Grayson WL, Wan LO, Marolt D, Drobnic M, Vunjak-Novakovic G. Tissue engineered bone grafts: Biological requirements, tissue culture, and clinical relevance. *Curr Stem Cell Res Ther* 2008;3:254–264.
- Ferrara N, Gerber HP, LeCouter J. The biology of VEGF and its receptors. *Nat Med* 2003;9:669–676.
- Carlevaro MF, Cermelli S, Cancedda R, Descalzi Cancedda F. Vascular endothelial growth factor (VEGF) in cartilage neovascularization and chondrocyte differentiation: Auto-paracrine role during endochondral bone formation. *J Cell Sci* 2000;113(Pt 1):59–69.
- Zelzer E, Mamluk R, Ferrara N, Johnson RS, Schipani E, Olsen BR. VEGFA is necessary for chondrocyte survival during bone development. *Development* 2004;131:2161–2171.
- Wernike E, Montjovent MO, Liu Y, Wismeyer D, Hunziker EB, Siebenrock KA, Hofstetter W, Klenke FM. VEGF incorporated into calcium phosphate ceramics promotes vascularisation and bone formation *in vivo*. *Eur Cell Mater* 2010;19:30–40.
- Leach JK, Kaigler D, Wang Z, Krebsbach PH, Mooney DJ. Coating of VEGF-releasing scaffolds with bioactive glass for angiogenesis and bone regeneration. *Biomaterials* 2006;27:3249–3255.
- Patel ZS, Young S, Tabata Y, Jansen JA, Wong ME, Mikos AG. Dual delivery of an angiogenic and an osteogenic growth factor for bone regeneration in a critical size defect model. *Bone* 2008;43:931–940.
- Young S, Patel ZS, Kretlow JD, Murphy MB, Mountziaris PM, Baggett LS, Ueda H, Tabata Y, Jansen JA, Wong M, Mikos AG. Dose effect of dual delivery of vascular endothelial growth factor and bone morphogenetic protein-2 on bone regeneration in a rat critical-size defect model. *Tissue Eng Part A* 2009;15:2347–2362.
- Hernandez A, Reyes R, Sanchez E, Rodriguez-Evora M, Delgado A, Evora C. *In vivo* osteogenic response to different ratios of BMP-2 and VEGF released from a biodegradable porous system. *J Biomed Mater Res A* 2012;100:2382–2391.
- Geuze RE, Theyse LF, Kempen DH, Hazewinkel HA, Kraak HY, Oner FC, Dhert WJ, Alblas J. A differential effect of bone

- morphogenetic protein-2 and vascular endothelial growth factor release timing on osteogenesis at ectopic and orthotopic sites in a large-animal model. *Tissue Eng Part A* 2012;18(19–20):2052–2062.
21. De la Riva B, Sanchez E, Hernandez A, Reyes R, Tamimi F, Lopez-Cabarcos E, Delgado A, Evora C. Local controlled release of VEGF and PDGF from a combined brushite-chitosan system enhances bone regeneration. *J Control Release* 2010;143:45–52.
 22. Senger DR, Ferruzzi CA, Streit M, Kotliansky VE, de Fougerolles AR, Detmar M. The alpha(1)beta(1) and alpha(2)beta(1) integrins provide critical support for vascular endothelial growth factor signaling, endothelial cell migration, and tumor angiogenesis. *Am J Pathol* 2002;160:195–204.
 23. Senger DR, Claffey KP, Benes JE, Perruzzi CA, Sergiou AP, Detmar M. Angiogenesis promoted by vascular endothelial growth factor: Regulation through alpha1beta1 and alpha2beta1 integrins. *Proc Natl Acad Sci USA* 1997;94:13612–13617.
 24. Brooks PC, Clark RA, Cheresh DA. Requirement of vascular integrin alpha v beta 3 for angiogenesis. *Science* 1994;264:569–571.
 25. Silva R, D'Amico G, Hodivala-Dilke KM, Reynolds LE. Integrins: The keys to unlocking angiogenesis. *Arterioscler Thromb Vasc Biol* 2008;28:1703–1713.
 26. Liu Z, Wang F, Chen X. Integrin alpha(v)beta(3)-Targeted Cancer Therapy. *Drug Dev Res* 2008;69:329–339.
 27. Buerkle MA, Pahernik SA, Sutter A, Jocznyk A, Messmer K, Dellian M. Inhibition of the alpha-v integrins with a cyclic RGD peptide impairs angiogenesis, growth, and metastasis of solid tumours in vivo. *Br J Cancer* 2002;86:788–795.
 28. Alghisi GC, Ponsonnet L, Ruegg C. The integrin antagonist cilen- gitide activates alphaVbeta3, disrupts VE-cadherin localization at cell junctions and enhances permeability in endothelial cells. *PLoS One* 2009;4:e4449.
 29. Maubant S, Saint-Dizier D, Boutillon M, Perron-Sierra F, Casara PJ, Hickman JA, Tucker GC, Van Obberghen-Schilling E. Blockade of alpha v beta3 and alpha v beta5 integrins by RGD mimetics induces anoikis and not integrin-mediated death in human endothelial cells. *Blood* 2006;108:3035–3044.
 30. Brooks PC, Montgomery AM, Rosenfeld M, Reisfeld RA, Hu T, Klier G, Cheresh DA. Integrin alpha v beta 3 antagonists promote tumor regression by inducing apoptosis of angiogenic blood vessels. *Cell* 1994;79:1157–1164.
 31. Danhier F, Le Breton A, Preat V. RGD-based strategies to target alpha(v) beta(3) integrin in cancer therapy and diagnosis. *Mol Pharm* 2012;9:2961–2973.
 32. De S, Razorenova O, McCabe NP, O'Toole T, Qin J, Byzova TV. VEGF-integrin interplay controls tumor growth and vascularization. *Proc Natl Acad Sci USA* 2005;102:7589–7594.
 33. Mahabeshwar GH, Feng W, Reddy K, Plow EF, Byzova TV. Mechanisms of integrin-vascular endothelial growth factor receptor cross-activation in angiogenesis. *Circ Res* 2007;101:570–580.
 34. Somanath PR, Malinin NL, Byzova TV. Cooperation between integrin alphavbeta3 and VEGFR2 in angiogenesis. *Angiogenesis* 2009;12:177–185.
 35. Reyes CD, Garcia AJ. Alpha2beta1 integrin-specific collagen-mimetic surfaces supporting osteoblastic differentiation. *J Biomed Mater Res A* 2004;69:591–600.
 36. Reyes CD, Petrie TA, Burns KL, Schwartz Z, Garcia AJ. Biomolecular surface coating to enhance orthopaedic tissue healing and integration. *Biomaterials* 2007;28:3228–3235.
 37. Shekaran A, Garcia JR, Clark AY, Kavanaugh TE, Lin AS, Guldberg RE, Garcia AJ. Bone regeneration using an alpha 2 beta 1 integrin-specific hydrogel as a BMP-2 delivery vehicle. *Biomaterials* 2014;35:5453–5461.
 38. Phelps EA, Landazuri N, Thule PM, Taylor WR, Garcia AJ. Bioartificial matrices for therapeutic vascularization. *Proc Natl Acad Sci USA* 2010;107:3323–3328.
 39. Duvall CL, Taylor WR, Weiss D, Guldberg RE. Quantitative micro-computed tomography analysis of collateral vessel development after ischemic injury. *Am J Physiol Heart Circ Physiol* 2004;287: H302–H310.
 40. Duvall CL, Taylor WR, Weiss D, Wojtowicz AM, Guldberg RE. Impaired angiogenesis, early callus formation, and late stage remodeling in fracture healing of osteopontin-deficient mice. *J Bone Miner Res* 2007;22:286–297.
 41. Ruckman J, Green LS, Beeson J, Waugh S, Gillette WL, Henninger DD, Claesson-Welsh L, Janjic N. 2'-Fluoropyrimidine RNA-based aptamers to the 165-amino acid form of vascular endothelial growth factor (VEGF165). Inhibition of receptor binding and VEGF-induced vascular permeability through interactions requiring the exon 7-encoded domain. *J Biol Chem* 1998;273: 20556–20567.
 42. dela Paz NG, D'Amore PA. Arterial versus venous endothelial cells. *Cell Tissue Res* 2009;335:5–16.
 43. Gneccchi M, Zhang Z, Ni A, Dzau VJ. Paracrine mechanisms in adult stem cell signaling and therapy. *Circ Res* 2008;103:1204–1219.
 44. Kumar S, Wan C, Ramaswamy G, Clemens TL, Ponnazhagan S. Mesenchymal stem cells expressing osteogenic and angiogenic factors synergistically enhance bone formation in a mouse model of segmental bone defect. *Mol Ther* 2010;18:1026–1034.
 45. Wang X, Wang Y, Gou W, Lu Q, Peng J, Lu S. Role of mesenchymal stem cells in bone regeneration and fracture repair: A review. *Int Orthop* 2013;37:2491–2498.
 46. Kretlow JD, Mikos AG. Review: Mineralization of synthetic polymer scaffolds for bone tissue engineering. *Tissue Eng* 2007;13: 927–938.
 47. Krishnan L, Willett NJ, Guldberg RE. Vascularization strategies for bone regeneration. *Ann Biomed Eng* 2014;42:432–444.
 48. Avraamides CJ, Garmy-Susini B, Varner JA. Integrins in angiogenesis and lymphangiogenesis. *Nat Rev Cancer* 2008;8:604–617.
 49. Frokjaer S, Otzen DE. Protein drug stability: A formulation challenge. *Nat Rev Drug Discov* 2005;4:298–306.
 50. Steiner D, Lampert F, Stark GB, Finkenzeller G. Effects of endothelial cells on proliferation and survival of human mesenchymal stem cells and primary osteoblasts. *J Orthop Res* 2012;30:1682–1689.
 51. Grellier M, Granja PL, Fricain JC, Bidarra SJ, Renard M, Bareille R, Bourget C, Amedee J, Barbosa MA. The effect of the co-immobilization of human osteoprogenitors and endothelial cells within alginate microspheres on mineralization in a bone defect. *Biomaterials* 2009;30:3271–3278.
 52. Grellier M, Ferreira-Tojais N, Bourget C, Bareille R, Guillemot F, Amedee J. Role of vascular endothelial growth factor in the communication between human osteoprogenitors and endothelial cells. *J Cell Biochem* 2009;106:390–398.
 53. Robinson SD, Hodivala-Dilke KM. The role of beta3-integrins in tumor angiogenesis: Context is everything. *Curr Opin Cell Biol* 2011;23:630–637.
 54. Reynolds LE, Wyder L, Lively JC, Taverna D, Robinson SD, Huang X, Sheppard D, Hynes RO, Hodivala-Dilke KM. Enhanced pathological angiogenesis in mice lacking beta3 integrin or beta3 and beta5 integrins. *Nat Med* 2002;8:27–34.
 55. Mahabeshwar GH, Feng W, Phillips DR, Byzova TV. Integrin signaling is critical for pathological angiogenesis. *J Exp Med* 2006; 203:2495–2507.
 56. Kaur S, Kenny HA, Jagadeeswaran S, Zillhardt MR, Montag AG, Kistner E, Yamada SD, Mitra AK, Lengyel E. beta3-, integrin expression on tumor cells inhibits tumor progression, reduces metastasis, and is associated with a favorable prognosis in patients with ovarian cancer. *Am J Pathol* 2009;175:2184–2196.
 57. Masson-Gadais B, Houle F, Laferriere J, Huot J. Integrin alphav-beta3, requirement for VEGFR2-mediated activation of SAPK2/p38 and for Hsp90-dependent phosphorylation of focal adhesion kinase in endothelial cells activated by VEGF. *Cell Stress Chaperones* 2003;8:37–52.
 58. Maes C, Carmeliet P, Moermans K, Stockmans I, Smets N, Collen D, Bouillon R, Carmeliet G. Impaired angiogenesis and endochondral bone formation in mice lacking the vascular endothelial growth factor isoforms VEGF164 and VEGF188. *Mech Dev* 2002; 111(1–2):61–73.
 59. Kaigler D, Wang Z, Horger K, Mooney DJ, Krebsbach PH. VEGF scaffolds enhance angiogenesis and bone regeneration in irradiated osseous defects. *J Bone Miner Res* 2006;21:735–744.
 60. Kempen DH, Lu L, Heijink A, Hefferan TE, Creemers LB, Maran A, Yaszemski MJ, Dhert WJ. Effect of local sequential VEGF and BMP-2 delivery on ectopic and orthotopic bone regeneration. *Biomaterials* 2009;30:2816–2825.

Human Mesenchymal Stem Cell Behavior on Segmented Polyurethanes Prepared with Osteogenic Chain Extenders. Journal of Materials Science: Materials in Medicine.

J Mater Sci: Mater Med (2016) 27:38
DOI 10.1007/s10856-015-5654-5



BIOCOMPATIBILITY STUDIES

Original Research

Human mesenchymal stem cell behavior on segmented polyurethanes prepared with biologically active chain extenders

Taylor E. Kavanaugh¹ · Amy Y. Clark² · Lerma H. Chan-Chan³ ·
Maricela Ramírez-Saldaña³ · Rossana F. Vargas-Coronado⁴ ·
José M. Cervantes-Uc⁴ · Fernando Hernández-Sánchez⁴ · Andrés J. García² ·
Juan V. Cauich-Rodríguez⁴

Received: 7 October 2015 / Accepted: 18 December 2015
© Springer Science+Business Media New York 2015

Abstract The development of elastomeric, bioresorbable and biocompatible segmented polyurethanes (SPUs) for use in tissue-engineering applications has attracted considerable interest because of the existing need of mechanically tunable scaffolds for regeneration of different tissues, but the incorporation of osteoinductive molecules into SPUs has been limited. In this study, SPUs were synthesized from poly (ϵ -caprolactone)diol, 4,4'-methylene bis (cyclohexyl isocyanate) using biologically active compounds such as ascorbic acid, L-glutamine, β -glycerol phosphate, and dexamethasone as chain extenders. Fourier transform infrared spectroscopy (FTIR) revealed the formation of both urethanes and urea linkages while differential scanning calorimetry, dynamic mechanical analysis, X-ray diffraction and mechanical testing showed that these polyurethanes were semi-crystalline polymers exhibiting high deformations. Cytocompatibility studies showed that

only SPUs containing β -glycerol phosphate supported human mesenchymal stem cell adhesion, growth, and osteogenic differentiation, rendering them potentially suitable for bone tissue regeneration, whereas other SPUs failed to support either cell growth or osteogenic differentiation, or both. This study demonstrates that modification of SPUs with osteogenic compounds can lead to new cytocompatible polymers for regenerative medicine applications.

1 Introduction

Biodegradable segmented polyurethanes (SPUs) represent a promising class of polymers for bone tissue reconstruction due to their controlled degradation, wide range of mechanical properties and acceptable biotolerance achieved through the use of biodegradable soft segments or labile linkages on the rigid segment [1, 2]. Biodegradable SPUs with appropriate mechanical properties have been synthesized by using 1,4-diisocyanatobutane and poly (ϵ -caprolactone) (PCL) as the biodegradable macrodiol and 1,4-diisocyanatebutane tyramine as the biodegradable chain extender [3]. Improvements in mechanical properties of polyurethanes for bone tissue regeneration via increases in hard segment led also to an increase in cell proliferation with a decrease in the osteogenic potential of human bone-derived cells [4]. The mechanical and biological properties of these polymeric matrices can be further improved by incorporating different types of bioactive fillers, such as hydroxyapatite (HA), β -tricalcium phosphate (β -TCP) as well as various bioactive glasses [5–12].

An attractive alternative to the use of SPU with varying mechanical properties but limited capacity of bone

Taylor E. Kavanaugh and Amy Y. Clark have been contributed equally to this work.

✉ Juan V. Cauich-Rodríguez
jvcr@cicy.mx

¹ Department of Biomedical Engineering, Georgia Institute of Technology and Emory University, 313 Ferst Drive, Atlanta, GA 30332, USA

² Woodruff School of Mechanical Engineering and Petit Institute for Bioengineering and Biosciences, Georgia Institute of Technology, 315 Ferst Drive, Atlanta, GA 30332, USA

³ CONACYT - Departamento de Física, Universidad de Sonora, Luis Encinas y Rosales, 83000 Hermosillo, Sonora, Mexico

⁴ Centro de Investigación Científica de Yucatán A.C., Calle 43 130, Col. Chuburná de Hidalgo, C.P. 97200 Mérida, Yucatán, Mexico

Published online: 24 December 2015

Springer

regeneration exhibited by differentiated cell is the culture of multipotent stem cell and then differentiate them into an osteoblast lineage. The fate of MSCs is greatly influenced by both intrinsic and extrinsic signals, including cell–cell and cell–substrate interactions, the gradients of oxygen, nutrient, protein concentrations and mechanical properties of the 2D or 3D substrate. For instance, Zanetta et al. [13] have demonstrated that MDI based polyurethane foams support cell proliferation and differentiation of MSC into osteoblasts. You et al. [14] showed that there is an enhanced osteogenic differentiation of hMSC on nanostructured UV curable polyurethanes. More recently, Alves et al. [15] grafted sulfonic groups on a commercial polyurethane (Elastollan) and studied the adhesion and spreading of human bone marrow stem cell. They found good cell adherence and spreading that developed a well established actin cytoskeleton on unmodified and modified PU. Finally, Kuo et al. [16] showed that single hMSC proliferation slightly increased with fiber diameter, while hMSC aggregates had similar proliferative capacity [16].

Despite these modifications of polyurethanes for the development of scaffolds for engineering bone tissue, biologically active components that support osteoblast proliferation and collagen synthesis [17] and that are commonly found in cell culture media have not been used in the synthesis of SPUs except for the work of Zhang et al. [18]. This group synthesized a polyurethane foam from lysine-di-isocyanate (LDI) and glycerol. Ascorbic acid (AA) was copolymerized with LDI-glycerol i.e. AA was used as part of the prepolymer but not as a chain extender. In the present study, we synthesized polyurethanes formulated with ascorbic acid, L-glutamine, dexamethasone, and β -glycerol phosphate as candidate polymeric materials for bone applications. In this regard, functional groups such as hydroxyl, amine and carboxylic present in the biologically active compounds were used for the chain extension reaction with isocyanate terminated PCL prepolymers. Even when these biologically active molecules are taken up directly by the cells it is hypothesized that their presence in the backbone of the polymer will allow a continuous release to induce cell proliferation and differentiation. Therefore, we also characterized the osteogenic activity of human mesenchymal stem cells (hMSCs) on these new polymers to identify suitable formulations for future in vivo studies.

2 Materials and methods

2.1 Polyurethane synthesis

Poly (ϵ -caprolactone) diol (PCL diol, $M_n = 2000$), 4,4(methylene-bis-cyclohexyl)isocyanate (HMDI) and stannous

octoate (SnO) were purchased from Sigma-Aldrich (Milwaukee, USA). Dimethyl formamide (DMF) from Sigma-Aldrich (Steinheim, Germany) and tetrahydrofuran (THF) from JT Baker (Phillipsburg, USA) were used as solvents in the synthesis or film preparation. Ascorbic acid (ASC), L-glutamine (GLU), dexamethasone (DEXA) and sodium β -glycerol phosphate (BETA) used as chain extenders were also obtained from Sigma-Aldrich (Milwaukee, USA).

Segmented polyurethanes (SPUs) with a molar ratio of 1:2:1 (PCL:HMDI:chain extender) were prepared by a two-step procedure in nitrogen atmosphere at 60 °C with 0.3 % w/w stannous octoate (SnO) as catalyst [19]. In the first step, PCL diol terminated (4 mmol, $M_n = 2000$) and SnO were dissolved in DMF. Next, the solution was mixed with an excess of HMDI (8.4 mmol) and stirred during 4 h in order to form an NCO-terminated prepolymer. In the second stage, the chain extender (4.4 mmol) was dissolved in DMF and added to the reaction and stirred during 2 h to extend the polymer. To stop the reaction, product was precipitated and washed with distilled water. Finally, the polymer was dried at 60 °C at reduced pressure. Scheme of Fig. 1 depicts the suggested structure of the synthesized polyurethanes. Table 1 shows the designation used in this study and the theoretical amount of soft and rigid segments [20].

2.2 Physicochemical characterization of SPUs

All characterization was conducted using solvent casting films except GPC that made use of the polymer obtained after synthesis.

2.2.1 Fourier transform infrared (FTIR) spectroscopy

Infrared spectra of the SPUs were obtained after casting a film on KBr disc with a Thermoscientific Nicolet 8700 FTIR (Madison, WI) in the spectral range from 4000 to 600 cm^{-1} averaging 50 scans with a resolution of 4 cm^{-1} .

2.2.2 Molecular weight measurement

Gel permeation chromatography (GPC) was used for determining the average molecular weight of the synthesized polyurethanes (5 mg/ml), using an Agilent 1100 GPC-SEC system equipped with Zorbax PSM (60S and 1000S) columns and a refractive index detector (Agilent Technologies, Germany). HPLC grade DMF without LiBr was used as eluent with a flow rate of 1 mL/min at 50 °C and the calibration curve was obtained with 1 mg/mL polystyrene molecular weight standards in the range from 1050 to 420,600 g/mol.

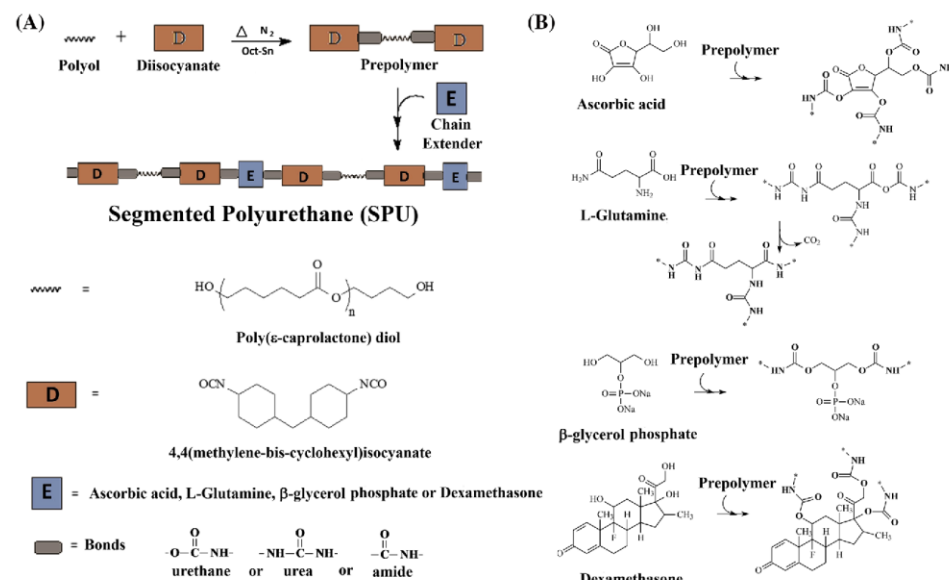


Fig. 1 **a** Suggested chain extension mechanism reaction of prepolymer with biologically active compounds. **b** Possible crosslinking reactions between isocyanate and chain extenders

Table 1 Identification of synthesized polyurethanes, content of soft and rigid segments and their molecular weight

SPU	SS (%)	SR (%)	Mn (g/mol)	Mw (g/mol)	PI
SPUASC	72.8	27.2	26,681	33,688	1.25
SPUGLU	73.7	26.3	49,737	86,871	1.74
SPUBETA	69.3	30.7	43,441	64,064	1.47
SPUDEXA	67.0	33.0	31,810	54,026	1.69

2.2.3 Thermal properties

The thermal behavior was evaluated with a differential scanning calorimetry (DSC) on a DSC 7 from Perkin Elmer (Norwalk, CT) using 5 mg of the polymer films encapsulated on aluminum pans. Melting temperature (T_m) was obtained during the first heating cycle from -100 to 100 °C at 5 °C/min under nitrogen atmosphere. Relative percent crystallinity (X_c) of the PCL in the SPUs was determined from the enthalpy of fusion using Eq. 1:

$$\%X_c = \frac{\Delta H_f}{w_{ss} \times \Delta H_f^0} \times 100 \quad (1)$$

Where ΔH_f is the enthalpy of melting of SPUs obtained experimentally, w_{ss} is the theoretical mass fraction of the flexible segment and ΔH_f^0 is the enthalpy of 100 % crystalline PCL taken as 136 J/g [21].

T_g was obtained by dynamic mechanical analysis with a Perkin Elmer DMA 7 (Norwalk, CT) in the extension mode. Strips obtained by THF casting of $20 \times 3 \times 0.1$ mm were heated from -100 to 100 °C at 5 °C/min using a static force of 90 mN and a dynamic force of 70 mN at 1 Hz.

For thermogravimetric analysis (TGA), 20 mg of the SPU films were heated from 50 to 700 °C at 10 °C/min under nitrogen atmosphere using a TGA 7 from Perkin Elmer (Norwalk, CT). From the first derivative curve, decomposition temperatures (T_d) were obtained.

2.2.4 Microstructure determination

2.2.4.1 X-ray diffraction (XRD) X ray diffraction measurements were carried out with a D-5000 Siemens diffractometer (Karlsruhe, Germany) using monochromatic radiation ($\text{CuK}\alpha$ $\lambda = 1.5418$ Å) at 35 kV and 24 mA. For these experiments, 1 cm² films were used and registered in

the range $5^\circ < 2\theta < 60^\circ$ with a step count of 3 s and a step size of 0.02° (2 θ).

2.2.4.2 Scanning electron microscopy (SEM) Morphology of the SPUs was observed by SEM using a JEOL 6360 LV (Tokyo, Japan). Films were gold coated and observed using an accelerating voltage of 20 kV.

2.2.5 Mechanical properties

Tensile mechanical properties were measured according to ASTM D-882 standard, using a Shimadzu precision universal testing machine (Model Autograph AGS-X, Kyoto, Japan). Samples ($n = 5$), obtained by solvent casting, of $30 \times 5 \times 0.11$ mm were tested with a 100 N load cell, a cross-head speed of 100 mm min^{-1} and a gauge length of 12.7 mm. The Young's modulus at 100 % of strain (E^{100}), tensile strength (σ) and strain to failure (ε) are reported.

2.3 Cytocompatibility studies

2.3.1 Polymer samples

The polymers examined were films of SPUGLU, SPUASC, SPUBETA and SPUDEXA obtained by THF casting. Thin sample discs (thickness of 0.11 mm) used for biocompatibility studies were cut out using a 12 mm biopsy punch, soaked in PBS overnight, sterilized in 200 proof ethanol, and then rinsed with PBS. Polymeric samples were stored in PBS until use.

2.3.2 Cell culture

Human mesenchymal stem cells (hMSCs) were obtained from Lonza. Cells were maintained on tissue culture polystyrene using Mesenchymal Stem Cell Growth Medium (MSCGM; Lonza pt3001) per manufacturer's instructions. Early passage hMSCs (<5) were used for all studies.

2.3.3 Cell number assay

hMSCs were seeded on polymer samples and tissue culture polystyrene (TCP, reference material) at 1000 cells/cm^2 . Cell number was analyzed at days 1 and 7 ($n = 4$) using the CyQUANT Cell Proliferation Assay (Life Technologies) per the manufacturer's instructions. Briefly, cells were washed with Ca/Mg-free PBS and frozen at -80°C until analyzed. Frozen cells were thawed and treated with 200 μL of the CyQUANT GR dye/lysis buffer for 2–5 min at room temperature and protected from light. Fluorescence

was measured at 480 nm excitation and 520 nm emission. Cell number was determined using a cell standard curve prepared using known cell numbers.

2.3.4 Osteogenic differentiation assays

hMSCs were seeded at $10,000 \text{ cells/cm}^2$ with four replicates [22, 23]. Controls included cells cultured on tissue culture plastic in osteogenic induction media (TCP ind) or growth media (TCP non ind). Cells were cultured in hMSC Mesenchymal Stem Cell Osteogenic Differentiation Medium (Lonza).

For alkaline phosphatase (ALP) activity assay, protein content was quantified using the Pierce BCA Protein Kit (Thermo) per the manufacturer's instructions. Briefly, cells were rinsed with Ca/Mg-free PBS at day 9. Cells were treated with ice-cold 50 mM Tris-HCl (pH 7.4), transferred to a centrifuge tube and sonicated to lyse the cells. Samples were centrifuged at $>10,000 \times g$ for 5 min. The supernatant was removed and used for further analysis. Samples were incubated at 37°C for 1–2 h with BCA working reagent and protein content was quantified by measuring absorbance at 562 nm in triplicate. ALP activity was quantified by reacting cell lysate with MUP substrate (50 mM NaHCO_3 , 10 mM diethanolamine, 500 μM MgCl_2 , 200 μM 4-methylumbelliferyl phosphate in H_2O , pH 9.5). Samples were protected from light and incubated for 1 h at 37°C . Fluorescence was read at an excitation of 360 nm and an emission of 465 nm. ALP activity was normalized by the protein content in each sample.

For mineralization assays, cultures at 21 days post-osteogenic induction were fixed with 10 % paraformaldehyde for 15 min at room temperature. Cells were rinsed with excess water and treated with 40 mM Alizarin red (pH 4.1) for 20 min at room temperature. Excess alizarin red was rinsed with water, and samples were transferred to 1.5 mL tubes. Acetic acid (10 % v/v) was added to each tube or well and incubated while shaking for 30 min. Samples were heated to 85°C for 10 min, centrifuged for 15 min at $20,000 \times g$, and supernatant was neutralized with ammonium hydroxide. Sample absorbance was read at 405 nm.

2.4 Statistical analysis

Cell number, ALP activity and Alizarin red quantification were analyzed using a one-way ANOVA followed by a Tukey's multiple comparisons test performed in GraphPad using an alpha value = 0.05. Significance was defined as $P < 0.05$.

3 Results

3.1 Spectroscopic studies

The chemical structure of the polyurethane was elucidated by FTIR. The IR spectra of SPUs are shown in Fig. 2. The absorption peaks at 3373 and 3525 cm^{-1} was assigned to N-H vibrations, while CH_2 asymmetric and symmetric stretching vibrations were observed at 2946 and 2869 cm^{-1} , respectively. Carbonyl stretching ($\text{C}=\text{O}$) appeared between 1729 and 1760 cm^{-1} , which includes the ester group from the PCL, and around 1700 cm^{-1} , which includes the urethane group (NHCOO). Amide II absorption (urethane N-H bending + C-N stretching) and amide III absorption (C-C stretching) were located at 1522 and 1233 cm^{-1} , respectively, while the peak at 1166 cm^{-1} was attributed to C-O-C stretching vibration in the soft segment. The peak at 1634 cm^{-1} was assigned to the urea linkages confirming the reaction of amine groups (from the glutamine) with NCO, although, the presence of water might also contribute in the other polyurethanes. Even though the bands of chain extenders usually overlapped, spectrum of SPUDEXA show the characteristic band at 1668 cm^{-1} due to the carbonyl-stretching vibration of the dexamethasone A-ring.

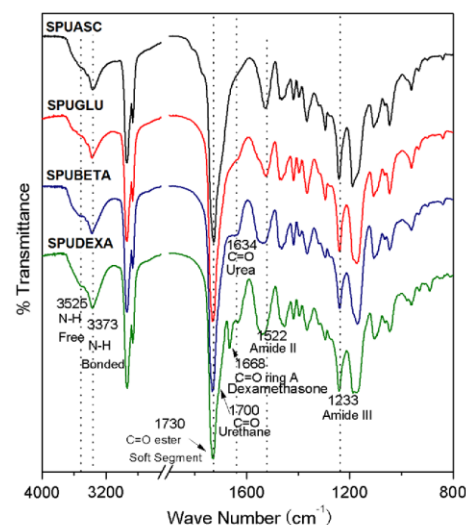


Fig. 2 FTIR spectra of SPUs prepared with biologically active chain extenders. SPUs with ascorbic acid (SPUASC), glutamine (SPUGLU), β -glycerol phosphate (SPUBETA) and dexamethasone (SPUDEXA)

As shown in Table 1, M_n and M_w were higher in SPUGLU while SPUDEXA exhibited lower M_n and M_w than SPUBETA. In contrast, SPUASC exhibited the lowest molecular weight. In spite of these low M_n and M_w values, they were high enough for film formation and mechanical testing.

3.2 Thermal properties

All types of SPUs containing PCL as the soft segment were semi-crystalline materials as they exhibited melting peaks between 51.0 $^{\circ}\text{C}$ and 53.8 $^{\circ}\text{C}$. However, the percentage of crystallinity followed the order SPUGLU/SPUASC > SPUDEXA/SPUBETA. The presence of a crystalline phase is attributed to PCL as the rigid segment (HMDI-chain extender) of these aliphatic polyurethanes which do not tend to crystallize but tend to form ordered regions as will be discussed later from XRD results. Although the presence of a melting peak suggested that the crystalline structure of the PCL is preserved due to its relatively high molecular weight ($M_n \approx 2000$), the reduction in crystallinity is caused by the high molecular weight of the chain extender (either DEXA or BETA) that impedes proper chain organization.

The $\tan \delta$ variation with temperature showed a well-defined α transition which was related to the soft segments of the SPU. For SPUASC and SPUDEXA, this was higher (-48 to -43 $^{\circ}\text{C}$) than for SPUGLU and SPUBETA (-51 $^{\circ}\text{C}$). The shift in the T_g of the amorphous phase PCL suggests that the rigid segment content is restricting PCL chain movement as the T_g of pure PCL was found at -60 $^{\circ}\text{C}$. The T_g obtained by DSC, although generally accepted to be lower compared to DMA, followed the opposite trend i.e. lower for SPUBETA (-37 $^{\circ}\text{C}$) than for SPUDEXA (-20.0 $^{\circ}\text{C}$), SPUASC (-21.1 $^{\circ}\text{C}$) and SPUGLU (-27 $^{\circ}\text{C}$).

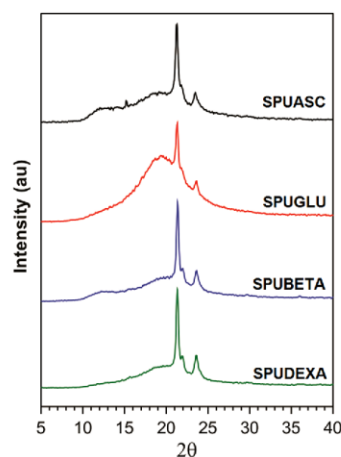
Thermogravimetric analysis of the SPUs showed a main decomposition temperature in the 365 to 398 $^{\circ}\text{C}$ range (denoted as T_{d2}) which was attributed to the decomposition of the flexible segment (PCL). However, small decomposition peaks were also detected at lower temperatures for SPUASC only ($T_{d1} = 203$ $^{\circ}\text{C}$) and at higher temperatures ($T_{d3} = 465$ – 478 $^{\circ}\text{C}$) being the later assigned to the rigid segments. Table 2 summarizes the thermal properties of SPUs.

3.3 Microstructure by XRD and SEM

Figure 3 shows the XRD patterns of SPUs. The semi-crystalline nature of these SPUs can be confirmed from the presence of reflections at $2\theta = 21.3^{\circ}$, 22.0° and 23.4° due to the PCL soft segments. The broad reflection with a maximum at 19.3° can be related to ordered regions from

Table 2 Thermal properties of SPUs prepared with biologically active chain extenders

SPU	T_g^1 (°C)	T_m^2 (°C)	X_c %	T_d^3 (°C)		
				T_{d1}	T_{d2}	T_{d3}
SPUASC	-48.4	53.8	38.0	203	398	478
SPUGLU	-51.2	51.4	40.0	—	370	472
SPUBETA	-51.5	51.0	20.0	—	365	465
SPUDEXA	-43.2	51.3	21.0	—	368	467

Measured by ¹DMA, ²DSC, ³TGA**Fig. 3** XRD patterns of SPUs prepared with biologically active chain extenders. SPUs with ascorbic acid (SPUASC), glutamine (SPUGLU), β -glycerol phosphate (SPUBETA) and dexamethasone (SPUDEXA)

the rigid segment formed. As seen in Fig. 3, there is a higher content of rigid segments (as observed from the higher intensity/area) in SPUGLU and SPUASC explaining their better mechanical performance.

Figure 4 shows the SEM images for SPU samples. The formation of agglomerates (spherulites) in the neat polyurethanes is evident only in SPUASC and SPUGLU, with the size of the spherulites being smaller in glutamine containing polymers. The absence of these structures in SPUBETA and SPUDEXA can be related to its poor crystallinity as shown by DSC and XRD. SPUDEXA also showed the presence of pores on its surface.

3.4 Mechanical properties

Analysis of the mechanical properties of SPUs showed an initial elastic behavior (less than 1 % as proved by

hysteresis analysis) and elastomer-like behavior in the sense that it sustained large deformations (see Fig. 5). SPUGLU and SPUASC exhibited higher moduli than the other formulations, but deformation was higher in SPUGLU. SPUBETA exhibited the lowest modulus, but a large strain to failure suggested lower crosslinking than SPUDEXA. Table 3 summarizes the tensile mechanical properties of the SPUs.

3.5 Cell adhesion and proliferation

hMSC adhesion and growth on SPU polymers were examined by quantifying cell numbers at days 1 and 7 (See Fig. 6). Equivalent cell numbers were observed among SPU polymers as well as the tissue culture polystyrene (TCP) reference at day 1. Over 7 days in culture, cell numbers increased for SPUBETA, indicating that this polymer supports cell proliferation. In contrast, there were no differences in cell numbers between days 1 and 7 for SPUASC and SPUGLU. The number of cells significantly decreased with time in culture for SPUDEXA, suggesting that although this polymer supports short term adhesion, it does not support long term cell adhesion or growth.

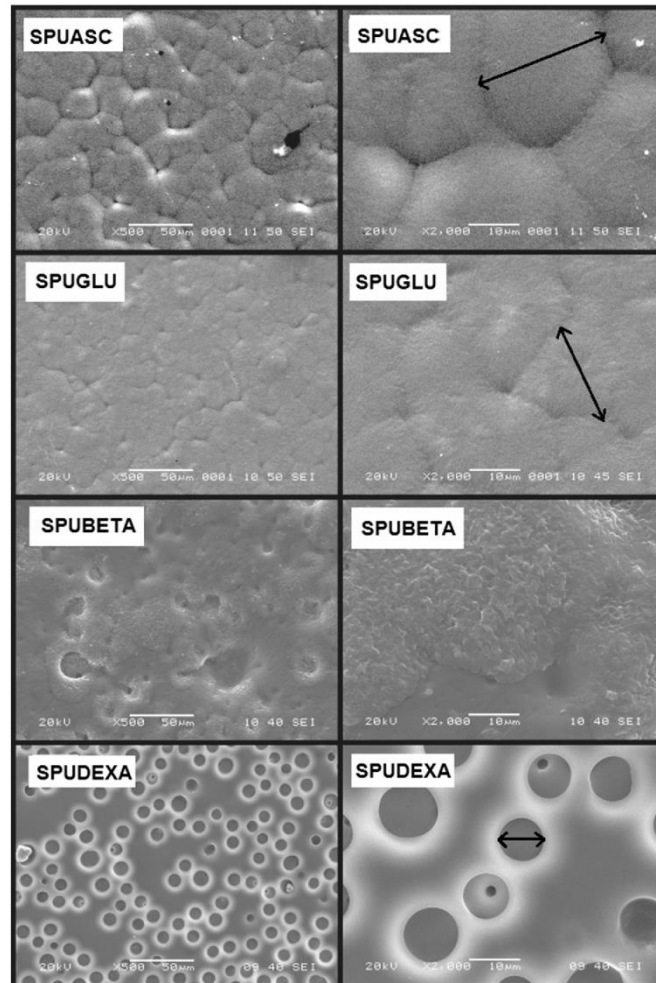
3.6 Osteogenic differentiation

Alkaline phosphatase is an early indicator of osteogenic differentiation due to its ability to catalyze the hydrolysis of phosphate esters leading to calcification. ALP enzymatic activity, assayed at day 9, indicated that SPUBETA supported osteogenic differentiation when compared to cells cultured in growth media on tissue culture polystyrene (Fig. 7a). Alizarin red staining for calcium deposits performed at day 21 shows high calcification on both SPUBETA and SPUGLU compared to cells grown in growth media on tissue culture polystyrene (Fig. 7b).

4 Discussion

In order for biodegradable SPUs to be used as a biomaterial within an implant, the ability for these SPUs to promote cellular adhesion and growth must be evaluated. As our interest is specifically for the use as an orthopedic implant, this material should also support osteogenic differentiation of hMSCs [24, 25]. In the present study, we synthesized various SPUs incorporating osteogenic compounds such as ascorbic acid, β -glycerol phosphate and dexamethasone as chain extenders. It is known that L-Ascorbic acid enhances collagen synthesis and up-regulates adenosine triphosphatase and alkaline phosphatase activity [26], but has also been shown to decrease cellular proliferation, possibly acting as one of the signals theorized as necessary for the

Fig. 4 SEM micrographs of SPUs prepared with biologically active chain extenders. SPUs with ascorbic acid (SPUASC), glutamine (SPUGLU), β -glycerol phosphate (SPUBETA) and dexamethasone (SPUDEXA). SPUASC and SPUGLU show formation of agglomerates (spherulites) marked by double arrows. Pores in the surface of SPUDEXA were observed and marked by a double arrow



progression from proliferation to the matrix maturation phase [27]. β -glycerol phosphate serves primarily as a source of inorganic phosphate ions, and in combination with L-Ascorbic acid, allows the formation and mineralization of the extracellular matrix in culture [26]. Dexamethasone is a synthetic glucocorticoid that exerts various inhibitory effects on the inflammatory processes and is known to play a key role in controlling the regulation of genes and cellular processes essential for cellular growth

and division [28]. On the other hand, dexamethasone exerts a powerful effect on the osteogenic differentiation of MSCs. Continual exposure to dexamethasone, beginning shortly after cell harvest, is required to drive and maintain the osteoblastic phenotype of marrow-derived progenitor cells. Although maintenance of the osteoblastic phenotype is desirable for long-term cultures, dexamethasone has been known to drive MSCs down the osteogenic pathway so quickly that they do not proliferate well [26].

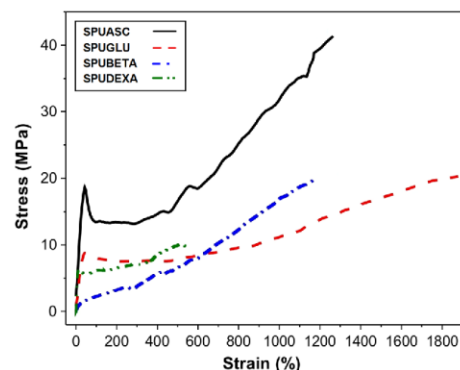


Fig. 5 Tensile stress-strain curve for SPUs prepared with biologically active chain extenders. SPUs with ascorbic acid (SPUASC), glutamine (SPUGLU), β -glycerol phosphate (SPUBETA) and dexamethasone (SPUDEXA)

Table 3 Tensile mechanical properties of SPUs prepared with biologically active chain extenders

SPU	E_{100} (MPa)	σ (MPa)	ε (%)
SPUASC	26.7 ± 25.6	47.75 ± 16.7	1298 ± 286
SPUGLU	12.0 ± 2.2	19.6 ± 11.2	1879 ± 302
SPUBETA	1.96 ± 0.19	19.00 ± 1.76	1141 ± 110
SPUDEXA	6.25 ± 0.38	10.77 ± 1.85	520 ± 70

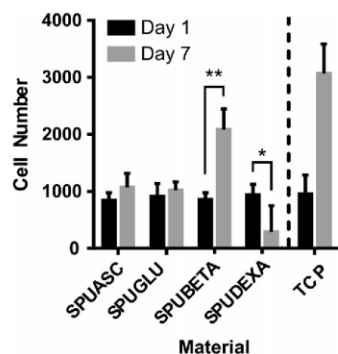


Fig. 6 hMSC number for cells cultured on SPUs. Cell number was quantified at days 1 and 7 by DNA content. Results were analyzed using a one-way ANOVA followed by a Tukey's multiple comparison test with an $\alpha = 0.05$. * P value < 0.05 , ** P value < 0.005

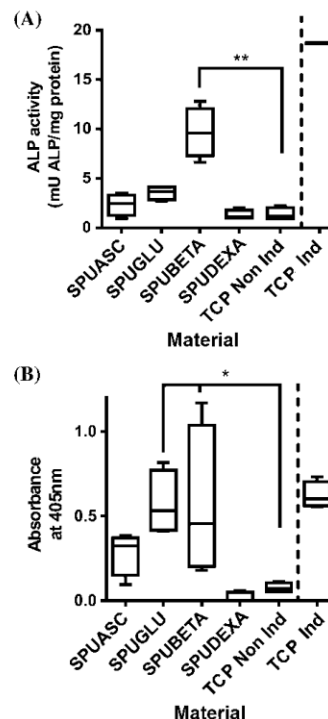


Fig. 7 ALP activity at day 9. **a** SPUBETA show a significant increase in ALP over non-induced hMSCs. **b** Mineralization of hMSCs quantified by Alizarin red staining after 21 days. SPUBETA and SPUGLU show significantly increased calcification over non-induced hMSCs. A one-way ANOVA followed by a Tukey's multiple comparison test with and $\alpha = 0.05$. * P value of 0.05, ** P value of 0.001

4.1 Physicochemical properties of SPUs with biologically active chain extenders

FTIR showed that the synthesized polymers contained urethane, urea or amide linkages depending on the chain extender used. Solubility tests (in deuterated chloroform or DMF) suggested that linear or slightly crosslinked polymers (SPUASC, SPUGLU, SPUBETA, SPUDEXA) were obtained in spite of the multifunctional nature of the chain extender. This can be attributed to the lower reactivity of carboxylic acids and secondary hydroxyl groups in glutamine and ascorbic acid/dexamethasone respectively [29, 30].

DSC and XRD showed that semicrystalline polyurethanes were obtained where crystallinity tended to decrease as the molecular weight of the chain extender increased. This can be explained as the formation of an ordered structure was hindered by a bulky molecule (dexamethasone) or due to the presence of phosphate groups (β -glycerol phosphate). It is also possible that the remaining hydroxyl groups formed intermolecular hydrogen bonds between PCL chains and the rigid segment competing with intramolecular PCL hydrogen bonds.

In the temperature interval of our dynamic mechanic experiments, the poly (ϵ -caprolactone) showed only the main relaxation associated with the co-operative rearrangements of the polymer chain in the amorphous phase. However, the T_g of PCL tend to increase due to chain movement restrictions, i.e. due to the presence of the bulky rigid segments (approximately 25 %) or even due to crosslinking. Therefore, SPUASC and SPUDExA showed a higher T_g than SPUGLU and SPUBETA. The different trend observed in terms of the T_g measured by DSC can be explained by further crosslinking reactions during the first heating cycle. In the case of SPUASC, these crosslinking reactions also account for the slightly higher thermal stability i.e. higher T_{d2} and T_{d3} .

In general, the mechanical behaviour of these materials can be attributed mainly to the PCL in the SPU matrix, as once unfolded and aligned, the PCL chains tend to sustain the load and to show an increase in resistance. However, M_n and M_w were higher in SPUGLU, which likely explains their higher Young's modulus. SPUDExA also exhibited high modulus, but in spite of exhibiting a lower M_n and M_w than SPUBETA, the crosslinking reaction might explain their mechanical performance. In contrast, SPUASC exhibited the lowest molecular weight but the highest modulus and tensile strength possibly due to crosslinking reactions as observed in the gel fraction of this polyurethane. SPUASC exhibited the highest Young's modulus (26.7 MPa) of the synthesized polyurethanes. This value is still far from the cortical bone (12–18 GPa) and spongy bone (100–500 MPa) or even foamed polyurethanes used to mimic trabecular bone [20, 31]. However, it is clear from previous reports that our polyurethanes can be improved by increasing molecular weight of PCL [3], by increasing rigid segment content [4] and by the addition of bioactive fillers [8, 9]. It is convenient to remember that for tissue engineering, as the tissue grows, the polymer degrades. In this sense, we expect that tissue formation will be accelerated by the presence of osteogenic molecules which will then compensate for their low mechanical properties.

4.2 Biological performance of SPU with biologically active chain extenders

To evaluate cell growth and number, hMSCs were cultured on the various SPUs. Resulting cell numbers showed all SPUs allowed for initial cell adhesion at day 1 at levels equivalent to the reference material. By day 7, cell number did not increase on SPUGLU and SPUASC suggesting cell death or the lack of support for long-term cell adhesion. Even when the amount of glutamine released from the polyurethanes (SPUs) was not quantified in the culture media, the decrease in cell number may be due to the degradation of L-glutamine to ammonia or the high concentration of L-glutamine used in this study compared to levels found in culture media (2–4 mM). In addition, the absence of alkaline nitrogen atoms in the lateral chain but the presence of an amide as the functional group in the lateral chain reduced cell adhesion. In the case of ascorbic acid, this was also used in higher amounts (approximately 3 wt% of ascorbic acid for SPU synthesis) compared to the recommended for osteoblast cell culture (50 μ g/ml or 150 mg/l). In low concentrations, ascorbic acid or L-ascorbate-2-phosphate, a long-acting ascorbic acid derivative, is essential for the expression of osteoblastic markers (collagen synthesis and alkaline phosphatase activity) and mineralization [31, 32].

SPUDExA showed reduced cell numbers, while SPUBETA showed a significant increase in cell number and all other SPUs at least sustained the number of cells that initially adhered. These results support the use of SPUBETA as a biomaterial as this showed significant cell growth over 7 days in culture. Therefore, we can speculate that degradation of SPUBETA by hydrolysis is occurring.

A typical complete media also contains 10 mM Na β -glycerophosphate, and 10 nM dexamethasone. Once again, even when β -glycerophosphate and dexamethasone were used in higher concentration for the SPU synthesis its initial effect was to allow cell adhesion.

Not only should a biomaterial allow for cell proliferation, as assessed by the cell number assays, it should also promote osteogenic differentiation of hMSCs if intended for orthopedic use. Increased ALP activity was observed for SPUBETA. Alizarin red staining, performed at day 21, stains for calcium and can be used as a measure of mineralization of hMSCs. SPUBETA had an increase in mineralization when compared to a non-induced hMSC control. This increase in mineralization is in agreement with the enhanced cell numbers and ALP activity. SPUGLU also showed increased Alizarin red staining when compared to the non-differentiated cells, but it did not support increases in ALP activity or cell numbers.

Dexamethasone has been reported to have an effect on mesenchymal cell morphology, expression of ALP, osteocalcin production and matrix mineralization [27]. However, in our study, SPUDXA induced low levels of ALP and mineralization. It is possible that transient exposure of stem cells to dexamethasone may be more effective in inducing and maintaining the osteoblastic phenotype. Further, in addition to medium components and their concentrations, the temporal presentation in which osteogenic supplements are added can affect both proliferative potential of the cells and their differentiated function.

5 Conclusion

In this study, we created SPUs that were synthesized from poly(ϵ -caprolactone)diol and 4,4'-methylene bis(cyclohexyl isocyanate) (HMDI) using osteogenic compounds such as ascorbic acid, L-glutamine, β -glycerol phosphate and dexamethasone as chain extenders. These SPUs have significant potential for the use in bone tissue regeneration due to their variable mechanical properties and high bio tolerance. From these SPUs, it was determined that SPUBETA allows hMSC adhesion and proliferation, high levels of ALP expression and high mineralization potential. Therefore, SPUBETA is a very promising material that has been distinguished for further investigation through in vivo studies and other mechanisms of characterization for bone tissue regeneration.

Acknowledgments These studies were supported by the Georgia Institute of Technology President's Undergraduate Research Award and the National Institute of Health (NIH R01 AR062368). We also want to thank Patricia Quintana and Daniel Aguilar Treviño for XRD experiments at Laboratorio Nacional de Nano y Biomateriales (LANBIO), Cinvestav-IPN, Unidad Mérida (Projects FOMIX-Yucatán 2008-108160 and CONACYT LAB-2009-01 no. 123913).

References

- Gogolewski S. Selected topics in biomedical polyurethanes. A review. *Colloid Polym Sci.* 1989;267(9):757–85. doi:10.1007/bf01410115.
- Middleton JC, Tipton AJ. Synthetic biodegradable polymers as orthopedic devices. *Biomaterials.* 2000;21(23):2335–46.
- Kavlock KD, Pechar TW, Hollinger JO, Guelcher SA, Goldstein AS. Synthesis and characterization of segmented poly (esterurethane urea) elastomers for bone tissue engineering. *Acta Biomater.* 2007;3(4):475–84.
- Bil M, Ryszkowska J, Wozniak P, Kurzydowski KJ, Lewandowska-Szumiel M. Optimization of the structure of polyurethanes for bone tissue engineering applications. *Acta Biomater.* 2010;6(7):2501–10.
- Salgado AJ, Coutinho OP, Reis RL. Bone tissue engineering: state of the art and future trends. *Macromol Biosci.* 2004;4(8):743–65.
- Boissard C, Bourban P-E, Tami A, Alini M, Eglin D. Nanohydroxyapatite/poly (ester urethane) scaffold for bone tissue engineering. *Acta Biomater.* 2009;5(9):3316–27.
- Wang L, Li Y, Zuo Y, Zhang L, Zou Q, Cheng L, et al. Porous bioactive scaffold of aliphatic polyurethane and hydroxyapatite for tissue regeneration. *Biomed Mater.* 2009;4(2):025003.
- Ryszkowska JL, Auguścik M, Sheikh A, Boccaccini AR. Biodegradable polyurethane composite scaffolds containing Bioglass® for bone tissue engineering. *Compos Sci Technol.* 2010;70(13):1894–908.
- Bonzani IC, Adhikari R, Houshyar S, Mayadunne R, Gunatillake P, Stevens MM. Synthesis of two-component injectable polyurethanes for bone tissue engineering. *Biomaterials.* 2007;28(3):423–33.
- Liu H, Zhang L, Zuo Y, Wang L, Huang D, Shen J, et al. Preparation and characterization of aliphatic polyurethane and hydroxyapatite composite scaffold. *J Appl Polym Sci.* 2009;112(5):2968–75.
- Liu H, Zhang L, Li J, Zou Q, Zuo Y, Tian W, et al. Physicochemical and biological properties of nano-hydroxyapatite-reinforced aliphatic polyurethanes membranes. *J Biomater Sci Polym Ed.* 2010;21(12):1619–36.
- de Oliveira AAR, de Carvalho SM, de Fátima Leite M, Oréfice RL, Magalhães Pereira M. Development of biodegradable polyurethane and bioactive glass nanoparticles scaffolds for bone tissue engineering applications. *J Biomed Mater Res B Appl Biomater.* 2012;100(5):1387–96.
- Zanetta M, Quirici N, Demarosi F, Tanzi M, Rimondini L, Fare S. Ability of polyurethane foams to support cell proliferation and the differentiation of MSCs into osteoblasts. *Acta Biomater.* 2009;5(4):1126–36.
- You M-H, Kwak MK, Kim D-H, Kim K, Levchenko A, Kim D-Y, et al. Synergistically enhanced osteogenic differentiation of human mesenchymal stem cells by culture on nanostructured surfaces with induction media. *Biomacromolecules.* 2010;11(7):1856–62.
- Alves P, Pinto S, Ferreira P, Kaiser J-P, Bruinink A, de Sousa HC et al. Improving cell adhesion: development of a biosensor for cell behaviour monitoring by surface grafting of sulfonic groups onto a thermoplastic polyurethane. *J Mater Sci Mater Med.* 2014;25:2017–26.
- Kuo Y-C, Hung S-C, Hsu S-H. The effect of elastic biodegradable polyurethane electrospun nanofibers on the differentiation of mesenchymal stem cells. *Colloids Surf B Biointerfaces.* 2014;122:414–22.
- Cabral MCT, Costa MA, Fernandes MH. In vitro models of periodontal cells: a comparative study of long-term gingival, periodontal ligament and alveolar bone cell cultures in the presence of β -glycerophosphate and dexamethasone. *J Mater Sci Mater Med.* 2007;18(6):1079–88.
- Zhang J, Doll BA, Beckman EJ, Hollinger JO. A biodegradable polyurethane-ascorbic acid scaffold for bone tissue engineering. *J Biomed Mater Res A.* 2003;67(2):389–400.
- Cetina-Diaz S, Chan-Chan L, Vargas-Coronado R, Cervantes-Uc J, Quintana-Owen P, Paakinaho K, et al. Physicochemical characterization of segmented polyurethanes prepared with glutamine or ascorbic acid as chain extenders and their hydroxyapatite composites. *J Mater Chem B.* 2014;2(14):1966–76.
- Asefnejad A, Behnamghader A, Khorasani MT, Farsadzadeh B. Polyurethane/fluorhydroxyapatite nanocomposite scaffolds for bone tissue engineering. Part I: morphological, physical, and mechanical characterization. *Int J Nanomedicine.* 2011;6(1):93–100.
- Bogdanov B, Toncheva V, Schacht E, Finelli L, Sarti B, Scandola M. Physical properties of poly (ester-urethanes) prepared from

- different molar mass polycaprolactone-diols. *Polymer*. 1999;40(11):3171–82.
22. Phillips JE, Petrie TA, Creighton FP, García AJ. Human mesenchymal stem cell differentiation on self-assembled monolayers presenting different surface chemistries. *Acta Biomater*. 2010;6(1):12–20.
 23. Shekaran A, García JR, Clark AY, Kavanaugh TE, Lin AS, Guldberg RE, et al. Bone regeneration using an alpha 2 beta 1 integrin-specific hydrogel as a BMP-2 delivery vehicle. *Biomaterials*. 2014;35(21):5453–61.
 24. Ishaug SL, Crane GM, Miller MJ, Yasko AW, Yaszemski MJ, Mikos AG. Bone formation by three-dimensional stromal osteoblast culture in biodegradable polymer scaffolds. *J Biomed Mater Res*. 1997;36(1):17–28.
 25. Reichert JC, Hutmacher DW. Bone tissue engineering. *Tissue engineering*. New York: Springer; 2011. p. 431–56.
 26. Holtorf HL, Jansen JA, Mikos AG. Flow perfusion culture induces the osteoblastic differentiation of marrow stromal cell-scaffold constructs in the absence of dexamethasone. *J Biomed Mater Res A*. 2005;72(3):326–34.
 27. Peter SJ, Liang CR, Kim DJ, Widmer MS, Mikos AG. Osteoblastic phenotype of rat marrow stromal cells cultured in the presence of dexamethasone, β -glycerolphosphate, and L-ascorbic acid. *J Cell Biochem*. 1998;71(1):55–62.
 28. Yoon JJ, Kim JH, Park TG. Dexamethasone-releasing biodegradable polymer scaffolds fabricated by a gas-foaming/salt-leaching method. *Biomaterials*. 2003;24(13):2323–9.
 29. Martínez-Valencia A, Carbajal-De la Torre G, Torres-Sánchez R, Téllez-Jurado L, Esparza-Ponce H. Production of polyurethane/nano-hydroxyapatite hybrid materials and microstructural characterization. *Int J Phy Sci*. 2011;6(11):2731–43. doi:[10.5897/IJPS11.313](https://doi.org/10.5897/IJPS11.313).
 30. Tripathi G, Basu B. A porous hydroxyapatite scaffold for bone tissue engineering: physico-mechanical and biological evaluations. *Ceram Int*. 2012;38(1):341–9.
 31. Roether J, Deb S. The effect of surface treatment of hydroxyapatite on the properties of a bioactive bone cement. *J Mater Sci Mater Med*. 2004;15(4):413–8.
 32. Deb S, Mandegar R, Di Silvio L. A porous scaffold for bone tissue engineering/45S5 Bioglass® derived porous scaffolds for co-culturing osteoblasts and endothelial cells. *J Mater Sci Mater Med*. 2010;21(3):893–905.

Tobacco Mosaic Virus Functionalized Alginate Hydrogel Scaffolds for Bone Regeneration in Rats with Cranial Defect. ACS Biomaterials Science and Engineering.



Article

pubs.acs.org/journal/abseba

Tobacco Mosaic Virus Functionalized Alginate Hydrogel Scaffolds for Bone Regeneration in Rats with Cranial Defect

Jittima Amie Luckanagul,^{†,*} Kamolrat Metavarayuth,[†] Sheng Feng,[†] Phudit Maneesaay,[§] Amy Y. Clark,^{||} Xiaoming Yang,[⊥] Andrés J. García,^{*,||} and Qian Wang^{*,†}

[†]Department of Chemistry and Biochemistry, University of South Carolina, 631 Sumter Street, Columbia, South Carolina 29208, United States

[§]Department of Food and Pharmaceutical Chemistry, Faculty of Pharmaceutical Sciences, Chulalongkorn University, 254 Phayathai Road, Wangmai, Pathumwan, Bangkok, Thailand 10330

[§]Department of Pathology, Faculty of Veterinary Medicine, Kasetsart University, 50 Ngamwongwan Road, Lat Yao, Chatuchak, Bangkok, Thailand 10903

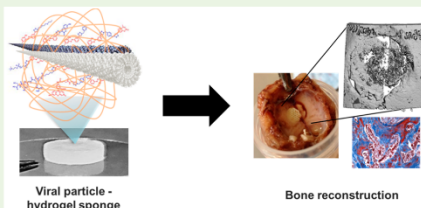
^{||}Woodruff School of Mechanical Engineering and Petit Institute for Bioengineering and Bioscience, Georgia Institute of Technology, 801 Ferst Drive, Atlanta, Georgia 30332, United States

[⊥]Medical Chronobiology Laboratory and Center for Colon Cancer Research, WJB Dorn VA Medical Center, 6439 Garners Ferry Road, Columbia, South Carolina 29209, United States

Supporting Information

ABSTRACT: Plant viruses have been highlighted among material research due to their well-defined structures in nanoscale, monodispersity, stability, and chemical functionalities. Each of the thousands coat protein subunits on a viral nanoparticle can be homogeneously modified, chemically and genetically, with a functional ligand leading to a high-density and spatial distribution of ligands on each particle (multivalency). Previous reports from our group have evidenced that substrates coated with Tobacco mosaic virus (TMV) and its mutant promote early osteogenesis of mesenchymal stem cells (MSCs). We then fabricated a three-dimensional (3D) biopolymeric scaffold with rod-like TMV in the form of a sponge-like hydrogel for tissue engineering purposes. The hydrogel was functionalized with the cellular recognition peptide, arginine–glycine–aspartic acid (RGD), through an incorporation of an RGD mutant of TMV (TMV-RGD). The virus-functionalized hydrogel materials were shown to aid bone differentiation of MSCs in vitro. Herein, we performed an in vivo study based on the TMV and TMV-RGD hydrogels in Sprague–Dawley rats with cranial bone defects. This report substantiated the hypothesis that TMV-functionalized hydrogel scaffolds did not cause systemic toxicity when implanted in the defect site and that the TMV-based hydrogel platform can support cell localization and can be further optimized for bone regeneration and repair.

KEYWORDS: virus nanoparticles, hydrogel, cranial defect, implant, bone regeneration, Tobacco mosaic virus



1. INTRODUCTION

There is a great need for clinical bone replacement in patients with bone loss after resection of tumors, bone loss after trauma, and voids created as a result of fractures. Even though bone has a good healing capacity compared to that of other tissues, the regeneration potential is limited in the case of large defects such as after tumor resection, major fractures, hip implant revision, or impaired healing capacity of the host.^{1,2} In such cases, the use of bone grafts or bone substitutes is indicated to promote healing and regeneration.^{2–4} Current clinical methods of treating skeletal defects are autograft and allograft bone transplantation. Autograft bone (bone transplanted from one part of the body to another in the same individual) provides an environment that bone cells like to grow in and make bone tissue. However, the supply of autograft bone is limited.

Allograft bone (bone from one person to another including those from cadaveric and living relatives) has slower rate of healing compared to that of autograft bone and the possibility of disease transfer. Hence, material scientists introduced the concept of tissue engineering using biocompatible artificial materials that offer an unlimited supply for treating bone defects.^{4,5}

The translation of therapeutics, including pharmaceuticals, medical devices, and medical strategies, into clinics requires animal studies. Despite ethical concerns and efforts to develop alternatives to animal experimentation, standardized animal

Received: December 28, 2015

Accepted: March 3, 2016



ACS Publications

© XXXX American Chemical Society

A

DOI: 10.1021/acsbiomaterials.5b00561
ACS Biomater. Sci. Eng. XXXX, XXX, XXX–XXX

models are crucial components in translational sciences and medical technology development.^{6–9} For bone tissue engineering, the rat calvarium or cranium allows for a reproducible defect that can be generated quickly and does not require fixation for stabilization of the skeleton, as is generally required with femoral defects.^{10,11} However, as an anatomical site experiencing less loading than long bones, the functional testing of a bone regeneration strategy intended to withstand biomechanical forces is not feasible in the cranial defect.¹² Thus, taking into consideration the objective of the biomaterial or bone regeneration strategy, the rat calvarial defect can serve as a rapid, high throughput method for *in vivo* evaluation of bone regeneration.¹³ For critical defects, i.e., defects that would not fully heal spontaneously or even to accelerate or guide the repair process, the use of bioactive scaffolding material could be of great advantage. Suitable materials can, in fact, fill the cavity or stabilize the defects while exerting beneficial stimuli that promote cell activity and proliferation.⁵

The goal of this study is to assess the potential for rod-like plant virus nanoparticles incorporated hydrogels as materials capable of enhancing bone formation/regeneration. The hydrogel is composed of Tobacco mosaic viruses (TMVs) as protein templates with a mixture of a natural hydrogel forming polymer that is biocompatible and biodegradable, sodium alginate (a sugar-based polymer derived from algae/seaweed). Alginate has been well established as a hydrogel forming polymer that is used extensively in biomedical applications.^{14,15} Therefore, we employed alginate as the supporting hydrogel to incorporate TMV particles. Alginate itself cannot guide cells toward bone differentiation, unless complex mixtures of protein materials (i.e., growth factors and cell binding sequences) are incorporated.¹⁶ Hereby, we rationalized that TMV can supplement the polymer backbone to promote bone formation based on the following foundations. First, our group has shown that TMV and its mutants on two-dimensional substrates can accelerate the differentiation of bone marrow-derived mesenchymal stem cells into bone cells through the stimulation of endogenous bone morphogenic protein-2 (BMP-2) production in early stage osteogenesis.^{17–19} Second, a large number of functionalities (cell anchorage sites and growth factors) can be placed on the surface of virus particles at the nanometer scale.^{20,21} The ability to place specific functional groups (cell anchorage sites and growth factors) at nanometer scales within the hydrogel has been an important direction for tissue engineering. The virus solution can be purified to be pathogen-free by sterile filtration. In history and at present, there have been no reports of TMV infections in mammals. Even in a case where the plant virus was to enter the mammalian cells, it does not have the proper material to replicate itself inside mammalian cells.^{18,22–24} By incorporating cell binding ligands on the external surface of TMV, we have shown that TMV can act as nanometer sized building blocks that can support mesenchymal stem cells and dramatically improve the transformation of cells into bone-like cells *in vitro*.^{19,25,26} We did not observe any decrease in cell survival even with very high doses of TMV. Additionally, from our previous studies reported for biocompatibility (subcutaneous) of TMV and its mutant (TMV-RGD) incorporated alginate hydrogel scaffold in mice, we did not observe any serious immune responses in comparison with the control group (mice subcutaneously implanted with an alginate-alone scaffold).¹⁷ Therefore, the proposed hydrogel will possibly provide a new way to prepare biomaterials for bone repairing applications.

2. MATERIALS AND METHODS

All chemicals were obtained from commercial suppliers and used as received unless otherwise noted. Wild-type TMV (TMV) and its RGD mutant (TMV-RGD) were isolated from infected tobacco leaves following previously established protocols.²⁰

Synthesis of Virus-Incorporated Porous Alginate Hydrogels.

The incorporation of TMV and its mutant (TMV-RGD) in porous alginate hydrogel was based on previously reported methods.²⁶ Briefly, 5% w/v low viscosity sodium alginate (Protanal LF 10/60 FT, 30–60 mPas for 1%, kindly provided by FMC Biopolymer UK Ltd.) was dissolved in 2% w/v sodium bicarbonate (NaHCO_3) and 4% w/v pluronic F108 solution. A molar equivalent of citric acid with respect to NaHCO_3 was added to the mixture while stirring at 500 rpm using an overhead stirrer, 115 V. Stirring was continued for 15 min at room temperature to allow CO_2 to fully develop. For the porous alginate hydrogel (PAH) modified with TMV (TMV-PAH) or PAH modified with mutant TMV-RGD (RGD-PAH), 0.1% w/v of virus was added to the solution 10 min after adding citric acid. The mixture was stirred for another 5 min. Afterward, the foamy alginate solution was cast in a 6.35 mm (0.25 in.) diameter, 2 mm thick aluminum mold and freeze-dried. The resulting solid foam disc was soaked in 2 M of CaCl_2 for 24 h to induce the formation of the calcium-based physical gel and then dialyzed against a large volume of 0.1 M CaCl_2 . Finally, the solid foam was freeze-dried, resulting in porous alginate hydrogel (PAH) for implantation in animal studies.

Animals, Lethality Test, and Animal Treatments. The procedures were performed in accordance with the guidelines for animal experimentation and the protocol approved by the Institutional Animal Care and Use Committee, University of South Carolina. NIH guidelines (or similar national regulations for non-U.S. residents) for the care and use of laboratory animals (NIH Publication #85-23 Rev. 1985) have been observed. Twelve-week-old male Sprague–Dawley rats were housed at $22 \pm 2^\circ\text{C}$ with a 12/12 h light/dark cycle and fed standard rodent chow and water *ad libitum*. Nineteen rats were randomly assigned to experimental groups. Two groups that were implanted by PAH and TMV-PAH consisted of 6 rats each, respectively. Another group implanted by RGD-PAH consisted of 7 rats. Disk-shaped hydrogels were implanted to fill the cranial bone defects created in surgery. Rats were given 2–4 mg/kg of carprofen 2–4 h before surgery subcutaneously for analgesia. Procaine penicillin (60,000 IU) was given SQ for infection prophylaxis. Instruments were autoclaved prior to use to minimize risk of postsurgical infection and cross-contamination. The animal was anesthetized with 3% isoflurane in oxygen. After the appropriate plane of anesthesia was obtained, the fur over each animal's cranium was shaved, and the skin was cleansed with normal saline to remove loose hair. A dry heating pad was used to keep the animal warm during surgery. A midline incision was made from the middle of the nasofrontal area to the external occipital protuberance, utilizing a sterile no. 15 scalpel blade. Full-thickness skin flaps were reflected laterally with a periosteal elevator to expose the calvaria. An 8 mm craniotomy was performed in all animals utilizing a dental handpiece system at low speed and with copious sterile saline irrigation to remove loose debris and to avoid the generation of frictional heat at the surgical site. Bone defects were standardized by using an 8 mm diameter trephine bur to outline the treatment area. A PTFE barrier membrane (kindly provided by Osteogenics Biomedical, Lubbock, TX) was inserted to form a barrier on top of the dura. Next, the hydrogel scaffold was carefully placed into the defect, and the second PTFE membrane was placed over the defect and under the periosteum. The periosteum was repositioned and closed utilizing continuous interlocking sutures using nylon suture material. Post-operative analgesic to relieve pain (carprofen (2–4 mg/kg)) was given orally at least once every 24 h for 48 h. The animals were weighed immediately before/after surgery and daily afterward for the first 2 days. Then they were weighed once a week until the experiment ended. Signs of pain or distress were monitored daily after surgery.

Blood withdrawal was performed on day 4, weekly at the first 4 weeks, and biweekly until the end point at week 10, after the surgery. Blood samples from all animals were subjected to total blood count

B

DOI: 10.1021/acsbomaterials.5b00561
ACS Biomater. Sci. Eng. XXXX, XXX, XXX–XXX

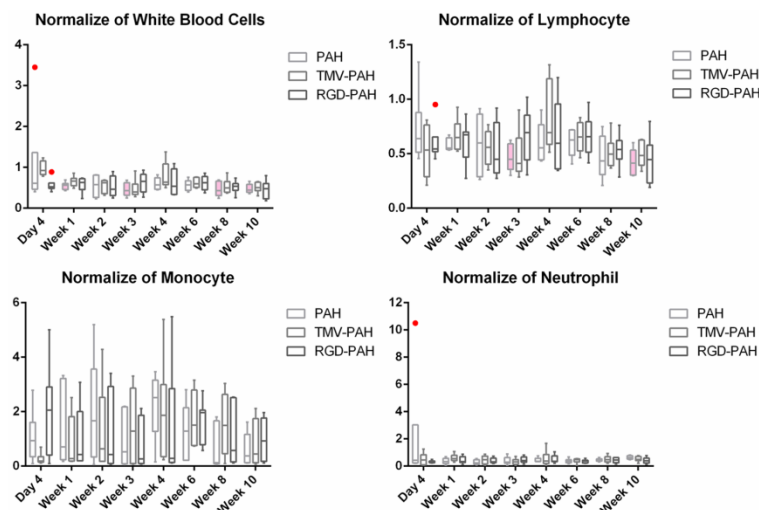


Figure 1. White blood count analysis of all rats with bone substitute implants. The total blood counts were monitored at 8 time points (day 4 and weeks 1, 2, 3, 4, 6, 8, and 10, postoperatively). The histograms show the numbers of total WBC, LYM, MON, and NEU normalized with the values measured from nontreated rats. Each bar indicates the minimum to maximum with the mean as the middle horizontal bar ($n = 6$ for PAH and TMV-PAH and $n = 7$ for RGD-PAH) \pm SD. From t test analysis comparing control (nontreatment) and experimental values, the filled bars represent statistical significance, $p < 0.05$. The red dots represent outliers.

and antigen–antibody ELISA assay specific to TMV. Three-hundred microliters of blood was withdrawn from the tail vein, while the animals were restrained using a restraint tube. After iodine scrubbing, a butterfly needle was inserted into the vein. The blood was then collected into the collection tube.

At the 10 week time point, the animals were euthanized. The implants were recovered together with their surrounding tissues. The excised implants with the surrounding tissues were then preserved in 10% neutral-buffered formalin for subsequent analyses. The spleen of every rat was isolated and weighted.

Microcomputed Tomography. The samples and the surrounding bone tissues were fixed in a 10% formalin solution for microcomputed tomography (Micro-CT, Skyscan 1076, Skyscan, Belgium) analysis and histopathology study 1 and 2 months after implantation. MicroCT was used to observe the new bone formation in the defected skull site. Each sample was fixed on the object stage, and imaging was performed on the sample for 360° of rotation with an exposure time of 20 min. MicroCT images were reconstructed over the region of interest (ROI) using CTAAn (Skyscan) and CTVol (Skyscan) to make 3D images.

Hematological Assay. For complete blood count (CBC), 10–50 μ L of blood was collected, transferred into a 1 mL BD Microtainer Tube with K_2 EDTA, and analyzed by VetScan HM5 Hematology System (company, country). The numbers of total white blood cells (WBC), neutrophils (NEU), monocytes (MON), lymphocytes (LYM), red blood cells (RBC), hemoglobin (HGB), and platelets (PLT) and mean platelet volume (MPV) were recorded and analyzed according to the calibrated instrumental protocol, which indicated the normal range of each parameter.

Paraffin Embedding and Histological Assays. The formalin fixed implanted hydrogels/tissues were decalcified using 10% formic acid in formalin for 1 week and then embedded in paraffin blocks individually with proper orientations. The 5 μ m tissue sections were prepared and stained with Masson's trichrome and hematoxylin and

eosin (H&E). On the basis of the amount of inflammatory cells observed within areas of implants, the degree of tissue inflammation was scored as 0, 1, and 2 (normal, none or rarely seen; slightly increased, 5 to 20 per 40 \times objective field; and obviously increased, > 20/40 \times objective field). According to the degree of fibrous or connective tissues and capillary blood vessels observed within the areas of implants, the tissue fibrosis and vascularization were scored as 0, 1, 2, and 3 (none; rarely seen, ≤ 2 vessels/40 \times field; slightly increased, 3–10/40 \times ; and obviously increased, >10 vessels/40 \times field, respectively). Bone regeneration was also evaluated and given the degree of new bone formation as follows: none or rarely seen; ≤ 2 /40 \times field, few or moderate; 3–10/40 \times field, and dense; > 10/40 \times field. Histological images were taken by a Nikon microscope and an Olympus digital camera.

Enzyme-Linked Immunosorbent Assay (ELISA). The serum samples for ELISA were obtained after centrifugation (2,000g, 15 min, 4 °C) of blood samples collected from every animal and stored at -80 °C. ELISA was performed no later than 3 months after the sera were collected. To coat wells with TMV antigen, a high protein-binding conical bottomed 96-well plate was used. Wild-type TMV (10 μ g/mL, 100 μ L) in phosphate buffered saline (PBS) was added to the microwells and incubated for 1 h at room temperature, followed by three PBS washes. Blocking for nonspecific binding was performed by adding 100 μ L of 1% bovine serum albumin (BSA) and incubating for 30 min at room temperature, followed by three PBS washes. Binding was performed by adding 100 μ L of serially diluted antiserum into microwells and incubating for 1 h at room temperature, followed by thorough washes. HRP conjugate antimouse IgG (Cayman Chemical Company) diluted at 1:20000 ratio was added and incubated for 30 min at room temperature. Tetramethyl benzidine (TMB Plus, Amresco) and 1 M H_2SO_4 were added in sequence to the wells according to the manufacturer's protocol, and the binding efficiency was monitored by measuring absorbance at 450 nm.

C

DOI: 10.1021/acsbomaterials.5b00561
ACS Biomater. Sci. Eng. XXXX, XXX, XXX–XXX

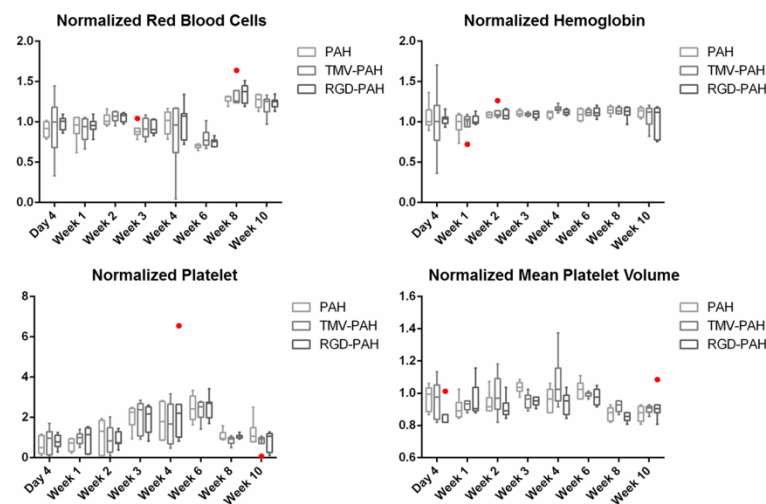


Figure 2. Hematology analysis of all rats with bone substitute implants. The total blood counts were monitored at 8 time points (day 4 and weeks 1, 2, 3, 4, 6, 8, and 10, postoperatively). The histograms show the numbers of RBC, HGB, PLT, and MPV normalized with the values measured from nontreated rats. Each bar indicates the minimum to maximum with the mean as the middle horizontal bar ($n = 6$ for PAH and TMV-PAH and $n = 7$ for RGD-PAH) \pm SD. From t test analysis comparing control (nontreatment) and experimental values, the filled bars represent statistical significance, $p < 0.05$. The red dots represent outliers.

Statistical Analysis. Statistical evaluation has been carried out using Graphpad Prism 6.0 software. For complete blood count, all groups were compared to each other using multiple t tests to assess whether there were statistically significant differences among them. Analysis of variance (ANOVA) was performed in all other experiments in this article.

3. RESULTS AND DISCUSSIONS

Surgical Recovery of Animals. The survival surgery of cranial bone defect creation with subsequent hydrogel implantation was carried out. Mean surgery time was 10 min ($SD = 4$). The animal's weight was measured immediately after the cranial defect survival surgery on each animal to monitor postsurgery weight loss. Figure S1A showed that all rats lost less than 5% of their initial weight measured before the operation. Blood loss during surgical procedure was also estimated to be less than 1 mL in all rats. The animals were closely monitored within the first 6 h after surgery and weighed every day for the first postoperative week and at least once every consecutive week, continuously for the entire experimental period. Postoperatively, the rats recovered quickly, gaining their baseline weight and returning to routine activities such as grooming, eating, and drinking in less than 48 h. The surgical wound healed within 1.5 weeks without postsurgical bleeding or wound infection. The surgical suture fell off spontaneously from the surgical site after the wound healed completely. From gross observations after cranial defect operation and implantation, all animals were normally active in eating, drinking, and grooming with no observable hair loss and aggressive behavior. The growth rate was evaluated by the body weight of rats at each time point normalized with their original weight before implantation. No differences in weight

gained among three groups of animals were observed. Comparing to the normal growth rate of Sprague–Dawley rats,²⁷ the weight gains are in agreement with unoperated rats (Figure S1B).

Systemic Inflammatory and Immunogenic Responses.

Complete blood count was analyzed from whole blood samples from each group of rats at every week for 4 weeks and then every other week until termination after 10 postoperative weeks. Figures 1 and 2 showed different blood counts at various time points in normalization to blood counts on day 0 before the operation. The host inflammatory responses after the surgery were evaluated by white blood count including total WBC, LYM, MON, and NEU counts. However, the comparison had no statistical difference for each parameter in each time point except for the PAH group. Rats implanted with PAH had statistically significant lower WBC at weeks 1, 3, 8, and 10, and LYM at weeks 3 and 10 compared to those of normal rats (multiple t tests, P value < 0.01). MON count from all rats was comparable with value shown in normal rat's blood (multiple t tests; no significant difference). We compared the postoperative WBC count between the viral particle non-exposure group (PAH) and exposure groups (TMV-PAH and RGD-PAH), and found no statistically significant differences of blood cells count across the groups. There were 2 outliers on day 4 white blood counts: one, from the RGD-PAH implanted group, expressed increased numbers of LYM and the corresponding WBC; another, from PAH implanted group, exhibited high NEU and its corresponding WBC. The elevated WBC counts could likely reflect the severity of the infection and associated inflammation. In such cases, the risk for poor wound healing should be highly suspected.²⁸ However, both

D

DOI: 10.1021/acsbiomaterials.5b00561
ACS Biomater. Sci. Eng. XXXX, XXX, XXX–XXX

rats had WBC counts leveled down to the values comparable to those of all other rats after 1 postoperative week (Figure 1).

Other blood parameters that indicate animal health and significant loss of blood such as RBC, HGB, PLT, and MPV were shown to be comparable to the values measured from nontreated rat's blood in all animals that were implanted with different types of hydrogels. Even though there were some outliers that appeared at different time points for each parameter, those outliers seemed to obtain only temporal changes in particular blood counts that returned to the normal values at the later time point (Figure 2).

Organ weight can be the most sensitive indicator of an effect of drug toxicity, as significant differences in organ weight between treated and control animals may occur in the absence of any morphological changes.²⁹ The spleen and liver are the main target organs for various nanomaterials in the circulatory system because these organs are part of the reticulo-endothelial system (RES) that has removing foreign agents from the circulation as one of its functions.^{30–32} In this study, we utilized viral nanoparticles in providing biofunctionality to the hydrogel to create an extracellular matrix preferable for cell attachment and growth. It was critical to evaluate the spleen enlargement that might occur from the immunogenic and/or elimination reaction of the body toward viral nanoparticles presented in the hydrogel implants. Figure 3 shows that the spleen weights measured after the animal sacrifice (at the age of 22 weeks) were not significantly different among all groups. The corresponding mean spleen weight of all rats was 1495 ± 236 mg/kg of total body weight, which is close to the value reported in the literature. The mean normal spleen weight of male Sprague–Dawley rat \pm SD, used to fit organ weights versus age in a previous study reported by Schoeffner et al., equaled to 1029 ± 191 mg/kg of total body weight.^{33,34} From each animal observed at the end of the experiment, there were no chronic and/or major inflammatory and toxicity reactions in the RES that could cause spleen enlargement in any group of animals.

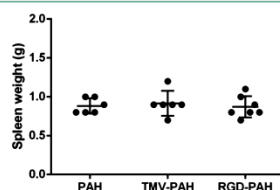


Figure 3. Rat spleen weight at the 10 weeks end point. Values expressed are the means ($n = 6$ for PAH and TMV-PAH and $n = 7$ for RGD-PAH) \pm SD.

Previously, we have discussed the immunogenicity of TMV in the hydrogels implanted subcutaneously at the lower back of BALB/c mice.¹⁷ The assay showed nonsignificant induction of specific anti-TMV immunoglobulin G (IgG) produced in mice. Here, with the distinct rat cranial defect model, we re-evaluated the humoral immune reaction caused by TMV and its RGD mutant in the hydrogels after bone defect replacement by TMV-PAH and RGD-PAH. From the ELISA assay, we found that TMV and its RGD mutant within the hydrogels led to an average anti-TMV titer at peak time (week 8) below 1000. Figure 4 reveals statistically higher anti-TMV antibody titers in

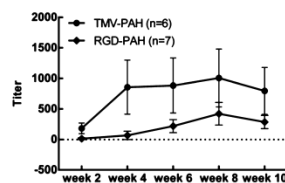


Figure 4. Immune response to TMV (anti-TMV titer) in the rats with bone substitute implant materials. Comparative serological analysis of the immune response to each type of hydrogels was carried out by ELISA at different time points including 2, 4, 6, 8, and 10 postoperative weeks. TCID₅₀ was shown as a titer for each plot. Values expressed are the means ($n = 6$ for TMV-PAH and $n = 7$ for RGD-PAH) \pm SEM.

rat sera collected from the animals implanted with TMV-PAH than those implanted with RGD-PAH hydrogels throughout the time points (ANOVA, P value <0.05), while the rats treated with PAH gave baseline (zero) titers. The ELISA was performed based solely on wild-type TMV (used as antigen coated on the ELISA plate). This could lead to the lower sensitivity in titer detection for the RGD-PAH group. Since it is not clear whether the antigen binding site of the antibodies produced against TMV wild-type and TMV-RGD share the same structure, the assay could be further optimized using different coatings for ELISA on sera collected from different groups of animals. Another possibility could be the difference of release profile between the wild-type TMV and the RGD mutant that escaped from the hydrogel scaffold into the circulation. Three out of 6 animals implanted with TMV-PAH expressed anti-TMV antibody as early as week 2. The titers were continuously increased to reach their maximum within week 8 when they started leveling off. Among 7 rats implanted with RGD-PAH, 4 rats produced antibodies against TMV. However, the initial time points that the titers were first detected varied from week 2 to week 8. Each individual titer for each rat at different time points was presented in Figure S2. This data suggested that there were only limited amounts of TMV antigen released from the hydrogels into the circulation system and that there is, however, a sustained humoral response to the viral nanoparticles at least up to 10 weeks.

Local Inflammatory Responses toward Hydrogel Implants. Histological sections of the explants were stained using Masson's trichrome method and the inflammation, fibrosis and connective tissue formation, and vascularization evaluated in the hydrogels. Figure 5 shows that RGD-PAH had higher scores on inflammation compared to that of the control PAH but that it is not significant from TMV-PAH (non-parametric ANOVA, P value >0.05). The average histopathological scores evaluated based on fibrosis or vasculature were not different among groups of implants. The descriptive statistics of each histopathological variable was demonstrated in Table S1. There were inflammatory cells observed in the following hydrogel implants with average scores of 1.2 (PAH) and 1.8 (TMV-PAH), and a maximum of 2.0 (RGD-PAH). The average scores of 2.0, 2.6, and 3.0 for PAH, TMV-PAH, and RGD-PAH, respectively, were given to the extent of connective and fibrous tissue (min–max = 0–3) formed in the hydrogels. Interestingly, every sample from the RGD-PAH group scored a maximum for inflammation and fibrosis variables, and gained at least a score of 2 for vasculature. The average scores for new

E

DOI: 10.1021/acsbomaterials.5b00561
ACS Biomater. Sci. Eng. XXXX, XXX, XXX–XXX

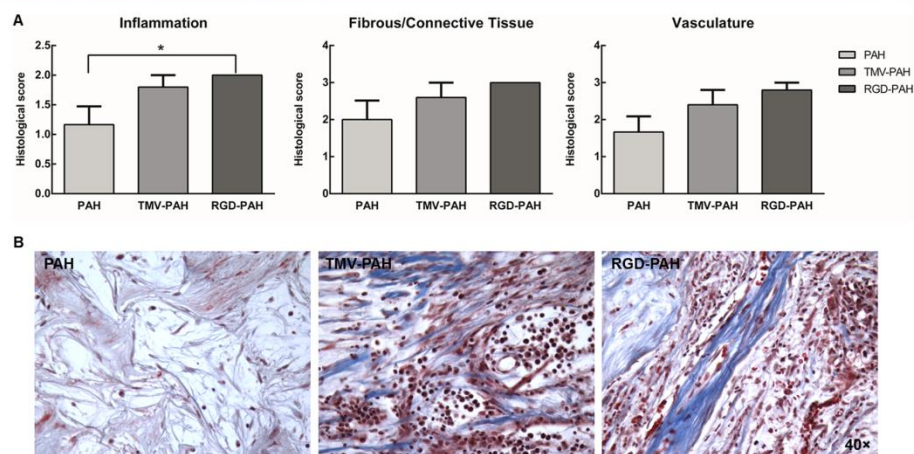


Figure 5. Histopathological analysis of bone substitute hydrogel implants via Masson's trichrome. (A) Histological scoring of three types of hydrogels in tissue excisions show different degrees of inflammation, fibrosis, and vascularization after 10 weeks of implantation. Values expressed are the means ($n = 6$ for PAH and $n = 5$ for TMV-PAH and RGD-PAH) \pm SEM. * $p < 0.05$. (B) Micrographs of corresponding Masson's trichrome stained sections from each type of hydrogel.

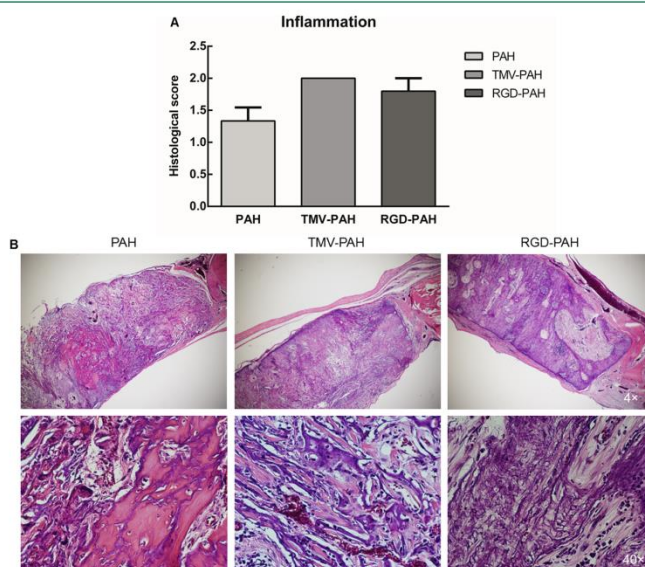


Figure 6. Inflammatory cell infiltration observed by H&E staining. (A) H&E histological scoring of three types of hydrogels confirm the differences in degrees of inflammation. Values expressed are the means ($n = 6$ for PAH and $n = 5$ for TMV-PAH and RGD-PAH) \pm SEM. * $p < 0.05$. (B) Micrographs of corresponding H&E stained sections from each type of hydrogel.

blood vessels formed in each type of hydrogel (min–max = 0–3) are 1.7 for PAH, 2.4 for TMV-PAH, and 2.8 for RGD-PAH.

These data were also confirmed by the H&E staining shown in Figure 6. In Figure 6A, the inflammation scores based on H&E

F

DOI: 10.1021/acsbiomaterials.5b00561
ACS Biomater. Sci. Eng. XXXX, XXX, XXX–XXX

given to the TMV-PAH and RGD-PAH explants were higher than that of PAH. One possible explanation could be that TMV might be able to induce more cytokine production from the migrating cells at the implantation site that could lead to more inflammatory cells being recruited. A previous report by Sitasuwan et al. found that elevated levels of cytokine-induced neutrophil chemoattractant-1 (CINC-1), CINC-2, macrophage inflammatory protein-3 α (MIP-3 α), and vascular endothelial growth factor (VEGF) were detected from the conditioned media for the bone marrow stromal cells grown on a TMV coated substrate.¹⁹ CINC-1 and MIP-3 α recruit neutrophils and monocytes that result in the induction of osteogenesis.³⁵ Cytokines and growth factors secreted by infiltrated inflammatory cells including neutrophils, monocyte-derived macrophages, and lymphocytes are the molecular messengers that promote inflammatory events, such as neutrophil and macrophage recruitment, as well as wound healing events, such as connective tissue synthesis and vasculature.^{35,36–38} Moreover, the RGD peptide introduced by the incorporation of TMV-RGD into the hydrogel implant could induce even more material–host interaction. However, it has not been conclusive whether RGD can regulate *in vivo* cell adhesion to biomaterials as it does *in vitro*.³⁹ Our observation was consistent with many reports in RGD-functionalized materials promoting materials and surrounding cell interaction *in vivo*. For example, Shu et al. reported that the inclusion of covalently attached RGD peptides onto hyaluronan-based hydrogels could enhance the formation of fibrous tissue *in vivo*, with increased production of procollagen by the fibroblasts in the newly formed fibrous tissue at 4 weeks after animal treatment.⁴⁰ The future study with larger animal numbers should be performed in order to confirm these results and obtain more statistically significant analyses. At this point, there might be a concern about the carcinogenicity of TMV and its derivatives as an inflammatory response shares various molecular targets and signaling pathways with the carcinogenic process. If the inflammation becomes chronic, the induction of cancerous cell transformation may occur.^{41,42} However, the possibility is low for TMV since it has a very short biological half-life.⁴³

Bone Healing Analysis. The new bone formation after the hydrogel implantation was evaluated by two methods: (1) microcomputed tomography (microCT) and (2) histological analysis of tissue excisions using Masson's trichrome staining technique. MicroCT is an X-ray-based imaging method that offers access to the 3D microarchitecture of bone. A computer combines a stack of virtual cross-sections, interpolating sections along different planes, to inspect the internal structure of the object. A quantitative 3D histomorphometric evaluation (i.e., determination of the volume of bone mass and of the microarchitecture indices of the newly formed bone) can then be performed on a cubic volume or on an irregularly shaped volume of interest.^{44,45} Here, we scanned the regenerated bone tissue excisions and quantified the new bone formed in each type of hydrogel implants using a microCT scanner. First, measurements of the angle of rotation and reconstruction of the 2D images were performed to ensure that all parts of the samples were scanned properly. All images from microCT analysis of the reconstructions are shown in Figure S3. Figure 7 shows that the RGD-PAH implant led to a slightly higher bone volume than the wild-type TMV hydrogel, yet no statistical significance in the average bone volume between groups of hydrogel implants was observed when quantified by microCT.

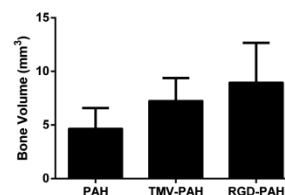


Figure 7. Bone regeneration in critical size defect areas with porous hydrogel bone substitutes. The bone volume regenerated in each type of hydrogel was quantified using microcomputed tomography (microCT). Values expressed are the means ($n = 6$ for PAH and $n = 5$ for TMV-PAH and RGD-PAH) \pm SEM.

The same samples were then subjected to histopathological analysis. Masson's trichrome shows the bone and non-mineralized osteoid seen in blue (aniline blue) and red (biebrich-scarlet), respectively. Figure 8 illustrates the representative image from each type of hydrogel sample corresponding to the bone density rank that obtained the highest frequency (rat number) within each hydrogel type. The insets of Figure 8 depicted descriptive statistical analysis showing the frequency of each level of bone tissue formed. For example, the histological image of RGD-PAH shown in the right panel of Figure 8 corresponded to the sample that was stained with dense bone tissue (weighted 60% of total rats treated with RGD-PAH). Figure 8 shows that the rats that received RGD-PAH implants had more probability to regenerate higher density of bone. Followed by the group that was treated with TMV-PAH, 60% of the animals in this group could regenerate a few or medium bone tissues. The group with PAH alone had the most probability in having none or rarely seen bone formation. This analysis suggested that by incorporating TMV particles into the hydrogel scaffold, the bone regeneration could be enhanced. This result also corresponded to the histological analysis from the previous section. This result yet contradicted with microCTs from which the insignificant difference in bone volume was compared. A possible explanation could be the effect from a pre-existing calcium cross-linker retained in the hydrogels before implant that might be interfering with the signal of bone formation under microCT. Therefore, further bone characterization studies such as mechanical push-out tests may be needed to confirm this finding. From microCT, we realized the lack of bone integration. One explanation could be the surgical procedure. Our implant was placed without direct contact with the resident bone; primary stability was only provided by the PTFE membrane sandwich rather than by any types of bone anchorage. The implants tended to move from the defect by time. In our future study, we will design an injectable implant that can better fill the defect and/or perform *in vivo* live monitoring of radiographic signs for osseointegration. With resonance frequency analysis, the acceptable stability and osseointegration of all implants can be indicated. Osseointegration requires certain biological conditions, including precise fit, a bioactive or biocompatible implant, primary stability, and adequate loading during the healing period.⁴⁶ Primary stability of the implant in bone is the most critical condition to achieve osseointegration, as new bone formation fills the marginal gap defect exclusively in the absence of micromovements.⁴⁷ It has been shown that in the absence of micromotion, the stable blood clot in the bone–implant

G

DOI: 10.1021/acsbomaterials.5b00561
ACS Biomater. Sci. Eng. XXXX, XXX, XXX–XXX

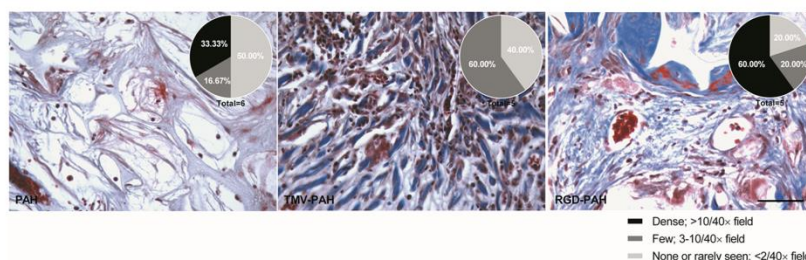


Figure 8. Histological analysis of regenerated bone at defect sites filled with hydrogel implants. Histological sections cut coronally through the defect after 10 weeks of implantation. The sections were stained with Masson's trichrome and imaged with 100 \times magnification. The regenerated bone was characterized by the presence of a collagen-rich matrix stained blue. The inset pie charts represent the number of rats that developed different degrees of bone regeneration at the defect site.

interface can mature into bone and help integrate the implant surface.^{48–50} Among combinations of hydrogel types, Pearson's statistical correlation test showed correlations between bone tissue formation in the hydrogel implants and two isolated histopathological variables including fibrous/connective tissue (correlation coefficient; $r = 0.6$) and neovascularization ($r = 0.6$). Consistent with many other studies, our data suggest that RGD, when attached to the implanted scaffolding materials, played an important role in cell recruitment that could eventually help promote bone regeneration.^{51–53} Accordingly, for our hydrogel system with virus nanoparticles, further detailed study is needed to confirm the physiological responses and bone induction activity.

4. CONCLUSIONS

The viral particle functionalized PAHs were comparatively investigated in terms of inflammation and healing of confined critical size cranial bone defects in rats. TMV- and RGD-PAH permitted the healing of critical size defects in the cranial segmental bone of rats, as did the PAH control gel, but, unlike the latter, RGD-PAH improved bone remodeling and maturation. The hydrogels elicited neither a systemic inflammatory reaction nor a severe immunogenic adverse effect. Therefore, virus-based combinatorial porous alginate hydrogel is potentially useful as bone replacement material in reconstructive orthopedic surgery, being a readily available biomaterial able to improve bone healing and maturation. However, more animal research with other models of bone defects (e.g., tibia and femur) and other higher animals will be needed before translation to the clinic.

■ ASSOCIATED CONTENT

Supporting Information

The Supporting Information is available free of charge on the ACS Publications website at DOI: 10.1021/acsbomaterials.5b00561.

Animal postoperative care and monitoring, individual titer for each rat at different time points, MicroCT images with two- and three-dimensional constructs of bone excisions from rats with PAH, TMV-PAH, and RGD-PAH implanted, and descriptive statistics table of histology variables from trichrome stained sections according to the type of hydrogel implant (PDF)

■ AUTHOR INFORMATION

Corresponding Authors

*(A.G.) Phone: 1-404-894-9384. Fax: 1-404-894-2291. E-mail: andres.garcia@me.gatech.edu.

*(Q.W.) Phone: +1-803-777-8436. Fax: +1-803-777-9521. E-mail: wang263@mailbox.sc.edu.

Funding

This work was partially supported by the South Carolina EPSCoR GEAR program, the USC ASPIRE Grant, and the NIH (R01 AR062368 and T32 GM008433).

Notes

The authors declare no competing financial interest.

■ ACKNOWLEDGMENTS

This work is partially supported by Rachadapisek Sompote Fund for Postdoctoral Fellowship, Chulalongkorn University. The authors would like to thank Katherine Gibson-Corley and Visarut Buranasudja of the University of Iowa for constructive advice on histopathology analysis.

■ ABBREVIATIONS

TMV, Tobacco mosaic virus; MSCs, mesenchymal stem cells; 3D, three-dimensional; RGD, arginine-glycine-aspartic acid; TMV-RGD, RGD mutant of TMV; BMP-2, bone morphogenic protein-2; PAH, porous alginate hydrogel; TMV-PAH, PAH modified with TMV; RGD-PAH, PAH modified with mutant TMV-RGD; PTFE, polytetrafluoroethylene; Micro-CT, micro-computed tomography; CBC, complete blood count; WBC, total white blood cell; NEU, neutrophil; MON, monocyte; LYM, lymphocyte; RBC, red blood cell; HGB, hemoglobin; PLT, platelet; MPV, mean platelet volume; RES, reticulo-endothelial system; H&E, hematoxylin and eosin; ELISA, enzyme-linked immunosorbent assay; PBS, phosphate buffer saline; BSA, bovine serum albumin; IgG, immunoglobulin G; CINC-1, cytokine-induced neutrophil chemoattractant-1; MIP-3 α , macrophage inflammatory protein-3 α ; VEGF, vascular endothelial growth factor

■ REFERENCES

- (1) Perry, C. R. Bone repair techniques, bone graft, and bone graft substitutes. *Clin. Orthop. Relat. Res.* **1999**, 360, 71–86.
- (2) Rimondini, L.; Nicoli-Aldini, N.; Fini, M.; Guzzardella, G.; Tschon, M.; Giardino, R. In vivo experimental study on bone regeneration in critical bone defects using an injectable biodegradable

H

DOI: 10.1021/acsbomaterials.5b00561
ACS Biomater. Sci. Eng. XXXX, XXX, XXX–XXX

- PLA/PGA copolymer. *Oral surgery, oral medicine, oral pathology, oral radiology, and endodontics* **2005**, 99 (2), 148–54.
- (3) Fini, M.; Nicoli Aldini, N.; Gandolfi, M. G.; Mattioli Belmonte, M.; Giavresi, G.; Zucchini, C.; De Benedittis, A.; Amati, S.; Ravaglioli, A.; Krayewski, A.; Rocca, M.; Guzzardella, G. A.; Biagini, G.; Giardino, R. Biomaterials for orthopedic surgery in osteoporotic bone: a comparative study in osteopenic rats. *Int. J. Artif. Organs* **1997**, 20 (5), 291–7.
- (4) Goldberg, V. M.; Stevenson, S. Natural history of autografts and allografts. *Clin. Orthop. Relat. Res.* **1987**, 225, 7–16.
- (5) Fini, M.; Motta, A.; Torricelli, P.; Giavresi, G.; Nicoli Aldini, N.; Tschon, M.; Giardino, R.; Migliaresi, C. The healing of confined critical size cancellous defects in the presence of silk fibroin hydrogel. *Biomaterials* **2005**, 26 (17), 3527–36.
- (6) Bodde, E. W.; Spauwen, P. H.; Mikos, A. G.; Jansen, J. A. Closing capacity of segmental radius defects in rabbits. *J. Biomed. Mater. Res., Part A* **2008**, 85 (1), 206–17.
- (7) Cancedda, R.; Giannoni, P.; Mastrogiacomo, M. A tissue engineering approach to bone repair in large animal models and in clinical practice. *Biomaterials* **2007**, 28 (29), 4240–50.
- (8) Pearce, A. L.; Richards, R. G.; Milz, S.; Schneider, E.; Pearce, S. G. Animal models for implant biomaterial research in bone: a review. *Eur. Cell. Mater.* **2007**, 13, 1–10.
- (9) Schmitz, J. P.; Hollinger, J. O. The critical size defect as an experimental model for craniomandibulofacial nonunions. *Clin. Orthop. Relat. Res.* **1986**, 205, 299–308.
- (10) Freeman, E.; Turnbull, R. S. The value of osseous coagulum as a graft material. *J. Periodontol. Res.* **1973**, 8 (4), 229–36.
- (11) Takagi, K.; Urist, M. R. The reaction of the dura to bone morphogenetic protein (BMP) in repair of skull defects. *Ann. Surg.* **1982**, 196 (1), 100–9.
- (12) Ferland, C. E.; Laverty, S.; Beaudry, F.; Vachon, P. Gait analysis and pain response of two rodent models of osteoarthritis. *Pharmacol. Biochem. Behav.* **2011**, 97 (3), 603–10.
- (13) Spicer, P. P.; Kretlow, J. D.; Young, S.; Jansen, J. A.; Kasper, F. K.; Mikos, A. G. Evaluation of bone regeneration using the rat critical size calvarial defect. *Nat. Protoc.* **2012**, 7 (10), 1918–29.
- (14) Hsiong, S. X.; Boontheekul, T.; Huebsch, N.; Mooney, D. J. Cyclic arginine-glycine-aspartate peptides enhance three-dimensional stem cell osteogenic differentiation. *Tissue Eng., Part A* **2009**, 15 (2), 263–72.
- (15) Eisel, P.; Yeh, J.; Latvala, R. K.; Shea, L. D.; Mooney, D. J. Porous carriers for biomedical applications based on alginate hydrogels. *Biomaterials* **2000**, 21 (19), 1921–7.
- (16) Halberstadt, C.; Austin, C.; Rowley, J.; Culberson, C.; Loebbeck, A.; Wyatt, S.; Coleman, S.; Blacksten, L.; Burg, K.; Mooney, D.; Holder, W., Jr. A hydrogel material for plastic and reconstructive applications injected into the subcutaneous space of a sheep. *Tissue Eng.* **2002**, 8 (2), 309–19.
- (17) Luckanagul, J. A.; Lee, L. A.; You, S.; Yang, X.; Wang, Q. Plant virus incorporated hydrogels as scaffolds for tissue engineering possess low immunogenicity in vivo. *J. Biomed. Mater. Res., Part A* **2015**, 103, 887.
- (18) Lee, L. A.; Muhammad, S. M.; Nguyen, Q. L.; Sitasuwan, P.; Horvath, G.; Wang, Q. Multivalent ligand displayed on plant virus induces rapid onset of bone differentiation. *Mol. Pharmaceutics* **2012**, 9 (7), 2121–5.
- (19) Sitasuwan, P.; Lee, L. A.; Bo, P.; Davis, E. N.; Lin, Y.; Wang, Q. A plant virus substrate induces early upregulation of BMP2 for rapid bone formation. *Integr. Biol.* **2012**, 4 (6), 651–60.
- (20) Bruckman, M. A.; Kaur, G.; Lee, L. A.; Xie, F.; Sepulveda, J.; Breitenkamp, R.; Zhang, X.; Joralemon, M.; Russell, T. P.; Emrick, T.; Wang, Q. Surface modification of tobacco mosaic virus with “click” chemistry. *ChemBioChem* **2008**, 9 (4), 519–23.
- (21) Lee, L. A.; Nguyen, Q. L.; Wu, L.; Horvath, G.; Nelson, R. S.; Wang, Q. Mutant plant viruses with cell binding motifs provide differential adhesion strengths and morphologies. *Biomacromolecules* **2012**, 13 (2), 422–31.
- (22) Karpova, O. V.; Ivanov, K. I.; Rodionova, N. P.; Dorokhov, Y. L.; Atabekov, J. G. Nontranslatability and dissimilar behavior in plants and protoplasts of viral RNA and movement protein complexes formed in vitro. *Virology* **1997**, 230 (1), 11–21.
- (23) Mallajosyula, J. K.; Hiatt, E.; Hume, S.; Johnson, A.; Jeevan, T.; Chikwamba, R.; Pogue, G. P.; Bratcher, B.; Haydon, H.; Webby, R. J.; McCormick, A. A. Single-dose monomeric HA subunit vaccine generates full protection from influenza challenge. *Hum. Vaccines Immunother.* **2014**, 10 (3), 586–595.
- (24) Yin, Z.; Nguyen, H. G.; Chowdhury, S.; Bentley, P.; Bruckman, M. A.; Miermont, A.; Gildersleeve, J. C.; Wang, Q.; Huang, X. Tobacco mosaic virus as a new carrier for tumor associated carbohydrate antigens. *Bioconjugate Chem.* **2012**, 23 (8), 1694–703.
- (25) Kaur, G.; Valarmathi, M. T.; Potts, J. D.; Jabbari, E.; Sabo-Attwood, T.; Wang, Q. Regulation of osteogenic differentiation of rat bone marrow stromal cells on 2D nanorod substrates. *Biomaterials* **2010**, 31 (7), 1732–41.
- (26) Luckanagul, J.; Lee, L. A.; Nguyen, Q. L.; Sitasuwan, P.; Yang, X.; Shazly, T.; Wang, Q. Porous alginate hydrogel functionalized with virus as three-dimensional scaffolds for bone differentiation. *Biomacromolecules* **2012**, 13 (12), 3949–58.
- (27) Sengupta, P. The Laboratory Rat: Relating Its Age With Human's. *Int. J. Prev. Med.* **2013**, 4 (6), 624–30.
- (28) Bee, Y.-S.; Lin, M.-C.; Sheu, S.-J.; Ng, J. D. Elevated white blood cell count may predict risk of orbital implant exposure. *Can. J. Ophthalmol.* **2014**, 49 (1), 45–49, <http://dx.doi.org/10.1016/j.jco.2013.08.013>.
- (29) Piao, Y.; Liu, Y.; Xie, X. Change trends of organ weight background data in sprague dawley rats at different ages. *J. Toxicol. Pathol.* **2013**, 26 (1), 29–34.
- (30) De Jong, W. H.; Hagens, W. L.; Krystek, P.; Burger, M. C.; Sips, A. J.; Geertsma, R. E. Particle size-dependent organ distribution of gold nanoparticles after intravenous administration. *Biomaterials* **2008**, 29 (12), 1912–9.
- (31) De Jong, W. H.; Van Der Ven, L. T.; Sleijffers, A.; Park, M. V.; Jansen, E. H.; Van Loveren, H.; Vandebriel, R. J. Systemic and immunotoxicity of silver nanoparticles in an intravenous 28 days repeated dose toxicity study in rats. *Biomaterials* **2013**, 34 (33), 8333–43.
- (32) Lankveld, D. P.; Oomen, A. G.; Krystek, P.; Neigh, A.; Troost-de Jong, A.; Noorlander, C. W.; Van Eijkeren, J. C.; Geertsma, R. E.; De Jong, W. H. The kinetics of the tissue distribution of silver nanoparticles of different sizes. *Biomaterials* **2010**, 31 (32), 8350–61.
- (33) Mirfazaelian, A.; Kim, K. B.; Lee, S.; Kim, H. J.; Bruckner, J. V.; Fisher, J. W. Organ growth functions in maturing male Sprague-Dawley rats. *J. Toxicol. Environ. Health, Part A* **2007**, 70 (5), 429–38.
- (34) Schoeffner, D. J.; Warren, D. A.; Muralidara, S.; Bruckner, J. V.; Simmons, J. E. Organ weights and fat volume in rats as a function of strain and age. *J. Toxicol. Environ. Health, Part A* **1999**, 56 (7), 449–62.
- (35) Kim, Y. S.; Min, K. S.; Jeong, D. H.; Jang, J. H.; Kim, H. W.; Kim, E. C. Effects of fibroblast growth factor-2 on the expression and regulation of chemokines in human dental pulp cells. *Journal of endodontics* **2010**, 36 (11), 1824–30.
- (36) Nunamaker, E. A.; Purcell, E. K.; Kipke, D. R. In vivo stability and biocompatibility of implanted calcium alginate disks. *J. Biomed. Mater. Res., Part A* **2007**, 83 (4), 1128–37.
- (37) Schutte, R. J.; Xie, L.; Klitzman, B.; Reichert, W. M. In vivo cytokine-associated responses to biomaterials. *Biomaterials* **2009**, 30 (2), 160–8.
- (38) Xia, Z.; Triffitt, J. T. A review on macrophage responses to biomaterials. *Biomed. Mater.* **2006**, 1 (1), R1–9.
- (39) Bellis, S. L. Advantages of RGD peptides for directing cell association with biomaterials. *Biomaterials* **2011**, 32 (18), 4205–10.
- (40) Shu, X. Z.; Ghosh, K.; Liu, Y.; Palumbo, F. S.; Luo, Y.; Clark, R. A.; Prestwich, G. D. Attachment and spreading of fibroblasts on an RGD peptide-modified injectable hyaluronan hydrogel. *J. Biomed. Mater. Res.* **2004**, 68 (2), 365–75.

- (41) Hussain, S. P.; Harris, C. C. Inflammation and cancer: an ancient link with novel potentials. *Int. J. Cancer* **2007**, *121* (11), 2373–80.
- (42) Medzhitov, R. Origin and physiological roles of inflammation. *Nature* **2008**, *454* (7203), 428–35.
- (43) Bruckman, M. A.; Randolph, L. N.; VanMeter, A.; Hern, S.; Shoffstall, A. J.; Taurog, R. E.; Steinmetz, N. F. Biodistribution, pharmacokinetics, and blood compatibility of native and PEGylated tobacco mosaic virus nano-rods and -spheres in mice. *Virology* **2014**, *449*, 163–73.
- (44) Holdsworth, D. W.; Thornton, M. M. Micro-CT in small animal and specimen imaging. *Trends Biotechnol.* **2002**, *20* (8), S34–S39, [http://dx.doi.org/10.1016/S0167-7799\(02\)0004-8](http://dx.doi.org/10.1016/S0167-7799(02)0004-8).
- (45) Kallai, I.; Mizrahi, O.; Tawackoli, W.; Gazit, Z.; Pelled, G.; Gazit, D. Microcomputed tomography-based structural analysis of various bone tissue regeneration models. *Nat. Protoc.* **2011**, *6* (1), 105–10.
- (46) Villa, R.; Polimeni, G.; Wikesjö, U. M. E. Implant osseointegration in the absence of primary bone anchorage: A clinical report. *J. Prosthet. Dent.* **2010**, *104* (5), 282–287, [http://dx.doi.org/10.1016/S0022-3913\(10\)00146-0](http://dx.doi.org/10.1016/S0022-3913(10)00146-0).
- (47) Lioubavina-Hack, N.; Lang, N. P.; Karring, T. Significance of primary stability for osseointegration of dental implants. *Clinical Oral Implants Research* **2006**, *17* (3), 244–250.
- (48) Berglundh, T.; Abrahamsson, I.; Lang, N. P.; Lindhe, J. De novo alveolar bone formation adjacent to endosseous implants. *Clin Oral Implants Res.* **2003**, *14* (3), 251–62.
- (49) Abrahamsson, I.; Berglundh, T.; Linder, E.; Lang, N. P.; Lindhe, J. Early bone formation adjacent to rough and turned endosseous implant surfaces. *Clinical Oral Implants Research* **2004**, *15* (4), 381–392.
- (50) Davies, J. E. Mechanisms of endosseous integration. *Int. J. Prosthodont.* **1998**, *11* (5), 391–401.
- (51) Chen, J.; Bly, R. A.; Saad, M. M.; AlKhodary, M. A.; El-Backly, R. M.; Cohen, D. J.; Kattamis, N.; Fatta, M. M.; Moore, W. A.; Arnold, C. B.; Marei, M. K.; Soboyejo, W. O. In-vivo study of adhesion and bone growth around implanted laser groove/RGD-functionalized Ti-6Al-4V pins in rabbit femurs. *Mater. Sci. Eng., C* **2011**, *31* (5), 826–832, <http://dx.doi.org/10.1016/j.msec.2010.12.019>.
- (52) Ferris, D. M.; Moodie, G. D.; Dimond, P. M.; Gioranni, C. W.; Ehrlich, M. G.; Valentini, R. F. RGD-coated titanium implants stimulate increased bone formation in vivo. *Biomaterials* **1999**, *20* (23–24), 2323–31.
- (53) Kroese-Deutman, H. C.; van den Dolder, J.; Spauwen, P. H.; Jansen, J. A. Influence of RGD-loaded titanium implants on bone formation in vivo. *Tissue Eng.* **2005**, *11* (11–12), 1867–75.

REFERENCES

1. Malliaras K, Kreke M, Marban E: **The stuttering progress of cell therapy for heart disease.** *Clin Pharmacol Ther* 2011, **90**:532-541.
2. Levit RD, Landazuri N, Phelps EA, Brown ME, Garcia AJ, Davis ME, Joseph G, Long R, Safley SA, Suever JD, et al.: **Cellular encapsulation enhances cardiac repair.** *J Am Heart Assoc* 2013, **2**:e000367.
3. Hou D, Youssef EA, Brinton TJ, Zhang P, Rogers P, Price ET, Yeung AC, Johnstone BH, Yock PG, March KL: **Radiolabeled cell distribution after intramyocardial, intracoronary, and interstitial retrograde coronary venous delivery: implications for current clinical trials.** *Circulation* 2005, **112**:1150-156.
4. Shear DA, Tate CC, Tate MC, Archer DR, LaPlaca MC, Stein DG, Dunbar GL: **Stem cell survival and functional outcome after traumatic brain injury is dependent on transplant timing and location.** *Restor Neurol Neurosci* 2011, **29**:215-225.
5. Cheng K, Li TS, Malliaras K, Davis DR, Zhang Y, Marban E: **Magnetic targeting enhances engraftment and functional benefit of iron-labeled cardiosphere-derived cells in myocardial infarction.** *Circ Res* 2010, **106**:1570-1581.
6. Terrovitis J, Lautamaki R, Bonios M, Fox J, Engles JM, Yu J, Leppo MK, Pomper MG, Wahl RL, Seidel J, et al.: **Noninvasive quantification and optimization of acute cell retention by in vivo positron emission tomography after intramyocardial cardiac-derived stem cell delivery.** *J Am Coll Cardiol* 2009, **54**:1619-1626.
7. Quevedo HC, Hatzistergos KE, Oskouei BN, Feigenbaum GS, Rodriguez JE, Valdes D, Pattany PM, Zambrano JP, Hu Q, McNiece I, et al.: **Allogeneic mesenchymal stem cells restore cardiac function in chronic ischemic cardiomyopathy via trilineage differentiating capacity.** *Proc Natl Acad Sci U S A* 2009, **106**:14022-14027.
8. Stabenfeldt SE, Munglani G, Garcia AJ, LaPlaca MC: **Biomimetic microenvironment modulates neural stem cell survival, migration, and differentiation.** *Tissue Eng Part A* 2010, **16**:3747-3758.
9. De Long WG, Jr., Einhorn TA, Koval K, McKee M, Smith W, Sanders R, Watson T: **Bone grafts and bone graft substitutes in orthopaedic trauma surgery. A critical analysis.** *J Bone Joint Surg Am* 2007, **89**:649-658.
10. Carragee EJ, Hurwitz EL, Weiner BK: **A critical review of recombinant human bone morphogenetic protein-2 trials in spinal surgery: emerging safety concerns and lessons learned.** *Spine J* 2011, **11**:471-491.
11. Caplan A: **New era of cell-based orthopedic therapies.** *Tissue Eng Part B Rev* 2009, **15**:195-200.

12. DJ Prockop D, N Bazhanov, RL Reger **Evolving paradigms for repair of tissues by adult stem/progenitor cells (MSCs).** *J Cell Mol Med* 2010, **14**:2190-2199.
13. da Silva Meirelles L, P.C. Chagastelles, and N.B. Nardi: **Mesenchymal stem cells reside in virtually all post-natal organs and tissues.** *J Cell Sci* 2006, **119**:2204-2213.
14. G Chamberlain J, B Ashton, J Middleton: **Concise review: mesenchymal stem cells: their phenotype, differentiation capacity, immunological features, and potential for homing.** *Stem Cells* 2007, **25**:2739-2749.
15. S Wakitani TM, N Nakamura, Y Toritsuka, Y Nakamura, S Horibe: **Autologous bone marrow stromal cell transplantation for repair of full-thickness articular cartilage defects in human patellae: two case reports.** *Cell Transplant* 2004, **13**:595-600.
16. V Gangji JH: **Treatment of osteonecrosis of the femoral head with implantation of autologous bone-marrow cells.** *J Bone Joint Surg Am* 2005, **87**:106-112.
17. Au P, Tam J, Fukumura D, Jain RK: **Bone marrow-derived mesenchymal stem cells facilitate engineering of long-lasting functional vasculature.** *Blood* 2008, **111**:4551-4558.
18. Kinnaird T, Stabile E, Burnett MS, Lee CW, Barr S, Fuchs S, Epstein SE: **Marrow-derived stromal cells express genes encoding a broad spectrum of arteriogenic cytokines and promote in vitro and in vivo arteriogenesis through paracrine mechanisms.** *Circ Res* 2004, **94**:678-685.
19. Kim HJ, Lee JH, Kim SH: **Therapeutic effects of human mesenchymal stem cells on traumatic brain injury in rats: secretion of neurotrophic factors and inhibition of apoptosis.** *J Neurotrauma* 2010, **27**:131-138.
20. Iso Y, Spees JL, Serrano C, Bakondi B, Pochampally R, Song YH, Sobel BE, Delafontaine P, Prockop DJ: **Multipotent human stromal cells improve cardiac function after myocardial infarction in mice without long-term engraftment.** *Biochem Biophys Res Commun* 2007, **354**:700-706.
21. Trounson A, McDonald C: **Stem Cell Therapies in Clinical Trials: Progress and Challenges.** *Cell Stem Cell* 2015, **17**:11-22.
22. Aggarwal S, Pittenger MF: **Human mesenchymal stem cells modulate allogeneic immune cell responses.** *Blood* 2005, **105**:1815-1822.
23. Beyth S, Borovsky Z, Mevorach D, Liebergall M, Gazit Z, Aslan H, Galun E, Rachmilewitz J: **Human mesenchymal stem cells alter antigen-presenting cell maturation and induce T-cell unresponsiveness.** *Blood* 2005, **105**:2214-2219.

24. Prockop DJ, Oh JY: **Mesenchymal stem/stromal cells (MSCs): role as guardians of inflammation.** *Mol Ther* 2012, **20**:14-20.
25. Ren G, Zhang L, Zhao X, Xu G, Zhang Y, Roberts AI, Zhao RC, Shi Y: **Mesenchymal stem cell-mediated immunosuppression occurs via concerted action of chemokines and nitric oxide.** *Cell Stem Cell* 2008, **2**:141-150.
26. Zimmermann JA, McDevitt TC: **Pre-conditioning mesenchymal stromal cell spheroids for immunomodulatory paracrine factor secretion.** *Cytotherapy* 2014, **16**:331-345.
27. Bartosh TJ, Ylostalo JH, Mohammadipoor A, Bazhanov N, Coble K, Claypool K, Lee RH, Choi H, Prockop DJ: **Aggregation of human mesenchymal stromal cells (MSCs) into 3D spheroids enhances their antiinflammatory properties.** *Proc Natl Acad Sci U S A* 2010, **107**:13724-13729.
28. Potapova IA, Brink PR, Cohen IS, Doronin SV: **Culturing of human mesenchymal stem cells as three-dimensional aggregates induces functional expression of CXCR4 that regulates adhesion to endothelial cells.** *J Biol Chem* 2008, **283**:13100-13107.
29. Kim S, Kim SS, Lee SH, Eun Ahn S, Gwak SJ, Song JH, Kim BS, Chung HM: **In vivo bone formation from human embryonic stem cell-derived osteogenic cells in poly(d,l-lactic-co-glycolic acid)/hydroxyapatite composite scaffolds.** *Biomaterials* 2008, **29**:1043-1053.
30. Levi B, Hyun JS, Montoro DT, Lo DD, Chan CK, Hu S, Sun N, Lee M, Grova M, Connolly AJ, et al.: **In vivo directed differentiation of pluripotent stem cells for skeletal regeneration.** *Proc Natl Acad Sci U S A* 2012.
31. Hunter KT, Ma T: **In vitro evaluation of hydroxyapatite-chitosan-gelatin composite membrane in guided tissue regeneration.** *J Biomed Mater Res A* 2012.
32. Lutolf MP, Weber FE, Schmoekel HG, Schense JC, Kohler T, Muller R, Hubbell JA: **Repair of bone defects using synthetic mimetics of collagenous extracellular matrices.** *Nat Biotechnol* 2003, **21**:513-518.
33. Engler AJ, Sen S, Sweeney HL, Discher DE: **Matrix elasticity directs stem cell lineage specification.** *Cell* 2006, **126**:677-689.
34. Discher DE, Janmey P, Wang YL: **Tissue cells feel and respond to the stiffness of their substrate.** *Science* 2005, **310**:1139-1143.
35. Trappmann B, Gautrot JE, Connelly JT, Strange DG, Li Y, Oyen ML, Cohen Stuart MA, Boehm H, Li B, Vogel V, et al.: **Extracellular-matrix tethering regulates stem-cell fate.** *Nat Mater* 2012, **11**:642-649.

36. Connelly JT, Gautrot JE, Trappmann B, Tan DW, Donati G, Huck WT, Watt FM: **Actin and serum response factor transduce physical cues from the microenvironment to regulate epidermal stem cell fate decisions.** *Nat Cell Biol* 2010, **12**:711-718.
37. Gao L, McBeath R, Chen CS: **Stem cell shape regulates a chondrogenic versus myogenic fate through Rac1 and N-cadherin.** *Stem Cells* 2010, **28**:564-572.
38. Huebsch N, Arany PR, Mao AS, Shvartsman D, Ali OA, Bencherif SA, Rivera-Feliciano J, Mooney DJ: **Harnessing traction-mediated manipulation of the cell/matrix interface to control stem-cell fate.** *Nat Mater* 2010, **9**:518-526.
39. Chaudhuri O, Gu L, Klumpers D, Darnell M, Bencherif SA, Weaver JC, Huebsch N, Lee HP, Lippens E, Duda GN, et al.: **Hydrogels with tunable stress relaxation regulate stem cell fate and activity.** *Nat Mater* 2015.
40. Bott K, Upton Z, Schrobback K, Ehrbar M, Hubbell JA, Lutolf MP, Rizzi SC: **The effect of matrix characteristics on fibroblast proliferation in 3D gels.** *Biomaterials* 2010, **31**:8454-8464.
41. Bian L, Hou C, Tous E, Rai R, Mauck RL, Burdick JA: **The influence of hyaluronic acid hydrogel crosslinking density and macromolecular diffusivity on human MSC chondrogenesis and hypertrophy.** *Biomaterials* 2013, **34**:413-421.
42. Phelps EA, Enemchukwu NO, Fiore VF, Sy JC, Murthy N, Sulchek TA, Barker TH, Garcia AJ: **Maleimide cross-linked bioactive PEG hydrogel exhibits improved reaction kinetics and cross-linking for cell encapsulation and in situ delivery.** *Adv Mater* 2012, **24**:64-70, 62.
43. Ghajar CM, Chen X, Harris JW, Suresh V, Hughes CC, Jeon NL, Putnam AJ, George SC: **The effect of matrix density on the regulation of 3-D capillary morphogenesis.** *Biophys J* 2008, **94**:1930-1941.
44. Enemchukwu NO, Cruz-Acuna R, Bongiorno T, Johnson CT, Garcia JR, Sulchek T, Garcia AJ: **Synthetic matrices reveal contributions of ECM biophysical and biochemical properties to epithelial morphogenesis.** *J Cell Biol* 2016, **212**:113-124.
45. Lutolf MP, Raeber GP, Zisch AH, Tirelli N, Hubbell JA: **Cell-Responsive Synthetic Hydrogels.** *Advanced Materials* 2003, **15**:888-892.
46. Boerckel JD, Kolambkar YM, Dupont KM, Uhrig BA, Phelps EA, Stevens HY, Garcia AJ, Guldberg RE: **Effects of protein dose and delivery system on BMP-mediated bone regeneration.** *Biomaterials* 2011, **32**:5241-5251.
47. Geuze RE, Theyse LF, Kempen DH, Hazewinkel HA, Kraak HY, Oner FC, Dhert WJ, Alblas J: **A differential effect of bone morphogenetic protein-2 and vascular**

- endothelial growth factor release timing on osteogenesis at ectopic and orthotopic sites in a large-animal model.** *Tissue Eng Part A* 2012, **18**:2052-2062.
48. Sakiyama-Elbert SE, Hubbell JA: **Development of fibrin derivatives for controlled release of heparin-binding growth factors.** *Journal of Controlled Release* 2000, **65**:389-402.
 49. Taylor SJ, McDonald JW, 3rd, Sakiyama-Elbert SE: **Controlled release of neurotrophin-3 from fibrin gels for spinal cord injury.** *J Control Release* 2004, **98**:281-294.
 50. Phelps EA, Landazuri N, Thule PM, Taylor WR, Garcia AJ: **Bioartificial matrices for therapeutic vascularization.** *Proc Natl Acad Sci U S A* 2010, **107**:3323-3328.
 51. Degano IR, Vilalta M, Bago JR, Matthies AM, Hubbell JA, Dimitriou H, Bianco P, Rubio N, Blanco J: **Bioluminescence imaging of calvarial bone repair using bone marrow and adipose tissue-derived mesenchymal stem cells.** *Biomaterials* 2008, **29**:427-437.
 52. Becquart P, Cambon-Binder A, Monfoulet LE, Bourguignon M, Vandamme K, Bensidhoum M, Petite H, Logeart-Avramoglou D: **Ischemia is the prime but not the only cause of human multipotent stromal cell death in tissue-engineered constructs in vivo.** *Tissue Eng Part A* 2012, **18**:2084-2094.
 53. Ehrbar M, Zeisberger SM, Raeber GP, Hubbell JA, Schnell C, Zisch AH: **The role of actively released fibrin-conjugated VEGF for VEGF receptor 2 gene activation and the enhancement of angiogenesis.** *Biomaterials* 2008, **29**:1720-1729.
 54. Moon JJ, Saik JE, Poche RA, Leslie-Barbick JE, Lee SH, Smith AA, Dickinson ME, West JL: **Biomimetic hydrogels with pro-angiogenic properties.** *Biomaterials* 2010, **31**:3840-3847.
 55. Leach JK, Kaigler D, Wang Z, Krebsbach PH, Mooney DJ: **Coating of VEGF-releasing scaffolds with bioactive glass for angiogenesis and bone regeneration.** *Biomaterials* 2006, **27**:3249-3255.
 56. Wernike E, Montjovent M-O, Liu Y, Wismeijer D, Hunziker EB, Siebenrock K-A, Hofstetter W, Klenke FM: **Vegf incorporated into calcium phosphate ceramics promotes vascularisation and bone formation in vivo.** *E Wernike et al. Promotion of biomaterial vascularization European Cells and Materials* 2010, **19**:30-40.
 57. Patel ZS, Young S, Tabata Y, Jansen JA, Wong ME, Mikos AG: **Dual delivery of an angiogenic and an osteogenic growth factor for bone regeneration in a critical size defect model.** *Bone* 2008, **43**:931-940.

58. Young S, Patel ZS, Kretlow JD, Murphy MB, Mountziaris PM, Baggett LS, Ueda H, Tabata Y, Jansen JA, Wong M, et al.: **Dose effect of dual delivery of vascular endothelial growth factor and bone morphogenetic protein-2 on bone regeneration in a rat critical-size defect model.** *Tissue Eng Part A* 2009, **15**:2347-2362.
59. Garcia JR, Clark AY, Garcia AJ: **Integrin-specific hydrogels functionalized with VEGF for vascularization and bone regeneration of critical-size bone defects.** *J Biomed Mater Res A* 2015.
60. Wan C, Shao J, Gilbert SR, Riddle RC, Long F, Johnson RS, Schipani E, Clemens TL: **Role of HIF-1alpha in skeletal development.** *Ann N Y Acad Sci* 2010, **1192**:322-326.
61. Wan C, Gilbert SR, Wang Y, Cao X, Shen X, Ramaswamy G, Jacobsen KA, Alaql ZS, Eberhardt AW, Gerstenfeld LC, et al.: **Activation of the hypoxia-inducible factor-1alpha pathway accelerates bone regeneration.** *Proc Natl Acad Sci U S A* 2008, **105**:686-691.
62. Tomlinson RE, Silva MJ: **HIF-1alpha regulates bone formation after osteogenic mechanical loading.** *Bone* 2015, **73**:98-104.
63. Donneys A, Weiss DM, Deshpande SS, Ahsan S, Tchanque-Fossuo CN, Sarhaddi D, Levi B, Goldstein SA, Buchman SR: **Localized deferoxamine injection augments vascularity and improves bony union in pathologic fracture healing after radiotherapy.** *Bone* 2013, **52**:318-325.
64. Zou D, Zhang Z, Ye D, Tang A, Deng L, Han W, Zhao J, Wang S, Zhang W, Zhu C, et al.: **Repair of critical-sized rat calvarial defects using genetically engineered bone marrow-derived mesenchymal stem cells overexpressing hypoxia-inducible factor-1alpha.** *Stem Cells* 2011, **29**:1380-1390.
65. Rios CN, Skoracki RJ, Mathur AB: **GNAS1 and PHD2 short-interfering RNA support bone regeneration in vitro and in an in vivo sheep model.** *Clin Orthop Relat Res* 2012, **470**:2541-2553.
66. Shen X, Wan C, Ramaswamy G, Mavalli M, Wang Y, Duvall CL, Deng LF, Guldberg RE, Eberhart A, Clemens TL, et al.: **Prolyl hydroxylase inhibitors increase neoangiogenesis and callus formation following femur fracture in mice.** *J Orthop Res* 2009, **27**:1298-1305.
67. Kanczler JM, Ginty PJ, Barry JJ, Clarke NM, Howdle SM, Shakesheff KM, Oreffo RO: **The effect of mesenchymal populations and vascular endothelial growth factor delivered from biodegradable polymer scaffolds on bone formation.** *Biomaterials* 2008, **29**:1892-1900.
68. Jabbarzadeh E, Starnes T, Khan YM, Jiang T, Wirtel AJ, Deng M, Lv Q, Nair LS, Doty SB, Laurencin CT: **Induction of angiogenesis in tissue-engineered scaffolds**

- designed for bone repair: a combined gene therapy-cell transplantation approach.** *Proc Natl Acad Sci U S A* 2008, **105**:11099-11104.
69. Lieberman JR, Daluiski A, Stevenson S, Wu L, McAllister P, Lee YP, Kabo JM, Finerman GA, Berk AJ, Witte ON: **The effect of regional gene therapy with bone morphogenetic protein-2-producing bone-marrow cells on the repair of segmental femoral defects in rats.** *J Bone Joint Surg Am* 1999, **81**:905-917.
 70. Lee RJ, Springer ML, Blanco-Bose WE, Shaw R, Ursell PC, Blau HM: **VEGF gene delivery to myocardium: deleterious effects of unregulated expression.** *Circulation* 2000, **102**:898-901.
 71. Zilberman Y, Kallai I, Gafni Y, Pelled G, Kossodo S, Yared W, Gazit D: **Fluorescence molecular tomography enables in vivo visualization and quantification of nonunion fracture repair induced by genetically engineered mesenchymal stem cells.** *J Orthop Res* 2008, **26**:522-530.
 72. Miller JS, Stevens KR, Yang MT, Baker BM, Nguyen DH, Cohen DM, Toro E, Chen AA, Galie PA, Yu X, et al.: **Rapid casting of patterned vascular networks for perfusable engineered three-dimensional tissues.** *Nat Mater* 2012, **11**:768-774.
 73. Hynes RO: **Integrins Bidirectional, Allosteric Signaling Machines.** *Cell* 2002, **110**:673-687.
 74. Burdick JA, Anseth KS: **Photoencapsulation of osteoblasts in injectable RGD-modified PEG hydrogels for bone tissue engineering.** *Biomaterials* 2002, **23**:4315-4323.
 75. Wang L, Stegemann JP: **Thermogelling chitosan and collagen composite hydrogels initiated with beta-glycerophosphate for bone tissue engineering.** *Biomaterials* 2010, **31**:3976-3985.
 76. Masters KS, Shah DN, Leinwand LA, Anseth KS: **Crosslinked hyaluronan scaffolds as a biologically active carrier for valvular interstitial cells.** *Biomaterials* 2005, **26**:2517-2525.
 77. Benoit DS, Schwartz MP, Durney AR, Anseth KS: **Small functional groups for controlled differentiation of hydrogel-encapsulated human mesenchymal stem cells.** *Nat Mater* 2008, **7**:816-823.
 78. Reyes CD, Garcia AJ: **Engineering integrin-specific surfaces with a triple-helical collagen-mimetic peptide.** *J Biomed Mater Res A* 2003, **65**:511-523.
 79. Reyes CD, Petrie TA, Burns KL, Schwartz Z, Garcia AJ: **Biomolecular surface coating to enhance orthopaedic tissue healing and integration.** *Biomaterials* 2007, **28**:3228-3235.

80. Shekaran A, Garcia JR, Clark AY, Kavanaugh TE, Lin AS, Guldberg RE, Garcia AJ: **Bone regeneration using an alpha 2 beta 1 integrin-specific hydrogel as a BMP-2 delivery vehicle.** *Biomaterials* 2014, **35**:5453-5461.
81. Shekaran A, Garcia AJ: **Extracellular matrix-mimetic adhesive biomaterials for bone repair.** *J Biomed Mater Res A* 2011, **96**:261-272.
82. Keselowsky BG, Collard DM, Garcia AJ: **Integrin binding specificity regulates biomaterial surface chemistry effects on cell differentiation.** *Proc Natl Acad Sci U S A* 2005, **102**:5953-5957.
83. Kim J, Kim IS, Cho TH, Kim HC, Yoon SJ, Choi J, Park Y, Sun K, Hwang SJ: **In vivo evaluation of MMP sensitive high-molecular weight HA-based hydrogels for bone tissue engineering.** *J Biomed Mater Res A* 2010, **95**:673-681.
84. Aota S, Nomizu M, Yamada KM: **The short amino acid sequence Pro-His-Ser-Arg-Asn in human fibronectin enhances cell-adhesive function.** *J Biol Chem* 1994, **269**:24756-24761.
85. Petrie TA, Raynor JE, Reyes CD, Burns KL, Collard DM, Garcia AJ: **The effect of integrin-specific bioactive coatings on tissue healing and implant osseointegration.** *Biomaterials* 2008, **29**:2849-2857.
86. Hennessy KM, Clem WC, Phipps MC, Sawyer AA, Shaikh FM, Bellis SL: **The effect of RGD peptides on osseointegration of hydroxyapatite biomaterials.** *Biomaterials* 2008, **29**:3075-3083.
87. Docheva D, Popov C, Mutschler W, Schieker M: **Human mesenchymal stem cells in contact with their environment: surface characteristics and the integrin system.** *J Cell Mol Med* 2007, **11**:21-38.
88. Popov C, Radic T, Haasters F, Prall WC, Aszodi A, Gullberg D, Schieker M, Docheva D: **Integrins alpha2beta1 and alpha11beta1 regulate the survival of mesenchymal stem cells on collagen I.** *Cell Death Dis* 2011, **2**:e186.
89. Goessler U, Bieback K, Bugert P, Heller T, Sadick H, Hörmann K, Riedel F: **In vitro analysis of integrin expression during chondrogenic differentiation of mesenchymal stem cells and chondrocytes upon dedifferentiation in cell culture.** *International Journal of Molecular Medicine* 2006.
90. Bengtsson T, Aszodi A, Nicolae C, Hunziker EB, Lundgren-Akerlund E, Fassler R: **Loss of alpha10beta1 integrin expression leads to moderate dysfunction of growth plate chondrocytes.** *J Cell Sci* 2005, **118**:929-936.
91. Knight CG, Morton LF, Onley DJ, Peachey AR, Messent AJ, Smethurst PA, Tuckwell DS, Farndale RW, Barnes MJ: **Identification in collagen type I of an integrin alpha2 beta1-binding site containing an essential GER sequence.** *J Biol Chem.* 1998, **273**:33287-33294.

92. Knight CG, Morton LF, Peachey AR, Tuckwell DS, Farndale RW, Barnes MJ: **The collagen-binding A-domains of integrins $\alpha(1)\beta(1)$ and $\alpha(2)\beta(1)$ recognize the same specific amino acid sequence, GFOGER, in native (triple-helical) collagens.** *J Biol Chem* 2000, **275**:35-40.
93. Knight CG, Morton LF, Peachey AR, Tuckwell DS, Farndale RW, Barnes MJ: **The Collagen-binding A-domains of Integrins $\alpha 1$ and $\alpha 2$ Recognize the Same Specific Amino Acid Sequence, GFOGER, in Native (Triple-helical) Collagens.** *Journal of Biological Chemistry* 2000, **275**:35-40.
94. Zhang WM, Kapyla J, Puranen JS, Knight CG, Tiger CF, Pentikainen OT, Johnson MS, Farndale RW, Heino J, Gullberg D: **$\alpha 1\beta 1$ integrin recognizes the GFOGER sequence in interstitial collagens.** *J Biol Chem* 2003, **278**:7270-7277.
95. Edinger M, et al: **Advancing animal models of neoplasia through in vivo bioluminescence imaging.** *Eur J Cancer* 2002, **38**:2128-2136.
96. J de Boer CvB, and C. Lowik: **Bioluminescent imaging: emerging technology for non-invasive imaging of bone tissue engineering.** *Biomaterials* 2006, **27**:1851-1858.
97. A Sacco RD, P Kraft, S Vitorovic, HM Blau: **Self-renewal and expansion of single transplanted muscle stem cells.** *Nature* 2008, **456**:502-506.
98. Sheyn D, Kallai I, Tawackoli W, Cohn Yakubovich D, Oh A, Su S, Da X, Lavi A, Kimelman-Bleich N, Zilberman Y, et al.: **Gene-modified adult stem cells regenerate vertebral bone defect in a rat model.** *Mol Pharm* 2011, **8**:1592-1601.
99. Lee JY, Kim S, Hwang do W, Jeong JM, Chung JK, Lee MC, Lee DS: **Development of a dual-luciferase reporter system for in vivo visualization of MicroRNA biogenesis and posttranscriptional regulation.** *J Nucl Med* 2008, **49**:285-294.
100. Vilalta M, Jorgensen C, Degano IR, Chernajovsky Y, Gould D, Noel D, Andrades JA, Becerra J, Rubio N, Blanco J: **Dual luciferase labelling for non-invasive bioluminescence imaging of mesenchymal stromal cell chondrogenic differentiation in demineralized bone matrix scaffolds.** *Biomaterials* 2009, **30**:4986-4995.
101. Allen AB, Gazit Z, Su S, Stevens HY, Guldberg RE: **In vivo bioluminescent tracking of mesenchymal stem cells within large hydrogel constructs.** *Tissue Eng Part C Methods* 2014, **20**:806-816.
102. Cheng AY, Garcia AJ: **Engineering the matrix microenvironment for cell delivery and engraftment for tissue repair.** *Curr Opin Biotechnol* 2013, **24**:864-871.
103. Murphy WL, McDevitt TC, Engler AJ: **Materials as stem cell regulators.** *Nat Mater* 2014, **13**:547-557.

104. Mikos AG, Papadaki MG, Kouvroukoglou S, Ishaug SL, Thomson RC: **Mini-review: Islet transplantation to create a bioartificial pancreas.** *Biotechnol Bioeng* 1994, **43**:673-677.
105. Lee KY, Mooney DJ: **Hydrogels for Tissue Engineering.** *Chemical Reviews* 2001, **101**:1869-1880.
106. Nicodemus GD, Bryant SJ: **Cell encapsulation in biodegradable hydrogels for tissue engineering applications.** *Tissue Eng Part B Rev* 2008, **14**:149-165.
107. Phelps EA, Headen DM, Taylor WR, Thule PM, Garcia AJ: **Vasculogenic bio-synthetic hydrogel for enhancement of pancreatic islet engraftment and function in type 1 diabetes.** *Biomaterials* 2013, **34**:4602-4611.
108. Salimath AS, Phelps EA, Boopathy AV, Che PL, Brown M, Garcia AJ, Davis ME: **Dual delivery of hepatocyte and vascular endothelial growth factors via a protease-degradable hydrogel improves cardiac function in rats.** *PLoS One* 2012, **7**:e50980.
109. Welzel PB, Prokoph S, Zieris A, Grimmer M, Zschoche S, Freudenberg U, Werner C: **Modulating Biofunctional starPEG Heparin Hydrogels by Varying Size and Ratio of the Constituents.** *Polymers* 2011, **3**:602-620.
110. Canal T, Peppas NA: **Correlation between mesh size and equilibrium degree of swelling of polymeric networks.** *J Biomed Mater Res* 1989, **23**:1183-1193.
111. Raeber GP, Lutolf MP, Hubbell JA: **Molecularly engineered PEG hydrogels: a novel model system for proteolytically mediated cell migration.** *Biophys J* 2005, **89**:1374-1388.
112. Reyes CD, Garcia AJ: **Alpha2beta1 integrin-specific collagen-mimetic surfaces supporting osteoblastic differentiation.** *J Biomed Mater Res A* 2004, **69**:591-600.
113. García AJ, Ducheyne P, Boettiger D: **Quantification of cell adhesion using a spinning disc device and application to surface-reactive materials.** *Biomaterials* 1997, **18**:1091-1098.
114. Munnix IC, Gilio K, Siljander PR, Raynal N, Feijge MA, Hackeng TM, Deckmyn H, Smethurst PA, Farndale RW, Heemskerk JW: **Collagen-mimetic peptides mediate flow-dependent thrombus formation by high- or low-affinity binding of integrin alpha2beta1 and glycoprotein VI.** *J Thromb Haemost* 2008, **6**:2132-2142.
115. Parsons JT: **Focal adhesion kinase: the first ten years.** *Journal of Cell Science* 2003, **116**:1409-1416.
116. Schaller MD: **Cellular functions of FAK kinases: insight into molecular mechanisms and novel functions.** *J Cell Sci* 2010, **123**:1007-1013.

117. Appeddu P: **Phosphorylation of Tyrosine 397 in Focal Adhesion Kinase Is Required for Binding Phosphatidylinositol 3-Kinase.** *Journal of Biological Chemistry* 1996, **271**:26329-26334.
118. Gutowski SM, Shoemaker JT, Templeman KL, Wei Y, Latour RA, Jr., Bellamkonda RV, LaPlaca MC, Garcia AJ: **Protease-degradable PEG-maleimide coating with on-demand release of IL-1Ra to improve tissue response to neural electrodes.** *Biomaterials* 2015, **44**:55-70.
119. Salimath AS, Garcia AJ: **Biofunctional hydrogels for skeletal muscle constructs.** *J Tissue Eng Regen Med* 2014.
120. Bryant SJ, Anseth KS: **Hydrogel properties influence ECM production by chondrocytes photoencapsulated in poly(ethylene glycol) hydrogels.** *J Biomed Mater Res* 2002, **59**:63-72.
121. Jha AK, Jackson WM, Healy KE: **Controlling osteogenic stem cell differentiation via soft bioinspired hydrogels.** *PLoS One* 2014, **9**:e98640.
122. Tan S, Fang JY, Yang Z, Nimni ME, Han B: **The synergetic effect of hydrogel stiffness and growth factor on osteogenic differentiation.** *Biomaterials* 2014, **35**:5294-5306.
123. Shih YR, Tseng KF, Lai HY, Lin CH, Lee OK: **Matrix stiffness regulation of integrin-mediated mechanotransduction during osteogenic differentiation of human mesenchymal stem cells.** *J Bone Miner Res* 2011, **26**:730-738.
124. Berner A, Reichert JC, Muller MB, Zellner J, Pfeifer C, Dienstknecht T, Nerlich M, Sommerville S, Dickinson IC, Schutz MA, et al.: **Treatment of long bone defects and non-unions: from research to clinical practice.** *Cell Tissue Res* 2012, **347**:501-519.
125. Laurencin C, Khan Y, El-Amin SF: **Bone graft substitutes.** *Expert Rev Med Devices* 2006, **3**:49-57.
126. Woo EJ: **Adverse events after recombinant human BMP2 in nonspinal orthopaedic procedures.** *Clin Orthop Relat Res* 2013, **471**:1707-1711.
127. Hynes RO: **Integrins: bidirectional, allosteric signaling machines.** *Cell* 2002, **110**:673-687.
128. Lin P, Lin Y, Lennon DP, Correa D, Schluchter M, Caplan AI: **Efficient lentiviral transduction of human mesenchymal stem cells that preserves proliferation and differentiation capabilities.** *Stem Cells Transl Med* 2012, **1**:886-897.
129. Dupont KM, Sharma K, Stevens HY, Boerckel JD, Garcia AJ, Guldberg RE: **Human stem cell delivery for treatment of large segmental bone defects.** *Proc Natl Acad Sci U S A* 2010, **107**:3305-3310.

130. Lutolf MP, Lauer-Fields JL, Schmoekel HG, Metters AT, Weber FE, Fields GB, Hubbell JA: **Synthetic matrix metalloproteinase-sensitive hydrogels for the conduction of tissue regeneration: engineering cell-invasion characteristics.** *Proc Natl Acad Sci U S A* 2003, **100**:5413-5418.
131. Gazit D, Turgeman G, Kelley P, Wang E, Jalenak M, Zilberman Y, Moutsatsos I: **Engineered pluripotent mesenchymal cells integrate and differentiate in regenerating bone: a novel cell-mediated gene therapy.** *The Journal of Gene Medicine* 1999, **1**:121-133.
132. Turgeman G, Pittman DD, Muller R, Kurkalli BG, Zhou S, Pelled G, Peyser A, Zilberman Y, Moutsatsos IK, Gazit D: **Engineered human mesenchymal stem cells: a novel platform for skeletal cell mediated gene therapy.** *J Gene Med* 2001, **3**:240-251.
133. Tai K, Pelled G, Sheyn D, Bershteyn A, Han L, Kallai I, Zilberman Y, Ortiz C, Gazit D: **Nanobiomechanics of repair bone regenerated by genetically modified mesenchymal stem cells.** *Tissue Eng Part A* 2008, **14**:1709-1720.
134. Kallai I, van Lenthe GH, Ruffoni D, Zilberman Y, Muller R, Pelled G, Gazit D: **Quantitative, structural, and image-based mechanical analysis of nonunion fracture repaired by genetically engineered mesenchymal stem cells.** *J Biomech* 2010, **43**:2315-2320.
135. Gamradt SC, Abe N, Bahamonde ME, Lee YP, Nelson SD, Lyons KM, Lieberman JR: **Tracking expression of virally mediated BMP-2 in gene therapy for bone repair.** *Clin Orthop Relat Res* 2006, **450**:238-245.
136. Dosier CR, Uhrig BA, Willett NJ, Krishnan L, Li MT, Stevens HY, Schwartz Z, Boyan BD, Guldberg RE: **Effect of cell origin and timing of delivery for stem cell-based bone tissue engineering using biologically functionalized hydrogels.** *Tissue Eng Part A* 2015, **21**:156-165.
137. Vila OF, Martino MM, Nebuloni L, Kuhn G, Perez-Amodio S, Muller R, Hubbell JA, Rubio N, Blanco J: **Bioluminescent and micro-computed tomography imaging of bone repair induced by fibrin-binding growth factors.** *Acta Biomater* 2014, **10**:4377-4389.
138. Kodama A, Kamei N, Kamei G, Kongcharoensombat W, Ohkawa S, Nakabayashi A, Ochi M: **In vivo bioluminescence imaging of transplanted bone marrow mesenchymal stromal cells using a magnetic delivery system in a rat fracture model.** *J Bone Joint Surg Br* 2012, **94**:998-1006.
139. Watson BM, Vo TN, Tatara AM, Shah SR, Scott DW, Engel PS, Mikos AG: **Biodegradable, phosphate-containing, dual-gelling macromers for cellular delivery in bone tissue engineering.** *Biomaterials* 2015, **67**:286-296.

140. Olivo C, Alblas J, Verweij V, Van Zonneveld AJ, Dhert WJ, Martens AC: **In vivo bioluminescence imaging study to monitor ectopic bone formation by luciferase gene marked mesenchymal stem cells.** *J Orthop Res* 2008, **26**:901-909.
141. Nakabayashi A, Kamei N, Sunagawa T, Suzuki O, Ohkawa S, Kodama A, Kamei G, Ochi M: **In vivo bioluminescence imaging of magnetically targeted bone marrow-derived mesenchymal stem cells in skeletal muscle injury model.** *J Orthop Res* 2013, **31**:754-759.
142. Hoffmann J, Glassford AJ, Doyle TC, Robbins RC, Schrepfer S, Pelletier MP: **Angiogenic effects despite limited cell survival of bone marrow-derived mesenchymal stem cells under ischemia.** *Thorac Cardiovasc Surg* 2010, **58**:136-142.
143. Bernardo ME, Fibbe WE: **Mesenchymal stromal cells: sensors and switchers of inflammation.** *Cell Stem Cell* 2013, **13**:392-402.
144. Shultz LD, Brehm MA, Garcia-Martinez JV, Greiner DL: **Humanized mice for immune system investigation: progress, promise and challenges.** *Nat Rev Immunol* 2012, **12**:786-798.
145. Nauta AJ, Fibbe WE: **Immunomodulatory properties of mesenchymal stromal cells.** *Blood* 2007, **110**:3499-3506.
146. Kim J, Hematti P: **Mesenchymal stem cell-educated macrophages: a novel type of alternatively activated macrophages.** *Exp Hematol* 2009, **37**:1445-1453.
147. Mountziaris PM, Mikos AG: **Modulation of the inflammatory response for enhanced bone tissue regeneration.** *Tissue Eng Part B Rev* 2008, **14**:179-186.
148. Gerstenfeld LC, Cullinane DM, Barnes GL, Graves DT, Einhorn TA: **Fracture healing as a post-natal developmental process: molecular, spatial, and temporal aspects of its regulation.** *J Cell Biochem* 2003, **88**:873-884.
149. Rojas-Pena ML, Olivares-Navarrete R, Hyzy S, Arafat D, Schwartz Z, Boyan BD, Williams J, Gibson G: **Characterization of distinct classes of differential gene expression in osteoblast cultures from non-syndromic craniosynostosis bone.** *J Genomics* 2014, **2**:121-130.
150. Wise JK, Sena K, Vranizan K, Pollock JF, Healy KE, Hughes WF, Sumner DR, Virdi AS: **Temporal gene expression profiling during rat femoral marrow ablation-induced intramembranous bone regeneration.** *PLoS One* 2010, **5**.
151. Kawakami Y, Ii M, Matsumoto T, Kuroda R, Kuroda T, Kwon SM, Kawamoto A, Akimaru H, Mifune Y, Shoji T, et al.: **SDF-1/CXCR4 axis in Tie2-lineage cells including endothelial progenitor cells contributes to bone fracture healing.** *J Bone Miner Res* 2015, **30**:95-105.

152. Egea V, von Baumgarten L, Schichor C, Berninger B, Popp T, Neth P, Goldbrunner R, Kienast Y, Winkler F, Jochum M, et al.: **TNF-alpha respecifies human mesenchymal stem cells to a neural fate and promotes migration toward experimental glioma.** *Cell Death Differ* 2011, **18**:853-863.
153. Kon T, Cho TJ, Aizawa T, Yamazaki M, Nooh N, Graves D, Gerstenfeld LC, Einhorn TA: **Expression of osteoprotegerin, receptor activator of NF-kappaB ligand (osteoprotegerin ligand) and related proinflammatory cytokines during fracture healing.** *J Bone Miner Res* 2001, **16**:1004-1014.
154. Lin Z, Rios HF, Volk SL, Sugai JV, Jin Q, Giannobile WV: **Gene expression dynamics during bone healing and osseointegration.** *J Periodontol* 2011, **82**:1007-1017.
155. Akdis M, Burgler S, Cramer R, Eiwegger T, Fujita H, Gomez E, Klunker S, Meyer N, O'Mahony L, Palomares O, et al.: **Interleukins, from 1 to 37, and interferon-gamma: receptors, functions, and roles in diseases.** *J Allergy Clin Immunol* 2011, **127**:701-721 e701-770.
156. Wu AC, Morrison NA, Kelly WL, Forwood MR: **MCP-1 expression is specifically regulated during activation of skeletal repair and remodeling.** *Calcif Tissue Int* 2013, **92**:566-575.
157. Willenborg S, Lucas T, van Loo G, Knipper JA, Krieg T, Haase I, Brachvogel B, Hammerschmidt M, Nagy A, Ferrara N, et al.: **CCR2 recruits an inflammatory macrophage subpopulation critical for angiogenesis in tissue repair.** *Blood* 2012, **120**:613-625.
158. Mercurio F, Manning AM: **NF-kappaB as a primary regulator of the stress response.** *Oncogene* 1999, **18**:6163-6171.
159. Novack DV: **Role of NF-kappaB in the skeleton.** *Cell Res* 2011, **21**:169-182.
160. Ucuzian AA, Gassman AA, East AT, Greisler HP: **Molecular mediators of angiogenesis.** *J Burn Care Res* 2010, **31**:158-175.
161. Gerwins P, Sköldenberg E, Claesson-Welsh L: **Function of fibroblast growth factors and vascular endothelial growth factors and their receptors in angiogenesis.** *Critical Reviews in Oncology/Hematology* 2000, **34**:185-194.
162. Daly C, Wong V, Burova E, Wei Y, Zabski S, Griffiths J, Lai KM, Lin HC, Ioffe E, Yancopoulos GD, et al.: **Angiopoietin-1 modulates endothelial cell function and gene expression via the transcription factor FKHR (FOXO1).** *Genes Dev* 2004, **18**:1060-1071.
163. Armulik A, Abramsson A, Betsholtz C: **Endothelial/pericyte interactions.** *Circ Res* 2005, **97**:512-523.

164. Tacchini L, De Ponti C, Matteucci E, Follis R, Desiderio MA: **Hepatocyte growth factor-activated NF-kappaB regulates HIF-1 activity and ODC expression, implicated in survival, differently in different carcinoma cell lines.** *Carcinogenesis* 2004, **25**:2089-2100.
165. Vogel S, Trapp T, Borger V, Peters C, Lakbir D, Dilloo D, Sorg RV: **Hepatocyte growth factor-mediated attraction of mesenchymal stem cells for apoptotic neuronal and cardiomyocytic cells.** *Cell Mol Life Sci* 2010, **67**:295-303.
166. Komori T: **Regulation of bone development and extracellular matrix protein genes by RUNX2.** *Cell Tissue Res* 2010, **339**:189-195.
167. Shu B, Zhang M, Xie R, Wang M, Jin H, Hou W, Tang D, Harris SE, Mishina Y, O'Keefe RJ, et al.: **BMP2, but not BMP4, is crucial for chondrocyte proliferation and maturation during endochondral bone development.** *J Cell Sci* 2011, **124**:3428-3440.
168. Tsuji K, Bandyopadhyay A, Harfe BD, Cox K, Kakar S, Gerstenfeld L, Einhorn T, Tabin CJ, Rosen V: **BMP2 activity, although dispensable for bone formation, is required for the initiation of fracture healing.** *Nat Genet* 2006, **38**:1424-1429.
169. Javed A, Afzal F, Bae JS, Gutierrez S, Zaidi K, Pratap J, van Wijnen AJ, Stein JL, Stein GS, Lian JB: **Specific residues of RUNX2 are obligatory for formation of BMP2-induced RUNX2-SMAD complex to promote osteoblast differentiation.** *Cells Tissues Organs* 2009, **189**:133-137.
170. Kaplan MH, Hufford MM, Olson MR: **The development and in vivo function of T helper 9 cells.** *Nat Rev Immunol* 2015, **15**:295-307.
171. Duque G, Huang DC, Macoritto M, Rivas D, Yang XF, Ste-Marie LG, Kremer R: **Autocrine regulation of interferon gamma in mesenchymal stem cells plays a role in early osteoblastogenesis.** *Stem Cells* 2009, **27**:550-558.
172. Baraniak PR, McDevitt TC: **Stem cell paracrine actions and tissue regeneration.** *Regen Med* 2010, **5**:121-143.
173. Garcia JR, Garcia AJ: **Biomaterial-mediated strategies targeting vascularization for bone repair.** *Drug Deliv Transl Res* 2016, **6**:77-95.
174. Feng JQ, Xing L, Zhang JH, Zhao M, Horn D, Chan J, Boyce BF, Harris SE, Mundy GR, Chen D: **NF-kappaB specifically activates BMP-2 gene expression in growth plate chondrocytes in vivo and in a chondrocyte cell line in vitro.** *J Biol Chem* 2003, **278**:29130-29135.
175. Graham TR, Odero-Marah VA, Chung LW, Agrawal KC, Davis R, Abdel-Mageed AB: **PI3K/Akt-dependent transcriptional regulation and activation of BMP-2-Smad signaling by NF-kappaB in metastatic prostate cancer cells.** *Prostate* 2009, **69**:168-180.

176. Seebach E, Freischmidt H, Holschbach J, Fellenberg J, Richter W: **Mesenchymal stroma cells trigger early attraction of M1 macrophages and endothelial cells into fibrin hydrogels, stimulating long bone healing without long-term engraftment.** *Acta Biomater* 2014, **10**:4730-4741.
177. Swartzlander MD, Blakney AK, Amer LD, Hankenson KD, Kyriakides TR, Bryant SJ: **Immunomodulation by mesenchymal stem cells combats the foreign body response to cell-laden synthetic hydrogels.** *Biomaterials* 2015, **41**:79-88.
178. Ishikawa F, Yasukawa M, Lyons B, Yoshida S, Miyamoto T, Yoshimoto G, Watanabe T, Akashi K, Shultz LD, Harada M: **Development of functional human blood and immune systems in NOD/SCID/IL2 receptor {gamma} chain(null) mice.** *Blood* 2005, **106**:1565-1573.
179. Shultz LD, Lyons BL, Burzenski LM, Gott B, Chen X, Chaleff S, Kotb M, Gillies SD, King M, Mangada J, et al.: **Human Lymphoid and Myeloid Cell Development in NOD/LtSz-scid IL2R null Mice Engrafted with Mobilized Human Hemopoietic Stem Cells.** *The Journal of Immunology* 2005, **174**:6477-6489.
180. Miura M, Miura Y, Padilla-Nash HM, Molinolo AA, Fu B, Patel V, Seo BM, Sonoyama W, Zheng JJ, Baker CC, et al.: **Accumulated chromosomal instability in murine bone marrow mesenchymal stem cells leads to malignant transformation.** *Stem Cells* 2006, **24**:1095-1103.
181. Tolar J, Nauta AJ, Osborn MJ, Panoskaltsis Mortari A, McElmurry RT, Bell S, Xia L, Zhou N, Riddle M, Schroeder TM, et al.: **Sarcoma derived from cultured mesenchymal stem cells.** *Stem Cells* 2007, **25**:371-379.
182. Rustad KC, Wong VW, Sorkin M, Glotzbach JP, Major MR, Rajadas J, Longaker MT, Gurtner GC: **Enhancement of mesenchymal stem cell angiogenic capacity and stemness by a biomimetic hydrogel scaffold.** *Biomaterials* 2012, **33**:80-90.
183. Cantu DA, Hematti P, Kao WJ: **Cell encapsulating biomaterial regulates mesenchymal stromal/stem cell differentiation and macrophage immunophenotype.** *Stem Cells Transl Med* 2012, **1**:740-749.
184. Seib FP, Prewitz M, Werner C, Bornhauser M: **Matrix elasticity regulates the secretory profile of human bone marrow-derived multipotent mesenchymal stromal cells (MSCs).** *Biochem Biophys Res Commun* 2009, **389**:663-667.
185. Sumanasinghe RD, Pfeiler TW, Monteiro-Riviere NA, Lobo EG: **Expression of proinflammatory cytokines by human mesenchymal stem cells in response to cyclic tensile strain.** *J Cell Physiol* 2009, **219**:77-83.
186. Arend WP: **The balance between IL-1 and IL-1Ra in disease.** *Cytokine & Growth Factor Reviews* 2002, **13**:323-340.

187. Waterman RS, Tomchuck SL, Henkle SL, Betancourt AM: **A new mesenchymal stem cell (MSC) paradigm: polarization into a pro-inflammatory MSC1 or an Immunosuppressive MSC2 phenotype.** *PLoS One* 2010, **5**:e10088.
188. Somoza RA, Correa D, Caplan AI: **Roles for mesenchymal stem cells as medicinal signaling cells.** *Nature Protocols* 2016, **11**.